INFORMATION TO USERS

This manuscript has been reproduced from the microfilm master. UMI films the text directly from the original or copy submitted. Thus, some thesis and dissertation copies are in typewriter face, while others may be from any type of computer printer.

The quality of this reproduction is dependent upon the quality of the copy submitted. Broken or indistinct print, colored or poor quality illustrations and photographs, print bleedthrough, substandard margins, and improper alignment can adversely affect reproduction.

In the unlikely event that the author did not send UMI a complete manuscript and there are missing pages, these will be noted. Also, if unauthorized copyright material had to be removed, a note will indicate the deletion.

Oversize materials (e.g., maps, drawings, charts) are reproduced by sectioning the original, beginning at the upper left-hand corner and continuing from left to right in equal sections with small overlaps.

Photographs included in the original manuscript have been reproduced xerographically in this copy. Higher quality 6" x 9" black and white photographic prints are available for any photographs or illustrations appearing in this copy for an additional charge. Contact UMI directly to order.

ProQuest Information and Learning
300 North Zeeb Road, Ann Arbor, MI 48106-1346 USA
800-521-0600



Downloaded from SHAREOK. Persistent Handle URL: https://hdl.handle.net/11244/452

UNIVERSITY OF OKLAHOMA

GRADUATE COLLEGE

LABORATORY IMAGING OF HYDRAULIC FRACTURES USING MICROSEISMICITY

A DISSERTATION

SUBMITTED TO THE GRADUATE FACULTY

in partial fulfillment of the requirements for the

degree of

DOCTOR OF PHILOSOPHY

BY

ZHENGWEN ZENG
Norman, Oklahoma
2002

UMI Number: 3045830



UMI Microform 3045830

Copyright 2002 by ProQuest Information and Learning Company.
All rights reserved. This microform edition is protected against unauthorized copying under Title 17, United States Code.

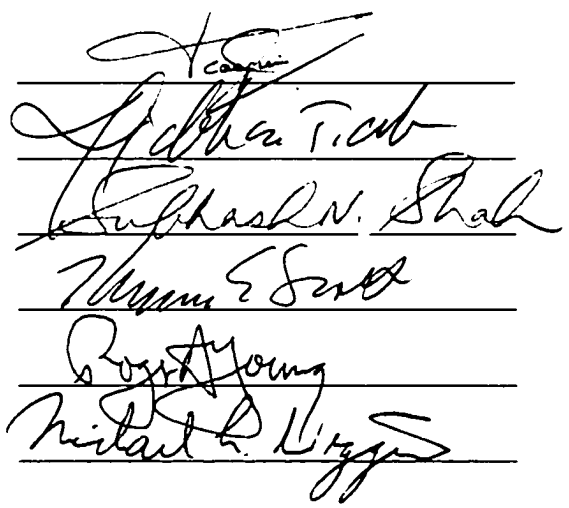
ProQuest Information and Learning Company
300 North Zeeb Road
P.O. Box 1346
Ann Arbor, MI 48106-1346

©Copyright by ZHENGWEN ZENG 2002
All Rights Reserved.

LABORATORY IMAGING OF HYDRAULIC FRACTURES USING MICROSEISMICITY

A DISSERTATION APPROVED FOR THE
MEWBOURNE SCHOOL OF PETROLEUM AND GEOLOGICAL
ENGINEERING

BY



Dedication

This dissertation is dedicated to Hong Liu, my wife, and Hedan, our daughter, for their love, patience, and support.

Acknowledgments

I would like to thank all those who helped me during my efforts towards this Ph.D. degree.

First of all, I would like to express my heartfelt thanks to my advisor, Prof. Jean-Claude Roegiers, for his visionary view about the future of rock mechanics; for leading me to the front of the petroleum-related rock mechanics; for his sound advice and generous support to my research and participation in national and international conferences; and, for his confidence about the future of this industry. It is a privilege to be his graduate student in this rough period of time.

My sincere gratitude also goes to Dr. Thurman E. Scott, Jr., for his interest and support of the research topic; and, for his full commitment in the experimental work and suggestions on the theoretical work.

I would like to sincerely thank each of my advisory committee members: to Prof. Subhash Shah for his guidance on non-Newtonian fluid mechanics and on modern hydraulic fracturing technology; to Prof. Djebbar Tiab for his introduction to well testing and for his book on petrophysics which introduced me to valuable experiments; to Prof. Michael Wiggins with whom I started my first class at The University of Oklahoma and learned the modern knowledge of fluid mechanics; and to Prof. Roger Young for his instructions in seismic exploration and advice on seismic sensors and on the theory of seismology.

Special thanks to Mr. Mike Shaw, Mr. Brian Silver, Mr. Julio Ronderos, Mr. Peter Keller, Mr. John Brumley, Mr. Kelvin Talkington, and Ms. Tammy Nelson, who helped me in my experimental work in various ways; and to Drs. Chandra Rai and Carl Sondergeld who helped measure the permeability of the extremely tight Jackfork sandstone.

Special thanks to Ms. Brooke Murrell, Ms. Chyrl Yerdon and Ms. Carla Cates for their help on various administrative affairs; to Mr. Donald Cruickshank for his

help in computer applications; and to Dr. Younane Abousleiman for the support in providing me with office space and computer resources after I no longer worked for the Rock Mechanics Institute.

Special thanks to a lot of individuals for their help and friendship, especially: to Dr. Xu Li and her family, for introducing me to Dr. Roegiers, helping me on my enrollment-related affairs and on my daily life in my initial days in this community; to Mr. Xianhong Yang and Dr. Wei Wang, for their help and encouragement in my study and research; and to Mr. Hongping Li, for his help in my effort of deciphering the data structure of the Vallen Acoustic Emission system.

I want to thank my family members: my father, Mr. Fanggao Zeng, for his understanding and encouragement; my mother, Ms. Xianglian Liu for her sacrifice to our big family until her last minute—her spirit of hard-working and kindness has been an important driving force in my life; my step-mother, Ms. Shuhua Lou, for taking care of my father when he suffered a stroke while this research was underway; my parents-in-law, Prof. Yingqing Liu and Ms. Yuzhen Tian, for their understanding and support; my brothers, Mr. Shichuan Zeng, Dr. Xuewen Zeng, Mr. Liwen Zeng and Mr. Fuwen Zeng, and my sister, Ms. Lanhua Zeng, for their longtime understanding and support towards my career efforts, and taking over most of my responsibilities to our father and other members in our big family.

Last but not the least, my special thanks to my wife, Hong Liu, and our daughter, Hedan, for their love, patience and support.

Table of Contents

Acknowledgments v

List of Figures xv

List of Tables xix

Abstract xxi

Chapter 1 Introduction 1

1.1 Industry's Concerns 2

1.2 Research Objectives 3

1.3 Dissertation Outline 4

Chapter 2 Review on Hydraulic Fracture Diagnostics 5

2.1 Development of Hydraulic Fracturing Technology 5

2.1.1 Origination 5

2.1.2 Damage Bypass 6

2.1.3 Massive Treatment 7

2.1.4 Tip Screen-out 7

2.1.5 The Future 8

2.2 Fundamentals of Hydraulic Fracturing Technology 9

2.2.1 Fracture Initiation 9

2.2.1.1 Stress Concentration Around A Borehole 9

2.2.1.2 Breakdown Pressure of An Inclined Borehole 12

2.2.1.3 Breakdown Pressure in Vertical Borehole 13
2.2.1.4 Breakdown Pressure in A Horizontal Borehole . . . 14
2.2.2 Fracture Orientation 17
2.2.3 Fracture Geometry 17
2.2.3.1 2-D Models 18
2.2.3.2 3-D Models 25
2.2.4 Hydraulic Fracturing Fluids 27
2.2.5 Hydraulic Fracturing Proppants 29
2.2.6 Remarks 31
2.3 Asymmetrical and Multiple Hydraulic Fractures 32
2.4 Current Hydraulic Fracture Diagnostic Techniques 35
2.4.1 Importance of Fracture Diagnosis 35
2.4.2 Pre-treatment Prediction 35
2.4.2.1 Fracture Modeling 35
2.4.3 Post-treatment Evaluation Technology 37
2.4.3.1 Impression Packers 37
2.4.3.2 Borehole Televiewer 38
2.4.3.3 Downhole Television 39
2.4.3.4 Radioactive Tracer 39
2.4.3.5 Temperature Log 39
2.4.3.6 Well Test 40
2.4.3.7 Production Analysis 40
2.4.4 Real-time Monitoring 41
2.4.4.1 Tiltmeter Technique 41
2.4.4.2 Microseismic Technique 42

2.4.5 Remarks 43

2.5 Microseismic Technique for Hydraulic Fracture Diagnosis 44

2.5.1 Brief Introduction of Microseismic Technique 44

2.5.2 Microseismic Technique for Laboratory Rock Mechanics Experiments 47

2.5.3 Microseismic Technique for Field Fracture Imaging 49

2.5.3.1 Verification of Induced Microseisms 49

2.5.3.2 Development of Tools and Observation Methods . . 53

2.5.3.3 Field Applications of Microseismic Technique . . . 55

2.5.4 Laboratory Hydraulic Fracturing Experiments and the Application of the Microseismic Technique 58

2.5.4.1 General Laboratory Work 58

2.5.4.2 Application of microseismic technology in laboratory Hydraulic Fracturing research 63

2.6 Discussion 65

Chapter 3 Development of A Simplex-based Microseismic Location Program **68**

3.1 Introduction 68

3.2 Simplex Algorithm for Microseismic Location 69

3.2.1 Physical Background of Microseismic Detection 69

3.2.2 Mathematical Principles of Microseismic Location 70

3.2.3 General Concept of the Simplex Optimization Algorithm . . 73

3.2.4 Simplex-based Algorithm for Microseismic Location 73

3.3 Development of the LOCATION Computer Program 75

3.3.1 Data Preparation 75

3.3.1.1 PAC Data Processing 75

3.3.1.2 Vallen Data Processing 78

3.3.2 Program Development 82
3.4 Verification of the LOCATION Program 85
3.4.1 Test 1: Synthetic Data from Various Parts of a Block 85
3.4.2 Test 2: Influence of Sensor Coverage 87
3.4.3 Test 3: Hsu-Nielson Source Events 88
3.4.4 Test 4: Event with Full Waveform Data from Other Researchers 89
3.5 Discussion 90
Chapter 4 Simulation of Microseismic Waveforms **92**
4.1 Introduction 92
4.2 Methodology 94
4.3 Development of the Formulae 94
4.3.1 Statement of the Problem 94
4.3.2 Governing Equations 95
4.3.3 Boundary Conditions 96
4.3.4 Betti's Reciprocity Theorem and Representation Theorem . 97
4.3.4.1 General Form of Representation Theorem 98
4.3.4.2 Representation Theorem on Body with Rigid Surface 100
4.3.4.3 Representation Theorem on Body with Free Surface 101
4.3.5 Representation of Microseismic Sources 101
4.3.6 Green's Function and The Spatial Derivatives 103
4.3.6.1 Green's Function 103
4.3.6.2 Generalization of the Green's Function 107
4.3.6.3 Spatial Derivatives of Green's Function 108
4.3.7 General Solution in Terms of Moment Tensor 110
4.3.8 Specific Solutions for Some Typical Microfractures 113

4.3.8.1 Mode-I Microfractures 114
4.3.8.2 Mode-II and Mode-III Microfractures 116
4.3.9 Discussion 119
4.3.9.1 Source Functions 119
4.3.9.2 Circular Microfractures vs. Elliptical Microfractures 121
4.4 Development of the WAVEFORM Simulator 121
4.4.1 Flowchart 121
4.4.2 Data Input 121
4.4.3 Observing Surface Identification and Coordinate Transformation 123
4.4.4 Calculation of Spatial Derivatives of Green's Function 126
4.4.5 Calculation of Displacements 126
4.4.6 Output Results 127
4.5 Validation of the WAVEFORM Program 127
4.5.1 Case 1. Mode-I Central Source, Epicentral Observer 127
4.5.2 Case 2. Mode-I Central Source, Offset Observers 128
4.5.3 Case 3 Mode-I Source at Different Depths, Epicentral Observer 129
4.5.4 Case 4. Mode-II Central Source, Offset Observers 130
Chapter 5 Petrophysical and Geomechanical Characterization of Jackfork Sandstone 132
5.1 Introduction 132
5.2 Geology of the Jackfork Formation 132
5.3 Petroleum Activities in the Jackfork Formation 134
5.4 Petrophysical Properties 136
5.4.1 Porosity, Bulk Density and Grain Density 136
5.4.2 Permeability 138

5.4.3 Seismic Velocities 139

5.5 Geomechanical Properties 141

5.5.1 Uniaxial Tensile Strength by Point Load Test 141

5.5.1.1 Point Load Test 141

5.5.1.2 Test Results 143

5.5.2 Uniaxial Compressive Strength, Young's Modulus and Poisson's Ratio 144

5.5.3 Triaxial Compressive Tests, Cohesion and Angle of Internal Friction 147

5.5.4 Fracture Toughness Test 151

5.5.4.1 CDISK Test 151

5.5.4.2 Theoretical background 153

5.5.4.3 K_{IC} Test Results 154

Chapter 6 Packer Influence on the Initiation of Hydraulic Fractures 156

6.1 Introduction 156

6.2 Experimental Setup 157

6.2.1 Description of the Materials 158

6.3 Experimental Observations 161

6.3.1 Test Tenn1 161

6.3.2 Test Tenn2 161

6.4 Numerical Modeling 162

6.4.1 Assumptions and Simplifications 163

6.4.2 Discretization and Boundary Conditions 163

6.4.3 External Load and Borehole Pressures 165

6.4.4 Simulation and Analysis of the Results 166

6.4.4.1 Case Tenn1-A 167

6.4.4.2 Case Tenn2-A 168
6.4.4.3 Case Tenn1-B 170
6.4.4.4 Case Tenn2-B 172
6.5 Discussion 173
Chapter 7 Applications: Imaging Asymmetrical Hydraulic Fractures 175
7.1 Introduction 175
7.2 Case 1: Asymmetrical Hydraulic Fractures in An Artificial Rock . . 177
7.2.1 Sample Preparation 177
7.2.1.1 Fabrication of the Artificial Rock 177
7.2.1.2 Wellbore Preparation 177
7.2.2 Procedures of the HF Experiment 180
7.2.3 Microseismic Data Acquisition and Processing 182
7.2.4 Images of the Asymmetrical Hydraulic Fractures 183
7.3 Case 2: Asymmetrical Hydraulic Fractures in Tennessee Sandstone . 186
7.3.1 Brief Introduction to the HF Experiment 186
7.3.2 Microseismic Observation and Data Reduction 187
7.3.3 The Asymmetrical Hydraulic Fracture Images 187
7.4 Case 3: Asymmetrical Hydraulic Fractures in Jackfork Sandstone . 189
7.4.1 Preparation of the HF Experiment 189
7.4.2 Test Procedures and Observed Results 191
7.4.3 Microseismic Data Acquisition 193
7.4.4 The Asymmetrical Hydraulic Fracture Images 196
7.5 Discussion 199
Chapter 8 Conclusions and Recommendations 201
8.1 Conclusions 201

8.2 Recommendations 203

Nomenclature **206**

References **213**

Appendix A: Derivation of Equation 4.25 **232**

Appendix B: Mode-I Fracture Toughness Formula for CDISK Test **233**

Appendix C: Hydraulic Fracturing Tests under Biaxial Stresses **239**

Appendix D: Sensitivity of the Microseismic Sensor **249**

Appendix E: Location Results of Experiment HF1 **251**

List of Figures

2.1 An example of frac and pack TSO treatment (from Nolte, 2000). . . 8

2.2 Global and local coordinate system (after McLennan et al., 1990). . 10

2.3 Stress and pressure profiles of horizontal borehole. 15

2.4 Geometry of the PKN model (from Mack and Warpinski, 2000). . . 19

2.5 Geometry of the KGD model (from Mack and Warpinski, 2000). . . 23

2.6 Principles of tiltmeters (from Wright et al. 1998b). 41

2.7 Schematics of induced microseisms (from Wright et al. 1998b). . . . 43

3.1 Simplex operations in 2D case (after Caceci and Cacheris, 1984). . . 74

3.2 The true HIT(signal) and the false HITs(noises) (from PAC, 1995). 76

3.3 An example of the full waveform and the noises before the first motion. 80

3.4 The file header and part of the first two microseismic events' parameters processed from the Vallen System-recorded waveform file. . . 82

3.5 Flowchart of the simplex-based microseismic LOCATION program. 83

3.6 GUI of the main menu of the LOCATION program in the data input stage. 84

3.7 The file header and part of the located events generated by LOCATION. 85

4.1 Fracture orientation and the transducer (from Ohtsu and Ono, 1984). 93

4.2 Methodology flowchart. 95

4.3 Coordinate system in the specimen. 96

4.4 A profile of a microseismic source model. 102

4.5 Definition of the geometry for the problem. 104

4.6 Kinematic parameters of the three typical microfracture modes. . . 114

4.7 Disk- and penny-shaped Mode-I micro-fractures. 115

4.8 Mode-II and Mode-III microfractures. 117

4.9 The three typical time functions of the microseismic source. 119

4.10 WAVEFORM simulator flowchart. 122

4.11 The original and the transformed coordinate systems for a sensor on $+X_3$ surface. 124

4.12 Epicentral first motions from Mode-I microfracturing. 128

4.13 First motions at offset observers from Mode-I microfractures. 129

4.14 Source depth influence on first motion acceleration waveforms. . . . 130

4.15 Mode-II micro-fracturing induced waveforms at three different points. 131

5.1 Distribution of the Jackfork formation (after Arbenz, 1984) 133

5.2 Sampling site of the Jackfork sandstone. 134

5.3 Some wells in the Jackfork formation (from Montgomery, 1996). . . 135

5.4 Experiemental set-up for seismic velocity measurement. 140

5.5 The point load test device (from ISRM, 1985 and Farmer, 1983). . . 141

5.6 Typical geometry of tested samples (from ISRM, 1985). 142

5.7 Load vs. deformation curves in point load test of Jackfork sandstone. 144

5.8 Stress-strain curves in uniaxial compressive tests for horizontal samples. 146

5.9 Stress-strain curves in uniaxial compressive tests for vertical samples. 146

5.10 Stress-strain curves in triaxial compresive tests of horizontal samples. 149

5.11 Stress-strain curves in triaxial compresive tests of vertical samples. . 150

5.12 Calculating cohesion and angle of internal friction using Mohr circles. 150

5.13 Geometry of the CDISK. 152

5.14 Load-displacement curves of fracture toughness tests. 155

6.1 Experimental setup for the asymmetrical loading. 158

6.2 Borehole structures (Zeng and Roegiers, 2001). 159

6.3 Injection time vs. borehole pressure in experiment Tenn1. 160

6.4 The longitudinal fracture in experiment Tenn1. 161

6.5 The transverse fracture in experiment Tenn2. 162

6.6 Coordinate system (Zeng and Roegiers, 2001). 164

6.7 The mesh in the studied domain (Zeng and Roegiers, 2001). 165

6.8 Overall σ_1 distribution in Tenn1-A (Zeng and Roegiers, 2001). . . 167

6.9 Near-wellbore σ_1 distribution in Tenn1-A (Zeng and Roegiers, 2001). 168

6.10 Overall σ_1 distribution in Tenn2-A (Zeng and Roegiers, 2001). . . 169

6.11 Near-wellbore σ_1 distribution in Tenn2-A (Zeng and Roegiers, 2001). 169

6.12 Overall σ_1 distribution in Tenn1-B (Zeng and Roegiers, 2001). . . . 171

6.13 Near-wellbore σ_1 distribution in Tenn1-B (Zeng and Roegiers, 2001). 171

6.14 Overall σ_1 distribution in Tenn2-B (Zeng and Roegiers, 2001). . . . 172

6.15 Near-wellbore σ_1 distribution in Tenn2-B (Zeng and Roegiers, 2001). 173

7.1 Cement sample in the MTS load frame. 180

7.2 Structure of the cement block (Scott, Zeng and Roegiers, 2000). . . 181

7.3 Monitoring the microseismic activities during the pressurization. . . 182

7.4 A 3D image of the asymmetrical hydraulic fracture in the cement block. 184

7.5 Image of the first 47 locatable events (Scott, Zeng and Roegiers, 2000). 184

7.6 Final stage images (Scott, Zeng and Roegiers, 2000). 185

7.7 Induced fracture in Tenn1 (Scott, Zeng and Roegiers, 2000). 186

7.8 Images from microseismic events (Scott, Zeng and Roegiers, 2000). . 188

7.9 Asymmetrical stresses in the Jackfork sandstone block. 189

7.10 The hand pump and the associated needle piston. 190
7.11 The hydraulic fracturing pumping system. 191
7.12 Microseismic monitoring and recording systems. 192
7.13 Borehole pressure vs. pumping time. 193
7.14 The asymmetrical hydraulic fractures in the Jackfork sandstone. . . 194
7.15 The sample and the sensors. 195
7.16 The structure of the YD-8 sensor (from BVMIC, 1992). 195
7.17 Images of the first 10 locatable microseismic events. 198
7.18 Image of the fractures by the first 20 locatable microseismic events. 198
7.19 Images by all the locatable microseismic events in HF1. 199
C.1 A 10 inch cubic hydrostone block with borehole and tubing. 240
C.2 The polyaxial loading frame (from Ong, 1994). 241
C.3 Polyaxial loading using the flatjacks (from Ong, 1994). 241
C.4 Rams used to supply the lateral stresses. 242
C.5 The MTS Test Star II loading frame (left) and the intensifier (right). 243
C.6 Pressure vs time curve in hydraulic fracturing Experiment 980521. . 245
C.7 The hydraulic fracture in Experiment 980521. 246
C.8 Pressure-time curve in Experiment 980701. 247
C.9 Non-planar hydraulic fracture in Experiment 98701. 248

List of Tables

1.1 Current methods (data: GRI, 1997) 3

1.2 Potential attendance (data: GRI, 1997) 3

2.1 Common crosslinkers (after Gulbis and Hodge, 2000) 28

2.2 Estimated closure stresses 31

2.3 Comparison of 2D models (data: Geertsma and Haafkens, 1979) . . 36

2.4 2D simulators for a 1-layer treatment (data: Warpinski et al., 1994) 36

2.5 3D simulators for a 3-layer treatment (data: Warpinski et al., 1994) 36

2.6 3D simulators for a 5-layer treatment (data: Warpinski et al., 1994) 37

3.1 Unknowns for different velocity models 71

3.2 Arrival time examples processed from PAC data 78

3.3 Located results of the first 10 synthetic data 86

3.4 Test of influence of sensor coverage 88

3.5 Location results of Hsu-Nielson sources 89

3.6 Location error of events from full waveforms 90

5.1 Bulk density, grain density and porosity 138

5.2 Permeability in different directions 139

5.3 Seismic velocity measurement 140

5.4 Uniaxial tensile strength 143

5.5 Uniaxial compressive strength and elasticity properties 147

5.6 Triaxial compressive strengths 149
5.7 Parameters and results of fracture toughness test 155
6.1 Properties of the materials 160
6.2 Cases and borehole pressures 166
7.1 Petrophysical properties of the artificial rock 178
7.2 Velocities in the block 179
7.3 Sensor coordinates on the cement block 180
7.4 Sensor coordinates on Tenn1 187
7.5 Sensor coordinates on the Jackfork sandstone block 196
7.6 Prarameters for data process 197
E.1 Location results of the Jackfork sandstone test 252
E.2 Location results of the Jackfork sandstone test (Cont. 1) 253
E.3 Location results of the Jackfork sandstone test (Cont. 2) 254

Abstract

This dissertation starts with an investigation of the industry's needs for future research and development of hydraulic fracturing (HF) technology. Based on the investigation results of a questionnaire answered by some industrial experts, it was found that reliable hydraulic fracturing diagnostic techniques are in need. Further critical review showed that the microseismic method was one of the most promising techniques which needed further development.

Developing robust algorithms and software for locating the coordinates of hydraulic fracturing-induced microseismic events, and for simulating the first motion of the induced waveforms were central tasks for this research. In the application of the software, initiation and propagation characteristics of asymmetrical hydraulic fractures were investigated. Along with this application, a newly discovered tight gas sandstone was systematically characterized; a method for measuring Mode-I fracture toughness was upgraded; and the packer influence on the initiation of asymmetrical fractures was numerically simulated. By completing this research, the following contributions have been made:

- Development of a simplex-based microseismic LOCATION program. This program overcame the shortcoming of ill-conditioning-prone conditions encountered in conventional location programs. In addition, it can be used for different velocity structures, either homogeneous, non-homogeneous, 2- or 3-dimensional.

- Development of a variance-based computer program, ArrTime, to automatically search the first arrival times from the full waveform data points. Using a five-point scanning window, this program is able to find the first arrival time in the full waveform within three points.

- Development of the first motion simulator of the induced microseismic waveforms. Using this WAVEFORM program, the first motion waveform am-

plitude in any direction at any location induced from seismic sources at an arbitrary location in a known fracturing mode can be calculated.

- Complete characterization of a newly discovered tight gas formation, the Jackfork sandstone. Through the work of this dissertation, the petrophysical and mechanical properties of this formation have been measured.

- Upgrade of a core sample-based method for the measurement of fracture toughness. By using a chevron-notched sample, this method is able to measure the Mode-I fracture toughness of common petroleum core samples. Furthermore, the measurement can be focused in any specific direction. This is very useful for the proper description of the material for the hydraulic fracture design.

- Discern of the packer influence on HF initiation. It is numerically shown that a properly functioning packer would transfer tensile stress concentrations from the sealed ends to the borehole wall in the maximum principal stress direction. In contrast, a malfunctioning packer would induce tensile stress concentrations at the sealed ends which, in turn, induces transverse fractures.

- Image of dynamics of the asymmetrical hydraulic fracture initiation and propagation.

1 Introduction

Hydraulic fracturing (HF) is a technology that consists of initiating a fracture from a sealed section of a borehole and then propagating it into the reservoir formation. It was originally applied to overcome near wellbore skin damage (Clark, 1949). Since then it has been expanded to include such applications as reservoir stimulation (Economides and Nolte, 2000), geothermal reservoir recovery (Robinson et al., 1971; Smith, 1982), waste disposal (Moschovidis et al., 1994), and control of sand production (Wedman et al., 1999). The same technology has also been adapted to measure the in-situ stress field (Haimson et al., 1988).

Hydraulic fracturing (HF) technology has made a significant contribution to the petroleum industry since its invention: production rates in many wells have experienced ten folds of increase (FOI) or even higher, speeding up the cash flow. In some low permeability reservoirs, HF stimulation has greatly increased the ultimate recovery. In recent years, HF has become a crucial tool in disposing drilling cuttings offshore, and in preventing sand production from poorly consolidated and unconsolidated formations.

The application of the HF technology has been very beneficial economically, especially in some challenging and complicated conditions. At the same time, the risk of failure increased greatly with the expanded applications of this technology.

In the past half century since the first application of HF treatment in 1947 in the Hugoton gas field, Grant County, Kansas, USA, this technology has been evolved enormously with continuous efforts from several generations of talented professionals.

However, there are still a lot of mysteries surrounding hydraulically induced

fractures. For example, how close is the real hydraulic fracture geometry to the predictive models? Is the fracture really symmetrical? How is the fracture initiated and propagated at different stages of pressurization? What is the dynamic displacement induced by the hydraulic fracturing? Before any effort is spent into answering these specific questions, opinions from the industrial professionals might help to set the direction of such efforts.

1.1 Industry's Concerns

When this research was in the inceptive stage, an industrial workshop on "Hydraulic Fracture Mechanics: Searching for the Next Breakthrough in Stimulation", was organized by Gas Research Institute (GRI, 1997). Seventy-six professionals from the production operators, service and consulting companies, and universities participated, discussed their recent advances and expressed their needs.

During this workshop, participants were asked to vote on 14 key aspects that needed to be improved; the top 3 being:

1. improve fracture diagnostics;
2. understand containment mechanisms; and,
3. investigate the impact of completion strategy on hydraulic fracture placement.

As to the question of current used fracture diagnostic methods, the following results were obtained, as shown in Table 1.1.

As to the question of topics that would be attended in future workshops, most people showed interest in learning advanced HF diagnostic technology, as shown in Table 1.2.

From the above survey, it is clear that the industry was eagerly waiting for some tools that could help diagnose the hydraulic fractures.

Table 1.1: Current methods (data: GRI, 1997)

Method	Number of users
Fracture modeling	33
Production data analyses	29
Radioactive tracers	25
Well testing	19
Temperature logs	17
Microseismic techniques	12
Tiltmeters	7
Others	4

Table 1.2: Potential attendance (data: GRI, 1997)

Topics	Potential participants
Advanced HF diagnostic technology	31
Impact of fracturing fluid on stimulation	26
Successful drilling practices	7
Surface logging	6
Building successful drilling alliances	4
Others	2

1.2 Research Objectives

Base on the above-mentioned industrial concerns and the critical literature review presented in the following chapter, the research objectives for this dissertation were set as below:

1. present a review on HF technology; especially on fracture imaging techniques;
2. develop a robust algorithm for microseismic location using the simplex theory;
3. create a simulator for calculating first motions of P-waves at any locations;
4. upgrade a fracture toughness test and systematically characterize a newly discovered tight gas sandstone reservoir;
5. numerically simulate the influence of the local stress field on the initiation of hydraulic fractures; and.

6. image the initiation and propagation of hydraulic fractures under asymmetrical stress field conditions.

1.3 Dissertation Outline

This dissertation includes 8 chapters.

Chapter 1 introduced concerns on HF technology and presented the research objectives for the dissertation.

Chapter 2 reviews the fundamentals of HF technology and the status of current fracture diagnostic techniques. Special attention is given to the microseismic techniques.

Chapter 3 presents a robust algorithm for locating induced microseismicity and validates the algorithm with synthetic and experimental data.

Chapter 4 derives the analytical solution for the displacement field and thus the first motion of the waveforms induced by a given hydraulic fracturing process. It shows the variation of the waveforms with the change of fracture modes, coordinates of the sources and receivers.

Chapter 5 systematically characterizes the geomechanical and petrophysical properties of a tight gas formation, the Jackfork sandstone, which is used to serve as one of the tested field cases. An upgraded method for measuring fracture toughness is also introduced.

Chapter 6 presents the local stress field influence on the initiation of fractures, using numerical modeling.

Chapter 7 gives three examples of stress-induced asymmetrical fractures and shows the images using the above-mentioned location algorithm.

Chapter 8 summarizes this dissertation and suggests directions for future work.

2 Review on Hydraulic Fracture Diagnostics

2.1 Development of Hydraulic Fracturing Technology

2.1.1 Origination

HF technology was originated from some field observations in acidizing, water flooding and cement squeezing (Howard and Fast, 1970). In the 1930s, petroleum engineers noticed that during acidizing and water flooding, the formation took very little fluid until the pressure reached a critical value. Once that critical pressure was reached, the formation took much more fluids than it normally would while the pressure remained almost constant.

A similar phenomenon was observed when squeezing cement. Cored samples from sidetracked holes confirmed that fractures had been induced along the weakness planes present in the sedimentary formation and the cement slurry had flowed into these places and settled as pancakes. Multiple fractures were observed in a cored sample where three cementing jobs were conducted and cement slurry of three different colors were located in three different fractures (Howard and Fast, 1970).

Due to the fact that the injection rate could be increased greatly once the critical pressure was reached and the formation was fractured, the idea of intentionally fracturing the formation to increase the injectivity and productivity of the well was

formed. This resulted in the first HF trial in the Hugoton gas field located in Grant County, Kansas, USA in 1947 (Howard and Fast, 1970).

Although this first trial was not as successful as expected in comparing the results to acidizing operations in the same reservoir, it was soon proven that HF was a very effective tool in overcoming near wellbore damage and in reaching deep reserves. Indeed, in this same reservoir, HF became the primary stimulation method by 1966.

At the same time, HF has been widely spread all over the world. By 1981, more than 800,000 HF operations had been performed. By 1988, this number had been over 1 million. It was estimated at about 35% to 40% of all newly drilled wells at that time were hydraulically fractured, and about 25% to 30% of the total U.S.A. oil reserves had been made economical via this process. HF stimulation was responsible for the economical recovery of 8 billion barrels of oil by the end of the 1980s (Veatch et al., 1990).

In fact, the wide spread application of HF technology was driven by the oil and gas market, which in return drove the development of HF technology. The development of this technology was roughly divided into three generations: damage bypass, massive treatment, and tip-screenout (Nolte, 2000).

2.1.2 Damage Bypass

The first generation of HF was applied to overcome near wellbore damage induced by drilling and completion. Usually the fracture size is limited within a short distance from the wellbore. The fracture can be propped or acidized. The function of this last technology is similar to matrix stimulation in overcoming near wellbore damage; the difference being that the flow is linear rather than radial. This technology was fully matured by the 1960s and was well summarized by Howard and Fast (1970).

One important consideration of using this technology is to avoid connecting to the water-bearing zone or gas cap; especially in high permeability formations.

2.1.3 Massive Treatment

The second generation of HF technology was used to fracture tight gas sandstones. Due to the increase of hydrocarbon prices in the 1970s, some low permeability reserves became economically recoverable. Compared to the damage bypass treatments, larger volumes (over 1 million gallons HF fluid and over 3 million lbm proppant) and long fracture lengths (several hundred to over one thousand feet) are achieved. This technology was very well documented in two books (Gidley et al., 1989; Economides and Nolte, 1990).

A key point here is to have the HF in the desired direction and contain the proppants to the desired height.

2.1.4 Tip Screen-out

The third generation of HF technology was characterized by changing the flow path in poorly consolidated or unconsolidated formations so as to prevent/control sand production. In contrast to the first and second generations of HF technology, this time HF is used in high permeability formations, and the main purpose is not to increase the production rate, but to reduce the near wellbore pressure gradient so as to prevent any solid particle motion.

The general idea of this technology is to break the formation near the wellbore with a certain amount of pad fluid. Then, a proppant slurry is pumped into the initiated fracture at a certain rate. Due to the high permeability of the formation, the fluid in the proppant slurry will leak off quickly and thus form a tip screen out (TSO). Subsequent proppant slurry will widen the fracture instead of propagating it. Because the proppants in the slurry plays similar function as the gravels in the gravel packing, this technology is also termed as "frac and pack". This technology is still under development, but brief introductions of this technology can be found in some publications and papers (e.g., Economides and Nolte, 2000).

Here again the critical point is to control the pad volume and the slurry pump

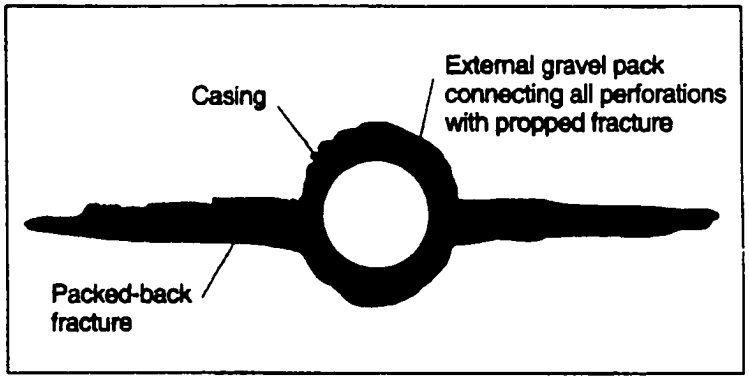


Figure 2.1: An example of frac and pack TSO treatment (from Nolte, 2000).

rate so that the fracture will be in the desired places, avoiding to connect to water bearing zones or other unwanted fluids, as shown in Figure 2.1 (Nolte, 2000).

2.1.5 The Future

In the future, HF technology will be integrated with reservoir management. Indeed it evolved gradually from a near wellbore treatment to reservoir considerations with the increase of penetration depth and the capability of pinpointing a specific by-passed zone. A recent development of fracturing through coiled tubing shows a great potential in re-stimulating previously by-passed zones (Schlumberger, 2001).

On the other hand, stimulation candidates for treatment have been expanded from formations of low permeability to formations of both low and high permeability. It is believed that, in the future, HF will develop to be a component in reservoir development optimization.

Yet the application of this technology has been widened, though the fundamental principles have essentially been kept unchanged.

2.2 Fundamentals of Hydraulic Fracturing Technology

2.2.1 Fracture Initiation

In order to introduce a fracture at the right place in the desired orientation, its initiation is important. This is mainly controlled by local stresses prevailing around the wellbore.

The focus for hydraulic fracture initiation is the breakdown pressure, even though, physically, fracture initiation might occur before the pressure reaches the breakdown pressure. Generally speaking, the breakdown pressure needs to overcome the stress concentration around a borehole in addition to the tensile strength of the rock.

2.2.1.1 Stress Concentration Around A Borehole

Assuming an arbitrary inclined infinite circular borehole in a homogeneous, isotropic, linearly elastic medium pressurized with fluid, the solution for the stress concentration around the borehole can be obtained by the superposition of Kirsch's solution, the anti-plane solution and the solution for an internally pressurized hole (Bradley, 1979). Assuming the far field principal stresses are σ_V, σ_H and σ_h, of which σ_V is vertical, σ_H and σ_h are horizontal, for an arbitrarily oriented inclined borehole, as shown in Figure 2.2, the local stress components due to σ_V, σ_H and σ_h,are as follows (McLennan et al., 1990):

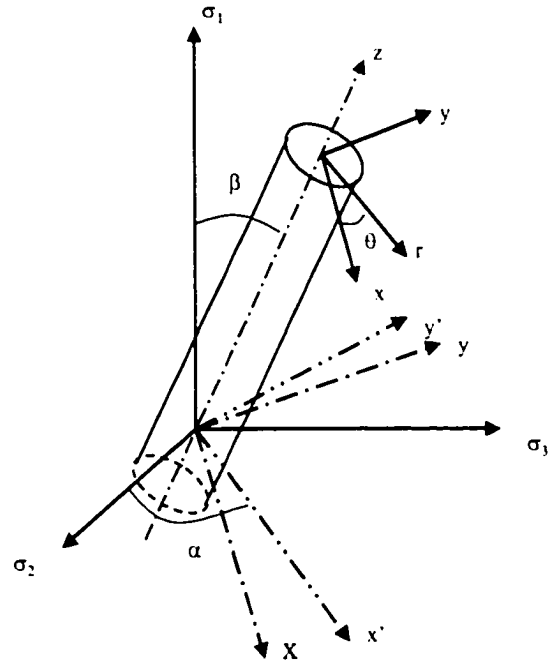


Figure 2.2: Global and local coordinate system (after McLennan et al., 1990).

$$\begin{Bmatrix} \sigma_x \\ \sigma_y \\ \sigma_z \\ \tau_{yz} \\ \tau_{xz} \\ \tau_{xy} \end{Bmatrix} = \begin{bmatrix} \sin^2\beta & \cos^2\beta\cos^2\alpha & \cos^2\beta\sin^2\alpha \\ 0 & \sin^2\alpha & \cos^2\alpha \\ \cos^2\beta & \sin^2\beta\cos^2\alpha & \sin^2\beta\sin^2\alpha \\ 0 & -\sin\alpha\cos\alpha\sin\beta & \sin\alpha\cos\alpha\sin\beta \\ -\sin\beta\cos\beta & \sin\beta\cos\beta\cos^2\alpha & \sin\beta\cos\beta\sin^2\alpha \\ 0 & -\sin\alpha\cos\alpha\cos\beta & \sin\alpha\cos\alpha\cos\beta \end{bmatrix} \begin{Bmatrix} \sigma_V \\ \sigma_H \\ \sigma_h \end{Bmatrix} \tag{2.1}$$

where:

$\sigma_V, \sigma_H, \sigma_h$—far field principal stresses;

$\sigma_x, \sigma_y, \sigma_z, \tau_{xy}, \tau_{xz}, \tau_{yz}$—components of the far field principal stresses at the near-wellbore region;

α—azimuth angle between σ_H and the borehole projection on the (σ_H, σ_h) plane; and,

β−inclined angle between σ_V and the borehole axis.

After applying an additional internal borehole pressure, p_w, the local stress components in the polar coordinate system become:

$$\begin{cases} \sigma_{rr} = \frac{\sigma_x+\sigma_y}{2}\left(1-\frac{r_w^2}{r^2}\right)+\frac{\sigma_x-\sigma_y}{2}\left(1-\frac{4r_w^2}{r^2}+\frac{3r_w^4}{r^4}\right)\cos(2\theta) \\ \qquad +\tau_{xy}\left(1-\frac{4r_w^2}{r^2}+\frac{3r_w^4}{r^4}\right)\sin(2\theta)+\frac{r_w^2}{r^2}p_w \\ \sigma_{\theta\theta} = \frac{\sigma_x+\sigma_y}{2}\left(1+\frac{r_w^2}{r^2}\right)-\frac{\sigma_x-\sigma_y}{2}\left(1+\frac{3r_w^4}{r^4}\right)\cos(2\theta) \\ \qquad -\tau_{xy}\left(1+\frac{3r_w^4}{r^4}\right)\sin(2\theta)-\frac{r_w^2}{r^2}p_w \\ \sigma_{zz} = \sigma_z-2\nu(\sigma_x-\sigma_y)\frac{r_w^2}{r^2}\cos(2\theta)-4\nu\tau_{xy}\frac{r_w^2}{r^2}\sin(2\theta) \\ \tau_{r\theta} = \left[\frac{\sigma_x-\sigma_y}{2}\sin(2\theta)+\tau_{xy}\cos(2\theta)\right]\left(1+\frac{2r_w^2}{r^2}-\frac{3r_w^4}{r^4}\right) \\ \tau_{rz} = \left[\tau_{xz}\cos\theta+\tau_{yz}\sin\theta\right]\left(1-\frac{r_w^2}{r^2}\right) \\ \tau_{\theta z} = \left[-\tau_{xz}\sin\theta+\tau_{yz}\cos\theta\right]\left(1+\frac{r_w^2}{r^2}\right) \end{cases} \tag{2.2}$$

where:

r_w−radius of the borehole;

r−radial distance from the center of the borehole; and,

θ−angle around the borehole from the local x−axis.

At the wall of the borehole, the above stresses are:

$$\begin{cases} \sigma_{rr} = p_w \\ \sigma_{\theta\theta} = (\sigma_x+\sigma_y-p_w)-2(\sigma_x-\sigma_y)\cos(2\theta)-4\tau_{xy}\sin(2\theta) \\ \sigma_{zz} = \sigma_z-2\nu(\sigma_x-\sigma_y)\cos(2\theta)-4\nu\tau_{xy}\sin(2\theta) \\ \tau_{r\theta} = 0 \\ \tau_{rz} = 0 \\ \tau_{\theta z} = 2(-\tau_{xz}\sin\theta+\tau_{yz}\cos\theta) \end{cases} \tag{2.3}$$

The above equation offers the general solution for the stress concentrations prevailing at the wall in an inclined borehole.

2.2.1.2 Breakdown Pressure of An Inclined Borehole

HF initiation is a tensile failure which occurs when the local minimum principal stress at a point on the wall reaches the tensile strength of the medium. The principal stresses at the wall of the borehole were derived by Daneshy (1973):

$$\begin{cases} \sigma_1 = \sigma_{rr} = p_w \\ \sigma_2 = \frac{\sigma_{zz}+\sigma_{\theta\theta}}{2} + \frac{1}{2}\sqrt{(\sigma_{\theta\theta} - \sigma_{zz})^2 + 4\tau_{\theta z}^2} \\ \sigma_3 = \frac{\sigma_{zz}+\sigma_{\theta\theta}}{2} - \frac{1}{2}\sqrt{(\sigma_{\theta\theta} - \sigma_{zz})^2 + 4\tau_{\theta z}^2} \end{cases} \tag{2.4}$$

The orientation of these local principal stresses in the local coordinate system are as follows:

1. σ_1 is in the radial direction;

2. σ_2 is tangent to the borehole wall and deviated from the borehole axis by an angle

$$\gamma = \frac{1}{2}\arctan\left(\frac{2\tau_{\theta z}}{\sigma_{\theta\theta} - \sigma_{zz}}\right) \tag{2.5}$$

and,

3. σ_3 is also tangent to the borehole wall and deviated from the borehole axis by $(90° - \gamma)$.

The breakdown pressure and the location of fracture initiation on the wall in the inclined borehole are obtained by minimizing p_w with respect to θ using:

$$\sigma_3 = T + p \tag{2.6}$$

where:

$T-$ the absolute value of tensile strength; and,

$p-$ the pore pressure at the point under consideration.

According to the above result, the trace of the fracture on the borehole wall makes an angle with the borehole axis. Based on the general principle of energy minimization, such a fracture will eventually reorient itself to propagate in the direction that is perpendicular to the minimum far field principal stress.

But this reorientation is not good for the fluid flow because the complex geometry will change the flow conditions and consume reservoir driving energy. This might be the reason that only vertical and horizontal wells were recommended for HF treatment (Economides and Nolte, 2000). However, a clear understanding of the physics allows us to consider borehole of any orientation.

2.2.1.3 Breakdown Pressure in Vertical Borehole

In this case, the overburden stress is usually one of the principal stress components and is parallel to the borehole. There are two possibilities for the fracture orientation: horizontal or vertical.

Case 1. Horizontal fracture

When the depth is shallower than about 2,000 ft, the vertical principal stress is usually the minimum principal stress and equal to the overburden (Roegiers, 1990). In this case, a horizontal fracture will initiate. The breakdown pressure, p_b, equals the overburden stress and is calculated as:

$$p_b = \sigma_v = \int_0^H \rho(h) g dh \tag{2.7}$$

where:

$H-$ depth; and,

$\rho(h)-$density at the depth h.

Case2. Vertical fracture

At depth larger than about 2,000 ft, the minimum principal stress is usually horizontal. Thus the hydraulically induced fracture is usually vertical. In this case, the breakdown pressure for an uncased, smooth wellbore is given by (Roegiers, 1990):

$$p_{b,upper} = 3\sigma_h - \sigma_H - p + T \tag{2.8}$$

where:

σ_h, σ_H – minimum and maximum horizontal principal stresses;

p – formation pore pressure at the fracture initiation point; and,

T – absolute value of the tensile strength of the formation.

In Eq.2.8, the subscript "upper" means this breakdown pressure defines the upper bound, because no fluid penetration is considered. When fluid penetration occurs before breakdown, poroelasticity effects need to be included (Detournay et al., 1986) and the breakdown pressure becomes:

$$p_{b,lower} = \frac{3\sigma_h - \sigma_H - 2\eta p + T}{2(1-\eta)} \tag{2.9}$$

where:

$\eta - \frac{\alpha(1-2\nu)}{2(1-\nu)}$, dummy variable;

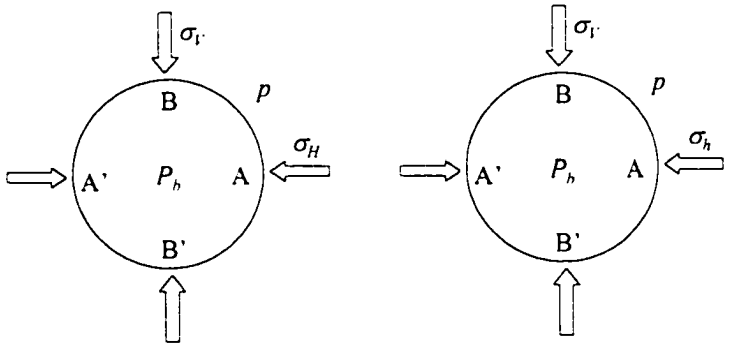
α – Biot's coefficient; and,

ν – Poisson's ratio of the formation rock.

A typical value of η is *0.25*. For low porosity rocks such as limestone, η is *0*. When the HF fluid penetrates to the vicinity of the borehole, the pore pressure increase corresponds to a decrease in the breakdown pressure. Therefore, in contrast to Eq.2.8, Eq.2.9 defines the lower bound of the breakdown pressure.

2.2.1.4 Breakdown Pressure in A Horizontal Borehole

In this case, two options are usually considered from a production engineering point of view (Brown and Economides, 1992). One is to drill the borehole along σ_h, the minimum horizontal stress; the other option is to drill along the σ_H, the maximum horizontal stress. Figure 2.3 schematically shows the cross-sections: the in-situ stresses, σ_V, σ_H and σ_h; the formation pressure, P; and the borehole pressure, P_b, in the two options. The breakdown pressures and the orientation of the induced fractures are as follows:



(a) Borehole along σ_h (b) Borehole along σ_H

Figure 2.3: Stress and pressure profiles of horizontal borehole.

Option 1. Borehole along σ_h

In this option, as shown in Figure 2.3 (a), there are two situations in terms of the magnitude of σ_H and σ_V.

1. $\sigma_H > \sigma_V$: Under this condition, the fracture initiates at points A and A' in Figure 2.3 (a). The stress at A and A' is:

$$\sigma_A = 3\sigma_V - \sigma_H - p \tag{2.10}$$

Accordingly, the upper and lower bounds of the breakdown pressures are:

$$\begin{cases} p_{b,upper} = 3\sigma_V - \sigma_H - p + T \\ p_{b,lower} = \frac{3\sigma_V - \sigma_H - 2\eta p + T}{2(1-\eta)} \end{cases} \tag{2.11}$$

where the variables are the same as that in the previous subsection.

The orientation of the fracture depends on the relative magnitude of σ_V and σ_h:

(a) if $\sigma_V > \sigma_h$, a longitudinal, horizontal fracture will initiate at the near-wellbore region, and then the fracture will be twisted into a transverse, vertical fracture and propagate away from the near-wellbore region, resulting in non-planar fractures; and,

(b) if $\sigma_V < \sigma_h$, a longitudinal, horizontal fracture will initiate and propagate in

the same orientation.

2. $\sigma_H < \sigma_V$: Under this condition, the fracture initiates at points B and B' in Figure 2.3 (a). The stress at B and B' is:

$$\sigma_B = 3\sigma_H - \sigma_V - p \tag{2.12}$$

Similarly, the upper and lower bounds of the breakdown pressures are:

$$\begin{cases} p_{b,upper} = 3\sigma_H - \sigma_V - p + T \\ p_{b,lower} = \frac{3\sigma_H - \sigma_V - 2\eta p + T}{2(1-\eta)} \end{cases} \tag{2.13}$$

where the variables are the same as that in the previous subsection.

This situation will generate a longitudinal, vertical fracture at the near-wellbore region, and then the fracture will be twisted into a transverse, vertical fracture and propagate away from the near-wellbore region, resulting in non-planar fractures.

Option 2. Borehole along σ_H

The cross-section is shown in Figure 2.3 (b). Similar to the analyses in **Option 1**, the breakdown pressures and the orientations of the fractures depend on the relative magnitude of σ_h and σ_V, as described below:

1. $\sigma_h > \sigma_V$:

Breakdown pressure bounds are:

$$\begin{cases} p_{b,upper} = 3\sigma_V - \sigma_h - p + T \\ p_{b,lower} = \frac{3\sigma_V - \sigma_h - 2\eta p + T}{2(1-\eta)} \end{cases} \tag{2.14}$$

Orientation: longitudinal, horizontal fracture initiates at points A and A', and propagates as a planar fracture.

2. $\sigma_h < \sigma_V$:

Breakdown pressure bounds are:

$$\begin{cases} p_{b,upper} = 3\sigma_h - \sigma_V - p + T \\ p_{b,lower} = \frac{3\sigma_h - \sigma_V - 2\eta p + T}{2(1-\eta)} \end{cases} \tag{2.15}$$

Orientation: longitudinal, vertical fracture initiates at points B and B', and propagates as a planar fracture.

In either of these two options, equations developed for the general inclined borehole can be used and will give the same results as above.

From the above introduction, it can be seen that the HF initiation is directly influenced by the local stresses, the borehole orientation and the formation properties.

2.2.2 Fracture Orientation

Without a proper and correct orientation, the fracture can not reach its target. Hubbert and Willis (1957) were the first to state that the preexisting stress conditions in the reservoir controlled fracture orientation; concluding that it was perpendicular to the minimum principal stress component. Based on the observation that breakdown pressures in most areas were less than the overburden pressures, they concluded that for the majority of HF operations, vertical fracturing was dominant. This conclusion still holds valid if the orientation of local stress field is consistent with that of the far stress field.

As indicated in the previous subsection, the local stress orientation can be totally different from that of the far stress field due to the borehole orientation. Some other factors such as pre-existing fractures can also introduce complexity in the fracture orientation. Therefore, only three-dimensional mapping of hydraulic fractures can provide a full description of its induced geometry.

2.2.3 Fracture Geometry

HF geometry is as important as the HF orientation to the success of reservoir stimulation. On the other hand, without a correct geometry, the reservoir performance optimization can not be achieved. For instance, if the fracture is not long enough, the drainage area would be not as big as designed. In contrast, if the HF is longer

than designed value, it might go out of the bounds and spoil the development strategy of the whole reservoir. A similar situation applies to the height of the induced HF. For the width, if the fracture is less than 2-3 times the proppant diameter, no effective flow can be pass through the fracture because of the lack of a continuous layer of proppant particles (Smith and Shlyapobersky, 2000). If the width is too large, the length and height would be reduced due to the volume balance. The ideal case is that the HF has the desired geometry. This requires the establishment of a relationship between the geometrical parameters and the operational parameters (pump rate, net pressure, etc.), the formation properties (Young's modulus, etc.), the HF fluid properties (viscosity, etc.).

The geometry of a hydraulic fracture is usually assumed to be symmetrical about the borehole and extending equally into the two opposite directions of the formation. Two-dimensional and three-dimensional models have been developed. In two-dimensional model, the fracture height is assumed constant, and only fracture length and fracture width are variables related to other properties. In three-dimensional model, the fracture length, height and width are all variables.

2.2.3.1 2-D Models

There are two original 2-D models: the PKN and KGD models. Each represents a set of different assumptions in deriving the analytical solutions. In addition, there are some other models, mainly upgrades from these two models.

The PKN Model

The PKN model was first developed by Perkins and Kern (1961), and later modified with the leakoff effect by Nordgren (1972). Based on Sneddon and his coworker's solutions (Sneddon,1946; Sneddon and Elliot, 1946) for the stress field and pressure associated with statically pressurized cracks, Perkins and Kern (1961) assumed a long fracture with constrained height, as shown in Figure 2.4.

The formulae for calculating the geometry (width, w) and the net pressure, p_{net},

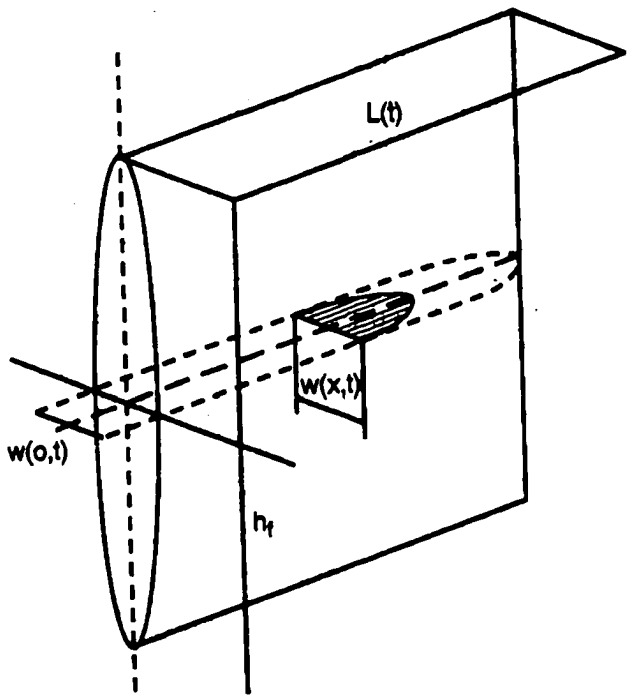


Figure 2.4: Geometry of the PKN model (from Mack and Warpinski, 2000).

of the HF are as follows:

$$\begin{cases} p_{net}(x,t) = \left[\frac{16\mu q_i E'^3 (L-x)}{\pi h_f^4}\right]^{\frac{1}{4}} \\ w(x,t) = 3\left[\frac{\mu q_i (L-x)}{E'}\right]^{\frac{1}{4}} \end{cases} \tag{2.16}$$

where:

$t-$ total pumping time;

$L-$ fracture length at t;

$w(x,t)-$ fracture width at the x from the wellbore at t;

$p_{net}(x,t)-$ net pressure at x from the wellbore at t;

q_i- total pump rate;

h_f- fracture height;

$\mu-$ fracturing fluid viscosity;

$E'-\frac{E}{1-\nu^2}$, plane strain modulus;

$E-$ Young's modulus; and.

ν– Poisson's ratio.

Based on this model the maximum fracture width, w_{max}, occurs at the borehole and the average fracture width, $\overline{w}$, is given by:

$$\overline{w} = \frac{\pi}{4} w_{\max} \tag{2.17}$$

This model implicitly assumes an infinite fracture length. So there is no direct formula for the fracture length. It neglects the fluid loss in leakoff and storage.

In addition, this model ignores any fracture mechanics aspects. This leads to the conclusion that, under typical hydraulic fracturing conditions, the pressure resulting from fluid flow is far larger than the minimum pressure required to extend a stationary fracture. Therefore once the fracture starts to propagate, it would continue to extend after pumping stopped, until the net pressure declines to less than the minimum pressure for propagation.

In order to overcome the lack of leak off and storage effect and to calculate the fracture length, other approaches such as the method by Carter (1957) were introduced.

Carter assumed that the total fluid injection rate, q_i, was consumed by q_L, the leakoff rate, and q_f, the fracture volume generation rate; hence,

$$q_i = q_L + q_f \tag{2.18}$$

Using the following leakoff model:

$$u_L = \frac{C_L}{\sqrt{t - t_{\exp}}} \tag{2.19}$$

and assuming a constant fracture width, $\overline{w}$, the fracture area, A_f, was obtained as:

$$\begin{cases} A_f = \frac{q_i \overline{w}}{4\pi C_L^2} \left[e^{S^2} \operatorname{erf} c\,(S) + \frac{2}{\sqrt{\pi}} S - 1 \right] \\ S = \frac{2C_L\sqrt{\pi t}}{\overline{w}} \end{cases} \tag{2.20}$$

where:

u_L – leakoff velocity;

C_L – leakoff coefficient;

t – total pumping time; and,

t_{exp} – time at which the fracture was exposed to the fluid.

The fracture length as a function of pumping time is then obtained by dividing the fracture area by twice the fracture height as shown in the following equation:

$$L(t) = \frac{A_f}{2h_f} \tag{2.21}$$

The application of this model involves iterations between the fracture length and the fracture width until a consistent solution is obtained. Then the borehore pressure can be calculated using Eq. (2.16).

Based on similar ideas, Howard and Fast (1970) introduced a nomograph method developed by Dowell. With this method, the fracture area is first determined from a set of graphs with given HF fluid properties. Then, the fracture penetration is determined with another graph.

In the above methods, the assumption of constant fracture width is not physically sound. Nordgren (1972) added the leakoff and storage effect with an increasing fracture width to Perkins and Kern's model and formed what is now called the PKN model. This model ends up with the following partial differential equation:

$$\frac{E'}{128\mu h_f}\frac{\partial^2 w^4}{\partial x^2} = \frac{8C_L}{\pi\sqrt{t - t_{\exp}(x)}} + \frac{\partial w}{\partial t} \tag{2.22}$$

Solution to Eq. (2.22) involves a numerical method with the definition of a dimensionless time, t_D:

$$t_D = \left[\frac{64C_L^5 E' h_f}{\pi^3 \mu q_i^2}\right]^{\frac{2}{3}} t \tag{2.23}$$

which is a stronger function of the leakoff coefficient ($C_L^{\frac{10}{3}}$) than of time (t^1). From this model the fracture width and length can be obtained as a function of time.

The advantage of this model is it does not involve any assumption of constant

fracture width. The disadvantage is obviously the lack of explicitly expressed analytical solutions. However, this has been partly remedied with the expressions of two limiting cases:

Case 1: storage dominated with $t_D < 0.01$

$$\begin{cases} L(t) = 0.39 \left[\frac{E' q_i^3}{\mu h_f^4}\right]^{\frac{1}{5}} t^{\frac{4}{5}} \\ w_w = 2.18 \left[\frac{\mu q_i^2}{E' h_f}\right]^{\frac{1}{5}} t^{\frac{1}{5}} \end{cases} \tag{2.24}$$

Case 2: leak-off dominated with $t_D > 1.0$

$$\begin{cases} L(t) = \frac{q_i t^{\frac{1}{2}}}{2\pi C_L h_f} \\ w_w = 4 \left[\frac{\mu q_i^2}{\pi^3 E' C_L h_f}\right]^{\frac{1}{4}} t^{\frac{1}{8}} \end{cases} \tag{2.25}$$

These two limiting cases give estimations of the fracture geometry with an error less than 10% when the dimensionless time requirements are met.

The PKN model is valid only when the fracture height is much smaller than the fracture length, typically less than $\frac{1}{3}$ of the tip to tip fracture length.

The KGD Model

This model was developed by Geertsma and de Klerk (1969) based on Khristianovich and Zheltov's (1955) solution on HF propagation and Barenblatt's (1962) fracture tip model. It assumes that the fracture width at any distance from the wellbore is independent of vertical position, i.e., a rectangular cross-section in the vertical direction, as shown in Figure 2.5.

Combining Khristianovich and Zheltov's assumption that the pressure in the fracture could be approximated by a constant pressure in the majority of the fracture body, except for a small region near the tip with no fluid penetration, and Barenblatt's concept of zero stress intensity factor at the close smooth tip, Geertsma and de Klerk derived the net pressure and fracture width at the wellbore as:

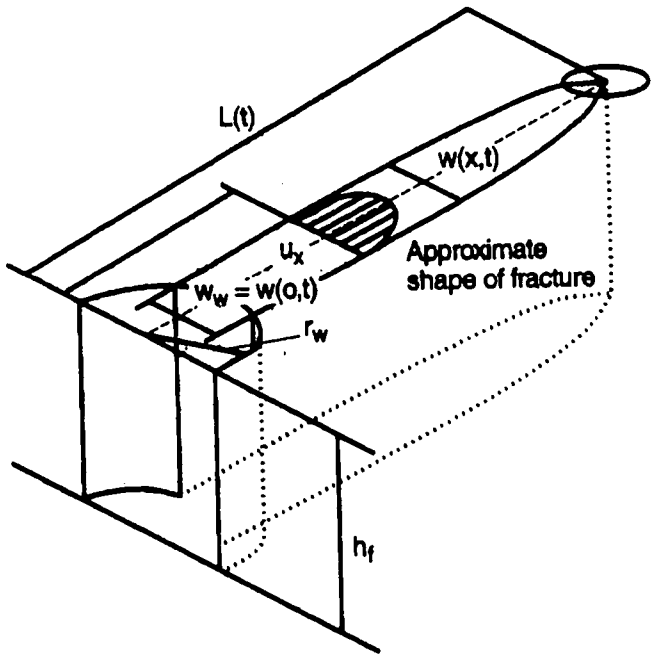


Figure 2.5: Geometry of the KGD model (from Mack and Warpinski, 2000).

$$\begin{cases} p_{net,w} \approx \left(\frac{21\mu q_t}{64\pi h_f L^2} E'^3\right)^{\frac{1}{4}} \\ w_w = \left[\frac{84}{\pi}\frac{\mu q_t L^2}{E' h_f}\right]^{\frac{1}{4}} \end{cases} \tag{2.26}$$

For the no-leak-off case, the fracture length and width can be calculated as:

$$\begin{cases} L(t) = 0.38\left[\frac{E' q_t^3}{\mu h_f^3}\right]^{\frac{1}{6}} t^{\frac{2}{3}} \\ w_w(t) = 1.48\left[\frac{\mu q_t^3}{E' h_f^3}\right]^{\frac{1}{6}} t^{\frac{1}{3}} \end{cases} \tag{2.27}$$

By including Carter's volume balance into the KGD model, Geertsma and de Klerk obtained the fracture length as:

$$\begin{cases} L(t) = \frac{q_t w_w}{64 C_L^2 h_f}\left(e^{S^2}\,\mathrm{erfc}\,(S) + \frac{2}{\sqrt{\pi}}S - 1\right) \\ S = \frac{8 C_L \sqrt{\pi t}}{w_w} \end{cases} \tag{2.28}$$

When the spurt loss, S_p, is included, w_w should be replaced by $w_w + \frac{8}{\pi}S_p$.

Radial Model

Radial fractures occur when the fractures initiate and grows from an unconfined point source. This can happen in two typical situations: horizontal fractures in a vertical well and transversely vertical fractures in a horizontal well. In either case the minimum principal stress is perpendicular to the fracture.

Both Perkins and Kern (1961) and Geertsma and de Klerk (1969) developed formulae for radial fractures. The radial length (radius of the fracture), R, and the width, w_w, of the KGD radial fracture are:

$$\begin{cases} R = \sqrt{\frac{q_i(4w_w+15S_p)}{30\pi^2 C_L^2}\left(e^{S^2}\operatorname{erf}c\left(S\right)+\frac{2}{\sqrt{\pi}}S-1\right)} \\ w_w = 2.56\left(\frac{\mu q_i R}{E'}\right)^{\frac{1}{4}} \\ S = \frac{15C_L\sqrt{\pi t}}{4w_w+15S_p} \end{cases} \tag{2.29}$$

For the no-fluid-loss case, the approximations for the geometry are:

$$\begin{cases} R = 0.52\left(\frac{E'q_i^3}{\mu}\right)^{\frac{1}{9}} t^{\frac{4}{9}} \\ w_w = 2.17\left(\frac{\mu^2 q_i^3}{E'^2}\right)^{\frac{1}{9}} t^{\frac{1}{9}} \end{cases} \tag{2.30}$$

For the large-fluid-loss case, the approximations for the geometry are:

$$\begin{cases} R = \frac{1}{\pi}\left(\frac{q_i^2 t}{C_L^2}\right)^{\frac{1}{4}} \\ w_w = 2.56\left(\frac{\mu q_i R}{E'}\right)^{\frac{1}{4}} \end{cases} \tag{2.31}$$

All the 2D fracture models assume that the fracture is planar. In the non-radial fracture models, full containment is assumed. The fracture is assumed to extend vertically to the full height of the pay zone, and only remain within the pay zone. In the radial fracture models, the fractures are assumed to initiate from a point source and propagated without restrictions.

While these assumptions greatly simplify the derivation of the solution, they not always represent the reality correctly. For instance, the pay zone thickness can be changed at different positions from the well to the tip. In addition, the containment

by the neighboring layers can not be satisfied all the time. So a varied fracture height is more close to reality. This leads to the development and application of 3D models.

2.2.3.2 3-D Models

There are no analytical solutions for 3-D models that can be simply and explicitly expressed. All 3-D HF simulation solutions need the application of numerical modeling.

There are three types of 3-D hydraulic fracturing models: pseudo 3-D models, planar 3-D models and general 3-D models. Different models have different assumptions and require different computational resources. Consequently, they are applicable to different situations.

Pseudo 3-D Models

These are quite similar to 2D models, except that the fracture is allowed to grow in height. There are two main types of P3D models: the lumped and the cell-based. The lumped P3D models assume an elliptical geometry in the fracture length direction and the fracture is symmetrical about the borehole. The fluid is assumed to flow from the perforations to the fracture tips, i.e., 1D flow. The cell-based P3D models assume that the fracture can be treated as a series of connected cells; each cell acting independently which means a plane strain condition.

The advantage of allowing height growth and relative simplicity in computing makes the P3D model-based simulators a practically useful tool in routine HF design (e.g., Palmer and Craig, 1984). But the 1-D fluid flow assumption limits their accuracy in predicting the hydraulic fracturing behavior.

Planar 3-D Models

These models assume that the fracture is planar and oriented perpendicular to the far-field minimum principal stress. The fracture grows in the length and height

within a narrow channel. This growth is controlled by linear fracture mechanics. The width of the fracture is controlled by the net pressure distribution in the fracture which is determined by the fluid flow rate in the fracture. The fluid flows in both length and height directions, i.e., a 2-D fluid flow. This 2-D fluid flow in turn is controlled by the fracture geometry. Therefore, this is a coupled problem between the fluid flow and the fracture growth in a linear elastic solid.

Due to the coupling nature between the fluid flow and the fracture initiation and propagation, simulators based on these models are very much time consuming in computation. They are usually used in situations where the containment is poor and the fracture extends into the top and the bottom barriers. Abou-Sayed and his coworkers (Abou-Sayed et al., 1984) presented a successful application of such a simulator in predicting the geometry of the HF growth in a poorly bounded pay zone .

General 3-D Models

There have no assumptions about the orientation of the fracture. They use the local stress field and fracture mechanics criteria as the guide for the initiation and propagation. Factors, such as wellbore orientation and perforation pattern, may cause the fracture to initiate in a particular direction before turning to the final preferred orientation which is perpendicular to the minimum far-field principal stress. Simulators incorporating such models are computationally intensive and usually require professional personnel to use them. Due to these reasons, they are mainly used as a research tool in some specific cases where detailed investigation is needed for such effects as near wellbore tortuosity in deviated boreholes (Brady et al., 1993).

A recent development in this area is the speeding up of computations with the development of advanced technology, such as parallel computing. For example, it takes hours to days for a single processor computer to solve a fully 3-D, linear elastic, boundary element solution of a complex geometry with one or more arbitrarily

shaped cracks problem. This same problem can be solved in less than an hour using a 32 or 64 processor system (Carter et al., 2000). Hence, such models might become industrial tool for HF simulation in the near future.

2.2.4 Hydraulic Fracturing Fluids

HF fluids play a crucial role in reaching the designed goals. They are used to initiate and propagate the fracture, to transport the proppant into the fracture and finally to clear the fracture after settling the proppants in place. Because of the varied properties of the reservoirs in permeability, porosity, pressure, temperature, material composition and other aspects, four different types of HF fluids: water-based fluids, oil-based fluids, foams and emulsions, have been developed for different reservoir conditions.

The ideal HF fluid needs to be viscous enough so that it can carry the proppants. On the other hand, it should break and clean up rapidly once the treatment is over, provide good fluid-loss control, exhibit low friction loss during pumping and be as economical as practical. In order to meet these requirements, different additives are added to the base fluid.

Water-based polymers are the most widely used HF fluids due to its relatively low cost. They can be used for various formation types, depths, pressures and temperatures.

In order to increase the viscosity, guar gum and other polymers are added. In situations where high proppant concentrations are needed, crosslinkers are used. They are compounds with metal ions that can react with guar or HPG through cis-OH pairs on the galactose side chains to form a complex molecule. When the complex molecules overlap each other, they react with other polymer strands and form a cross-linked network (Gulbis and Hodge, 2000).

These cross-linked molecules are easy to be broken when they are subjected to high shear rate. Similarly, the inherited Brownian motion makes the complex network unstable when the environmental conditions, such as pH range and tem-

Table 2.1: Common crosslinkers (after Gulbis and Hodge, 2000)

Crosslinker	**Borate**	**Titanate**	**Ziconate**	**Aluminum**
Polymers	Guar, HPG, CMHPG	Guar, HPG, CMHPG, CMHEC[a]	Guar[b], HPG[b], CMHPG, CMHEC[a]	CMHPG, CMHEC
pH range	8-12	3-11	3-11	3-5
Max temperature ($^\circ F$)	325	325	400	150
Shear degraded	No	Yes	Yes	Yes
a - Low pH (3-5) crosslinking only; b- High pH (7-10) crosslinking only				

perature, are changed. Therefore, each cross-linked fluid has its own range of applications. Table 2.1 shows the characteristics of the most commonly used crosslinkers (Gulbis and Hodge, 2000).

If high viscous fracturing fluids are left in the fracture, the effectiveness of the treatment would be largely reduced. Gel breakers are used to separate the polymers into small-molecular-weight fragments. The most widely used breakers are oxidizers and enzymes (Gulbis and Hodge, 2000).

Under the high pumping pressures usually required in stimulation, fracturing fluids can leakoff into the formation. Depending on the permeability of the formation and the fluid viscosity, the fluid loss can be very serious. Fluid-loss control additives are needed to reduce this leakoff. Typical fluid-loss additives include silica flours and oil-soluble resins. In some cases, dispersed fluids have to be used to reduce the fluid loss.

Other additives, such as friction reducers, bactericides, temperature stabilizers and clay stabilizers, may be needed sometimes.

Due to the addition of all these additives, the HF fluid can be a very complex material that can not be described by simple fluid behavior. More importantly, how such a complex fluid flows under formation pressure and temperature conditions in the hydraulically induced fracture is a problem that no simple theoretical means can solve. At the University of Oklahoma, a Fracture Fluid Characterization Facility (FFCF) has been built up to research this problem. Using this facility, tests on

fluid rheology, fluid-loss, perforation pressure loss and proppant transportation have been conducted (Shah et al., 1998).

2.2.5 Hydraulic Fracturing Proppants

Proppants are used to keep the fracture open after the HF treatment is completed. Because the fracture conductivity is proportional to the cubic power of the fracture width which is closely related to the distribution of the proppants in the fracture, the selection of proppant is very important to the success of the stimulation treatment.

The most important properties of the proppants include (1) proppant strength, (2) grain size and size distribution, (3) quantities of fines and impurities, and (4) proppant density.

In order to keep the fracture open, the proppants must be strong enough to resist the closure stresses[1]. There are four typical proppants that can be used for different closure stresses:

- sand—closure stress less than 6,000 psi;
- resin-coated proppant (RCP)—closure stress less than 8,000 psi;
- intermediate-strength proppant (ISP)—closure stress less than 10,000 psi; and,
- high-strength proppant—closure stress larger than 10,000 psi .

Quantitatively, the closure stress is larger than the effective minimum principal in-situ stress, but as an first order approximation, it can be estimated using the latter based on some typical formation properties, as described below.

In the case of no tectonic stresses, the total minimum horizontal stress, σ_h, can be expressed as (Thiercelin and Roegiers, 2000):

[1] The closure stress, also called closure pressure, was previously defined as the pressure to reopen an existing hydraulic fracture (Wapinski, 1990); recently it is redefined as the fluid pressure at which an existing fracture globally closes (Gulrajani and Nolte, 2000).

$$\sigma_h = \frac{\nu}{1-\nu}\sigma_v + 2\eta P \tag{2.32}$$

where:

ν−Poisson's ratio of the formation rock,

σ_v−overburden stress,

$\eta = \frac{\alpha(1-2\nu)}{2(1-\nu)}$, dummy variable:

α−Biot's coefficient; and,

P−formation pore pressure.

Rewriting Eq. (2.32) in terms of stress gradient (with respect to depth, z):

$$\frac{d\sigma_h}{dz} = \frac{\nu}{1-\nu}\frac{d\sigma_v}{dz} + 2\eta\frac{dP}{dz} \tag{2.33}$$

Using the following typical reservoir formation properties: $\nu = 0.25$, $\alpha = 0.75$, $\eta = 0.25$ (Thiercelin and Roegiers, 2000), $\frac{d\sigma_v}{dz} = 1.10\ psi/ft$, $\frac{dP}{dz} = 0.465\ psi/ft$ (Tiab and Donaldson, 1996), the minimum principal stress gradient in a normally pressurized formation is:

$$\frac{d\sigma_h}{dz} = 0.831\ psi/ft \tag{2.34}$$

According to the theory of poromechanics (Cheng and Detournay, 1993), the effective minimum principal stress, $\sigma_h^{'}$, can be expressed as:

$$\sigma_h^{'} = \sigma_h - \alpha P \tag{2.35}$$

so the depth gradient of the effective minimum principal stress, $\frac{d\sigma_h^{'}}{dz}$, can be calculated from Eq. (2.34) and the typical data:

$$\begin{aligned} \frac{d\sigma_h^{'}}{dz} &= \frac{d\sigma_h}{dz} - \alpha\frac{dP}{dz} \\ &= 0.482\ psi/ft \end{aligned} \tag{2.36}$$

Corresponding to this gradient of the effective minimum in-situ principal stress, the closure stress at different depths can be estimated, as shown in Table 2.2.

Table 2.2: Estimated closure stresses

Depth, ft	Estimated closuree stress, psi
4,000	1,928
6,000	2,892
8,000	3,856
10,000	4,820
15,000	7,320
20,000	9,640

Accordingly, the working depths of the four aforementioned proppants, based on their capabilities to resist closure stresses, are:

- sand—12, 448 ft;
- resin—16, 598 ft;
- intermediate-strength proppant (ISP)— 20, 747 ft; and,
- high-strength proppant—depth larger than 20, 747 ft.

Because in many cases, the reservoir formations are abnormally pressured, the closure stress can be even lower. So it seems that the sand and resin can work for most hydraulic fracturing working depths.

But this is only true at the beginning of the stimulation. When the reservoir starts producing, the pore pressure decreases rapidly, which in turn increases the closure stresses. Therefore, the closure stress for selecting the proppants should be the one that corresponding to the abandonment condition, not the initial reservoir pressure.

2.2.6 Remarks

Due to the difference in depth, borehole orientation and local stress field, the induced fractures changes from place to place. Different 2D and 3D models have been developed to describe these fractures. It is true that no theoretical model can precisely depict the real fracture. But the optimized development of the oilfield

needs the precise description of the induced fractures. This calls for the application of hydraulic fracture diagnosis.

2.3 Asymmetrical and Multiple Hydraulic Fractures

From the previous section, it can be seen that all the theoretical models assume the hydraulic fractures to have two identical and symmetrical wings. However, in the real world, asymmetrical fractures have been observed.

In an effort to investigate the containment mechanism of hydraulic fractures in tight formations, mineback operations have been conducted in the U.S.A. Department of Energy's Nevada Test Site. Warpinski et al. (1982) observed asymmetrical and multiple fractures. In one case, the fracture propagated downward vertically instead of outward horizontally. In another case, the outline of the induced fracture had an irregular shape: neither symmetrical about the vertical borehole, nor symmetrical about any horizontal axis. In the third case, the horizontal wellbore induced 5 parallel fracture strands: three of them initiating from the wellbore, two starting outside the wellbore. Among the former three, two could be considered as approximately aligned on both sides of the wellbore.

Bennett et al. (1983) studied the effect of the hydraulic fracture asymmetry on the production rate. Defining the asymmetry ratio as the ratio of the propped length of the longer wing to that of the shorter wing, it was found that the asymmetry ratio influenced the production rate adversely. In some cases, the production rate dropped to less than 60% of that from an otherwise identically and symmetrically propped vertical fracture. In the vertical asymmetrical aspect, it was found that if the proppants were carried downward, the production rate could be seriously reduced. In the worst case, the production rate could be reduced to that of an unfractured well.

Since 1979, the U.S. Department of Energy and the United States Steel Cor-

poration began to investigate the dynamics of coalbed methane reservoirs in the eastern Warrior Basin, Alabama, involving use of hydraulic fracturing technology. In the mineback of these hydraulic fractures, T-shaped geometries were observed, with a 120 ft vertical component and a pancake horizontal component of similar size, on the top (Boyer et al., 1986). In addition, the vertical component near the wellbore was a single fracture in the bottom half of the coal seam, but bi-fractured in the upper half of the coal seam.

Using a general three-dimensional numerical simulator, Vandamme and Jeffrey (1986) simulated the pressure behavior of the T-shaped fractures. By splitting the T-fracture into two L-fractures, they found that the interaction between the horizontal and the vertical components influenced the overall geometry of the fracture; and the width of the vertical component was reduced when the horizontal component extended over it.

Palmer et al. (1991) observed two different types of pressure behavior in hydraulically fracturing the coalbed seams in the Black Warrior Basin: one had a high breakdown pressure and a low propagation pressure; the other had both high breakdown and propagation pressures. Analyses indicated that the later case of high propagation pressure was the result of a T-shaped fracture.

Abass et al. (1992) investigated the generation of non-planar fractures in laboratory experiments. They found that initiation of the non-planar fractures was controlled by the wellbore orientation and the in-situ stress field. For a horizontal wellbore, the angle between the borehole axis and the maximum horizontal in-situ stress dominated the fractures: when the angle ranged from 0° to 50°, a single vertical fracture would be induced; when the angle varied between 50° and 70°, densely spaced multiple fractures would be generated at the wellbore, and reoriented to propagate outward; and, when the angle was between 70° and 90°, T-shaped fractures would be created from the wellbore.

Weng (1993) reported the analytical work on the fracture initiation and propagation from a deviated wellbore. Due to the relative orientation of the wellbore,

the in-situ stresses and the perforations, the fracture could re-orient in the near-wellbore region via turning and twisting. When the fractures were initiated from different perforations separately, they could link-up at the near-wellbore region, but the friction loss in this case would be much higher than that in the case of a single fracture. In other cases, the separately initiated fractures could propagate independently and form multiple fractures.

Jeffrey (1995) reported some new observations about asymmetrical hydraulic fractures from minebacks in coal seams in Australia. In general, the two wings were found asymmetrically propagated. In one extreme case, one wing was found about 10 times longer than the other wing.

Weijers et al. (2000) suggested simultaneous propagation of multiple hydraulic fractures. The formation of multiple fractures influenced the fracturing pressures and fracture dimensions. Analyses showed that the multiple fractures were a adverse factor from the production point of view.

From the above mentioned work, it can be seen that asymmetrical fractures are very common. The asymmetry exists in both horizontal and vertical directions. They can also occur in both vertical , deviated and horizontal wells. They reduce the efficiency of the stimulation and decrease the production potential.

Obviously, a clear and reliable image of the hydraulic fractures, especially their asymmetry, is needed in order to optimize future hydraulic fracturing stimulation treatments and reservoir management. Mineback is a useful tool for revealing the asymmetry of hydraulic fractures in field experiments. In order to image the asymmetry of hydraulic fractures in real world stimulation, other techniques are needed. In the following section, the hydraulic fracture diagnostic techniques will be reviewed.

2.4 Current Hydraulic Fracture Diagnostic Techniques

2.4.1 Importance of Fracture Diagnosis

Knowing the hydraulic fracture geometry is very important to the determination of optimum well location for tight gas reservoir development, water flooding, enhanced oil recovery, thermal recovery from geothermal wells, and thermal stimulation of tar sands. Under the same economic conditions, infill well locations can be selected to optimize drainage in low permeability reservoirs and to avoid early water breakthrough during water injection. For the successful application of frac and pack technology, the fracture must be controlled to surround the wellbore and extend shortly into the formation. Therefore, it is important that the geometry of the fracture be predicted before treatment, monitored during treatment and post-treatment evaluated.

2.4.2 Pre-treatment Prediction

2.4.2.1 Fracture Modeling

As mentioned above, the pre-treatment prediction technology refers to fracture simulators based on different propagation models. Depending on the selected propagation model, different results for the same problem can be arrived at.

Geertsma and Haafkens (1979) compared the calculations of four different 2D fracture design models. For identical input data, these models gave the design and prediction results as shown in Table 2.3.

It can be seen from this comparison that the effective fracture length varied greatly, from 185 ft to 486 ft. Also the effective width changed very much, from 0.16 in to 0.31 in.

By the 1990's both 3D and 2D simulators had been widely used to conduct HF treatment design and to predict the fracture geometry. In 1994 Warpinski et

Table 2.3: Comparison of 2D models (data: Geertsma and Haafkens, 1979)

Parameter	unit	**KGD**	**PKN**	**Daneshy**	**Nordgren**
Pad volume	bbl	750	1,350	320	1,650
Proppant slurry	bbl	1,250	650	1,680	350
Sand concentration	lbm/gal	3	2.5	2.5	3.5
Total amount of sand	lbm	157,500	68,000	176,000	51,000
Viscosity after pad	cp	36	36	36	36
Created frac length	ft	698	804	670	845
Effective frac length	ft	486	240	453	185
Created frac width	in	0.22	0.17	0.43	0.16
Effective frac width	in	0.20	0.16	0.31	0.16
Effective frac height	ft	98	94	97	85
Avg frac conductivity	Darcy-ft	7.1	6.5	9.8	6.5

Table 2.4: 2D simulators for a 1-layer treatment (data: Warpinski et al., 1994)

Parameter	unit	Max	Min	Mean	Std dev.	Num. of sim.
Frac length	ft	4,629	1,808	3,048	897	14
Frac height	ft	170				
Frac width at well	in	1.24	0.54	0.86	0.20	13
Average frac width	in	0.97	0.28	0.58	0.22	14
Net pressure at well	psi	1,986	61.8	988.19	815.11	12

al. (1994) published a comparison study of these simulators. The Gas Research Institute Staged Field Experiment No. 3 was used as the test example. In total, 34 simulators were tested for Newtonian and power law HF fluid for single layer, 3-layer and 5-layer treatments. Users of the 34 simulators included the major operators, service companies and consultants. Tables 2.4-2.6 show the statistic results of the major parameters calculated for the single layer, 3-layer and 5-layer treatment.

Table 2.5: 3D simulators for a 3-layer treatment (data: Warpinski et al., 1994)

Parameter	unit	Max	Min	Mean	Std dev.	Num. of sim.
Frac length	ft	3,289	902	2,433.75	922.57	8
Frac height	ft	596	337	409.5	86.94	8
Frac width at well	in	1.1	0.65	0.82	0.18	8
Average frac width	in	0.66	0.21	0.36	0.15	8
Net pressure at well	psi	1,433	1,005	1,189.88	160.73	8

Table 2.6: 3D simulators for a 5-layer treatment (data: Warpinski et al., 1994)

Parameter	unit	Max	Min	Mean	Std dev.	Num. of sim.
Frac length	ft	3,124	1,042	2,164.18	770.19	11
Frac height	ft	602	330	443.45	89.57	11
Frac width at well	in	1.18	0.49	0.82	0.21	11
Average frac width	in	0.66	0.25	0.42	0.15	7
Net pressure at well	psi	1,358	766	1,066.41	186.31	11

From these comparisons, it is clear that the HF simulators predict geometries with great deviation. Taking the fracture length as an example, the maximum prediction is about 3 times longer than the minimum prediction, and the standard deviation is more than 30% of the mean. Other parameters have similar characteristics in the distribution.

Given such a wide range of predictions, it is hard for the petroleum engineers to make proper decisions in managing the reservoir. Therefore, the HF simulator predictions can only be used as a reference to the possible reality. Observations using other physical means are needed.

HF simulators are also used to analyze the fracture geometry by matching the pressure history after the treatment. But matching the pressure history only supplies limited constraints which is not enough to obtain a unique solution. This kind of back-analysis must be combined with results from other methods, such as real-time monitoring or post-treatment well logging.

2.4.3 Post-treatment Evaluation Technology

2.4.3.1 Impression Packers

Impression packers are inflatable packers that can be run along the tubing and set at the targeted intervals. These are deformable rubber element which will deform and retain an impression of the wellbore wall. If there is a fracture along the wellbore, its orientation and azimuth can be determined from one or more of this kind of impressions, provided the impression packers are retrieved in the original

orientation.

This technique was widely used to determine hydraulic fracture orientation and azimuth since the 1960's (Fraser and Pettitt, 1962; Teufel et al., 1984). Now it is still used in the practice of in-situ stress measurement in rock mechanics engineering (Haimson, 1993).

2.4.3.2 Borehole Televiewer

Borehole televiewer is a sonic borehole logging tool introduced by Zemanek et al.(1969). It emits high frequency (1.3 MHz) sonic pulses; and receives and records the reflection of these pulses from the borehole wall. The tool scans around the borehole while moving along the borehole axis. If there is a fracture, no reflected signal would be received. In this way, the height and the width of the fracture can be detected.

Bredehoeft et al. (1976) reported a 50% success rate in using this technique to identify hydraulically fractured zones. Smith et al. (1982) compared this technique with downhole television and concluded that both give consistent results, but the televiewer log was most interpretable over intervals where spalling along the fracture edges had occurred.

The advantage of this technique is its ease to run due to its compatibility in operation with standard logging tools. In addition, the use of high frequency pulse signal makes it insensitive to wellbore fluids, whether it is water, oil, gas or drilling mud. The disadvantage of it is that the tool usually can not reach its full potential. It is also hard to keep the tool at the center of the borehole which is crucial for the success of the application. In addition, an in-gage hole is required in order to get dependable results. In case of breakouts, washout, spalling, etc., the quality would be decreased.

2.4.3.3 Downhole Television

Downhole television is a visual technique that uses an optical lens to image the borehole walls. If the conditions in the borehole can meet the requirements for the application of this tool, it would be the best technique to determine the fracture height, width, orientation and azimuth. The biggest problem with this technique is that the borehole fluid is not always clean and transparent.

2.4.3.4 Radioactive Tracer

Radioactive tracer technique includes two steps. The first step is to add the radioactive material into the proppant or the fluid; or both during the pumping stage. The second step is to run a gamma ray log after the hydraulic fracturing treatment. Using this method, the placement of the proppant within 2-ft of the wellbore can be imaged. By using different isotopes , the placement of the fluids at different pumping stages can be identified.

If the radioactive material is environmentally acceptable, this technique can be used to supply dependable information about the fracture orientation and height near the wellbore (Cipolla and Wright, 2000). It can also show the distribution of the pumped fluid in different zones.

2.4.3.5 Temperature Log

Because temperatures of the injected fluids and the formations are different, this feature can be used to identify the hydraulic fracture height. That is the principle of temperature log for diagnosing hydraulic fractures (Dobkins, 1981).

The application of this technology includes two runs of the logging tool. The first run conducted before the treatment results in a baseline of the thermal behavior of the wellbore. After the hydraulic fracturing treatment, a second log is obtained. Because the formation temperature is usually higher than that of the injected fluids, the temperature in the second log should have a lower value at the interval corresponding to the fracture. By comparing the two temperature logs, the

fracture height can be identified.

But the use of this technique could be misleading, especially when the fracture is not aligned with the wellbore (Holditch, 1989), or when the formation does not have a good confinement on height growth, or when large difference in thickness exists (Smith, 1982).

2.4.3.6 Well Test

Well test has been used to estimate reservoir and fracture properties for a long time. Similar to normal transient pressure analysis, the analysis for well test in a vertically fractured reservoir includes four steps (Poe and Economides, 2000):

(1) Plot both the pressure and pressure derivative data onto log-log curve coordinates (Tiab and Kumar, 1980), and identify the flow regimes according to the slope (e.g., unit slope stands for wellbore storage, half-slope for fracture storage, quarter slope for bilinear flow, etc.);

(2) Verify the identified flow regimes and estimate properties of the reservoir and the fracture using the data in the specific regimes;

(3) Simulate and modify the entire transient history using the estimated properties; and,

(4) Finally validate the obtained parameter estimates in conjunction with the flow regime limits.

The advantage of applying the well test method to fracture diagnostics is that it is based on sound theoretical analyses. The disadvantage is that the real fracture might be more complex than the simplified models could handle.

2.4.3.7 Production Analysis

This method is to match the production data with different fracture models, similar to the prediction of future performance of a fractured reservoir (Poe et al., 1995).

Because the solution is not unique, this method alone could not determine the required parameters of the fracture. In addition, the computational burden would

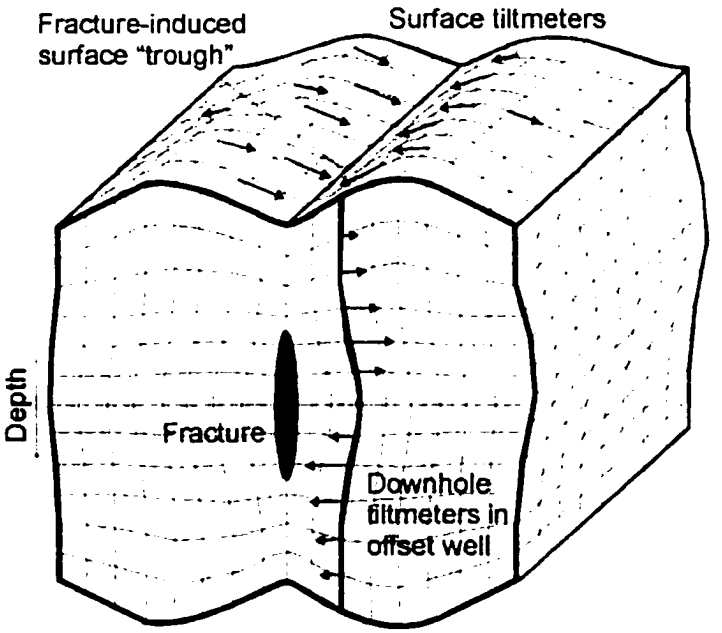


Figure 2.6: Principles of tiltmeters (from Wright et al. 1998b).

be huge, depending on the scale of the fracture and the expected resolution.

Nevertheless, it can be a good tool for validating estimates from other methods; it can also be used to estimate the input parameters.

2.4.4 Real-time Monitoring

2.4.4.1 Tiltmeter Technique

Bubble-level indicators measure the surface and downhole tilt due to the creation of the hydraulically induced fracture and inverse the tilt data to image this fracture. Figure 2.6 schematically demonstrates the surface and downhole tilt vectors induced by a fracture (Wright et al. 1998b).

The first tiltmeter fracture imaging was conducted in late 1970's. The original application was simply to determine the hydraulic fracture azimuth for well placement decisions. Since then, tiltmeters have developed rapidly and expanded their applications. The accuracy of tiltmeters has improved from 10 nano-rad to 1 nano-

rad. Maximum depth for surface tiltmeters to be able to operate has deepened from 3,000 ft to 6,000 ft, and now over 10,000 ft (Wright et al., 1998a). The application of downhole tiltmeters further enhanced the capability of the tiltmeter technique (Wright et al., 1998b).

According to Cipolla and Wright (2000), this last technique can determine the fracture height and length; which surface tiltmeters can easily determine the fracture azimuth and dip. It can also supply information about asymmetry and width as well as fracture volume.

This technique has the advantage of supplying a direct, far-field observation. It gives all the major geometric parameters about the fracture. Another advantage is that tiltmeters can be left in place for long term.

There are some disadvantages of using this method. The first one is it requires a large surface area to install the surface tiltmeters. In order to get the best deformation data, the tiltmeters must be set in a circular area around the treatment well. The ideal radius of this circle is between 15% and 75% of the depth of the treatment well. The second disadvantage is that the noise can have an amplitude as high as the signals. Due to the high sensitivity of the instrument, environmental factors such as wind, surface transportation, earth tide, etc. will influence the results. A third disadvantage is the cost of using this method is higher than some other methods. Also this method can not be used on deep wells.

The tiltmeter technique is currently one of the most actively used methods in mapping hydraulic fractures currently. It is mainly used in new areas where hydraulic fracturing stimulations have not been conducted before. It is also used in places where other methods do not give satisfied results.

2.4.4.2 Microseismic Technique

When the formation is hydraulically fractured, a lot of microseismic activities, or microseisms, are generated along the fractures, as shown in Figure 2.7 (Wright et al. 1998b). Detecting these microseisms and locating their positions gives the

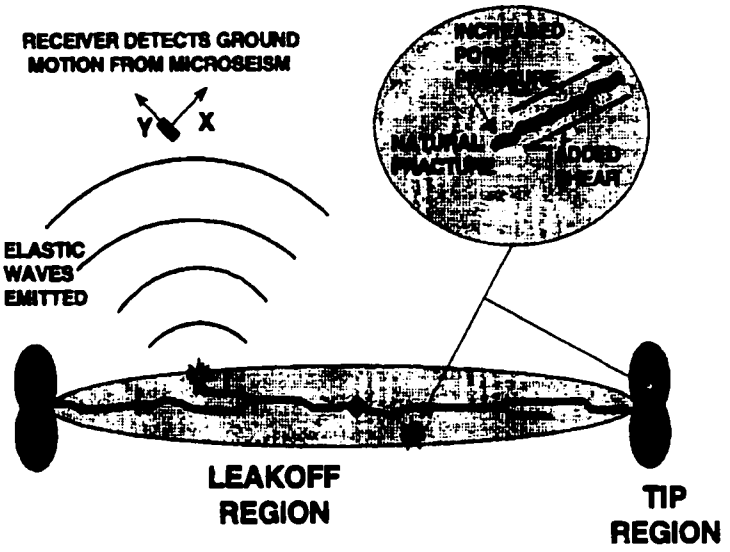


Figure 2.7: Schematics of induced microseisms (from Wright et al. 1998b).

image of the hydraulic fracture. Similar to the tiltmeter technique, this method is a far-field direct method. It can supply the length, height, azimuth and asymmetry of the fracture. It can also supply the dynamic information of the treatment; that is, features the fracture growth versus time.

The microseismic technique has been considered as the most promising fracture imaging technique for a long time due to its obvious direct relation to the fracture development. Experimental application of this technique has been reported in different places. But commercial service of this technique has not been available until recently. Status of this technique will be detailed in the following section.

2.4.5 Remarks

Hydraulic fracturing is a growing technology. With the expanded application areas and the increased cost of such treatments, diagnostics of the induced fractures becomes more and more important.

Diagnostic techniques developed with the development of the hydraulic fracture technology. Each diagnostic technique has its advantages and disadvantages, and

different techniques work for different situations. It is true that there is no single technique that can work alone to give all the fracture parameters. But this does not mean that there is no prevailing technique. In fact, based on field experience, it has been repeatedly shown that microseismicity is the most promising technology for mapping HF. The combination of the tiltmeters and the microseismicity could give all the requested geometrical parameters of the induced fracture.

In addition, microseismicity has the potential of real time mapping. Its application to natural fracture characterization and reservoir management is another important driving force for its rapid development.

2.5 Microseismic Technique for Hydraulic Fracture Diagnosis

2.5.1 Brief Introduction of Microseismic Technique

When a piece of material, such as rock, is subjected to load, it will deform, and fail when the load reaches a given limit. The deformation and failure of the material is characterized by the initiation and propagation of new cracks and/or reactivation and slip of old cracks. Accompanying the crack creation and reactivation is the rapid release of energy from a localized source or sources of transient elastic waves. These released elastic waves are called microseisms (MS) or acoustic emissions (AE).

Other terms, such as microseismics, microseismic activity, microseismicity, rock noises, rock talk, seismo-acoustic activity, elastic shocks, subaudible noise, etc., are also used to describe the same phenomenon. It was recommended that microseismic activity or acoustic emission should be used (Hardy and Leighton, 1977). Usually microseismics is used for rock-related phenomena and acoustic emission for metal and other material-related phenomena. In this dissertation, both terms will be used equivalently according to the context.

The recognition of the acoustic emissions in metals and microseisms in rocks

happened at almost the same time in the 1930s. In 1936, Forster and Scheil discovered "clicks" during the formation of martensite in high-nickel content steel. This led to the discovery of acoustic emissions (Scott, 1991).

In 1938, Obert detected some "spurious signals" generated automatically by the rock when he was measuring seismic velocities in rock in an effort to correlate the seismic velocity to the polar load in the lead-zinc mines in Northeastern Oklahoma. This phenomenon was encountered again when Obert and Duvall conducted a similar seismic velocity test in a 5,000 ft deep copper mine in Northern Michigan. However, this time it was easy to identify the source of these signals because the evidence of high stress was present everywhere. In fact, part of this mine was subject to numerous rockbursts (Obert, 1977).

It was clear that the acoustic emission and microseism phenomena are the results of stress adjustment. So the acoustic emission and microseism events can serve as an indicator for the stress status inside the material. This led to the development of the acoustic emission and microseism technology, or AE/MS technology.

Since these discoveries, acoustic emission and microseismicity have developed independently as two different disciplines for several decades.

In 1953, Kaiser published his work on relationship between acoustic emission rate and loading history. This milestone work setup the foundation for modern AE research, and led to the name of Kaiser effect.

In 1971 the ASTM issued the 1st standard about AE as a nondestructive testing method (ASTM, 1971). Since then, AE has been widely used as an non-destructive test (NDT) tool in many different areas, such as in the material industry to check the flaws, in the nuclear industry to supervise the reactors; in the aviation and space industry to inspect the integrity of some important parts; in the petroleum and chemical industries to monitor high pressure pipes and tanks; and in mechanical engineering to oversee cutting and other similar processes. With the increasing practice, new standards have been revised and issued (e.g. ASNT, 1987).

Microseism, on the other hand, has developed rapidly with the adoption of the-

ories and instrumental techniques from seismology. It has been developed in both laboratory investigations and field applications. The discovery that microseisms generated in rocks under high stress is significant which provided the basis for detecting and delineating areas of high stress; and, further, monitoring rock stability and predicting rockbursts. Since the building of the first microseism network in South Africa in 1939, a lot of monitoring stations for rockburst prediction have been set up in various mines all over the world (e.g. Hardy and Leighton, 1977).

In 1967, seventeen sparsely distributed research individuals working in the acoustic emission field in the USA and Canada organized the Acoustic Emission Working Group (AEWG). In 1970, Hardy, a geomechanics professor working on microseisms at the Pennsylvania State University, joined the Acoustic Emission Working Group. This began the coupling and cross-fertilization of the two similar but previously isolated fields. From 1975 to 1996, a series of six conferences on Acoustic Emission / Microseismic Activity in Geologic Structures and Materials were held at the Pennsylvania State University (Hardy and Leighton, 1977, 1980, 1984; Hardy, 1989, 1995, 1998). Papers published in these proceedings reflected a major trend of acoustic emission work in the geological engineering related topics. They covered different aspects in this field, such as instrumental development, theoretical analysis, laboratory investigation and field application.

In 1969, the Japanese Committee on Acoustic Emission (JCAE) was established. In 1972, the JCAE and the AEWG inaugurated the first U.S.-Japan Joint Symposium on Acoustic Emission. Since then, this symposium became the biennial International Acoustic Emission Symposia (Drouillard, 1996). The proceedings of these symposia have recorded the major on-going progress of acoustic emission research all over the world. While the diversified topics covered by the symposia made the proceedings a complete document (e.g. Yamaguchi et al., 1990), they were less attractive than those on some specified topics: for example, people working in hydraulic fracturing would have no interest in things related to paper making.

In contrast to the above conferences and symposia hosted by the same organi-

zation at the relatively fixed cities, the International Symposia on Rockburst and Seismicity in Mines were hosted by different organizers in different countries, but on relatively narrow topics. Since 1982, four symposia on this topic have been held in South Africa, USA, Canada and Poland (Gibowicz and Lasoki, 1997). Papers in these proceedings were mainly on the field application of the MS technique.

Lord (1975) published an excellent review on the early development of acoustic emission technology. A review on early history of AE/MS technique was offered by Hardy (1977). Drouillard (1996) edited a historical description on the development of AE/MS technique.

2.5.2 Microseismic Technique for Laboratory Rock Mechanics Experiments

In laboratory-related research, acoustic emission studies have been mainly conducted to either substantiate field observations or to investigate some fundamental aspects of the geological structures and materials during deformation and failure. Among these studies, the AE rate, the Kaiser's effect, the source location, and the source mechanisms have been investigated more extensively due to their direct connection to some practical problems. Lockner (1993) systematically summarized the role of acoustic emission in the study of experimental rock mechanics. It was concluded that significant progress has been made in mapping fault nucleation and propagation through the use of 3D AE event location. This supplied a foundation for the application of AE mapping technique to laboratory studies of hydraulic fractures.

In recent years, rock mechanics-related AE lab research moved to solving practical problems. Masuda et al. (1993) investigated the characteristics of induced AE activity when fluid was injected into dry granite samples under hydrostatic pressure and into saturated granite samples under differential stress state. It was found that no AE was induced in the dry sample while thousands of AE were detected in the

second case. Further research showed that the induced AE activity in the saturated sample was controlled by the pre-existing in-situ differential stress state and the heterogeneity of the fracture strength in the host rock. This result could be helpful to the interpretation of induced MS activities during water/gas/steam flooding in enhanced oil recovery.

Cox and Meredith (1993) tried to develop a method to predict the material damage from measurable AE parameters. The preliminary results were encouraging. The problem in using this method resides the completeness of AE recording. If this problem can be solved and the model can be validated, it would be very useful for the accurate assessment of the rock status in mining and other underground engineering.

Hashida (1993) used AE as an indicator for the fracture initiation in the fracture toughness test using the J-integral method. The same material was also tested using the chevron bend (CB) and the short rod (SR) geometries; both methods were suggested by the International Society for Rock Mechanics (ISRM). Comparison of the results from the J-integral / AE method and those from the CB and SR method showed that the J-integral /AE method can provide a suitable evaluation procedure for core-based fracture toughness test of rocks while the ISRM recommended CB and SR methods were geometry dependent. From this paper it is clear that some simple but reliable method for the measurement of fracture toughness from core-based rock specimens is needed, because the J-integral / AE method is inconvenient in specimen preparation and the detection of crack initiation.

Jung et al.(1994) established the relationship between the root mean of the squared amplitude (RMS) of the AE waveform and the indentation strength of the rock. Using this easily measurable RMS, the rock hardness and drillability could be evaluated. If some standard could be set up and a portable AE device become available in the field, this result could be valuable to mining, tunneling and petroleum drilling.

Pestman and van Munster (1996) defined a damage surface in the stress space.

Like the yield surface in plasticity, the damage surface is defined as the locus of points in 3D stress space beyond which additional damage would develop. Physically this damage surface is indicated by the onset of AE in the triaxial compressive test. The shape of a damage surface provides a means of characterizing the state of damage corresponding to the state of stress to which the material has previously been subjected. This concept also gives a new approach for the application of Kaiser's effect in rocks.

Zietlow and Labuz (1998) used acoustic emissions at peak load to define the size of the intrinsic process zone during three-point bending test of four different rocks. It was found that this kind of process zone varied with different materials greatly, but kept almost unchanged for different beam sizes of the same material. This offered a new means to characterize the material.

2.5.3 Microseismic Technique for Field Fracture Imaging

AE/MS technology has been experimentally used for mapping HF in the field for some time. A brief review on the development of this technology for field work would help understand the potential, the limits and the future of it. Development of this technology can be classified into several aspects. Except for the confirmation of the HF-induced MS, they are related to and influenced by each other. Once one aspect is changed, other related aspects might be changed accordingly.

2.5.3.1 Verification of Induced Microseisms

The Oak Ridge Experiment

The idea of using hydraulic fracturing-induced microseisms to map the geometry of the fractures started from the Oak Ridge National Laboratory (McClain, 1971). In the 1960s the Oak Ridge National Laboratory was trying to adopt the hydraulic fracturing technique from the petroleum industry to dispose radioactive wastes in shale formations. Because of the high risk of environmental contamination, it was essential to have information about the direction, location, extent, and orientation

of these hydraulically induced fractures.

After analyzing the dynamic and mechanical process of hydraulic fracturing in shale, it was expected that the initiation and propagation of the fracture should generate a very low amplitude acoustic relief wave that would be transmitted through the rock as a seismic signal.

In order to verify this hypothesis, a series of six experiments were conducted. Different types of seismometers were used. Due to the low magnitude of the tensile strength of the shale, high attenuation of the formation and weathered surface zone to elastic waves, and the strong background noises, the verification was proven to be difficult.

In the first five experiments, using trial and error, the existence of microseisms induced by hydraulic fracturing, and their detectability by highly sensitive instruments in the proper frequency band was confirmed. In the last experiment, using a network composed of five short-period seismometers run by Century Geophysical Corporation of Tulsa, Oklahoma, eighty-nine microseisms directly induced from the hydraulic fracturing were recorded. Twenty-nine of them were successfully located with an accuracy of about 100 ft. Locations of these microseisms show that the fracture was almost horizontal and propagated northwesterly from the injection well. It was believed that a network with several redundant sensors would greatly improve the location accuracy.

The greatest value of this investigation was that it not only confirmed the possibility of using induced microseisms to image hydraulic fractures, but also illustrated the various difficulties in using this technique and the direction of future efforts for solving the problem. In all the six tests, all the sensors were installed on the surface.

The Morgantown Experiment

Following the work at Oak Ridge, the Morgantown Energy Research Center initiated a project in 1970 to investigate the technique of mapping hydraulically induced fractures in space and time by monitoring acoustic emission from stressed

rocks (Shuck, 1974; Shuck and Keech, 1977). This project was to investigate the hydraulic fracturing process related to wave generation and propagation, to design a monitoring system for detecting the induced microseisms, to conduct laboratory experiments to determine mechanical, physical and acoustic properties of oriented cores and to map hydraulic fractures, to test the system and the technique in field experiments, and to develop tools for data reduction and results display. With a 12-hydrophone network, initial results showed that acoustic sources in the tested field could be located within a radius of 8 to 10 ft (Shuck, 1974), a great improvement from that reported by McClain (1971).

The El Paso Experiment

In 1973 and 1974, El Paso Natural Gas Co., Sandia Laboratories and Globe Universal Sciences started joint field experiments of detecting and measuring hydraulic fracture dimensions and orientations in real tight gas stimulation in the San Juan Basin, New Mexico and in the Green River Basin, Wyoming (Power et al., 1975; Power, 1977).

In the San Juan Basin experiment, a hydrophone and a geophone were installed in the fracturing well, 400 ft below the perforations, using a dual-case completion technique. Six surface geophones were placed circling the treatment wellbore, five at a distance of 2,500 ft, one at 800 ft. These transducers had different working frequencies: the hydrophone had a broad frequency range with half-power points at 20 and 5,000 Hz on the low and high ends, and the geophones had a natural frequency of 2 Hz (Power et al., 1975). The recording started 24-hour before the treatment and lasted until 24-hour after the treatment. Both the downhole and the surfaces geophones did not detect any recognizable microseisms due to the high-level background noises. The downhole hydrophone was able to detect some consistent signals that were classified as microseisms. Using the arrival time difference of the P- and S-waves, these microseisms were located at a distance from about 200 ft to 450 ft from the hydrophone (Power, 1977). Experience from this experiment

indicated that transducers with the right sensitivity and frequency range were the key for detecting the microseisms while filtering the noises.

In the Green River Basin experiment, a large surface microseismic array was deployed forming a north-south/east-west cross extending 5,280 ft from the treatment well. Each arm of the array consisted of nine 24-seismometer subarrays with a single three-dimensional seismometer at the ends of each arm. Each subarray was digitally recorded broadband as a single channel at a 2-millisecond sampling rate. The subarrays were designed to suppress noises from the well site (Power et al., 1975). While suffering from low signal-to-noise ratio, the recorded results were processed using complex procedures and coherent events were located. Hypocenter isodensity contours indicated a radiating fracture in the northeast and southwest direction. In addition to the surface microseismic array, several other seismic transducers were installed at various distances from the treatment well, both on the surface and downhole. A surface electrical potential system was also used to measure the change of the potential gradients. All these three tools gave comparable and compensatory results; but none could independently offer complete images.

From these two field experiments, it was concluded that fracturing-related signals were generated during and for sometime after the fracturing process. It was highly probable that the characteristics of the fracture induced microseisms and the background noises were site-dependent. Therefore, there might be no universally applicable parameters, such as sensor frequencies, sampling rates, etc., for the setup of the monitoring system. Instead, a detailed site characterization could provide useful information for the selection of the monitoring system, and thus greatly improve the imaging capability at the same technical level.

Based on the results of these three series of different field experiments, it was confirmed that the HF process generates microseisms. If these microseisms could be detected with proper accuracy, their source location could give a description of the geometry of the HF. So now the most important thing is to develop a tool, the proper observation and a proper data processing method.

2.5.3.2 Development of Tools and Observation Methods

The monitoring systems improved from experiment to experiment. Two national laboratories, the Sandia and the Los Alamos, were the pioneers in developing the detecting transducers.

In the Oak Ridge experiments, vertical and horizontal seismometers with natural frequencies of 1.0 Hz, 2.0 Hz, and 1,000Hz were used in different tests (McClain, 1971). In the first five tests, only a single vertical seismometer was used. In the sixth test, four vertical and one horizontal transducers were networked. The results showed that networking and high frequency sensors gave better results.

In the Morgantown experiments, 12 geophones and hydrophones were networked and installed on the surface, in shallow observation wells and in deep open and cased observation wells (Shuck and Keech, 1977).

In the El Paso experiments (Power et al., 1975; Power, 1977), the monitoring system was greatly enhanced. This included the number, the design and the connection of the sensors. Sensors were networked into arrays and subarrays. Both surface and downhole observations were conducted. Three-dimensional sensors developed by Sandia were installed in a shallow observation well for the first time. In a following MHF treatment , a 3-component (3C) geophone developed by Sandia Labs was clamped into the treatment well. MS were detected during shut-in period (Schuster, 1978). Since then, downhole 3C sensors replaced surface sensors and became dominant transducers in the HF mapping.

In the Fenton Hill Hot Dry Rock project, 4 sets of 3C geophones developed by Los Alamos Labs were used. Clear P- and S-waves were detected. Based on the hodograph from the vibration of the horizontal components, the source azimuth was determined. The source distance was calculated from the arrival time difference between the P- and S-waves (Albright and Person, 1982).

In the UK Hot Dry Rock project, the first on-line location system in the world was installed. By installing hydrophones and geophones in the observation well and geophones on the surface, the system was able to map the fracture height, length,

and azimuth at the same time (Batchelor et al., 1983). But this system could not work in the petroleum industry because, usually, observation wells are not available.

The transducers were improved greatly in the Gas Research Institute's Staged Field Experiment and Multiple Well Experiment, both were designed to evaluate and to improve various HF tools and models (e.g., Sorrells and Mulcahy, 1986; Thorne and Morris, 1988a). Sorrells and Mulcahy (1986) proposed a method to estimate the fractures' dip, which relaxed the implicit assumption of vertical fractures in the previous method; but it has not been widely used. At about the same time, Sandia Labs developed a new tools: a 4C transducer with 4 geophones in each of the 4 axes. The 4 geophones in each axis increased the sensitivity to four times of that for a single geophone in each axis. The 4-axis structure eliminated the possible resonance influence from the clamp arm, because they were arranged in such a way that each axis made the same angle with the horizontal plane and the plane of the clamp arm (Thorne and Morris, 1988b).

A 3C accelerometer was developed by Sarda et al. (1988) at the Institute Français du Pétrole. In contrast to previous hydrophone- or geophone-based tools which had a relatively low responding frequency range, this tool worked in the high frequency range (10 kHz) and the location error was reduced to 1-ft.

The first slimhole 3C microseismic accelerometer was developed by Cassell et al. (1990) in Schlumberger. This tool could not only work in slimhole, but also withstand high pressures (20,000 psi) and high temperatures (250°C). The working frequency of this tool is 2kHz. It was successfully used in a 43-degree inclined borehole. But because of the fast attenuation for high frequency signals, this tool could only detect near wellbore (5 to 45 m) microseismic events.

Using the continuous microseismic radiation (CMS) of the background signals after the injection, Fix et al. (1991) proposed a so-called H/Z method to estimate the fracture height in the treatment well. Based on field observations, it was found that the horizontal and vertical components of these signals varied with the tool's position inside the treatment well. When the tool was within the interval of the

fracture, the H/Z ratios would be higher than that outside the fracture.

In order to keep the advantages of high resolution of the accelerometers and deep range of detection of the geophones, broadband (100-1,500 Hz) accelerometer-based 3C downhole microseismic tools were developed by Sandia Labs (Sleef et al., 1993). Field experiments showed that this new tool was much better than the previous generations.

Although theoretically a single 3C microseismic transducer can determine the source location, it is true that extra transducers increase the resolution of the location. This led to the development of multi-level 3C downhole microseismic transducers (Warpinski et al., 1995). In the Multiple Well Experiment Site, a 4-level 3D accelerometer system developed by Sandia Labs was used and asymmetrical fractures were detected, which was different from theoretical and numerical modeling.

2.5.3.3 Field Applications of Microseismic Technique

During the development of the HF imaging technology, knowledge about HF was also accumulated.

In the first HF imaging experiment, the fractures induced by the injection of nuclear waste was determined as being almost horizontal and extended to the northwest (McClain, 1971). Because the depth in this experiment was only about 1,000 ft, this result confirmed the conventional concept that at shallow depths, HF were mainly horizontal. But the non-circular geometry might be only part of the whole fractures due to the limit of the monitoring capacity.

The most valuable result from the Mogantown HF imaging experiment was that the HF consisted of a series of discrete small cracking events, each of these events had a frequency of 80 to 500 Hz in that specific oilfield (Shuck, 1974).

The El Paso experiment indicated that HF-related signals were generated during and after the fracturing process: the best parameters for the detecting systems seemed site-dependent (Power et al., 1975).

The experiment in the Fenton Hill Hot Dry Rock Site, USA obtained the first

successful HF images (Albright and Person, 1982). Four major progresses were achieved in this experiment. First, the HF induced events were mainly shear failure mechanisms, rather than tensile. Secondly, the hodogram method was adopted to determine the source azimuth (the direction from the source to the sensor), which was derived from the first motion of the waveforms in the 3 vibrating components of the transducer. Thirdly, the source location of the event could be determined from the arrival time difference of the P- and S-waves. And finally, the overall hydraulic fractures were mapped by the hypocenters of the individual microseisms. The requirement of the clearly recorded P-wave first motions in different vibrating components of the transducer limited its coverage of detection, especially in some highly attenuative materials such as sedimentary rocks. In addition, due to the requirement for distinguishable *P*- and *S*-wave first motions, this method had a blind radius within which the microseismic events could not effectively detected.

Following the success in the Fenton Hill Experiment, the UK Hot Dry Rock Experiment became the first one that could offer the fracture length, height and azimuth at the same time (Batchelor et al., 1983). This was because of the availability of many properly distributed observation wells, a condition not normally possible in the petroleum industry.

While the main purposes of the Gas Research Institute's Staged Fracture Experiments and Multiple Well Experiments were designed to test and improve the related tools for the diagnostics of the hydraulic fractures, the microseismic images did reveal some aspects of the complexity of hydraulic fractures. Typically, (1) the facture length from the microseismic image was usually different from the model prediction(e.g. Thorne and Morris, 1988b; Robinson et al., 1991), (2) the fracture height growth was usually more complex than the models(Warpinski et al., 1996 and 1997), (3) the overall HF geometry was asymmetrical rather than symmetrical (Warpinski et al., 1995), and (4) the HF usually produced a zone of multiple fractures rather than one single fracture(Peterson et al., 1996).

Vinegar et al.(1992) investigated the process zone in diatomite formations using

active seismic and passive microseismic image method. The two methods consistently indicated that the HF in the diatomite caused a 40 ft wide process zone.

Keck et al. (1994) reported the application of the microseismic imaging technique to waste solid injection in deep wells. The image results showed the maximum fracture length was 1,200 ft, a consistent result with numerical models.

Jupe et al. (1998) and Gaucher et al. (1998) introduced the application of the multi-level 4C accelerometers in imaging the MHF injection in the European Hot Dry Rock geothermal reservoir in Soultz-sous-Forets, Alsace, France. This was the first application of the microseismic imaging technology in an anisotropic, heterogeneous, naturally fractured reservoir. The imaging results were helpful to the grid in the numerical modeling and the recorded P- and S-waveforms were used to identify the fracture network and the maximum in-situ stress direction.

Hopkins et al. (1998) used 3C geophones and 4-level 3C accelerometers in offset wells to map the HF in a naturally fractured gas reservoir in the Devonian shale of Antrim formation. The imaged results revealed a penny-shaped zone of induced fractures with almost equal length and height, while the facture zone was non-vertical and asymmetrical. This image was confirmed by cored samples from directional drilling, and by transient pressure analyses.

The "Drill Cuttings Injection Field Experiment" in Mounds, Tulsa, Oklahoma was the most recent cooperative investigation on the hydraulic fracturing process supported by the Department of Energy (Moschovidis et al., 1998). Microseismic imaging results from an observation well using 5-level 3C accelerometers showed that the disposal domain was in general aligned with the maximum horizontal stress, but the height and length growth occurred with continued injections (Warpinski et al., 1999). The overall geometry was more complex than expected.

Wolhart et al. (2000) applied the MS mapping technique to optimizing HF operations in the naturally fractured Arcabuz-Culebra Gas Field in Mexico. The mapping results confirmed the geomechanical modeling results for one of the HF treatment optimization.

Bell and Kraaijevanger (2000) applied the MS mapping technique to monitor a massive hydraulic fracture stimulation in the Athel formation, South Oman. This was a micro-Darcy tight gas formation. The mapped results from offset wells during the stimulation and production showed that the induced fractures had different orientations in different intervals. This result offered fundamental data for the optimized development of this reservoir.

In addition to mapping the HF treatment, this technology has also been used to characterize reservoirs (Maxwell et al., 1998; Evans et al., 2000), estimate hot steam heated volumes (Snell et al., 1999; 2000), identify pre-existing fault reactivation (Phillips et al., 1998), and monitor and prevent casing failure (Boone et al., 1999).

From the above introduction of field observations, it can be seen that the hydraulic fractures have geometries that are much more complex than predicted by any theoretical model. They are usually not a single fracture, but a zone of multiple fractures; the two wings are usually not symmetrical; and the fracture planes are not vertical.

Because the real conditions vary from one field to another, more complex geometry can occur. As field experiments are very expensive, less controllable and not repeatable, a logical alternative is to use laboratory experiments to investigate the complexity of hydraulic fractures under controllable and controlled conditions.

2.5.4 Laboratory Hydraulic Fracturing Experiments and the Application of the Microseismic Technique

2.5.4.1 General Laboratory Work

Haimson and Fairhurst (1969) tested the hydraulic fracturing breakdown pressures of porous permeable hydrostones specimens under different conditions. It was found that the fracture orientation was controlled by the tectonic stresses. The breakdown pressure was lower than the theoretical result for impermeable rocks, but higher than that for permeable rocks. In addition, the larger the borehole diameter, the

lower the breakdown pressure: the higher the pressurization rate, the higher the breakdown pressure.

Daneshy (1973) presented a theoretical investigation and experimental observations on the initiation of inclined hydraulic fractures. According to his research, the inclined fractures were usually initiated in shear, but often intersected the borehole diametrically in two opposite axial lines that gave an impression of axial fracture. At the borehole these inclined fractures were usually not perpendicular to the minimum compressive stress. But after it extended away from the borehole, the fracture orientation would convert to be perpendicular to the minimum compressive stress.

Ahmed et al. (1983) experimentally studied the effects of stress distribution on the hydraulic fracture geometry using layered one-meter cubic blocks of grout. It was demonstrated that fractures propagated from higher to lower stressed regions. This was important to the containing of hydraulic fractures within a selected pay zone.

Hallam and Last (1990) carried out hydraulic fracturing experiments on 12-inch hydrostone cubic blocks to investigate the geometry of hydraulic fractures in modestly deviated boreholes. They suggested that the rough surfaces of the fractures from deviated boreholes reported by Daneshy (1973) were due to a number of starter fractures that formed in parallel planes, perpendicular to the minimum principal stress that may or may not link up. For small wellbore deviation, starter fractures link up to form a single fracture in good communication with the wellbore. For large deviation, starter fractures may not link up and what might appear to be a single non-planar fracture actually consists of an array of slightly overlapped, non-linked fractures.

Falls et al. (1992) conducted hydraulic fracturing experiments on two unloaded big granite cylindrical samples and imaged the induced fractures with acoustic emissions. The distribution of acoustic emissions recorded after breakdown clearly indicated two parallel fractures controlled by pre-existing cracks.

Abass et al. (1992) investigated three types of non-planar fracture propagation

from a horizontal wellbore through experiments. They suggested that multiple parallel fractures at the wellbore might be created for wellbore orientations up to 50° from the direction of maximum horizontal stress. For azimuth ranging from 50° to 70°, a single fracture might be initiated at the wellbore, then due to reorientation, closely spaced multiple fractures might be generated. T-shaped fractures were initiated when the wellbore was aligned in the direction of the minimum principal stress.

Weijers et al. (1992) investigated the induced fractures in horizontal wells that were drilled in the direction parallel to the minimum horizontal stress. Depending on the injection rates, three geometry types were observed: (1) initiation of axial fracture along the wellbore together with transverse fractures located in the preferred plane (relatively low treating pressures), (2) gradual fracture reorientation (intermediate treating pressures), and (3) multiple fractures and stepwise reorientation (high treating pressures).

Matsunaga et al. (1993) conducted hydraulic fracturing experiments on biaxially loaded 20 cm cubes of granite, marble and andesite with water and oil as hydraulic fracturing fluid. The acoustic emissions were detected to image the fracture growth and analyze the failure mechanisms. It was found that the initiation and extension mechanisms of the hydraulic fractures were strongly influenced by the rock permeability and texture as well as the fluid viscosity.

Guo et al. (1993a, b) developed a set of triaxial loading equipment and conducted hydraulic fracturing experiments on gypstone blocks of 305×305×305 mm and 610×584×305 mm blocks to investigate the effects of the least principal stress and injection rate on the hydraulic fracturing propagation behavior. It was concluded that the rate of fracture propagation decreased with the rise of the minimum principal stress. Radial flow dominated the leak-off before breakdown and linear flow along the fracture controlled the leak-off after the breakdown. A low injection rate resulted in a slow pressure decline after breakdown, meaning a less effective propagation and shorter fracture. A high injection rate caused a quick pressure

decline and generated longer fractures. The breakdown pressures increased with injection rate, and were generally higher than any theory could predict. For example, the tensile strength derived from the breakdown pressure and the applied stress field was 33 times larger than the directly measured tensile strength. While the reason was not explicitly given, it was observed that when the injection rate increased from 0.106 cm^3/sec to 3.114 cm^3/sec, the breakdown pressure increased from 3.88 MPa to 11.00 MPa. This indicated that a proper injection rate was the key for obtaining the proper breakdown pressure.

Schmitt and Zoback (1993) experimentally investigated the fluid infiltration effect on the breakdown pressure of low porosity rock by conducting hollow cylinder tests on glass and granite. By pressurizing glass and granite specimens at different confining pressure, it was found that glass followed the linear elastic theory for the pre-scratched specimens. The granite, however, showed dependence on pressurization rate. Test with pressurization rate in a range of three orders indicated that the higher the rate, the higher the breakdown pressure. This was attributed to the effect of fluid infiltration in the low porosity material. The implication of this study to the hydraulic fracturing was that proper pressurization rate was important in order to get the right breakdown pressure and other related parameters.

Weijers and de Pater (1994) experimentally investigated the interaction and link-up of hydraulic starter fractures close to a perforated wellbore. In a cased-perforated well, the hydraulic fracturing treatment may initiate inclined starter fracture. Whether these starter fractures connect to each other would influence the near wellbore frictional loss. The observation showed that link-up of starter fractures the confining stress difference and the pressure in the fracture during a treatment. A large stress difference in the plane perpendicular to the perforations prevented the starter fractures from linkage. This again showed the importance of local stress field in controlling the fracture initiation.

Ong (1994) conducted a series of hydraulic fracturing experiments on 18-in cubic cement blocks. Close agreements between the theoretical and experimental fracture

initiation pressure foe some borehole configurations, coupled with the observed tensile failure modes, suggested that the linear elastic theory was applicable for this brittle material. These observations also disqualify the opinion that linear elastic theory predictions were conservative.

Morita et al. (1996 a, b) conducted 40 hydraulic fracturing experiments on 30-in cubic blocks of Berea sandstone, Castle sandstone and Mancos shale using water- and oil-based drilling mud as fracturing fluids. It was found that the drilling mud prevented the sample from immediate breakdown after the fracture initiation. Instead, three distinct zones, the fracture process zone, the non-invaded zone and the de-hydrated zone, developed at the fracture tip. Length of these zones varied from 0.3-in to 3.0-in, depending on the fluids and the rock properties. The breakdown pressure in these tests was found to be a function of Young's modulus of the formation, wellbore size and type of the drilling fluids, and could not be predicted by existed theories.

Willson et al. (1999) conducted laboratory hydraulic fracturing experiments to investigate the mechanisms of drill cuttings injection in various formations. It was observed that multiple fractures were formed in a wide range of formations as a result of intermittent injection. In competent rocks, fractures initiated at the wellbore; in poorly consolidated sandstones the fractures were more dendritic in character. The new observations generated new challenges to numerical simulators.

Chudnovsky et al. (2001) proposed a hydraulic fracture model that accounts for the fracture toughness anisotropy in a layered media. The model showed that the hydraulic fracture could be contained even under uniform stress conditions and with a moderate fracture toughness ratio of 1/3. The model was validated by experiments on diatomite blocks.

Song and Haimson (2001) checked the pressurization rate effect on the breakdown of Tablerock sandstone in hollow cylinder hydraulic fracturing test. They noticed that under undrained conditions (sample was jacketed), the breakdown pressure increased with pressurization rate. In the unjacketed sample, the observed

breakdown pressure was different from that predicted by poroelasticity.

2.5.4.2 Application of microseismic technology in laboratory Hydraulic Fracturing research

Byerlee and Lockner (1977) developed a 6-channel acoustic emission system and used it to monitor the induced acoustic emissions during the injection of water into a cylindrical sandstone sample under 1,000 bar confining pressure and 4,000 bar differential stress. The water was injected under constant pressure of 500 bar. It was found that acoustic emissions were randomly distributed before the fracture initiated. Once the fracture was initiated, the acoustic emissions localized at the fracture tip. The acoustic emission activity moved forward when the fracture propagated. This was not a strict hydraulic fracturing experiment; instead, it was similar to waterflooding. However, the result indicated that the acoustic emissions were occurring at the fracture tip which meant that by locating the fracturing induced acoustic emissions, the fracture geometry could be mapped.

Zoback et al. (1977) investigated the effect of borehole pressurization rate on the breakdown and fracture initiation pressures. It was found that the pressurization rate had a marked influence on the breakdown pressure while the fracture initiation pressure was not influenced. During these experiments acoustic emission rate monitored from a single transducer was used as one of the indicators for the fracture initiation. It was found that this acoustic emission rate had a consistent indication for the hydraulic fracture initiation with that from sample deformation.

Solberg et al. (1980) experimentally investigated the injection rate influence on the fracture mechanisms and the permeability of the induced fractures under geothermal conditions, using acoustic emission rates. The experimental results showed that the high injection rate induced a sudden burst of acoustic emissions accompanying the generation of tensile fractures whereas a low injection rate induced an exponentially increase of acoustic emissions with the generation of shear failures. The intermediate injection rate with elevated differential stress on the

other hand induced fewer acoustic emissions but the permeability of the induced fractures was an order higher than the other two cases.

Majer and Doe (1986) checked the feasibility of using the acoustic emission technique to image the hydraulically induced fractures in laboratory tests. A laboratory hydraulic fracturing experiment was carried out on a 300×300×450 mm salt block. Triaxial loads were applied to the specimen. Using a group of 5 acoustic emission transducers installed on the surfaces around the block, the experimental results showed that: (1) there was abundant detectable discrete seismic activity during the process of hydraulic fracturing, (2) the acoustic emission events were either directly related to the actual path of the hydraulic fracture or included in the overall dimensions of the hydraulic fracture, and (3) the hydraulic fracture growth was not symmetrical and did not follow the often assumed symmetrical paths.

Savic et al. (1993) developed a data acquisition system that could be used to detect the hydraulic fracture tips with active seismic waves. Experiments showed that the material property was a key factor that determined if the fracture could be detected using this method. This might be used to explain the failure of recording induced seismic signals in the field in some microseismic imaging experiments.

Winkler (1995) reported a newly developed acoustic emission system for hydraulic fracturing mapping experiments. This system had 8-channels and could digitally record the full waveforms.

Itakura and Sato (1998) investigated the hydraulic fracturing induced AE activity and its fractal properties in 100 mm cubic tuff and granite specimens. The hypo-central locations of the hydraulic fracturing induced acoustic emissions were found to be fractals, and seismic gaps were observed in the pre-stressed specimens. While the observation might be correct in general, there were two questions on this test result: (1) distribution of the acoustic emissions did not show direct relation to the fractures, (2) breakdown pressures of the same rock varied from 10.9 to 24.8 MPa under the same conditions, indicating that the experimental pressurization rate of 2MPa/min. might be too high to catch all the events.

Ishida et al. (2000) investigated the grain size effect on the hydraulic fracturing behavior of granite rocks. Four 20 cm cubic granite specimens with large and small grain sizes were tested under bi-axial stresses perpendicular to the borehole. No stress was applied in the borehole direction. The rift plane was perpendicular to the borehole. It was found that in the specimens with large grains the induced fractures were perpendicular to the borehole, while in the specimens with small grains the fractures were parallel to the borehole. The breakdown pressures decreases with the grain size while the located acoustic emissions increased with the grain size. The authors considered this as the grain size effect: this explanation can be true from the point of view of Griffith's fracture initiation theory.

2.6 Discussion

From the above review, it is seen that hydraulic fracturing technology has become a useful tool in overcoming near wellbore damage, improving tight gas reservoir production, and controlling sand production in poorly consolidated formations. But in a lot of cases, the current theory can not give satisfactory description of the induced fractures. This could be due to inaccurate measurement of the formation properties such as in-situ stress field, tensile strength and fracture toughness, or incomplete relationship among some operational parameters such as the breakdown pressure and the pumping rates.

On the other hand, the optimized development of reservoirs requires the accurate description of the geometry of the induced fractures. So hydraulic fracture diagnoses are needed. Among the current diagnostic techniques, surface and downhole microseismic techniques have been considered as the most promising means for imaging the induced fractures.

The surface microseismic technique installs many conventional seismic sensors around the imaged domain to record the P-wave arrival times of the induced microseisms. Sources of the microseisms are located by solving the quadratic equations

through linearization. This linearization leaves a lot of microseisms unlocatable due to the easily ill-conditioned feature of the simplified equations. This problem will be solved by developing a simplex-based, robust algorithm for the location of the microseisms, which is explained in Chapter 3.

The downhole microseismic technique uses one or only several 3-C or 4-C seismic sensors to record the arrival times of the P- and S-waves. Because the source distance is calculated from the difference of the traveling time of the P- and S-waves, and the azimuth of the source is determined from the first motion of the P-wave in each component of the sensors, a clearly identifiable P-wave first motion is the key for the accurate location of the microseismic sources. But in the same microseismic event, the amplitude of the first motion of P-waves are much smaller than that of the S-waves in nature, it is very often that the first motion of the P-wave in one or more of the multi-component sensor is not clear and thus not able to be used for the location. In these cases, the first motion of the P-wave recorded at an arbitrary location in any orientation from an arbitrary source can be calculated, the ambiguity can be largely reduced. Such a forward simulator will be developed using the Betti's Reciprocity theorem and the Green's function in Chapter 4.

The success in the design and operation of the hydraulic fracturing treatments depends on the complete characterization of the targeted formation. Among all the measurements, the fracture toughness is the most controversial one due to the inapplicability of the standard methods in the usually size-limited, anisotropic, and cylindrical samples from the petroleum drilling. A method that can measure the fracture toughness in small disc samples in an arbitrary direction is needed. This demand is met with the introduction of an upgraded Chevron-notched disk test, which will be illustrated in Chapter 5, together with the complete characterization of a newly discovered tight gas sandstone.

From the above review, it has been seen from time to time that different fractures have been induced under similar conditions. While different explanations have been given, the fundamental reason is the difference of local stress field. A case study

through 3-dimensional nonlinear numerical modeling will be displayed to show how the small difference in packer length would change the local stress field and thus induce fractures with completely different orientations. This will be covered in Chapter 6.

Asymmetrical fractures have been observed in both the field and the laboratory. Images on the development of these fractures will enhance the understanding to this complex phenomenon. A series of experiments have been conducted to generate asymmetrical fractures via the application of intentional asymmetrical load. The initiation and propagation of the asymmetrical fractures have been imaged with the previously developed microseismic technique and is described in Chapter 7.

3 Development of A Simplex-based Microseismic Location Program

3.1 Introduction

Two types of sensors have been used in detecting fracturing-induced microseismic signals: the conventional, single-component geophones and accelerometers[1], and the three- or four- component (3-C or 4-C) geophones and accelerometers. Manufacturing of the multi-component sensors involves putting the different components in a small space and pointing to the same intersection strictly. In additon, these components need to be able to response the same signal harmoniously. This requires very advanced technology, and in turn, makes the price high.

In comparison with the multi-component sensors, the advantages of using conventional, single-component sensors are that they are easy to install and operate. The disadvantage is that locating each of the microseismic event requires detecting the signal at four or more different, non-planar observing locations, because there are at least four unknowns in the related equations, as will be shown in the next section. Because of the errors in detecting the signals, identifying the first motions and in describing the velocity structures of the materials, redundant sensors are normally used so as to increase the location accuracy.

Even though, it is still often seen that only 10 to 15% of the recorded microseismic events could be located (Bachelor et al., 1983; Keck and Withers, 1994); and

[1]Geophone and accelometer have different structures which make the former a type of sensor for velocity measurement and the latter a type of transducer for acceleration detection (Young, 1998).

the image of the induced fractures expressed by those located events were no more than some "clouds" (Murphy et al., 1999).

One of the reasons for such unsatisfactory results is that the microseismic location algorithm was based on the linearization of the quadratic equations of the signal travel time using Taylor's series expansion (Byerlee and Lockner, 1977; Rothman, 1977). This linearization process drops all the terms with power of 2 or higher, which leads to an exaggerated error effect. When there are errors in P-wave arrival times in some sensors, which is often very common, this method can result in solutions being weighted in favor of the most erroneous arrival time (Gibowicz and Kijko, 1994). Thus the linearized microseismic location algorithm is easy to be ill-conditioned due to the abnormally high noise level in one sensor.

In order to overcome this difficulty, a non-linear microseismic location algorithm is needed. Prugger and Gendzwill (1988) introduced the simplex method for microearthquake location in underground mining with complex velocity structures and obtained relatively good results. That idea has been adopted in this dissertation; a computer program has been coded and tested. This chapter introduces the related theory, the preparation of the original data, the development and the verification of the computer program.

3.2 Simplex Algorithm for Microseismic Location

3.2.1 Physical Background of Microseismic Detection

Like a natural earthquake observational network, a microseismic monitoring system is composed of two main parts: a number of sensors (accelerometers, geophones, hydrophones, ...) which are attached to the observed object to detect the vibration; and an electronic device connected to the sensors to record the detected signals.

When there is a rapid strain energy release (a microseismic event), an elastic wave is generated. The sensors detect this wave and transfer it into an electrical voltage which is proportional to the intensity of the wave. Once the electric voltage

exceeds a prefixed level (threshold), a recording device is triggered and a number of parameters pertinent to the microseismic event, such as event time, intensity, and duration, are recorded. As the distance from the source to different sensors are different, the arrival times for the P-wave from the source to different sensors are usually different. If full waveforms are recorded, the system will record the electric voltage continuously for a period of time after being triggered.

No matter what type of recording system is used, in order to locate the microseismic events, the key parameters requested from the recordings are the P-wave arrival time and the corresponding identification number of the sensor. Based on these two parameters, the source location of the microseismic events can be determined according to the mathematical principles described below.

3.2.2 Mathematical Principles of Microseismic Location

In order to be general, assume a microseismic monitoring system having N sensors at N locations (X_J, Y_J, Z_J) $(J = 1, 2, ..., N)$, and a microseismic event which arrives at these sensors at times T_J $(J = 1, 2, ..., N)$.

The purpose of the microseismic location is to find the coordinates of the source of the microseismic event, (X_0, Y_0, Z_0), from the detected P-wave arrival times, $T_J (J = 1, 2, ...N)$. The arrival time, T_J , at sensor J is the sum of two parts: the travel time from the source to the sensor, dT_J, and the event occurring time, T_0[2]. The travel time, dT_J, can be expressed as a function of the source coordinates, (X_0, Y_0, Z_0), the sensor coordinates, (X_J, Y_J, Z_J), and the velocity components, (V_X, V_Y, V_Z). The event occurring time, T_0, is unknown. If the velocities are known, there are four unknowns, (X_0, Y_0, Z_0, T_0), in total. In contrast, if the velocities are not known, the number of total unknowns may vary from 5 to 7, depending on the velocity structure of the material, as shown in Table 3.1 below.

Consider the general case, that is, the anisotropic velocity model with seven

[2]Occurring time is the instant when the event occurs in the time axis. The detected time is the instant when the signal reaches the sensor. The difference between the detected time and the occurring time is the travel time for the signal from the source to the corresponding sensor.

Table 3.1: Unknowns for different velocity models

Velocity model	Unknowns	Number of unknowns
Given velocities	X_0,Y_0,Z_0,T_0	4
Isotropic	X_0,Y_0,Z_0,T_0,V	5
Transverse	X_0,Y_0,Z_0,T_0,V_X,V_Z	6
Anisotropic	X_0,Y_0,Z_0,T_0,V_X,V_Y,V_Z	7

unknowns. Mathematically, this problem is solved using the following steps:

Step 1: *Calculate the distance from* (X_0,Y_0,Z_0) *to* (X_J,Y_J,Z_J);

$$D_J = \sqrt{(X_0 - X_J)^2 + (Y_0 - Y_J)^2 + (Z_0 - Z_J)^2} \tag{3.1}$$

Step 2: *Find the velocity in the direction from* (X_0, Y_0, Z_0) *to* (X_J, Y_J, Z_J);

Based on the accurate solutions developed by Backus (1970), Nur (1971) suggested that the velocity in any direction in an anisotropic material can be calculated using the first order of approximation given by:

$$V_J = \sqrt{V_X^2 l_J^2 + V_Y^2 m_J^2 + V_Z^2 n_J^2} \tag{3.2}$$

where l_J, m_J, n_J are the direction cosines of the ray-path from (X_0, Y_0, Z_0) to (X_J, Y_J, Z_J). The direction cosines, l_J, m_J, n_J, are calculated as below:

$$\begin{cases} l_J = \frac{X_0 - X_J}{\sqrt{(X_0-X_J)^2+(Y_0-Y_J)^2+(Z_0-Z_J)^2}} \\ m_J = \frac{Y_0 - Y_J}{\sqrt{(X_0-X_J)^2+(Y_0-Y_J)^2+(Z_0-Z_J)^2}} \\ n_J = \frac{Z_0 - Z_J}{\sqrt{(X_0-X_J)^2+(Y_0-Y_J)^2+(Z_0-Z_J)^2}\surd} \end{cases} \tag{3.3}$$

Applying Eq.(3.3) to Eq.(3.2) gives:

$$V_J = \sqrt{\frac{V_X^2(X_0 - X_J)^2 + V_Y^2(Y_0 - Y_J)^2 + V_Z^2(Z_0 - Z_J)^2}{(X_0 - X_J)^2 + (Y_0 - Y_J)^2 + (Z_0 - Z_J)^2}} \tag{3.4}$$

Step 3: *Calculate travel time from* (X_0, Y_0, Z_0) *to* (X_J, Y_J, Z_J);

$$dT_J = \frac{D_J}{V_J} \tag{3.5}$$

Applying Eqs.(3.1) and (3.4) to Eq.(3.5), the travel time becomes:

$$dT_J = \frac{(X_0 - X_J)^2 + (Y_0 - Y_J)^2 + (Z_0 - Z_J)^2}{\sqrt{V_X^2(X_0 - X_J)^2 + V_Y^2(Y_0 - Y_J)^2 + V_Z^2(Z_0 - Z_J)^2}} \tag{3.6}$$

Step 4: *Calculate theoretical arrival time, T_J^T , at sensor-J*:

$$T_J^T = T_0 + \frac{(X_0 - X_J)^2 + (Y_0 - Y_J)^2 + (Z_0 - Z_J)^2}{\sqrt{V_X^2(X_0 - X_J)^2 + V_Y^2(Y_0 - Y_J)^2 + V_Z^2(Z_0 - Z_J)^2}} \tag{3.7}$$

On the other hand, the actual arrival time, T_J^M, is measured at the sensor-J. Because N sensors are used in total, N equations similar to Eq.(3.7) can be obtained. Theoretically, if $N > 7$, then X_0, Y_0, Z_0, T_0, V_X, V_Y, V_Z should be obtainable. But Eq.(3.7) is non-linear. From these N equations, no direct solution can be obtained. In order to avoid the disadvantage encountered by the linearization method, the following approaches are followed to find the solutions:

Step 5: *Calculate residual time at sensor-J for an assumed solution (X_0, Y_0, Z_0, T_0, V_X, V_Y, V_Z);*

$$\begin{aligned} T_{res_J} &= |T_J^M - T_J^T| \\ &= |T_J^M - (T_0 + \frac{(X_0 - X_J)^2 + (Y_0 - Y_J)^2 + (Z_0 - Z_J)^2}{\sqrt{V_X^2(X_0 - X_J)^2 + V_Y^2(Y_0 - Y_J)^2 + V_Z^2(Z_0 - Z_J)^2}})| \end{aligned} \tag{3.8}$$

Step 6: *Calculate total time residual in all N sensors for the assumed solution* (X_0, Y_0, Z_0, T_0,V_X, V_Y, V_Z);

$$T_{res_N} = \sum_{J=1}^{N} |T_J^M - (T_0 + \frac{(X_0 - X_J)^2 + (Y_0 - Y_J)^2 + (Z_0 - Z_J)^2}{\sqrt{V_X^2(X_0 - X_J)^2 + V_Y^2(Y_0 - Y_J)^2 + V_Z^2(Z_0 - Z_J)^2}})| \tag{3.9}$$

Now the task is to find a set of (X_0, Y_0, Z_0, V_X, V_Y, V_Z, T_0) that makes T_{res_N} minimum. This is achieved by using the following simplex optimization algorithm.

3.2.3 General Concept of the Simplex Optimization Algorithm

Simplex optimization was first described by Nelder and Mead (1965). The general idea is to first define an information space composed of the unknowns, and then construct a simplex with one vertex more than the number of unknowns. For instance, if there are 2 unknowns, the information space is two-dimensional and the simplex has 3 vertices. In the general case of microseismic location, there are 7 unknowns. So the information space is 7-dimensional and the simplex has 8 vertices. A group of coordinates for all the unknowns is then searched in the information space by the four types of simplex operations: reflecting, contracting, expanding and shrinking. This is an iterative process. With the progress of the searching, the simplex becomes smaller and smaller in the information space and ideally retrogrades to be a point at last. The coordinates of that point in the information space is the optimized solution to the problem. In reality, once the distance between the two farthest vertices in the simplex is less than a limit (criterion), the search will be stopped and the coordinates of the vertex that produces the maximum or minimum to the function will be chosen as the solution. Whether the solution will produce a minimum or a maximum to the function depends on the feature of the problem. In the microseismic source location problem, the function to be optimized is the total time residual. So the vertex that produces minimum time residual will be the solution.

3.2.4 Simplex-based Algorithm for Microseismic Location

Using the general idea of simplex optimization and the mathematical principles described before, the simplex algorithm for microseismic location is demonstrated through the following steps:

Step 1: *Construct the initial simplex:*

In the general case of microseismic location, there are 7 unknowns; hence the

initial simplex is composed of 8 vertices, each having 7 components, (X_{0I}, Y_{0I}, Z_{0I}, V_{XI}, V_{YI}, V_{ZI}, T_{0I}) (I = 1, 2, ... 8). In order to insure that none of the vertices would be covered by others, each vertex needs to have at least one component larger than the smallest component in all the other vertices.

Step 2: *Calculate and rank the time residuals for each vertex:*

The worst vertex is defined as the one which has the largest time residual and the best is the one that has the least time residual. All the vertices are ranked according to their time residuals.

Step 3: *Conduct simplex operation:*

Substitute the worst vertex by proper simplex operations (reflection, expansion, contraction and shrinkage) (Caceci and Cacheris, 1984). As an example, Figure 3.1 shows the four simplex operations in a 2-D simplex BMW. In the figure, B refers to the best vertex, M to the middle vertex and W the worst vertex. Depending on the change of the simplex function value (i.e., time residual in the microseismic location case), reflection (represented by R) of W, expansion (represented by E) of R, or contraction (represented by C) of W, or shrinkage of both M and W would have to be conducted in one iteration of the simplex operation.

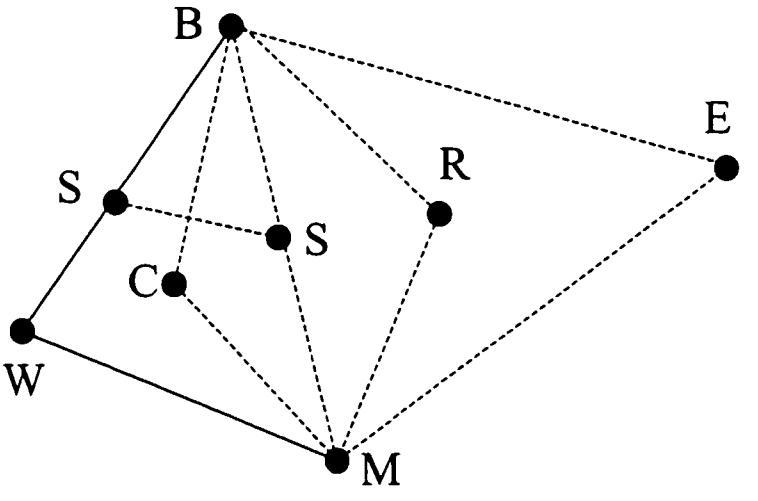


Figure 3.1: Simplex operations in 2D case (after Caceci and Cacheris, 1984).

Step 4: *Iterate the simplex operation:*

Repeat Steps 2 and 3 until the required criteria, either in terms of distance between the two farthest vertices, or the time residual, or the number of iterations, is satisfied. Then the coordinates of the best vertex is the solution for $(X_0, Y_0, Z_0, V_X, V_Y, V_Z, T_0)$.

If the velocity model is different from the anisotropic model, the unknowns will be reduced and thus the dimensions of the information space. The simplest case is that all velocity components are given. In this case, the simplex has only 5 vertices. In the next section, a computer program, LOCATION, will be developed following the above simplex algorithm.

3.3 Development of the LOCATION Computer Program

3.3.1 Data Preparation

Three types of acoustic emission / microseismic recording systems have been used during this investigation. The first is an 8-channel Spartan, the second a 20-channel MISTRAS, both manufactured by Physical Acoustics Corporation (PAC), USA; the third is a 15-channel AMSY4-SF made by Vallen Systeme GmbH, Germany. The PAC and the Vallen systems work in different ways and their data structures are different; hence interpretation and processing their data will require different ways.

3.3.1.1 PAC Data Processing

The PAC systems measure the voltage at the output of each sensor. Once the output voltage exceeds a pre-set threshold, the channel connected to that sensor will be triggered. A high speed circuit will run to detect and calculate the sensor ID, the trigger time, the peak amplitude, the accumulated energy, the duration time, and

some other parameters (PAC, 1995). This defines a HIT. Among these data, the absolute trigger time, defined as the time since the start of the test corresponding to the occasion that the threshold is exceeded, and the sensor ID are the most important parameters to the microseismic location operation. The data from each channel is recorded according to the trigger order.

Because each channel is triggered independently, it is possible that some weak signals have been detected by only a few sensors while other strong ones by more sensors. It is also possible that some reflections have been falsely recorded, as shown in Figure 3.2. So correctly identifying the microseismic signals from the recorded HITs is very important.

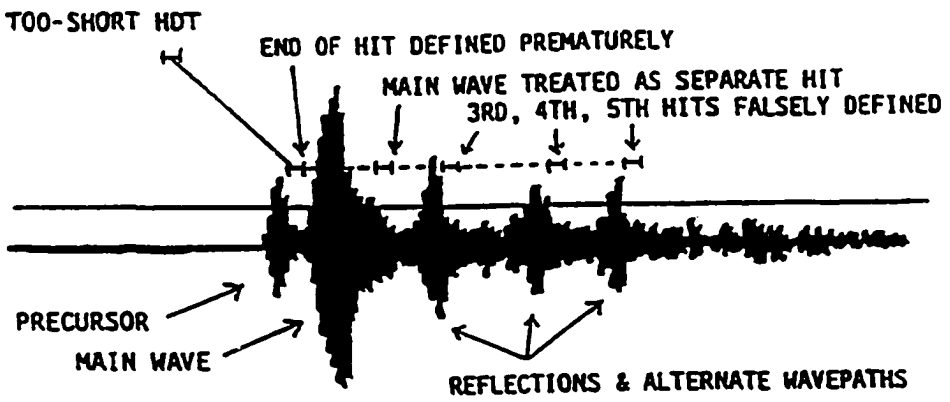


Figure 3.2: The true HIT(signal) and the false HITs(noises) (from PAC, 1995).

There are three techniques to improve identifying a microseismic event. The first is to configure proper System Timing Parameters before the test, such as Peak Definition Time (PDT) (also know as Rise Time-Time Out, or RTTO), HIT Definition Time (HDT) (also known as Single Channel Event Time-Out, or SCETO), and HIT Lockout Time (HLT) (also known as Re-arm Time Out, or RTO) (PAC, 1995). In this way, the next HIT will not be triggered until the first one has died out. This can greatly reduce the reflections from the previous HIT.

The second technique is to define a lockout-time during data processing. As

mentioned above, the HITs are recorded in a serial way according to their trigger time. Therefore, the HITs from the same microseismic event should be next to each other. The lockout-time defines such a time-window that will properly cover the HITs detected by the two farthest separated sensors from the same microseismic event, excluding those that belong to a different microseismic event.

The third technique is to define a minimum number, 5, for instance, of triggered sensors as the minimum requirement for defining an event. A group of consequential HITs will not define a microseismic event if the number of triggered sensors is less than that minimum number. In addition, if a sensor is repeated among a group of HITs, these HITs do not define an microseismic event either.

Using these techniques, the original PAC files were processed and the arrival time data files were finally obtained. Shown in Table 3.2 is a section of such an arrival time file from Test 9910-2. The data were processed with a lockout time of 50.0 μs[3]. In the displayed section, the first event triggered 21 sensors[4], but the two events followed it triggered only five sensors each.

It has been realized that the PAC systems have the advantage of fast recording. However, the disadvantage is that a lot of HITs are simply noise. The discrimination between noises and signals is not robust. For instance, if the lockout time was 30 μs instead of 50 μs in processing the data shown in Table 3.2, then the first event shown in Table 3.2 would only include the first 17 sensors.

This disadvantage can be overcome by recording the full waveforms of the same event at all the sensors. This can be realized by using a multiple channel transient data acquisition system with proper pre-trigger and total sample lengths. The Vallen AMSY4-SF is such a system.

[3]The frequency of rock fracturing-induced microseismic event can be close to the MHz level. A sampling rate of 10 MHz or even higher is commonly used, which requires a time service resolution of 0.1 μs from the recording system.

[4]Four more channels were added to the 20-channel PAC system after the malfunction of two previous channels, so the sensor ID ranged from 1 to 23.

Table 3.2: Arrival time examples processed from PAC data

Arrival time, s	Sensor	Note	Arrival time, s	Sensor ID	Note
0	0	New event	495.3953455	13	
495.3953165	14		495.3953478	1	
495.3953168	23		495.3953545	19	
495.3953183	22		495.3953558	11	
495.3953193	10		495.3953610	21	
495.3953200	8		0	0	New event
495.3953205	5		500.6693935	15	
495.3953225	15		500.6693978	9	
495.3953278	9		500.6694133	21	
495.3953308	4		500.6694168	10	
495.3953345	20		500.6694378	14	
495.3953350	18		0	0	New event
495.3953373	3		601.1586735	6	
495.3953385	16		601.1586740	9	
495.3953388	7		601.1586768	7	
495.3953420	6		601.1586978	20	
495.3953448	12		601.1586998	13	

3.3.1.2 Vallen Data Processing

1. System hardware and test setup

The 15-channel AMSY4-SF made by Vallen Systeme GmbH, Germany is a high resolution digital transient recording system (Vallen, 1998). It can record the full waveforms from 15 sensors and save them as digital signals using a 16-bit AD (analog-to-digital) converter.

Each channel can be configured independently. The Vallen System supplies three trigger modes: Normal, Master and Slave, and Pool. The Normal mode triggers each channel independently. The Master and Slave mode controls the trigger in this way: the Master channel not only triggers itself, but also trigger the Slave channels affiliated to it; the Slave channels can not trigger themselves, but are controlled by the Master channel they affiliate to. The Pool mode triggers the system in such a way that once a single channel triggers, all the rest in the pool mode will be triggered. The last mode was used for the microseismic tests in this study.

Each channel has a 32 MB buffer memory which allows the storage of 64,000 waveforms for 512 samples each. If the sample length is 1024 or 2048, then the storage capacity would be 32,000 or 16,000 waveforms, which is big enough for normal tests. In the microseismic tests, a sample length of 1024 or 2048 was used.

Because the threshold is higher than zero, the first motion might be lost if the waveform is recorded from the trigger point. A pre-trigger length is set to avoid this situation. In the microseismic tests, 400 samples were selected as the pre-trigger length.

2. Arrival Time Data Process

(1) Data structure of the Vallen System

The Vallen System digitalizes the transient waveforms and saves them in the memory in a serial way. Each time when the system is set up to start recording, a TRAnsient data file is opened. It has a file header of 37,888 bytes for the system configuration and the test information (Vallen, 1998).

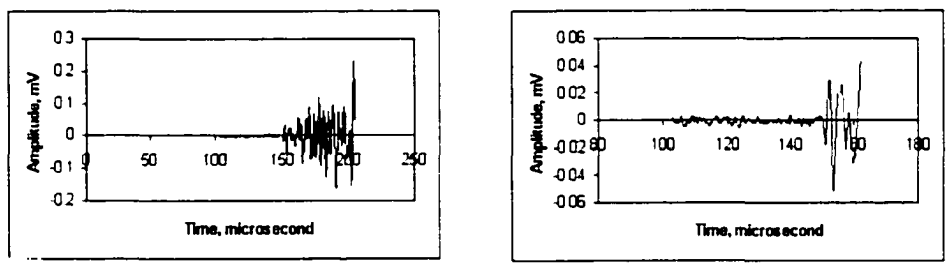
After the file header, the microseismic event data are saved according to the event occurrence order. The waveform detected at each sensor is called a WAVESET. The recorded data for each WAVESET is called a RECORD. The WAVESETs of the same microseismic event are stored in a random order[5]. Each RECORD has its own header of 128 bytes which stores the WAVESET information, such as trigger time, channel ID, etc.

Because the software attached to the hardware is not designed for the purposes of hydraulic fracturing experiments, a way to retrieve the requested information from the waveform data file is needed. The manufacturer supplied an option by exporting the waveform data as ASCII data. This is helpful if the data volume is small. For tests run in this research, the number of recorded WAVESETs ranged from 16,215 to 63,477 with sampling length of 1,024 or 2,048 points. The conversion to ASCII data does not offer an efficient solution in this situation. The best way is to operate on the waveform data directly, requiring the knowledge of the detailed

[5]This was observed in reviewing the waveforms of the test data and was further confirmed by Mr. Forker in Vallen GmbH, Germany in a phone talk on November 13, 2001.

data structure in each record.

Because the detailed data structure was not available from the system manufacturer, it was deciphered through trial-and-error. With this deciphered data structure in hand, the requested information for the microseismic waveforms at each channel, such as P-wave arrival times and sensor IDs, could be retrieved or calculated through operating the waveform data. Figure 3.3 shows an example of the retrieved full waveform (a) and the noises before the first motion (b).



(a) (b)

Figure 3.3: An example of the full waveform and the noises before the first motion.

(2) Searching for the P-wave arrivals

From Figure 3.3, it can be seen that there are noises before the first motion. By reviewing the waveforms from different tests, it was found that low level noises commonly existed. Identification of the first motions and thus the P-wave arrivals in this case is achieved through the following three steps:

Step 1: calculate the variance at each sample point using a 5-point window and the average amplitude of the first 200 points.

Step 2: estimate the first motion from the ratio of variances of two neighboring points. Because the variances among random noises do not change very much, a variance ratio of 2 to 5 can properly indicate the first motion.

Step 3: search the P-wave arrival backward from the estimated first motion. The P-wave arrival is defined as the point where the absolute amplitude is 2 larger[6]

[6]In a 16-bit system, the waveform amplitudes can vary from -32.768 to +32767, corresponding to the output at the sensor from -5.000 mV to +5.000 mV.

than the absolute average amplitude of the first 200 points, assuming that the first motion does not appear in the first 200 points based on the reviewing of the recorded waveforms.

This 3-step searching procedure has been coded into the ArrTime program (Zeng, 2002). Manual verification of the processed data showed an error of 2 to 3 points, which was 0.2 to 0.3 μs in terms of arrival times based on the 10 MHz sampling rate.

(3) ArrTime program and the processed Vallen waveform data

In addition to identifying the P-wave arrival, the ArrTime program splits the cumulatively stocked WAVESETs into different microseismic events, counts total triggered sensors in each event, gets the trigger time of the event, records the WAVESET ID, the sensor ID, the noise level, the maximum signal amplitude, the P-wave arrival time in microseconds, the first motion peak arrival time and its amplitude.

Figure 3.4 shows the arrival time file header and part of the processed results of the first two microseismic events. The file header records the original waveform file, the resulted arrival time file, the sample length, the sampling interval in μs/point (the reciprocal of sampling rate), the start and the end wavesets processed, and the signal-noise ratio defined previously.

Among the retrieved and calculated data of each microseismic event, the first line shows the event information which includes the event ID (MSID), the number of triggered sensors (Sensor) and the event trigger time in millisecond (Time)[7].

Followed the event information are the WAVESET data, which include the WAVESET ID (Set), the sensor ID and the channel connected to the sensor (Chl), the noise (Noise) defined as the maximum absolute amplitude in the first 200 points, the maximum signal amplitude (SigMax) defined as the maximum absolute amplitude for the whole sampled WAVESET, the relative P-wave arrival time (ArrT)

[7] The Vallen System uses an absolute clock which takes the zero at the beginning of each month and counts the time in millisecond. So the time of 2,544,524,325,509 shown in Figure 3.4 means 29dd:10hh:48mm:44.325 509 ss.

```
Source File:                c:\allusr\zeng\data\hf6\hf6.TRA
Result File:                c:\allusr\zeng\data\hf6\hf6.ART
Sample Length:               1024
Sampling Interval:           0.1
Start wave set:              1
End wave set:                63477
Signal-Noise Ratio:          2

MSID/Set     MSChl/Chl   Time/Noise      SigMax      ArrT,micros   Peak,micros   PeakAmp

 1             15          2544524325.5090
 1             3            3              64          43.5          43.9          -7
 2             4           -5              42          41.1          41.4          -8
 3             5           -5             -27          56.4          60            -11
 4             6           -3              39          49.9          50.3          -5
 5             7           -4             -54          33.3          33.9          -11
 6             8           -3              42          47.3          47.7           8
 7             9           -3             -60          44.7          45.6          -5
 8             10          -3              61          34.5          34.9           12
 9             11          -4             -42          54.1          56.2          -8
 10            12          -3             -51          45.6          46.5           5
 11            13          -2              74          33.1          33.3          -5
 12            14          -3             -72          46.9          47.9           6
 13            15          -3             -82          45.4          45.8           8
 14            1            3             -33          53.6          54.1           6
 15            2           -4             -69          46.4          47.5          -9
 2             15          2544535447.2565
 16            11          -3             -120         55.9          56.3          -10
 17            12          -4             -166         49            49.4          -13
 18            13          -4             -167         37.3          37.6          -8
```

Figure 3.4: The file header and part of the first two microseismic events' parameters processed from the Vallen System-recorded waveform file.

defined as the time from the start point of sampling to the P-wave arrival point, the relative time (Peak Time) and the amplitude (Peak Amp) of the first motion peak.

With these arrival times processed from the original files recorded by the PAC and/or the Vallen systems, the LOCATION program can be called to find the coordinates of each microseismic event based on the simplex algorithm introduced in the previous section (Zeng, 2002).

3.3.2 Program Development

Based on the simplex algorithm developed in the previous section, a computer program named LOCATION was written to conduct the microseismic source location (Zeng, 2002). Figure 3.5 shows the pertinent flowchart.

The program is composed of the following five blocks:

1. *Input data.*

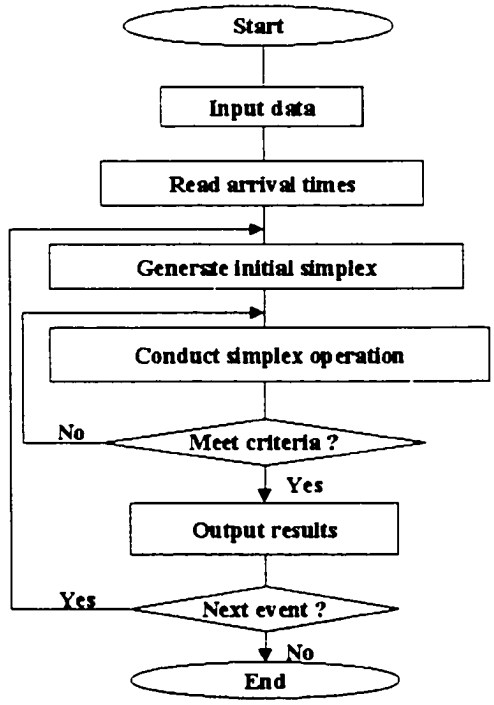


Figure 3.5: Flowchart of the simplex-based microseismic LOCATION program.

This block prepares some control data for the executions. The input data include geometric limits of the monitored objects, estimated lockout time, number of used sensors, sensor coordinates, velocity models and initial velocities, and criteria for simplex operations (ending criteria, maximum iteration), and start and end microseismic events.

Figure 3.6 shows the graphic user interface (GUI) of the main menu of LOCATION in the data input stage.

2. *Read arrival times.*

This block opens the previously prepared arrival time file, reads the sensor ID and the arrival times for the microseismic events according to some criteria. Depending on the characteristics of the arrival time file, the microseismic event filtering criteria can be one single condition or a combination of several conditions. For example, for the PAC arrival time file, the minimum number of triggered sensors was used as the criterion. For the Vallen data, the noise level, the maximum signal

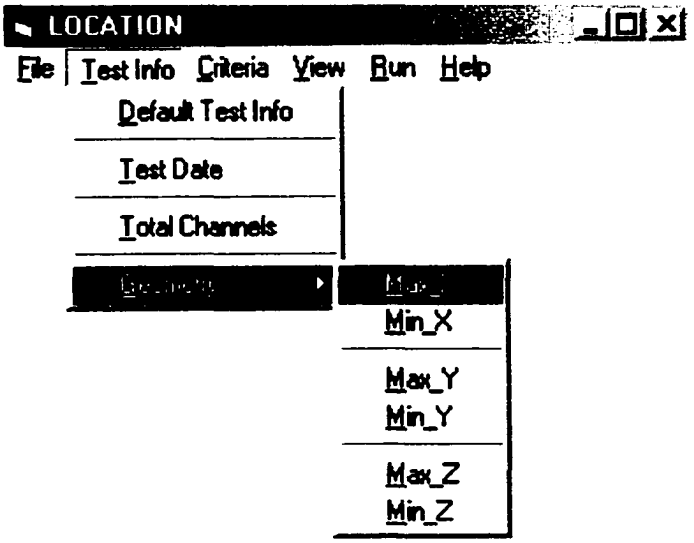


Figure 3.6: GUI of the main menu of the LOCATION program in the data input stage.

amplitude and the number of triggered sensors were used together in selecting the microseismic events.

3. *Generate initial simplex.*

The geometric limits of the monitored object are used to generate the geometric coordinates of the vertices. The occurring time at each vertex is randomly generated by using the earliest arrival time among the triggered sensors and the lockout time. The velocity components in each vertex are randomly generated according to the velocity model and the initial velocities.

4. *Conduct simplex operation.*

This part calculates the time residual for each vertex. The worst vertex is substituted by a new one. The handling will continue until one of the three criteria: the vertices distance, the time residual or the iterations, is met.

5. *Output results.*

Once the simplex operation is finished for one microseismic event and meets the residual distance and/or time criteria, the results are saved. If the operation ends

due to reaching the iteration criterion, the results are not saved. In this case, the event will be considered as unlocatable. The program will continue to handle the next event until the end event or the end of the file. Figure 3.7 displays the results of the file header and the first several microseismic events. The LOCATION and other related programs have been developed in Visual BASIC.

```
This file stores the location result of : c:\allusr\zeng\data\hf6\hf6.LOC
Arrival time file is :      c:\allusr\zeng\data\hf6\hf6.ART
Sensor file is :            c:\allusr\zeng\data\hf6\hf6.SEN
Velocity file is :          c:\allusr\zeng\data\hf6\hf6.VEL
Location result file is :   c:\allusr\zeng\data\hf6\hf6.LOC
TestDate =      12
TotalChl =      15
MaxNoise =      6
MinAmp =        66
MinSigs =       6
StartMSID =     1
EndAEID =       10000
MaxSpxDia =     10
MaxIter =       200
MaxX =          73
MinX =         -73
MaxY =          52
MinY =         -52
MaxZ =          56
MinZ =         -56

MSID          WaveSet       XO mm         YO mm         ZO mm         D_res mm      T_res micros
 2             30           -30.8          8.3          -32           8.05          3.05
 7             105           39.1         -16.2          27           8.05          3.05
 9             135          -16.1         -49.3         -42.9         9.05          2.05
 20            300          -1.1           12.8          3            8.05          3.05
 28            420          -4.5          -19.3          43           9.05          2.05
 29            435          -43.5         -37.9          4.2          9.05          2.05
```

Figure 3.7: The file header and part of the located events generated by LOCATION.

3.4 Verification of the LOCATION Program

The LOCATION program was verified using synthetic data, pencil break events, and some full waveform microseismic data from researchers in a petroleum company.

3.4.1 Test 1: Synthetic Data from Various Parts of a Block

A cement block with a dimension of $419 \times 419 \times 431mm$ was used to produce synthetic data. An orthogonal coordinate system was defined to be originated from the center of the block. Eight sensors were designed to cover the block on

all the six surfaces in all three directions. The block was divided into even grids in the three directions, with 100 mm between two neighboring grid lines in each direction. In total, 125 grids were created. These grids were used as the artificial sources to generate the synthetic data of microseismic arrival times with a randomly distributed trigger time in a resolution of 0.1 microsecond.

The microseismic LOCATION program was then used to locate these artificial microseismic events. Table 3.3 compares the first 10 synthetic sources and the calculated sources. The absolute error is defined as the distance from the calculated source to the true source. The relative error is defined as the ratio of the absolute error to the maximum dimension of the specimen (i.e., the distance between two diagonal corners). Among all the 125 sources, only 12 could not be located within the 200 iterations. So more than 90% of the artificial microseismic events can be located. The rest were all located within an error level similar to that in Table 3.3.

Table 3.3: Located results of the first 10 synthetic data

ID	True source (mm)	Cal source (mm)	Abs err (mm)	Rel err (%)
1	-200.0,-200.0,-200.0	-202.3,-202.4,-202.4	4.1	0.6
2	-200.0,-200.0,-100.0	-195.6, -195.6,-99.9	6.2	0.8
3	-200.0,-200.0,0.0	-203.3,-204.2,1.3	5.5	0.8
4	-200.0,-200.0,100.0	-195.7, -191.9, 93.5	11.2	1.5
5	-200.0,-200.0,200.0	-191.3,-194.6,191.2	13.5	1.8
6	-200.0,-100.0,-200.0	-207.2, -99.0, -217.0	7.3	1.0
7	-200.0,-100.0,-100.0	-199.2, -100.0, -99.5	0.9	0.1
8	-200.0,-100.0,0.0	-200.6,-101.1,-1.0	1.6	0.2
9	-200.0,-100.0,100.0	-195.5,-100.6,99.1	4.6	0.6
10	-200.0,-100.0,200.0	-198.3,-98.1,191.2	3.1	0.4

In additon, random error influence on the location results is also tested. The first tested factor was initial occurring time. It was found that when the initial occurring time was randomly generated between the earliest arrival time minus the lockout time and the earliest arrival time plus the lockout time, the LOCATION program located the results properly. If the initial occurring time was generated out of this range, the located results were heavily influenced. This test result set up

the principle for the generation of the initial occurring time during the preparation of the initial simplex.

The velocity influence was tested by randomly changing the velocities from the true velocities in certain percentage. The test results showed that the change of the velocities within 30% of the true velocities would have no obvious influence on the location results. Therefore, the change of the velocities due to the fracturing of the specimen would not adversely change the location results.

The third tested term was the arrival times. It was found that the arrival time has a large influence on the location results. By the arrival times were changed within ± 2 microseconds of the true arrival times, the location results were not influenced. When the change was ± 5 microseconds, the location results were very poor. When the change was ± 10 microseconds, the location results were totally different.

Therefore, obtaining accurate arrival times would improve the location results greatly. The application of high sampling rate, (e.g., 10 MHz, or 0.1 microsecond/point), and the using of the ArrTime program are two valuable steps in improving the location results.

3.4.2 Test 2: Influence of Sensor Coverage

In the previous synthetic data test, the sensors were designed to be distributed on all the 6 surfaces of the block. In real experiments, loads are applied in one, two or even three directions. Under these cases, the sensors can not always be installed on the places that best cover the block. So the influences of the sensor coverage to the location should be tested.

In this synthetic data test, the same cement block was used. But the sensors were assumed to be installed onto four surfaces in two directions of the block. The origin of the coordinate system was also shifted from the block center to the center of the bottom. Synthetic arrival time data of 15 microseismic events randomly located within the cement block were prepared. The LOCATION program was used to find

Table 3.4: Test of influence of sensor coverage

ID	True source (mm)	Cal source (mm)	Abs err(mm)	Rel err (%)
1	38.1, 25.4, 76.2	38.1, 25.3, 75.8	0.4	0.1
2	76.2, 127.0, 381.0	76.8, 126.0, 378.6	2.7	0.4
3	127.0,127.0,330.2	125.6,126.8,329.2	1.8	0.2
4	-101.6,-101.6,355.6	-102.9, -102.2, 353.2	2.8	0.4
5	177.8, 152.4,406.4	180.9,155.4,409.0	5.1	0.7
6	-76.2,76.2,228.6	-74.5, 75.0, 229.1	2.2	0.3
7	76.2,-76.2,228.6	-76.7, 76.3, 228.0	0.8	0.1
8	25.4,25.4,25.4	24.5,25.8,18.0	7.5	1.0
9	0,25.4,355.6	1.6,24.2,353.5	2.9	0.4
10	0,0,304.6	5.3,2.7,299.4	8.0	1.1
11	0,177.8,152.4	17.1,171.7,159.5	19.5	2.7
12	101.6,101.6,101.6	103.3,100.5,101.8	2.0	0.3
13	25.4,50.8,381.0	31.7,42.2,372.5	13.7	1.9
14	127.0,127.0,101.6	134.2,125.6,97.3	8.5	1.2
15	50.8,177.8,304.8	50.3,181.6,301.1	5.3	0.7

the event source coordinates. Table 3.4 shows the results. The program located 13 events with an error of less than 10 mm, 2 with an error between 10 and 20 mm.

3.4.3 Test 3: Hsu-Nielson Source Events

In order to generate reproducible acoustic emission / microseismic signals, Hsu et al. (1977) introduced a mechanical device consisting of a mechanical pencil of 0.3 mm "lead" mounted on a hinged stand. By breaking this pencil lead, a well-defined step unction can be triggered. This was called the Hsu-Nielson source (ASTM, 1994).

Following this idea, a mechanical pencil of 0.5 mm "lead" with a fulcrum was used to generate artificial acoustic emission / microseismic signals. Ten events induced by this Hsu-Nielson source were triggered on the specimen surfaces and the travel time of these events were recorded. By processing these travel time data, the LOCATION program was tested. The results are shown in Table 3.5.

The results showed that 4 events were located with an error of less than 25 mm, 3 events were located with an error from 26 to 50 mm, and 3 other events were

Table 3.5: Location results of Hsu-Nielson sources

ID	True source (mm)	Cal source (mm)	Abs err(mm)	Rel err(%)
1	50.8,-209.6,355.6	54, -220, 365	14.4	2.0
2	0,-209.6,279.4	6.7, -212, 301	22.8	3.1
3	-76.2,-209.6,76.2	-97,-223,47	38.3	5.2
4	127,-209.6,76.2	135, -208, 61	17.3	2.4
5	209.6, -76.2,101.6	231,-58,114	30.7	4.2
6	209.6,-152.4,355.6	218,-193, 417	74.1	10.1
7	209.6,0,355.6	174, -56, 333	70.1	9.6
8	209.6,0,101.6	155,-9,86	57.5	7.9
9	0,209.6,152.4	11,210,147	12.3	1.7
10	-76.2,209.6,228.4	-65,205,270	43.3	5.9

located with an error between 51 and 75 mm.

In comparing to the results of Test 1 and Test 2, the location error in this Test is much higher. Further investigation showed that the errors were related to the surface on which the events were triggered. For example, all the 3 events with the largest location errors were triggered from the top surface which had a small incident angle to the sensors. All events with the smallest location errors were triggered from side walls where the incident angles were large.

In the real experiments, microseismic events are inside the sample. The incident angles to the sensors are usually larger than those of the surface events. So the location errors should be reduced greatly.

3.4.4 Test 4: Event with Full Waveform Data from Other Researchers

Full waveform data of 12 microseismic events from an experiment done by researchers in a petroleum company were used to further test the LOCATION program. Table 3.6 shows the source locations obtained by another location program utilized by that company and the results located with the LOCATION program. The difference showed the distance between the two different sources.

This test showed that the located results were almost exactly the same as the

Table 3.6: Location error of events from full waveforms

Event	Gievn source (mm)	Cal source (mm)	Difference(mm)
1	0,0,0	0,0,0	0
2	50.8,0,216	50.8,0,216	0
3	102,0,216	102,0,216	0
4	152,0,216	152, 0, 216	0
5	50.8,0,-216	50.8,0,-216	0
6	0,0,229	0,0, 229	0
7	37.3, 9.8, 208	37.3, 9.7, 207.5	0.5
8	32.2,14.8,201	32.2,14.8,201.2	0.2
9	95.4,1.5,222	95.4,1.5,222.3	0.3
10	16.7,-20.7,-8.8	16.7,-20.7,-8.8	0
11	-0.2, -17.7, -1.8	-0.2,-17.7,1.8	0
12	-14.4,-3.8,-4.4	-14.4,-3.8,-4.4	0

actual sources. In comparing to the location results of pencil breaks shown above, this may imply that the full waveform data make the microseismic location more accurate.

From the four tests, it can be seen that the LOCATION program worked rather well for the synthetic data and the full waveform data. Some surface pencil breaks were located with large errors due to their small incident angle to the sensors.

3.5 Discussion

A lot of time has been spent on imaging the geometry of hydraulic fractures by a number of people in the petroleum industry. Microseismic techniques have been proven one of the most promising methods to depict the fracture by locating the induced microseismic events. The popularly used microseismic location algorithm was based on linearizing the non-linear equations using Taylor's expansion which made the location algorithm easy to be ill-conditioned and thus could not locate the recorded microseismic events as expected.

Adopting the general idea of simplex optimization, a robust algorithm for microseismic event location was developed. The related computer program LOCATION

was coded and tested with synthetic data, pencil break events, and events from full waveform data. All these tests showed that this simplex-based microseismic location program can locate most of the given microseismic events at a reliable and acceptable accuracy, except for events from the surface pencil breaks which have small incident angles.

In addition, it was noticed that the location error for events processed from full waveform data were extremely low. So full waveforms should be used for locating microseismic events. But the normally existing noises before the first motion cause difficulties in identifying the accurate P-wave arrival times and the first motion. If there is a tool that can calculate the first motion of the waveform at an known observing point from a given source, then the located results can be checked by comparing the recorded and the calculated first motions. This calls for the development of a forward microseismic waveform simulator, the topic of the next chapter.

4 Simulation of Microseismic Waveforms

4.1 Introduction

Chapters 2 and 3 called for the development of a forward simulator to improve the location accuracy through the correct identification of the first motion. In additon, such a simulator is also needed for selecting the favorite locations for the sensors in the observed domain. The development of such a simulator will be introduced in this chapter.

Synthetic seismograms have been a useful tool for seismologists to study the dynamic parameters of natural earthquakes (Aki and Richards, 1980; Bullen and Bolt, 1985; Lay and Wallace, 1995). Due to the existing similarities between natural earthquakes, field and laboratory detected microseismics (Mogi, 1962; Scholz, 1968; Gibowicz and Kijko, 1994), the technique of synthetic seismograms can, therefore, be adapted to simulate waveforms of the first motion associated with such microseismics.

Ohtsu and Ono (1984, 1986) generalized the seismological representation theorem for microseismic sources and derived formulae for displacement fields of pure Mode-I and pure Mode-II fractures. Using this theory, induced waveforms due to disbonding and/or pulling-out[1] have been studied. The author assumed that the fracture lies into a plane that includes one or two of the coordinate axes; and all the sensors were attached onto the free surface, similar to natural earthquake de-

[1] A specially designed experiment which mainly caused tensile fracturing.

tection (Ohtsu et al., 1987; Ohtsu et al., 1989), as schematically shown in Figure 4.1 (Ohtsu and Ono, 1984).

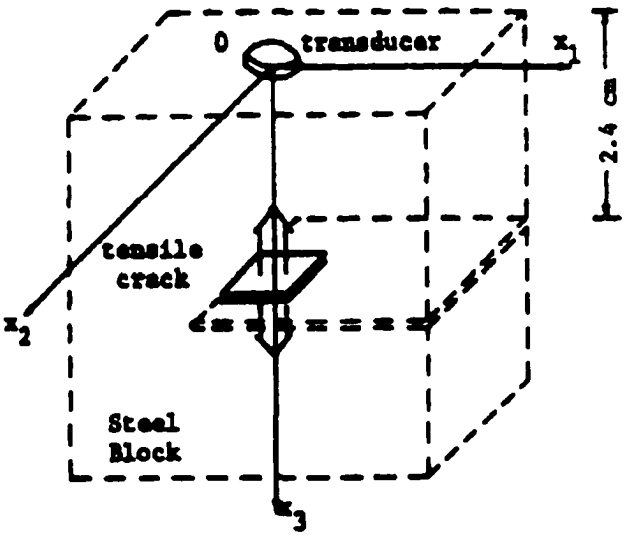


Figure 4.1: Fracture orientation and the transducer (from Ohtsu and Ono, 1984).

While this sensor configuration might be useful in simulating the waveforms of first motion induced by disbonding and pulling-out, it is practically not useful in most cases, because usually a three-dimensional coverage of the sensors over the observed domain is expected. In additon, the fracture is usually not parallel to the observing surface. The reason for such a "special" experimental configuration is for the applicability of their theory which assumed that fracturing plane has a special angle with respect to the observing surface (Ohtsu and Ono, 1984 and 1986).

Obviously this assumption is a tough restriction to the practical application. This theory needs to be expanded so as to be able to calculate the waveforms of the first motion from any source, at any observing positions or surfaces. The following sections will derive the theory, develop the computer program, and validate the program with some examples.

4.2 Methodology

The problem is solved following the flowchart shown in Figure 4.2. First the problem is described assuming sensors on a three-dimensional block. Then the governing equations are established according to the principle of conservation of linear momentum.

Based on the size of tested blocks used in laboratory experiments, the relatively short wavelength and small source scales make the problem a simplified half-space Lamb's problem. Due to the geometrical symmetry, the solutions can be expanded to any surface by rotating the axes of the original problem.

Betti's theorem of reciprocity relates two groups of sources and displacements for Lamb's problem. With this theorem, the displacement field of a given force can be expressed in terms of a known displacement solution from a known force. With Green's function, a computable displacement solution induced by a known force (the unit force), the representation theorem in a half space, is obtained.

Microseismic sources can be expressed by equivalent forces. With these equivalent forces, the displacement field induced from the microseismic sources, i.e., the microseismic source representation theorem, is obtained. This representation theorem can be further converted into the convolution of two physically meaningful terms, the spatial derivatives of Green's function and the moment tensor.

Using the fracture propagation direction, the normal to the fracture plane and the dislocation vector, the general solution of the displacement field for a fracture in the three-dimensional space is obtained.

4.3 Development of the Formulae

4.3.1 Statement of the Problem

Figure 4.3 shows an unconfined block with its Cartesian coordinate system. Assume there occurs an internal microfracturing at $S(\mathbf{x_S})$ at time $t = \tau$. The task is to find

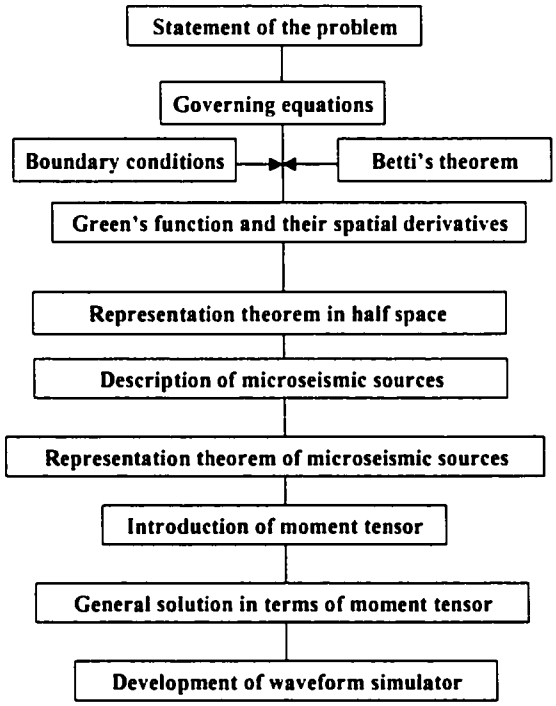


Figure 4.2: Methodology flowchart.

the displacement $\mathbf{u}(\mathbf{x}, t)$ detected by microseismic sensors attached at A, B and C as well as other locations on the free surfaces of the block.

4.3.2 Governing Equations

Assume the material of the block is homogeneous, isotropic, linear elastic and adiabatic conditions prevail (no heat exchange with the outside). This makes the block a linear momentum conservation system. According to the principle of conservation of linear momentum, the total linear momentum of an isolated system remains constant. Therefore, for a uniform elastic domain in the Cartesian coordinate system, the conservation of linear momentum can be written as (Johnson, 1974):

$$\rho \frac{\partial^2}{\partial t^2} \mathbf{u}(\mathbf{x}, t) = \mathbf{f}(\mathbf{x},\mathbf{t}) + (\lambda + 2\mu) \nabla [\nabla \cdot \mathbf{u}(\mathbf{x},t)] - \mu \nabla \times \nabla \times \mathbf{u}(\mathbf{x}, t) \qquad (4.1)$$

where,

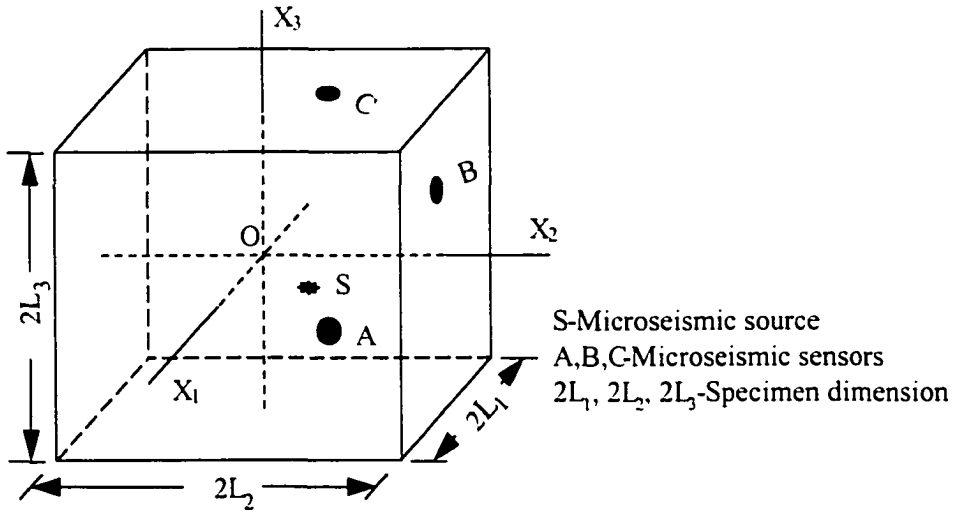


Figure 4.3: Coordinate system in the specimen.

$\left\{ \begin{array}{l} \mathbf{x} = \text{Cartesian coordinate;} \\ t = \text{time;} \\ \mathbf{u} = \text{displacement;} \\ \mathbf{f} = \text{body force;} \\ \rho = \text{material density;} \\ \lambda, \mu = \text{Lamé's elastic constants; and,} \\ \nabla = \frac{\partial}{\partial x_1}\mathbf{x}_1 + \frac{\partial}{\partial x_2}\mathbf{x}_2 + \frac{\partial}{\partial x_3}\mathbf{x}_3, \text{the del operator.} \end{array} \right.$

This is the governing equation in vector form; it represents three scalar equations for each of the three coordinate axes.

4.3.3 Boundary Conditions

Due to the free surface assumption, there are no tractions on these surfaces. So the boundary conditions for this problem are:

$$\begin{aligned} T_{ij}(\mathbf{x}.t) &= \lambda\left[u_{i,i}(\mathbf{x}.t)\right]\delta_{ij} + \mu\left[u_{i,j}(\mathbf{x}.t) + u_{j,i}(\mathbf{x}.t)\right] \\ &= 0 \qquad (i,j = 1,2,3; \quad x_i = \pm L_1, \pm L_2, \pm L_3) \end{aligned} \tag{4.2}$$

where,

$$\begin{cases} T = \text{surface traction; and} \\ \delta = \text{delta function.} \end{cases}$$

In the present study the block surfaces are assumed free of external forces. A typical block size has dimensions of 420 mm×420 mm×432 mm (16.5 in×16.5 in×17 in). The wave velocity is about 4 km/s, and the dominant frequency of microseismic events is in the order of 100 to 2,000 kHz (Lockner, 1993). So the typical microseismic wavelength may be ranging from 2 to 40 mm. Compared to the wavelength, each surface of the block can therefore be considered as a free surface in a half space.

Due to the geometrical symmetry of the observed domain, only solutions on one surface, say $x = +L_3$, are needed. Solutions for other surfaces can be obtained by rotating the coordinate system and shifting the axes accordingly while maintaining the right hand rule.

Now the basic problem is to solve Eq.(4.1) by satisfying the boundary conditions defined in Eq. (4.2) on the surface corresponding to $x_3 = +L_3$.

4.3.4 Betti's Reciprocity Theorem and Representation Theorem

Assume two groups of body forces, $\mathbf{f}_1$ and $\mathbf{f}_2$, acting on the same block separately; their corresponding displacements are $\mathbf{u}_1$ and $\mathbf{u}_2$. Betti's reciprocity theorem relates these two groups of the forces and their displacements as follows (Aki and Richards, 1980):

$$\begin{aligned} \iiint_V (\mathbf{f}_1 - \rho\frac{\partial^2 \mathbf{u}_1}{\partial t^2}) \cdot \mathbf{u}_2 dV + \iint_S \mathbf{T}(\mathbf{u}_1, \mathbf{n}) \cdot \mathbf{u}_2 dS &= \iiint_V (\mathbf{f}_2 - \rho\frac{\partial^2 \mathbf{u}_2}{\partial t^2}) \cdot \mathbf{u}_1 dV \\ &\quad + \iint_S \mathbf{T}(\mathbf{u}_2, \mathbf{n}) \cdot \mathbf{u}_1 dS \end{aligned} \tag{4.3}$$

where,

$\mathbf{f}_1, \mathbf{f}_2$ = the two body forces;

$\mathbf{u}_1, \mathbf{u}_2$ = the two displacement fields induced by $\mathbf{f}_1$and $\mathbf{f}_2$, separately;

V, S = volume and surface of the observed domain;

$\mathbf{n}$ = normal to the surface;

$\mathbf{T}$ = tractions on the surfaces; and,

ρ = density.

The physical meaning of this theorem is that the work done on the second group of displacements, $\mathbf{u}_2$, by the first group of body forces equals the work done on the first group of displacements, $\mathbf{u}_1$, by the second group of body forces. This relationship means that once the displacement induced by one force is known, the displacement by the other force can be obtained. It sets up the foundation for the application of Green's function, the displacement of a unidirectional unit impulse, in calculating the displacement of any force.

If the displacement fields are zero before time $\tau \leq \tau_0$, Betti's theorem can be simplified as:

$$\begin{aligned} & \int_{-\infty}^{\infty} dt \iiint_V [\mathbf{u}_1(\mathbf{x},t) \cdot \mathbf{f}_2(\mathbf{x},\tau - t) - \mathbf{u}_2(\mathbf{x},\tau - t) \cdot \mathbf{f}_1(\mathbf{x},t)]\, dV \\ = & \int_{-\infty}^{\infty} dt \iint_S \{\mathbf{u}_2(\mathbf{x},\tau - t) \cdot \mathbf{T}[\mathbf{u}_1(\mathbf{x},t), \mathbf{n}) - \mathbf{u}_1(\mathbf{x},t) \cdot \mathbf{T}(\mathbf{u}_2(\mathbf{x},\tau - t), \mathbf{n}]\}\, dS \end{aligned} \tag{4.4}$$

where the terms are the same as those in Eq.(4.3). This temporal integration form of Betti's theorem enables the possibility of calculating the displacements caused by some time-dependent forces, such as earthquakes, nuclear explosions and microseismics.

4.3.4.1 General Form of Representation Theorem

The representation theorem is a formula expressing displacements at a general point $(\mathbf{x}, t)$ in terms of the quantities that originated the motion. The generating

source of the motion includes the body forces as well as the applied tractions and initial displacements over the surface of the observed domain. The goal is to find an expression for the displacements u due both to body force f throughout the volume V and, at the same time, respecting the boundary conditions on S.

Assume a unidirectional unit impulse, $g_i = \delta_{ij}\delta(x-\xi))\delta(t-\tau)$, being applied at $(\xi, 0)$ in the $n-$direction, and denote the $i-$component of displacement at a general point $(\mathbf{x}, t)$ by $G_{in}(\mathbf{x}, t; \xi, 0)$. Using Betti's reciprocity theorem expressed in Eq.(4.4), the displacements due to both the body force f throughout V and to the boundary conditions, T_i and u_i, on S can be expressed as follows (Aki and Richards, 1980):

$$\begin{aligned} u_n(\xi,\tau) &= \int_{-\infty}^{\infty} dt \iiint_V f_i(\mathbf{x},t) G_{in}(\mathbf{x},\tau-t;\xi,0) dV \\ &+ \int_{-\infty}^{\infty} dt \iint_S \{G_{in}(\mathbf{x},\tau-t;\xi,0) T_i[\mathbf{u}(\mathbf{x},t),\mathbf{n}] \\ &- u_i(\mathbf{x},t) c_{ijkl} n_j \frac{\partial}{\partial \xi_l} G_{kn}(\mathbf{x},\tau-t;\xi,0)\} dS \end{aligned} \tag{4.5}$$

Shifting the source and the receiver, the above equation becomes:

$$\begin{aligned} u_n(\mathbf{x},t) &= \int_{-\infty}^{\infty} d\tau \iiint_V f_i(\xi,\tau) G_{in}(\xi,t-\tau;\mathbf{x},0) dV(\xi) \\ &+ \int_{-\infty}^{\infty} d\tau \iint_S \{G_{in}(\xi,t-\tau;\mathbf{x},0) T_i[\mathbf{u}(\xi,\tau),\mathbf{n}] \\ &- u_i(\xi,\tau) c_{ijkl}(\xi) n_j \frac{\partial}{\partial \xi_l} G_{kn}(\xi,t-\tau;\mathbf{x},0)\} dS(\xi) \end{aligned} \tag{4.6}$$

where,

$$\begin{cases} u_n = \text{displacement in the } n\text{-direction at } (\mathbf{x}, t), \text{ to be found;} \\ f = \text{body force;} \\ G_{kn} = \text{Green's function;} \\ \frac{\partial}{\partial \xi_l} G_{kn} = \text{spatial derivatives of the Green's function;} \\ c_{ijkl} = \text{elastic constant;} \\ T = \text{tractions at } (\xi, \tau) \text{ on } S, \text{ boundary condition;} \\ u_i = \text{displacement on S at } (\xi, \tau), \text{ boundary conditions; and,} \\ n = \text{normal to } S. \end{cases}$$

This is the general representation theorem in elasto-dynamics. In order to calculate the displacements at the observing point $\mathbf{x}$, the Green's function needs to be converted so that the source and the receiver can be exchanged. This needs to be obtained using Betti's reciprocity theorem; but the operation is only valid when the boundary is homogeneous. So two cases, rigid surface and free surface, need to be considered.

4.3.4.2 Representation Theorem on Body with Rigid Surface

If the block has a rigid boundary S, the Green's function on the surface will be zero. Denoting G^{rigid} as the Green's function for this case, the integration of the first part of the second term in Eq. (4.6) is zero, that is,

$$\int_{-\infty}^{\infty} d\tau \iint_S \left\{ G_{in}^{rigid}(\xi, t-\tau; \mathbf{x}, 0) T_i \left[\mathbf{u}(\xi, \tau), \mathbf{n} \right] dS(\xi) \right\} = 0 \tag{4.7}$$

using the reciprocal theorem for G^{rigid}, Eq. (4.6) becomes:

$$\begin{aligned} u_n(\mathbf{x}, t) \;=\; & \int_{-\infty}^{\infty} d\tau \iiint_V f_i(\xi, \tau) G_{ni}^{rigid}(\mathbf{x}, t-\tau; \xi, 0) dV \\ & - \int_{-\infty}^{\infty} d\tau \iint_S u_i(\xi, \tau) c_{ijkl} n_j \frac{\partial}{\partial \xi_l} G_{nk}^{rigid}(\mathbf{x}, t-\tau; \xi, 0) dS \end{aligned} \tag{4.8}$$

4.3.4.3 Representation Theorem on Body with Free Surface

If the block has a free surface S , the traction on the free surface will be zero. Denoting this Green's function as G^{free}, then the integration of the second part of the second term in Eq. (4.6) is zero, that is,

$$\int_{-\infty}^{\infty} d\tau \iint_S u_i(\xi,\tau)\left[c_{ijkl}n_j\frac{\partial}{\partial\xi_l}G_{kn}^{free}(\xi,t-\tau;\mathbf{x},0)\right]dS(\xi)=0 \qquad (4.9)$$

similarly, using the reciprocal theorem on G^{free}, Eq. (4.6) becomes:

$$\begin{aligned} u_n(\mathbf{x},t) &= \int_{-\infty}^{\infty} d\tau \iiint_V f_i(\xi,\tau)G_{ni}^{free}(\mathbf{x},t-\tau;\xi,0)dV \\ &\quad + \int_{-\infty}^{\infty} d\tau \iint_S G_{ni}^{free}(\mathbf{x},t-\tau;\xi,0)T_i(\mathbf{u}(\xi,\tau),\mathbf{n})dS \end{aligned} \qquad (4.10)$$

4.3.5 Representation of Microseismic Sources

There are two types of sources, the external and the internal, that can cause displacements on the surface of the observed domain. Taking the earth as the observing domain, the external sources include such motions as meteorite impacts, rocket launching and surface explosions. The internal sources include earthquakes, underground nuclear explosions and volcanic eruptions. In the laboratory experiment, microseismic sources inside the rocks can be considered as an internal source to the block in terms of this classification. So theories used to describe the internal seismic sources can be adapted to analyze such microseismic sources.

In order to express a microseismic source, a microfracture including two adjacent internal surfaces, F^+ and F^-, need to be included, as shown in Figure 4.4. In Figure 4.4, V represent the observed domain, and S the external boundary surfaces.

If a dislocation occurs on F^+ and F^-, the displacement field is discontinuous there and the equation of motion is no longer satisfied throughout the interior of the domain, V. But is it still satisfied throughout the interior of the surfaces $S+F^++F^-$. So by taking $S+F^++F^-$ as the new boundary surfaces, the representation theorem can still be applied. Furthermore, the external surfaces S

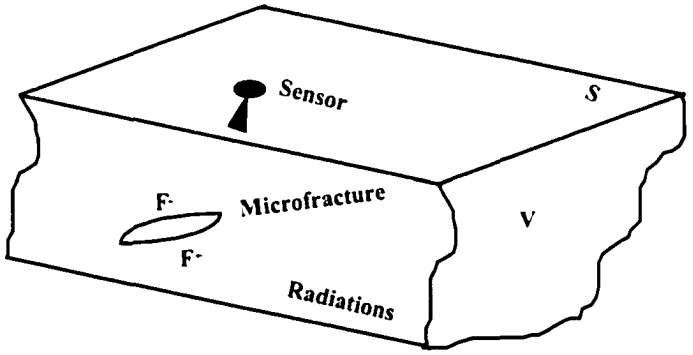


Figure 4.4: A profile of a microseismic source model.

is of no more direct interest, so homogeneous boundary conditions for $\mathbf{u}$ and G can be assumed on S. With these assumptions, the microseismic induced displacement field in the observed domain of V can be represented as:

$$\begin{aligned} u_n(\mathbf{x},t) &= \int_{-\infty}^{\infty} d\tau \iiint_V f_p(\eta,\tau) G_{np}(\mathbf{x},t-\tau;\eta,0) dV(\eta) \\ &+ \int_{-\infty}^{\infty} d\tau \iint_F \left\{ \left[u_i(\xi,\tau)\right] c_{ijpq}(\xi) n_j \frac{\partial}{\partial \xi_q} G_{np}(\mathbf{x},t-\tau;\xi,0) \right. \\ &\left. - G_{np}(\mathbf{x},t-\tau;\xi,0) \left[T_p(\mathbf{u},\mathbf{n})\right] \right\} dF(\xi) \end{aligned} \tag{4.11}$$

where,

$$\begin{cases} \eta = \text{the general position with in } V; \\ \xi = \text{the general position on } F; \\ \mathbf{n} = \text{normal on } F \text{ from } F^- \text{ to } F^+; \text{ and,} \\ [u], [T] = \text{differences of } u \text{ and } T \text{ between the values on } F^+ \text{and } F^-. \end{cases}$$

On the internal surfaces F^+ and F^-, there is no restrictions on the Green's function G. So it can be assumed to have the form that will be convenient for the analysis. For the displacements u, the dislocation on F leads to non-zero value.

$$[u] = u(\xi,\tau)\,|_{F^+} - u(\xi,\tau)\,|_{F^-} \tag{4.12}$$

For the traction T, the tiny dimension of the microseismic source makes it valid to

assume a spontaneous rupture, which means the traction must be continuous on F. But,

$$T(-\mathbf{n}) = -T(\mathbf{n}) \tag{4.13}$$

so the difference of T between the values on F^+ and F^- is zero, that is,

$$\begin{aligned} [T] &= T_p^{F^+}[\mathbf{u}(\xi,\tau),\mathbf{n}] - T_p^{F^-}[\mathbf{u}(\xi,\tau),\mathbf{n}] \\ &= 0 \end{aligned} \tag{4.14}$$

Assuming G and its spatial derivatives with respect to source, $\frac{\partial G}{\partial \xi_q}$, on F are continuous and no body forces are present, Eq. (4.11) can be simplified as:

$$u_n(\mathbf{x},t) = \int_{-\infty}^{\infty} d\tau \iint_F [u_i]\, c_{ijpq}(\xi) n_j \frac{\partial}{\partial \xi_q} G_{np}(\mathbf{x}, t-\tau; \xi, 0) dF(\xi) \tag{4.15}$$

This shows that the dislocation on the microfracture F alone is enough to determine the microseismic displacement field throughout the observed domain. Therefore, once the dislocation, $[u_i(\xi,\tau)]$, on the microfracture F is defined, and the spatial derivatives of Green's function with respect to the microseismic source, $\frac{\partial G}{\partial \xi_q}$, are known, the displacements, $u_n(\mathbf{x},t)$, induced by the microseismic event can be calculated.

4.3.6 Green's Function and The Spatial Derivatives

4.3.6.1 Green's Function

From the above derivation, it is clear that the Green's function and its spatial derivatives are needed in the calculation of the displacement field. As mentioned above, Green's function refers to the displacement solution to Eq.(4.1) under the action of an unidirectional unit impulse (Aki and Richards, 1980). While this is

the way it has been for many years in this field. a more general case with a general pulse function as shown in the following equation would be closer to the reality: i.e.

$$\mathbf{f}(\mathbf{x}.t) = f_i \mathbf{e}_i \delta(x_i - x_i')\delta(t - t') \tag{4.16}$$

The solution for such a general impulsive force is the Green's function. Its solution can be expressed as:

$$\begin{aligned} \mathbf{u}(\mathbf{x}.t) &= G(\mathbf{x}.t;\mathbf{x}'.t') \\ &= g_1(x.t;x'.t') + g_2(x.t;x'.t') + g_3(x.t;x'.t') \end{aligned} \tag{4.17}$$

This problem can be solved using the Laplace's transform (Johnson. 1974). Assuming the source is at $S(0,0,x_3',0)$ and the observing point at the surface $D(x_1,x_2,L_3,t)$. as shown in Figure 4.5.

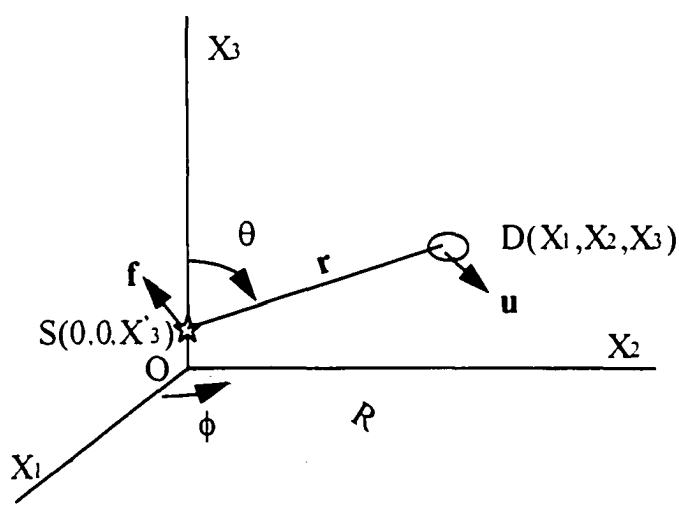


Figure 4.5: Definition of the geometry for the problem.

The main results are as follows (Johnson. 1974):

$$G = \left\{ \begin{array}{c} g_1(x_1.x_2,L_3,t;0,0,x_3',0) \\ g_2(x_1.x_2,L_3,t;0.0,x_3',0) \\ g_3(x_1.x_2,L_3,t;0,0,x_3',0) \end{array} \right\}$$

$$
\begin{aligned}
= & \frac{1}{\pi^2 \mu r} \frac{\partial}{\partial t} \int_0^{\sqrt{((t/r)^2-\alpha^{-2})}} H(t - r/\alpha) \\
& \times \Re e \left\{ \eta_\alpha \sigma^{-1} \left[(t/r)^2 - \alpha^{-2} - p^2 \right]^{-\frac{1}{2}} \mathbf{M}(q, p, L_3, t, x_3') \right\} \mathbf{f} dp \\
& + \frac{1}{\pi^2 \mu r} \frac{\partial}{\partial t} \int_0^{p_2} H(t - t_2) \\
& \times \Re e \left\{ \eta_\beta \sigma^{-1} \left[(t/r)^2 - \beta^{-2} - p^2 \right]^{-\frac{1}{2}} \mathbf{N}(q, p, L_3, t, x_3') \right\} \mathbf{f} dp \qquad (4.18)
\end{aligned}
$$

where,

$$
\begin{cases}
\alpha = (\frac{\lambda+\mu}{\rho})^{\frac{1}{2}}, & P- \text{ wave velocity;} \\
\beta = (\frac{\mu}{\rho})^{\frac{1}{2}}, & S - \text{ wave velocity;} \\
H(t) = \text{the Heaviside unit step function to indicate the arrival of P-/S-waves;} \\
r, \theta = \text{geometrical parameters as defined in Figure 4.5;} \\
p_2 = \begin{cases} ((\frac{t}{r})^2 - \beta^{-2})^{\frac{1}{2}}, & \text{if } \sin(\theta) \le \beta/\alpha; \\ \left[(\frac{(\frac{t}{r} - (\beta^{-2} - \alpha^{-2})^{\frac{1}{2}} \cos(\theta)}{\sin(\theta)})^2 - \alpha^{-2} \right]^{\frac{1}{2}}, & \text{if } \sin(\theta) > \beta/\alpha; \end{cases} \\
t_2 = \begin{cases} \frac{r}{\beta}, & \text{if } \sin(\theta) \le \beta/\alpha; \\ \frac{r}{\alpha} \sin(\theta) + r(\beta^{-2} - \alpha^{-2})^{\frac{1}{2}} \cos(\theta), & \text{if } \sin(\theta) > \beta/\alpha; \end{cases} \\
\eta_\alpha = (\alpha^{-2} + p^2 - q^2)^{\frac{1}{2}}, & \text{for } \Re e\{\eta_\alpha\} \ge 0; \\
\eta_\beta = (\beta^{-2} + p^2 - q^2)^{\frac{1}{2}}, & \text{for } \Re e\{\eta_\beta\} \ge 0; \\
\sigma = \gamma^2 + 4\eta_\alpha \eta_\beta (q^2 - p^2), & \text{intermediate variable; and,} \\
\gamma = \eta_\beta^2 + p^2 - q^2, & \text{intermediate variable.}
\end{cases}
$$

In the first integral of Eq.(4.18), q (for the P-wave part) is given by the expression:

$$
q = -\frac{t}{r} \sin(\theta) + i \left[(\frac{t}{r})^2 - \alpha^{-2} - p^2 \right]^{\frac{1}{2}} \cos(\theta) \qquad (4.19)
$$

while in the second integral q (for the S-wave part) is given by:

$$
q = -\frac{t}{r} \sin(\theta) + i \left[(\frac{t}{r})^2 - \beta^{-2} - p^2 \right]^{\frac{1}{2}} \cos(\theta) \qquad (4.20)
$$

where $i = \sqrt{-1}$.

$\mathbf{M}$ and $\mathbf{N}$ are 3×3 matrices. Their elements are as follows:

$$
\left.
\begin{aligned}
M_{11} &= 2\eta_\beta\left[(q^2+p^2)\cos^2\phi - p^2\right] \\
M_{12} &= 2\eta_\beta(q^2+p^2)\sin\phi\cos\phi \\
M_{13} &= 2q\eta_\alpha\eta_\beta\cos\phi \\
M_{21} &= M_{12} \\
M_{22} &= 2\eta_\beta\left[(q^2+p^2)\sin^2\phi - p^2\right] \\
M_{23} &= 2q\eta_\alpha\eta_\beta\sin\phi \\
M_{31} &= q\gamma\cos\phi \\
M_{32} &= q\gamma\sin\phi \\
M_{33} &= \eta_\alpha\gamma
\end{aligned}
\right\} \tag{4.21}
$$

$$
\left.
\begin{aligned}
N_{11} &= \eta_\beta^{-1}\left\{\eta_\beta^2\gamma - (\gamma - 4\eta_\alpha\eta_\beta)\left[(q^2+p^2)\sin^2\phi - p^2\right]\right\} \\
N_{12} &= \eta_\beta^{-1}(q^2+p^2)(\gamma - 4\eta_\alpha\eta_\beta)\sin\phi\cos\phi \\
N_{13} &= -q\gamma\cos\phi \\
N_{21} &= N_{12} \\
N_{22} &= \eta_\beta^{-1}\left\{\eta_\beta^2\gamma - (\gamma - 4\eta_\alpha\eta_\beta)\left[(q^2+p^2)\cos^2\phi - p^2\right]\right\} \\
N_{23} &= -q\gamma\sin\phi \\
N_{31} &= -2q\eta_\alpha\eta_\beta\cos\phi \\
N_{32} &= -2q\eta_\alpha\eta_\beta\sin\phi \\
N_{33} &= 2\eta_\alpha(q^2-p^2)
\end{aligned}
\right\} \tag{4.22}
$$

The physical meaning of Eq.(4.18) is as follows. The first term represents the compressional waves (P-waves) part, the second term represents the shear waves, all generated from the same source. The time t_2 in Eq. (4.18) is the arrival time of the direct shear wave when $\sin(\theta) \leq \frac{\beta}{\alpha}$ and the arrival time of the diffracted SP-waves when $\sin(\theta) > \frac{\beta}{\alpha}$.

Because each force has three components and each force component causes three displacement components in the Green's function, the explicit expression of the Green's function $\mathbf{G}$ consists of nine such displacements. These nine displacements have a one-to-one correspondence with the elements of the matrices $\mathbf{M}$ and $\mathbf{N}$. By convention, $g_{ij}(x_1, x_2, L_3, t; 0, 0, x_3', 0)$ represents the displacement in the

$i^{th}-$direction at receiver (x_1, x_2, L_3, t) caused by a unit force in the $j^{th}-$direction at the source $(0, 0, x_3', 0)$. In this situation, g_{ij} is the result of Eq.(4.18) when only M_{ij} and N_{ij} are included in the integrals. This is a more convenient way of expressing the Green's function.

4.3.6.2 Generalization of the Green's Function

Case 1: Source not along x_3- axis

Although the above results are derived for $x_1 = x_2 = t = 0$, there is no restriction upon the generality of the results. The problem is invariant with respect to a translation in either the x_1- or x_2-directions or the $t-$axis. This leads to:

$$g_{ij}(x_1, x_2, L_3, t; x_1', x_2', x_3', t') = g_{ij}(x_1 - x_1', x_2 - x_2', L_3, t - t'; 0, 0, x_3', 0) \quad (4.23)$$

Physically this means that the observed waveforms would be the same when both the source and the observer move the same distance in the same direction. The change in time only shifts the waveforms to occur in another occasion.

Case 2: Source on the free surface and receiver at depth

Green's function can also be generalized to represent the result of the source at the free surface and the receiver at depth. Starting with the general reciprocal relation for Green's functions (Burridge and Knopoff, 1964):

$$g_{ij}(\mathbf{x}, t; \mathbf{x}', t') = g_{ji}(\mathbf{x}', -t'; \mathbf{x}, -t) \quad (4.24)$$

it can be proved that:

$$g_{ij}(x_1, x_2, x_3, t; 0, 0, L_3, 0) = g_{ji}(-x_1, -x_2, L_3, t; 0, 0, x_3, 0) \quad (4.25)$$

Derivation of Eq. (4.25) is shown in Appendix A.

Case 3: Step source function

If the source function is a step function instead of a delta function, then the result is identical to Eq.(4.18) except that the differentiation with respect to time

is no longer included, that is,

$$
\begin{aligned}
G &= \frac{1}{\pi^2 \mu r} \int_0^{\sqrt{((t/r)^2-\alpha^{-2})}} H(t - r/\alpha) \\
&\quad \times \Re e \left\{ \eta_\alpha \sigma^{-1} \left[(t/r)^2 - \alpha^{-2} - p^2 \right]^{-\frac{1}{2}} \mathbf{M}(q, p, L_3, t, x_3') \right\} \mathbf{f} dp \\
&\quad + \frac{1}{\pi^2 \mu r} \int_0^{p_2} H(t - t_2) \\
&\quad \times \Re e \left\{ \eta_\beta \sigma^{-1} \left[(t/r)^2 - \beta^{-2} - p^2 \right]^{-\frac{1}{2}} \mathbf{N}(q, p, L_3, t, x_3') \right\} \mathbf{f} dp
\end{aligned} \tag{4.26}
$$

4.3.6.3 Spatial Derivatives of Green's Function

From Eq. (4.6), it can be seen that in order to calculate the microseismic induced displacements, the spatial derivatives of Green's function with respect to the source coordinate, $\frac{\partial}{\partial \xi_q} G_{np,q}(\mathbf{x}, t - \tau; \xi, 0)$, are needed. From the Green's function shown in Eq. (4.18), the spatial derivatives with respect to source can be calculated directly as follows (Johnson, 1974):

$$
\begin{aligned}
G_{,k'} &= \frac{1}{\pi^2 \mu r} \frac{\partial^2}{\partial t^2} \int_0^{\sqrt{((t/r)^2-\alpha^{-2})}} H(t - r/\alpha) \\
&\quad \times \Re e \left\{ \eta_\alpha \sigma^{-1} \left[(t/r)^2 - \alpha^{-2} - p^2 \right]^{-\frac{1}{2}} \mathbf{M}_{,\mathbf{k}'}(q, p, L_3, t, x_3') \right\} \mathbf{f} dp \\
&\quad + \frac{1}{\pi^2 \mu r} \frac{\partial}{\partial t} \int_0^{p_2} H(t - t_2) \\
&\quad \times \Re e \left\{ \eta_\beta \sigma^{-1} \left[(t/r)^2 - \beta^{-2} - p^2 \right]^{-\frac{1}{2}} \mathbf{N}_{,\mathbf{k}'}(q, p, L_3, t, x_3') \right\} \mathbf{f} dp
\end{aligned} \tag{4.27}
$$

where η_α, η_β, p_2, t_2, γ, σ and q are the same as defined in Eq.(4.18). The individual terms of $\mathbf{M}_{,k'}$ and $\mathbf{N}_{,k'}$ are as follows:

$$
\left.
\begin{aligned}
M_{11,1'} &= -2q\eta_\beta \left[(q^2+3p^2)\cos^2\phi - 3p^2\right]\cos\phi \\
M_{12,1'} &= -2q\eta_\beta \left[(q^2+3p^2)\cos^2\phi - p^2\right]\sin\phi \\
M_{13,1'} &= -2\eta_\alpha\eta_\beta \left[(q^2+p^2)\cos^2\phi - p^2\right] \\
M_{21,1'} &= M_{12,1'} \\
M_{22,1'} &= -2q\eta_\beta \left[(q^2+3p^2)\sin^2\phi - p^2\right]\cos\phi \\
M_{23,1'} &= -2\eta_\alpha\eta_\beta (q^2+p^2)\sin\phi\cos\phi \\
M_{31,1'} &= -\gamma \left[(q^2+p^2)\cos^2\phi - p^2\right] \\
M_{32,1'} &= -\gamma (q^2+p^2)\sin\phi\cos\phi \\
M_{33,1'} &= -q\eta_\alpha\gamma\cos\phi
\end{aligned}
\right\} \tag{4.28}
$$

$$
\left.
\begin{aligned}
N_{11,1'} &= -q\eta_\beta^{-1}\left\{\eta_\beta^2\gamma - (\gamma - 4\eta_\alpha\eta_\beta)\left[(q^2+3p^2)\sin^2\phi - p^2\right]\right\}\cos\phi \\
N_{12,1'} &= -q\eta_\beta^{-1}(\gamma - 4\eta_\alpha\eta_\beta)\left[(q^2+3p^2)\cos^2\phi - p^2\right]\sin\phi \\
N_{13,1'} &= \gamma\left[(q^2+p^2)\cos^2\phi - p^2\right] \\
N_{21,1'} &= N_{12,1'} \\
N_{22,1'} &= -q\eta_\beta^{-1}\left\{\eta_\beta^2\gamma - (\gamma - 4\eta_\alpha\eta_\beta)\left[(q^2+3p^2)\cos^2\phi - 3p^2\right]\right\}\cos\phi \\
N_{23,1'} &= \gamma(q^2+p^2)\sin\phi\cos\phi \\
N_{31,1'} &= 2\eta_\alpha\eta_\beta\left[(q^2+p^2)\cos^2\phi - p^2\right] \\
N_{32,1'} &= 2\eta_\alpha\eta_\beta(q^2+p^2)\sin\phi\cos\phi \\
N_{33,1'} &= -2q\eta_\alpha(q^2-p^2)\cos\phi
\end{aligned}
\right\} \tag{4.29}
$$

$$
\left.
\begin{aligned}
M_{11,2'} &= M_{12,1'} \\
M_{12,2'} &= M_{22,1'} \\
M_{13,2'} &= M_{23,1'} \\
M_{21,2'} &= M_{12,2'} \\
M_{22,2'} &= -2q\eta_\beta\left[(q^2+3p^2)\sin^2\phi - 3p^2\right]\sin\phi \\
M_{23,2'} &= -2\eta_\alpha\eta_\beta\left[(q^2+p^2)\sin^2\phi - p^2\right] \\
M_{31,2'} &= M_{32,1'} \\
M_{32,2'} &= -\gamma\left[(q^2+p^2)\sin^2(\phi) - p^2\right] \\
M_{33,2'} &= -q\eta_\alpha\gamma\sin\phi
\end{aligned}
\right\} \tag{4.30}
$$

$$
\left.
\begin{aligned}
N_{11,2'} &= -q\eta_\beta^{-1}\left\{\eta_\beta^2\gamma - (\gamma - 4\eta_\alpha\eta_\beta)\left[(q^2+3p^2)\sin^2\phi - 3p^2\right]\right\}\sin\phi \\
N_{12,2'} &= -q\eta_\beta^{-1}(\gamma - 4\eta_\alpha\eta_\beta)\left[(q^2+3p^2)\sin^2(\phi) - p^2\right]\cos\phi \\
N_{13,2'} &= N_{23,1'} \\
N_{21,2'} &= N_{12,2'} \\
N_{22,2'} &= -q\eta_\beta^{-1}\left\{\eta_\beta^2\gamma - (\gamma - 4\eta_\alpha\eta_\beta)\left[(q^2+3p^2)\cos^2\phi - p^2\right]\right\}\sin\phi \\
N_{23,2'} &= \gamma\left[(q^2+p^2)\sin^2\phi - p^2\right] \\
N_{31,2'} &= N_{32,1'} \\
N_{32,2'} &= 2\eta_\alpha\eta_\beta\left[(q^2+p^2)\sin^2\phi - p^2\right] \\
N_{33,2'} &= -2q\eta_\alpha(q^2-p^2)\sin\phi
\end{aligned}
\right\} \tag{4.31}
$$

$$
M_{ij,3'} = -\eta_\alpha M_{ij} \tag{4.32}
$$

$$
N_{ij,3'} = -\eta_\beta N_{ij} \tag{4.33}
$$

Physically, the spatial derivatives can be considered as the solution to the problem where the source is a couple with unit moment rather than a simple force.

4.3.7 General Solution in Terms of Moment Tensor

In Eq.(4.15), $[u_i(\xi,\tau)]c_{ijpq}n_j$ has the dimension of MT^2, which corresponds to the moment per unit area. Denoting this quantity as m_{pq}, so:

$$
m_{pq} = [u_i(\xi,\tau)]c_{ijpq}n_j \tag{4.34}
$$

m_{pq} is called the moment density (Jost and Herrmann, 1989).

In isotropic linear elastic material,

$$
c_{ijpq} = \lambda\delta_{ij}\delta_{pq} + \mu(\delta_{ip}\delta_{jq} + \delta_{iq}\delta_{jp}) \tag{4.35}
$$

Assuming that the dislocation distribution along the microfracture is $[u_c(\xi)s(\tau)]$, denoting the dislocation direction as $[v_j] = [v_1, v_2, v_3]$ and the normal to the microfracture as $[n_j] = [n_1, n_2, n_3]$, then the dislocation vector can be expressed as:

$$
\begin{aligned}
[u_i(\xi,\tau)] &= [u_1, u_2, u_3] \\
&= [v_1, v_2, v_3]u_c(\xi)s(\tau)
\end{aligned} \tag{4.36}
$$

Now the moment density can be expressed as:

$$
\begin{aligned}
m_{pq} &= [u_i(\xi,\tau)]c_{ijpq}n_j \\
&= [v_1, v_2, v_3]u_c(\xi)s(\tau)\begin{bmatrix} c_{11pq} & c_{12pq} & c_{13pq} \\ c_{21pq} & c_{22pq} & c_{23pq} \\ c_{31pq} & c_{32pq} & c_{33pq} \end{bmatrix}\begin{bmatrix} n_1 \\ n_2 \\ n_3 \end{bmatrix}
\end{aligned} \tag{4.37}
$$

But,

$$
\left.
\begin{aligned}
c_{11pq} &= \lambda\delta_{pq} + \mu(\delta_{1p}\delta_{1q} + \delta_{1q}\delta_{1p}) \\
c_{22pq} &= \lambda\delta_{pq} + \mu(\delta_{2p}\delta_{2q} + \delta_{2q}\delta_{2p}) \\
c_{33pq} &= \lambda\delta_{pq} + \mu(\delta_{3p}\delta_{3q} + \delta_{3q}\delta_{3p}) \\
c_{12pq} &= c_{21pq} = \mu(\delta_{1p}\delta_{2q} + \delta_{1q}\delta_{2p}) \\
c_{13pq} &= c_{31pq} = \mu(\delta_{1p}\delta_{3q} + \delta_{1q}\delta_{3p}) \\
c_{23pq} &= c_{32pq} = \mu(\delta_{2p}\delta_{3q} + \delta_{2q}\delta_{3p})
\end{aligned}
\right\} \tag{4.38}
$$

so,

$$
\begin{aligned}
m_{pq} = {} & u_c(\xi)s(\tau)[\lambda v_k n_k\delta_{pq} + 2\mu(v_1n_1\delta_{1p}\delta_{1q} + v_2n_2\delta_{2p}\delta_{2q} + v_3n_3\delta_{3p}\delta_{3q}) + \\
& \mu(v_1n_2 + v_2n_1)(\delta_{1p}\delta_{2q} + \delta_{1q}\delta_{2p}) + \mu(v_1n_3 + v_3n_1)(\delta_{1p}\delta_{3q} + \delta_{1q}\delta_{3p}) + \\
& \mu(v_2n_3 + v_3n_2)(\delta_{2p}\delta_{3q} + \delta_{2q}\delta_{3p})]
\end{aligned} \tag{4.39}
$$

where $v_k n_k = v_1n_1 + v_2n_2 + v_3n_3$.

From this,

$$\left.\begin{aligned} m_{11} &= u_c(\xi)s(\tau)(\lambda v_k n_k + 2\mu v_1 n_1) \\ m_{22} &= u_c(\xi)s(\tau)(\lambda v_k n_k + 2\mu v_2 n_2) \\ m_{33} &= u_c(\xi)s(\tau)(\lambda v_k n_k + 2\mu v_3 n_3) \\ m_{12} &= m_{21} = \mu u_c(\xi)s(\tau)(v_1 n_2 + v_2 n_1) \\ m_{13} &= m_{31} = \mu u_c(\xi)s(\tau)(v_1 n_3 + v_3 n_1) \\ m_{23} &= m_{32} = \mu u_c(\xi)s(\tau)(v_2 n_3 + v_3 n_2) \end{aligned}\right\} \tag{4.40}$$

so,

$$\begin{aligned} [m_{pq}] &= \begin{bmatrix} m_{11} & m_{12} & m_{13} \\ m_{21} & m_{22} & m_{23} \\ m_{31} & m_{32} & m_{33} \end{bmatrix} \\ &= \begin{bmatrix} \lambda v_k n_k \delta_{pq} + 2\mu v_1 n_1 & \mu(v_1 n_2 + u_2 n_1) & \mu(v_1 n_3 + v_3 n_1) \\ \mu(v_1 n_2 + v_2 n_1) & \lambda v_k n_k + 2\mu v_2 n_2 & \mu(v_2 n_3 + v_3 n_2) \\ \mu(v_1 n_3 + v_3 n_1) & \mu(v_2 n_3 + v_3 n_2) & \lambda v_k n_k + 2\mu v_3 n_3 \end{bmatrix} u_c(\xi)s(\tau) \end{aligned} \tag{4.41}$$

Denote the spatial derivative of the Green's function with respect to the source as $G_{x_i p,q}$, so:

$$G_{x_i p,q} = \frac{\partial}{\partial \xi_q} G_{x_i p}(\mathbf{x}, t-\tau; \xi, 0) \tag{4.42}$$

Using the sign of convolution, * , the displacement field can be written as:

$$u_{x_i}(\mathbf{x}, t) = \iint_F G_{x_i p,q} * m_{pq} dF \tag{4.43}$$

But,

$$[G_{x_i p,q}] = \begin{bmatrix} G_{x_i 1,1} & G_{x_i 1,2} & G_{x_i 1,3} \\ G_{x_i 2,1} & G_{x_i 2,2} & G_{x_i 2,3} \\ G_{x_i 3,1} & G_{x_i 3,2} & G_{x_i 3,3} \end{bmatrix} \tag{4.44}$$

As $G_{x_i,p,q}$ can be calculated separately and m_{pq} can be determined once the dislocation at the source is defined: the displacement field of any point in any direction can be calculated as following:

$$\begin{aligned} u_{x_i}(\mathbf{x},t) &= \iint_F G_{x_i,p,q} * m_{pq} dF \\ &= [(\lambda v_k n_k + 2\mu v_1 n_1) G_{x_{i1},1} + (\lambda v_k n_k + 2\mu v_2 n_2) G_{x_{i2},2} \\ &\quad + (\lambda v_k n_k + 2\mu v_3 n_3) G_{x_{i3},3} + \mu(v_1 n_2 + v_2 n_1)(G_{x_{i1},2} + G_{x_{i2},1}) \\ &\quad + \mu(v_1 n_3 + v_3 n_1)(G_{x_{i1},3} + G_{x_{i3},1}) \\ &\quad + \mu(v_2 n_3 + v_3 n_2)(G_{x_{i2},3} + G_{x_{i3},2})] * s(\tau) \left[\iint_F u_c(\xi) dF \right] \end{aligned} \tag{4.45}$$

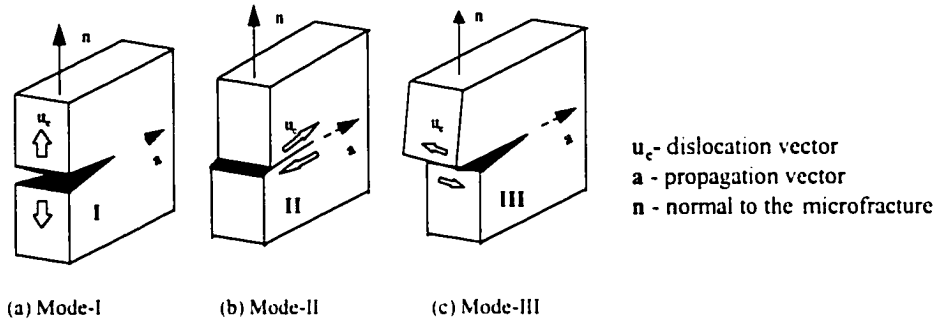
Once the source function is given in terms of the source dislocation function, $u_c(\xi)$, the rise time function, $s(\tau)$, the normal to fracture, $\mathbf{n}(n_1, n_2, n_3)$, and the dislocation vector, $\mathbf{v}(v_1, v_2, v_3)$, the displacement field in the specimen can thus be calculated.

Eq. (4.45) is the general displacement solution on the free surface induced by a microseismic event due to a general microfracture inside the specimen. The specific solutions for some typical microfractures can be easily obtained from this general solutions as demonstrated by the following examples.

4.3.8 Specific Solutions for Some Typical Microfractures

In fracture mechanics, fractures are classified into three modes: tensile (Mode-I), in-plane shear (Mode-II) and anti-plane shear (Mode-III)[2]. Similar classification can be applied to microfractures, as shown in Figure 4.6. It is clear that the dislocation source functions are different in these modes. So different displacement fields should be expected.

[2]In geology, Mode-II and Mode-III microfracturing are both called shearing. Mode-II and Mode-III were considered separately in this dissertation to make the theoretical research complete.



(a) Mode-I (b) Mode-II (c) Mode-III

Figure 4.6: Kinematic parameters of the three typical microfracture modes.

4.3.8.1 Mode-I Microfractures

General Formulae

In Mode-I, the dislocation vector is normal to the microfracture plane. So,

$$v_j = n_j \tag{4.46}$$

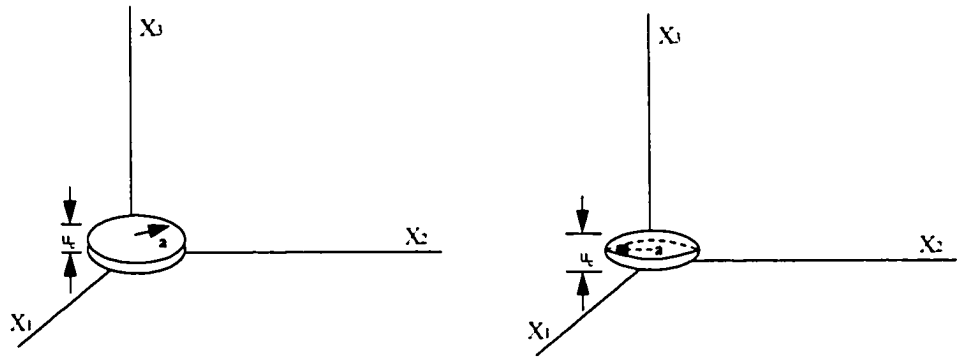
Applying this relation to Eq.(4.45), the general formulae for the displacement field become:

$$\begin{aligned} u_{x_i}(\mathbf{x},t) = & [(\lambda n_k n_k + 2\mu n_1^2)G_{x_i1,1} + (\lambda n_k n_k + 2\mu n_2^2)G_{x_i2,2} + (\lambda n_k n_k + 2\mu n_3^2)G_{x_i3,3} \\ & +2\mu n_1 n_2(G_{x_i1,2} + G_{x_i2,1}) + 2\mu n_1 n_3(G_{x_i1,3} + G_{x_i3,1}) \\ & +2\mu n_2 n_3(G_{x_i2,3} + G_{x_i3,2})] * s(\tau)\left[\iint_F u_c(\xi)dF\right] \end{aligned} \tag{4.47}$$

Usually two models, disk-shaped and penny-shaped microfractures, are widely used (refer to Figure 4.7).

Disk-shaped Mode-I Microfracture

Assuming a disk-shaped Mode-I microfracture F with a radius, a, located in the $\xi_3 = 0$ plane so that $[\mathbf{u}]$ has non-zero components, $u_c(\xi)s(\tau)$, only in the ξ_3-direction. That is:



(a) Disk-shaped Mode-I microfracture (b) Penny-shaped Mode-I microfracture

Figure 4.7: Disk- and penny-shaped Mode-I micro-fractures.

$$[u] = \begin{bmatrix} u_1 \\ u_2 \\ u_3 \end{bmatrix} = \begin{bmatrix} 0 \\ 0 \\ u_c(\xi)s(\tau) \end{bmatrix} \tag{4.48}$$

and,

$$[n] = \begin{bmatrix} n_1 \\ n_2 \\ n_3 \end{bmatrix} = \begin{bmatrix} 0 \\ 0 \\ 1 \end{bmatrix} \tag{4.49}$$

then the induced displacement fields detected on the free surfaces are as follows:

$$\left.\begin{aligned} u_{x_1}(\mathbf{x},t) &= \pi a^2 u_c[\lambda G_{11,1} + \lambda G_{12,2} + (\lambda+2\mu)G_{13,3})] * s(\tau) \\ u_{x_2}(\mathbf{x},t) &= \pi a^2 u_c[\lambda G_{21,1} + \lambda G_{22,2} + (\lambda+2\mu)G_{23,3})] * s(\tau) \\ u_{x_3}(\mathbf{x},t) &= \pi a^2 u_c[\lambda G_{31,1} + \lambda G_{32,2} + (\lambda+2\mu)G_{33,3})] * s(\tau) \end{aligned}\right\} \tag{4.50}$$

where,

$\left\{\begin{array}{l} a - \text{the radius of the disk-shaped microfracture;} \\ u_c - \text{the average dislocation on the microfracture; and,} \\ s(\tau) - \text{the source time function of the fracturing.} \end{array}\right.$

Penny-shaped Mode-I Microfracture

The penny-shaped microfracture is similar to the disk-shaped one; the major difference is that the dislocation attenuates from $u_c s(t)$ at the center to 0 at the boundary. Assuming a similar geometry, the dislocation at an arbitrary point with a distance, r, away from the center of the microfracture is given by:

$$u(r) = \left[1 - \left(\frac{r}{a}\right)^2\right]^{\frac{1}{2}} u_c \tag{4.51}$$

where $r \leq a$.

In comparing to the terms for the disk-shaped microfracture, all of them are kept unchanged except the fracture dislocation, and

$$\begin{aligned} \iint_F u(r)dF &= \int_0^{2\pi} \left\{ \int_0^a \left[1 - \left(\frac{r}{a}\right)^2\right]^{\frac{1}{2}} u_c r dr \right\} d\theta \\ &= \frac{2}{3}\pi a^2 u_c \end{aligned} \tag{4.52}$$

so the induced displacement fields for the penny-shaped microfracture detected on the free surfaces are given by:

$$\left.\begin{aligned} u_{x_1}(\mathbf{x},t) &= \tfrac{2}{3}\pi a^2 u_c[\lambda G_{11,1} + \lambda G_{12,2} + (\lambda+2\mu)G_{13,3})] * s(\tau) \\ u_{x_2}(\mathbf{x},t) &= \tfrac{2}{3}\pi a^2 u_c[\lambda G_{21,1} + \lambda G_{22,2} + (\lambda+2\mu)G_{23,3})] * s(\tau) \\ u_{x_3}(\mathbf{x},t) &= \tfrac{2}{3}\pi a^2 u_c[\lambda G_{31,1} + \lambda G_{32,2} + (\lambda+2\mu)G_{33,3})] * s(\tau) \end{aligned}\right\} \tag{4.53}$$

Comparing Eqs.(4.50) and (4.53), it is found that the induced displacement fields are essentially the same. So it can be inferred that these two models can not be distinguished from the detected waveforms.

4.3.8.2 Mode-II and Mode-III Microfractures

General Formula

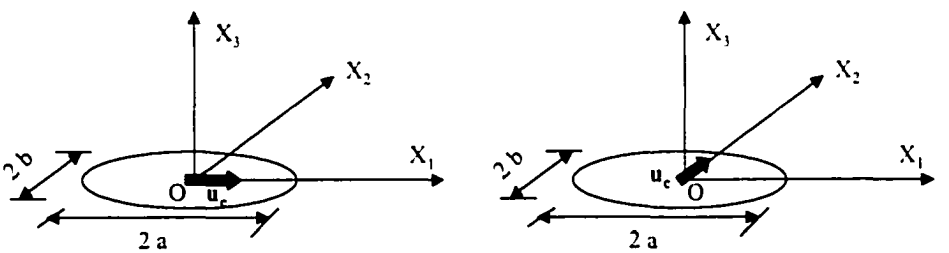
In pure shear, the normal to the microfracture, $\mathbf{n}[n_j]$, is perpendicular to the dislocation vector, $\mathbf{v}[v_j]$. In order to describe the situation precisely, one will assume an elliptical microfracture in the $x_3 = 0$ plane with its long axis a parallel to x_1

and its short axis b parallel to x_2. The microfracture is assumed to propagate along its long axis. Under these assumptions, Mode-II and Mode-III can be defined as shown in Figure 4.8.

The $\mathbf{n}[n_j]$ and $\mathbf{v}[v_j]$ for Mode-II microfractures are given by:

$$[n] = \begin{bmatrix} n_1 \\ n_2 \\ n_3 \end{bmatrix} = \begin{bmatrix} 0 \\ 0 \\ 1 \end{bmatrix} \tag{4.54}$$

$$[v] = \begin{bmatrix} v_1 \\ v_2 \\ v_3 \end{bmatrix} = \begin{bmatrix} 1 \\ 0 \\ 0 \end{bmatrix} \tag{4.55}$$



(a) Mode-II microfracture (b<a) (b) Mode-III microfracture (b<a)

Figure 4.8: Mode-II and Mode-III microfractures.

Similarly, the $\mathbf{n}[n_j]$ and $\mathbf{v}[v_j]$ for Mode-III microfractures are:

$$[n] = \begin{bmatrix} n_1 \\ n_2 \\ n_3 \end{bmatrix} = \begin{bmatrix} 0 \\ 0 \\ 1 \end{bmatrix} \tag{4.56}$$

$$[v] = \begin{bmatrix} v_1 \\ v_2 \\ v_3 \end{bmatrix} = \begin{bmatrix} 0 \\ 1 \\ 0 \end{bmatrix} \tag{4.57}$$

With these directions, the displacement fields induced by microseismic events associated with Mode-II and Mode-III microfractures can easily be calculated.

Mode-II Microfractures

Assume a dislocation along the long axis direction of the fracture of $u_c s(\tau)$ everywhere. The microseismic induced displacement field from this microfracture is given by:

$$\begin{aligned} u_{x_i}(\mathbf{x},t) &= \iint_F G_{x_i p,q} * m_{pq} dF \\ &= \pi ab\mu u_c (G_{x_i 1,3} + G_{x_i 3,1}) * s(\tau) \end{aligned} \tag{4.58}$$

so,

$$\left.\begin{aligned} u_{x_1}(\mathbf{x},t) &= \pi ab u_c \mu [G_{11,3} + G_{13,1})] * s(\tau) \\ u_{x_2}(\mathbf{x},t) &= \pi ab u_c \mu [G_{21,3} + G_{23,1})] * s(\tau) \\ u_{x_3}(\mathbf{x},t) &= \pi ab u_c \mu [G_{31,3} + G_{33,1})] * s(\tau) \end{aligned}\right\} \tag{4.59}$$

Mode-III Microfractures

Similar to the situation in Mode-II, assume the dislocation in the short axis direction along the fracture to be $u_c s(\tau)$ everywhere. The displacement field from this fracture is given by:

$$\begin{aligned} u_{x_i}(\mathbf{x},t) &= \iint_F G_{x_i p,q} * m_{pq} dF \\ &= \pi ab\mu u_c (G_{x_i 2,3} + G_{x_i 3,2}) * s(\tau) \end{aligned} \tag{4.60}$$

that is:

$$\left.\begin{aligned} u_{x_1}(\mathbf{x},t) &= \pi ab u_c \mu [G_{12,3} + G_{13,2})] * s(\tau) \\ u_{x_2}(\mathbf{x},t) &= \pi ab u_c \mu [G_{22,3} + G_{23,2})] * s(\tau) \\ u_{x_3}(\mathbf{x},t) &= \pi ab u_c \mu [G_{32,3} + G_{33,2})] * s(\tau) \end{aligned}\right\} \tag{4.61}$$

Comparing Eqs.(4.58) and (4.60), it is found that the displacement field induced by the microseismic events associated with the Mode-II and the Mode-III microfractures are different.

4.3.9 Discussion

4.3.9.1 Source Functions

The source function, $[u(\xi, \tau)]$, consists of two parts: (i) the distribution of the dislocation discontinuity, $[u(\xi)]$, along the microfracture plane; and (ii) the change of the dislocation geometry over time $s(\tau)$. The size of the dislocation discontinuity, $[u(\xi)]$, can be estimated by microscopic photography. Its space distribution is usually simplified by considering either homogeneous (disk-shaped and shear models) or attenuating (penny-shaped). The microfracture geometry can be considered as circular or elliptical.

For the microseismic sources, there are three typical time functions, $s(\tau)$: the Dirac delta function, the Heaviside step function and the Ramp function. Figure 4.9 shows these functions schematically.

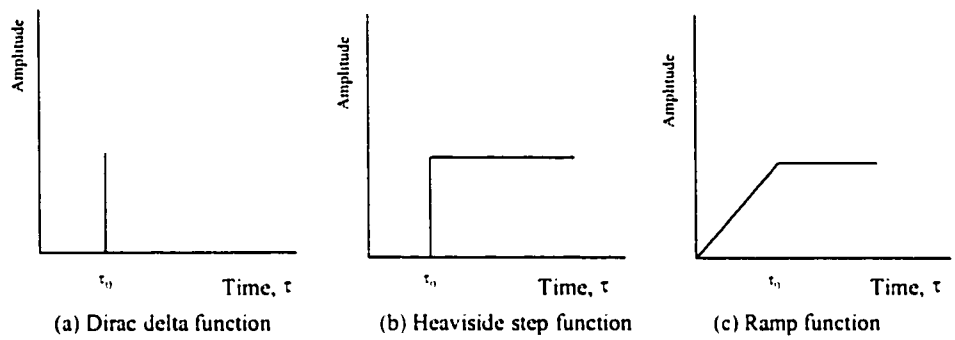


Figure 4.9: The three typical time functions of the microseismic source.

Dirac Delta Function

If the microfracturing is considered to be induced instantaneously and if the dislocation discontinuity returns immediately to the original level, the source can be described by an impulsive function, i.e., the Dirac delta function:

$$s(\tau) = \delta(\tau) \tag{4.62}$$

In this case, the convolution is very simple because the convolution of any signal

with a delta function is itself.

Step Function

If the source process is considered to be finished in ar. instant and then the dislocation discontinuity is kept at that level. the source can be described by a step function represented by the Heaviside function:

$$s(\tau) = H(\tau) \tag{4.63}$$

Ramp Function

If the source is considered to be applied for a limited period of time and then the dislocation discontinuity kept at a constant level, the source can be described by a ramp function:

$$s(\tau) = R(\tau) \tag{4.64}$$

Two Examples of Source Functions

The real microseismic source process might be very complex. Through deconvolution of the detected waveforms. the temporal part of the source function can be obtained. The following are two examples used to describe some microseismic events in steel and in concrete.

Example 1: Steel Disbonding Process (Yuyama et al., 1988):

$$\begin{cases} \text{Disk-shaped fracture, a=0.02 mm:} \\ u_c = 0.002 \text{ mm;} \\ \frac{d^2 s(\tau)}{d\tau^2} = -\cos(\frac{\pi}{\tau_0}\tau - \frac{\pi}{2})\sin(\frac{\pi}{\tau_0}\tau - \frac{\pi}{2}) \qquad 0 < \tau < \tau_0; \text{ and,} \\ \tau_0 = 2\ \mu s. \end{cases}$$

Example 2: Concrete Micro-fracturing Process (Ohtsu, 1988):

$$\begin{cases} \text{Disk-shaped fracture, } a = 0.025 \text{ mm;} \\ u_c = 0.005 \text{ mm;} \\ s(\tau) = \frac{\tau}{\tau_0} - \frac{2}{3\pi}\sin(2\pi\frac{\tau}{\tau_0})\sin(\frac{\tau}{\tau_0}\pi - \frac{\pi}{2}) \qquad 0 < \tau < \tau_0; \text{ and,} \\ \tau_0 = 1\ \mu s. \end{cases}$$

4.3.9.2 Circular Microfractures vs. Elliptical Microfractures

Disk- and penny-shaped geometrical models have been widely used in discussing the fracturing processes. This is convenient when talking about tensile microfractures (Mode-I). But for shear processes, an elliptical geometrical model is preferred for the purpose of distinguishing Mode-II from Mode-III shearing. The real process may be a combination of all three modes (Lockner, 1993).

Due to the change of many different factors, as partly discussed above, the first motion waveforms are different for different combination of these factors. A complete description of these differences need the help of a computer simulator. Development of such a simulator is introduced in the next section.

4.4 Development of the WAVEFORM Simulator

The focus of the waveform study is to identify the arrival time of the first motion and the corresponding waveform. Therefore, only the P-wave part is included in the calculation of the Green's function and its spatial derivatives. But the trailed S-wave part can be easily added following the theoretical formulae developed in the previous section.

4.4.1 Flowchart

Based on the theory introduced in the previous section, the WAVEFORM simulator was developed following the flowchart shown in Figure 4.10 (Zeng, 2002). The functions for each step are explained below.

4.4.2 Data Input

The input data include the geometry of the observed domain, the material properties, the sensor coordinates, the source information and the sampling set-up.

In this study the observed domain is assumed to be a rectangular block. Only

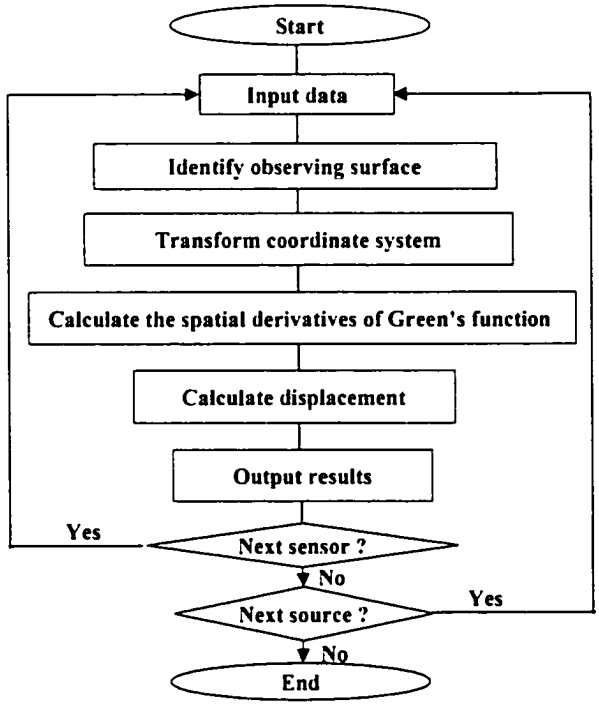


Figure 4.10: WAVEFORM simulator flowchart.

half lengths in each direction are needed to be considered due to inherent symmetry.

The material properties include material density, P- and S-wave velocities. Other properties such as Young's modulus, Poisson's ratio, shear modulus, etc., are derived from existing elastic relationships.

The sensor coordinates refer to the sensor's position in the original coordinate system. They will be transformed to the new coordinate system during subsequential operations.

The source information include the coordinates, the mode (Mode-I or II, or other combined mode), the shape and related geometrical sizes, normal to the microfracture planes, dislocation vector, rise-time function.

The sampling set-up includes the sampling length and sampling interval[3]. The sampling length should be long enough so that the first motion can be sampled.

[3]The sampling length and the sampling rates are used because numerical integrations are involved in the calculation of the spatial derivatives of the Green's function shown in Eq. (4.27).

This is determined by the travel time along the specific ray path from the source to he sensor. The sampling interval should be properly selected so that the change in the source function can be properly represented.

4.4.3 Observing Surface Identification and Coordinate Transformation

The theory derived in the previous section is based on the assumptions that the observed domain is a half space and the sensor is placed on a free surface. In additon, the coordinate system is set up in such a way that the seismic source is on the axis of the vertical axis (Johnson, 1974).

In the hydraulic fracturing tests conducted in this study, the sensors were installed on different surfaces of the tested rectangular block. As mentioned before, the observed block can be simplified as a half space. Because the sensors can be on any surface of the block, identification of the surface is needed. This is conducted by comparing the sensor coordinates to the limits of the block.

Once the observing surface is identified, a new coordinate system is defined following the right hand rule. In addition, the new system obeys the rules below:

1. The origin of the new coordinate system is the epicenter of the microseismic source on the free surface;

2. The third axis is downward toward the inside of the half space on the free surface; and

3. The other axes are set to parallel the original axes.

Shown in Figure 4.11 is such a new coordinate system for a sensor on the $+X_3$ surface.

The conversion from the original coordinate system to the new coordinate system follows the transformation law for Cartesian coordinates (Kreyszig, 1993). Assum-

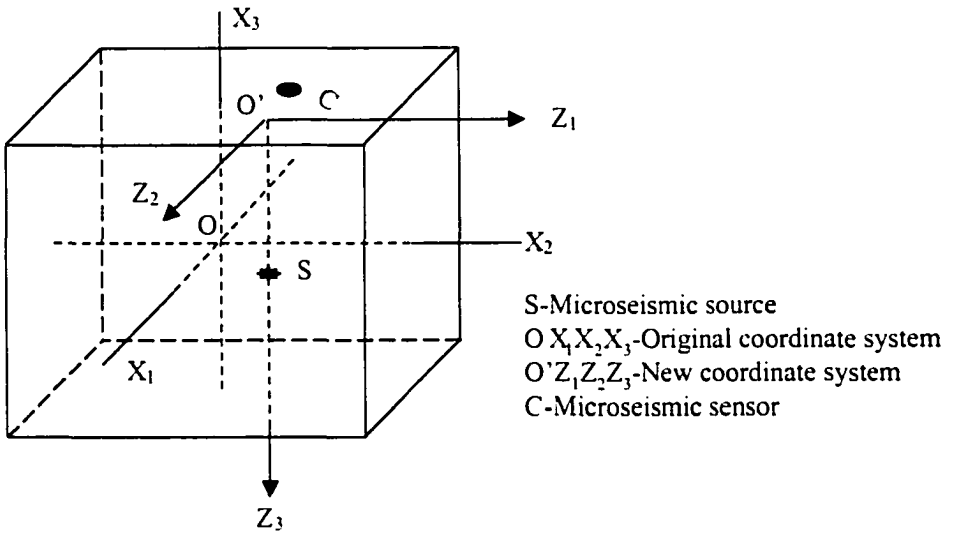


Figure 4.11: The original and the transformed coordinate systems for a sensor on $+X_3$ surface.

ing the coordinates of the source and the sensor in Figure 4.11 to be $S(x_{10}, x_{20}, x_{30})$ and $C(x_1, x_2, L_3)$, the transformation procedures can be demonstrated as below.

(1) Relationships between axes

Axes of the new coordinate system are parallel to the axes of the original system following:

$$\left\{ \begin{array}{c} +Z_1 \\ +Z_2 \\ +Z_3 \end{array} \right\} \Leftrightarrow \left\{ \begin{array}{c} +X_2 \\ +X_1 \\ -X_3 \end{array} \right\} \tag{4.65}$$

(2) Transformation matrix

The Cartesian coordinate transformation is conducted via a transformation matrix whose members are defined by:

$$c_{ij} = \mathbf{z}_i \cdot \mathbf{x}_j \qquad i, j = 1, 2, 3 \tag{4.66}$$

where $\mathbf{z}_i$ and $\mathbf{x}_j$are the unit vectors along $+Z_i$ in the new system and along $+X_j$ in the original system respectively. Based on Eqs. (4.65) and (4.66), the transfor-

mation matrix for the case shown in Figure 4.11 is obtained as:

$$[c] = \begin{bmatrix} 0 & 1 & 0 \\ 1 & 0 & 0 \\ 0 & 0 & -1 \end{bmatrix} \tag{4.67}$$

(3) Transformation formulae

Assuming $X_j(x_1, x_2, x_3)$ are the coordinates of a point in the old system, their coordinates in the new system, $Z_m(z_1, z_2, z_3)$, are given by:

$$z_m = \sum_{j=1}^{3} c_{mj} x_j + b_m \qquad m = 1, 2, 3 \tag{4.68}$$

where c_{mj} are defined by Eq. (4.67) and b_m are constants to be determined.

Applying Eq. (4.67) to Eq. (4.68), it gives:

$$\begin{cases} z_1 = x_2 + b_1 \\ z_2 = x_1 + b_2 \\ z_3 = -x_3 + b_3 \end{cases} \tag{4.69}$$

From the definition of the new coordinate system, it can be seen that the coordinates of the new origin O′ are $O'_x(x_{10}, x_{20}, L_3)$ in the original system and $O'_z(0, 0, 0)$ in the new system. Applying the coordinates of O'_x and O'_z to Eq.(4.69), the constants of b_m $(m = 1, 2, 3)$ are found as:

$$\begin{cases} b_1 = -x_{20} \\ b_2 = -x_{10} \\ b_3 = L_3 \end{cases} \tag{4.70}$$

where L_3 is the half length of the block in the X_3 direction, as shown in Figure 4.3. Thus the final form of the transformation formulae are:

$$\begin{cases} z_1 = x_2 - x_{20} \\ z_2 = x_1 - x_{10} \\ z_3 = -x_3 + L_3 \end{cases} \tag{4.71}$$

Using Eq.(4.71), any point in the original system with known coordinates can be converted to the new system.

When the observer (sensor) is on other surfaces, the same procedures can be followed for the coordinate transformation.

4.4.4 Calculation of Spatial Derivatives of Green's Function

The calculation of the spatial derivatives of the Green's function is straightforward, as shown in Eq. (4.27). For the integration part, the four-point Gauss numerical integration is used (Kreyszig, 1993).

In addition, because the first motions of the $P-$waves are the focus of the WAVEFORM simulator, only the $\mathbf{M}_{.k'}$ in Eqs. (4.28),(4.30) and (4.32) are calculated. If the second term in Eq. (4.27) is included and the $\mathbf{N}_{.k'}$ in Eqs. (4.29),(4.31) and (4.33) are calculated, the $S-$ wave part would be included. Under this situation, the sampling length would have to be extended so that the full waveform can be included.

4.4.5 Calculation of Displacements

Using the spatial derivatives obtained from the above mentioned step and the input data about the microseismic source, the displacement at each sampling time in each direction in the $O'Z_1Z_2Z_3$ coordinate system can be calculated following the general displacement equation defined in Eq. (4.45).

The commonly measured parameters in the laboratory and in the field are velocities and accelerations. These parameters can be readily obtained when the displacements are known. In the WAVEFORM simulator, these parameters are calculated by numerically differentiating the displacements once and twice.

4.4.6 Output Results

The output of the results include the time, the displacements u_1, u_2, and u_3, the velocities V_1, V_2, and V_3, and the accelerations, a_1, a_2, and a_3 on the observed surface in the directions parallel to the Z_1, Z_2, and Z_3 axes.

This program has been developed in FORTRAN.

4.5 Validation of the WAVEFORM Program

Several cases have been designed to validate the WAVEFORM simulator program. The observed domain was a cement block of 420 mm×420 mm×432 mm (16.5 in×16.5 in×17 in) mentioned previously; it was assumed to be homogeneous, isotropic, and linear elastic with the following properties: density $\rho = 1625\ kg/m^3$, $P-$wave velocity $V_p = 4.0\ km/s$, and $S-$wave velocity $V_s = 2.5\ km/s$. Other related properties, such as Young's modulus, Poisson's ration, shear modulus and Lamé's elastic constants, have been calculated based on the theory of elasticity.

The validation was conducted by changing the depth of the sources, the offset distance of the observers, and the microfracturing modes. The simulated first motions include waveforms of displacements, velocities and accelerations. By comparing the results, the simulator was validated.

4.5.1 Case 1. Mode-I Central Source, Epicentral Observer

Case 1 is a Mode-I microfracturing source at the block center parallel to the surface. The sensor was located at the epicenter of the source on the $+X_1$ surface. An impulsive source lasting 1 μs was assumed and the sampling interval was 0.1 μs. The first motion of the waveforms in the $+X_1-$, $+X_2-$ and $+X_3-$directions were simulated. Figure 4.12 shows the displacement, the velocities and the accelerations in these three directions.

Because the waveforms come from a Mode-I source, theoretically there should

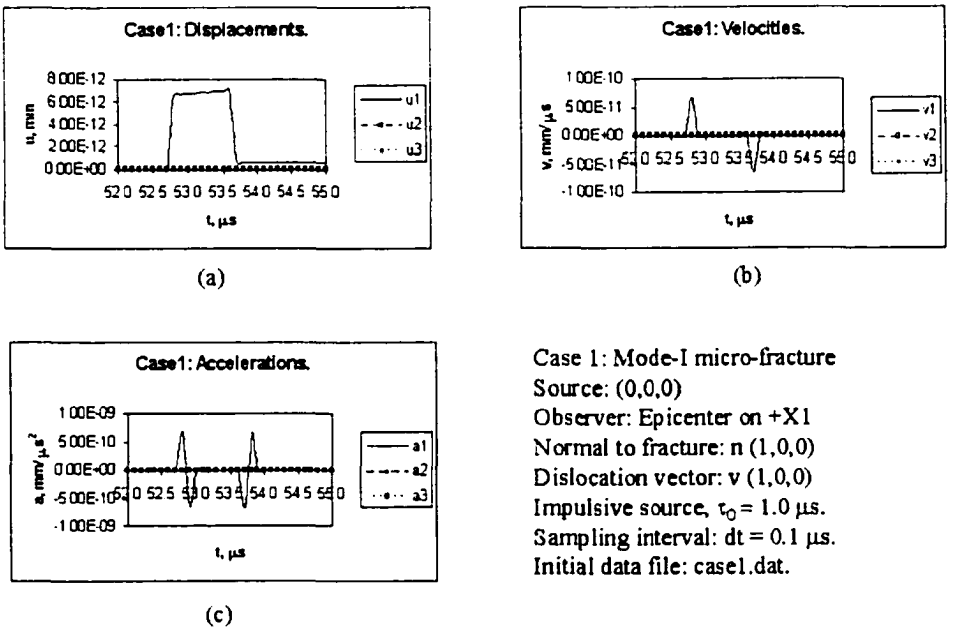


Figure 4.12: Epicentral first motions from Mode-I microfracturing.

be only vibrations in the normal direction (X_1) at the epicenter. In Figure 4.12, it can be seen that only the components along the X_1-direction of the displacements, velocities and accelerations are none-zero. So the above point has been confirmed from the simulated results.

4.5.2 Case 2. Mode-I Central Source, Offset Observers

Case 2 has the same source as Case 1. Three different offset observers, P_1(210, 100, 0), P_2(210, 0, 100), and P_3(210, 100, 50), were used, as shown in Figure 4.13 (a). Theoretically, there should be only vibrations in the X_1- and X_3-directions in P_1, and in X_1- and X_2-directions in P_2. In P_3, there should be vibrations in all three directions, but the component along X_3 should be stronger than that in X_2.

Figure 4.13 (b), (c) and (d) shows the first motion acceleration waveforms in these observation points. It can be seen that the above theoretical predictions have been validated.

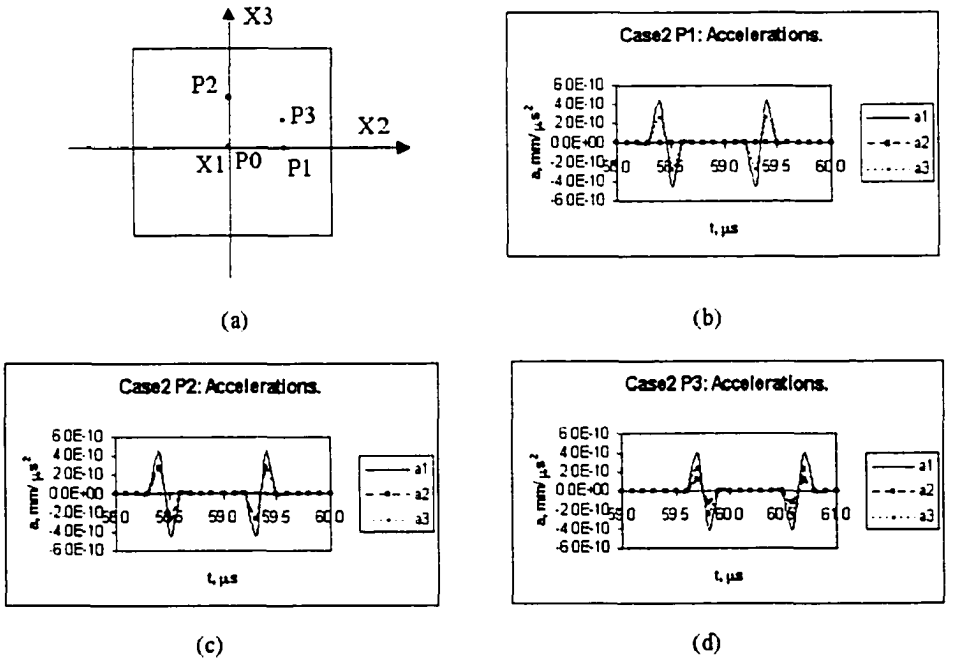


Figure 4.13: First motions at offset observers from Mode-I microfractures.

4.5.3 Case 3 Mode-I Source at Different Depths, Epicentral Observer

Case 3 had the same observer as Case 1. The source is similar to Case 1, but three different depths, 50 mm (referred to as P_1), 100 $mm(P_2)$ and 200 mm (P_3), were used. This case is designed to validate the influence of the depth on the waveform amplitude. Theoretically, the deeper the source is, the weaker the amplitude.

Figure 4.14 shows the first motion waveforms of acceleration for these three sources. The peak amplitudes from sources P_1, P_2 and P_3 are 2.85×10^{-9} $mm/\mu s^2$, 1.40×10^{-9} $mm/\mu s^2$, and 6.94×10^{-10} $mm/\mu s^2$, respectively. It is obvious that the deeper the source, the weaker the waveform; validating the theoretical prediction.

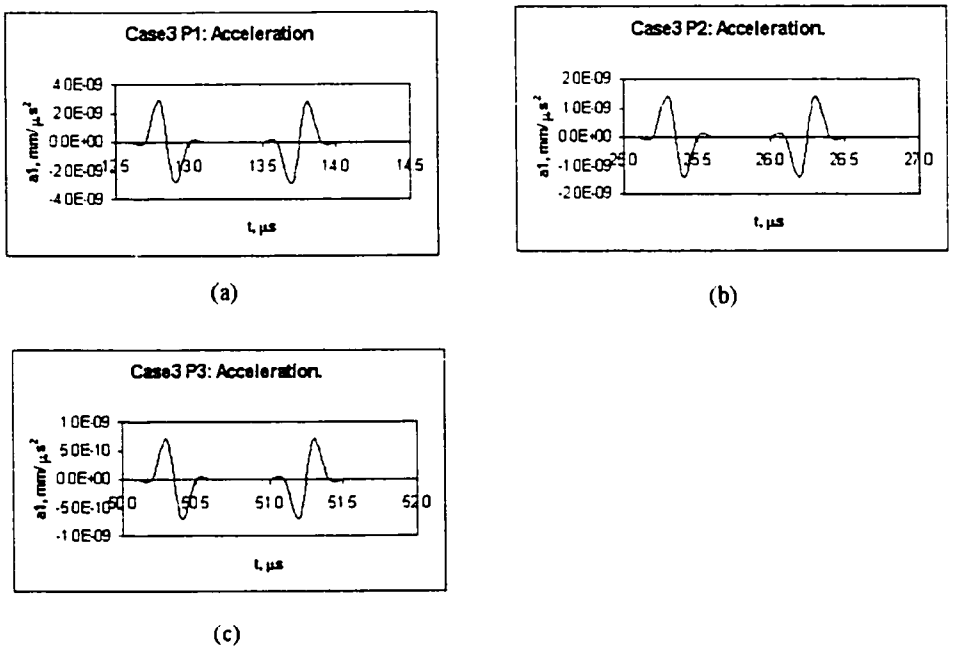


Figure 4.14: Source depth influence on first motion acceleration waveforms.

4.5.4 Case 4. Mode-II Central Source, Offset Observers

Case 4 was designed to validate the simulation of Mode-II microfracturing. The source was assumed to be located at the block center. The fracture was elliptical with the long axis along the X_2-direction and short axis long the X_1-direction. The shear motion is along the $+X_2-$direction. Three sensors were installed in three different locations. $P_1(210,\ 100,\ 100)$, $P_2(210,\ -100,\ 100)$, and $P_3(210,\ -100,\ -100)$, on the $+X_1$ surface, as shown in Figure 4.15 (a). The arrows in that figure represent the moving vector of the microfracturing.

Under this configuration, the well-known seismology theory will predict that the waveforms detected at P_1 and P_3 would be the same while the waveform at P_2 would be opposite in the motion direction, yet the peak amplitude of all these three would be the same.

Figure 4.15 (b), (c) and (d) show the simulated accelerations at P_1, P_2 and P_3. By comparing these waveforms, it is clear that the simulation results agree with

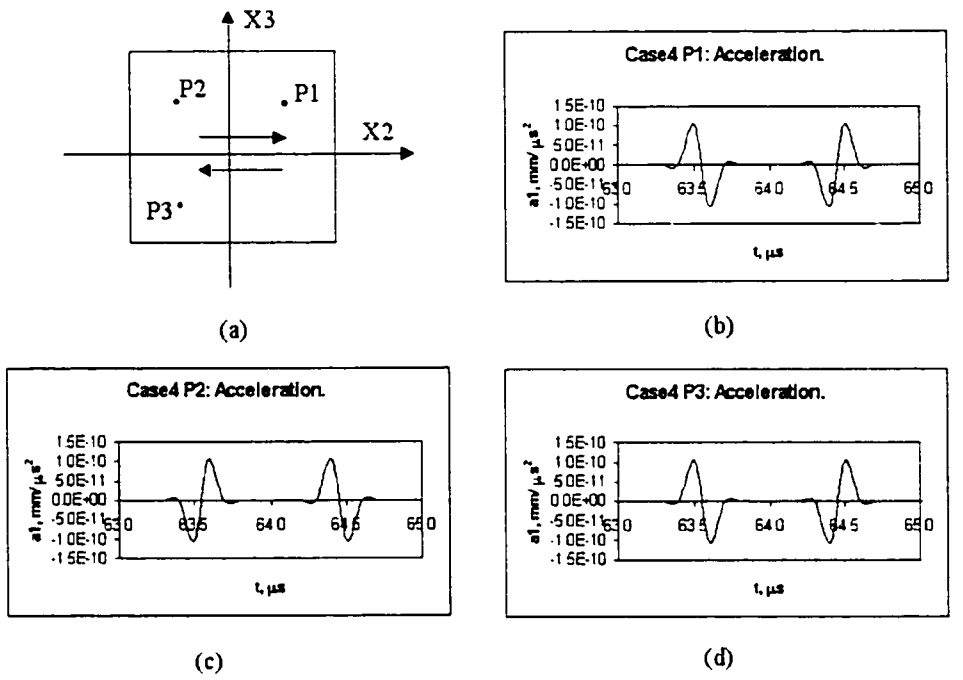


Figure 4.15: Mode-II micro-fracturing induced waveforms at three different points.

the theoretical predictions.

From the above validations, it is proper to say that the WAVEFORM simulator can reasonably calculate the waveforms of the first motion induced by different microfracturing sources.

5 Petrophysical and Geomechanical Characterization of Jackfork Sandstone

5.1 Introduction

The Jackfork sandstone formation has become of interest in recent years because substantial gas reserves have been found in it (Montgomery, 1996). As the formation is very tight, hydraulic fracturing treatments are normally required. Unfortunately, no systematic investigations on the petrophysical and geomechanical properties of the formation have been carried out so far.

5.2 Geology of the Jackfork Formation

The Jackfork sandstone was named for the Jackfork Mountain in the frontal Ouachita Mountains located in Pittsburg and Pushmataha Counties, Oklahoma (Taff, 1902). It is a Pennsylvania formation that extends from southeastern and central southern Oklahoma to southwestern Arkansas in the Ouachita Mountains area (Winter, 1984). Figure 5.1 shows the distribution of Jackfork sandstone in part of the Ouachita Mountain area (Arbenz, 1984).

The thickness of the Jackfork sandstone formation varies between 5,000 and 6,000 ft. Traditionally, the Jackfork formation was considered as a rapid deposit of turbidite currents. However, recent stratigraphic and sedimentological studies indicated that some part of this formation might be of submarine channel origin (Pauli, 1994), shallow marine and deltaic (Tillman, 1994), all of which imply pos-

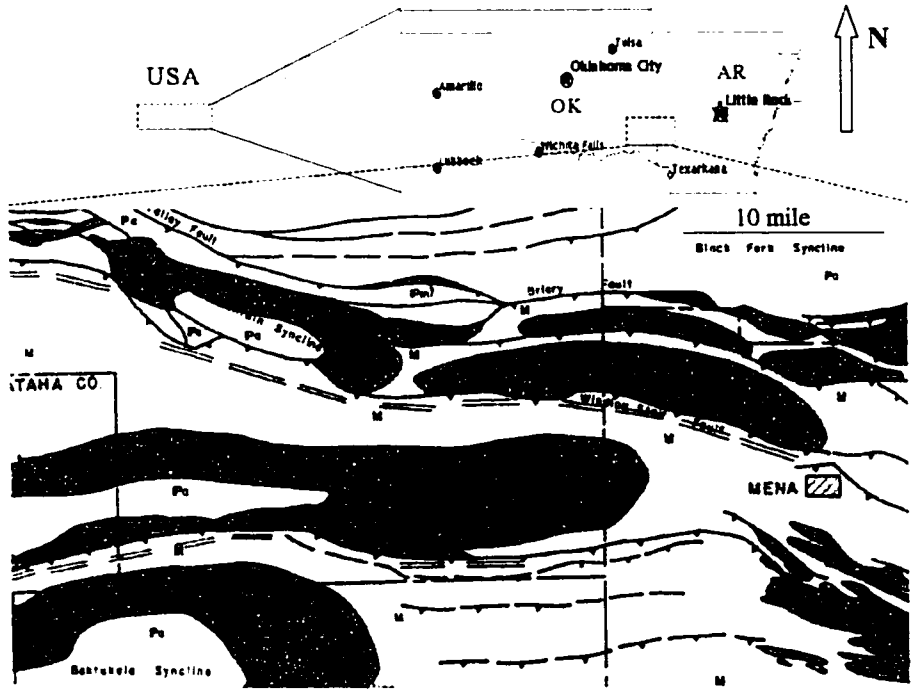


Figure 5.1: Distribution of the Jackfork formation (after Arbenz, 1984)

sible reservoirs on a much larger scale.

The age of the Jackfork sandstone has been determined to be Morrowan (Lower Pennsylvanian) because some fossils of that age have been collected from several localities in the middle and upper Jackfork Group near Little Rock, Arkansas.

Near the Jackfork sandstone formation are Johns Valley shale on the top and Stanley shale at the bottom. The Jackfork formation has been highly stressed due to the development of folds and thrusts during its geological history. The bedding planes have been turned to sub-vertical (Arbenz, 1984).

Mineral composition of the Jackfork sandstone have been determined by Morris et al. (1979). Based on 200 grains per thin section, they showed that 77.3% of all the minerals was quartz while feldspars averaged 2.9%, lithic fragments 3.7%, cement 10%, and 6% fine materials unidentifiable with a microscope.

The above material composition was also reflected on the landscape. The strong Jackfork sandstone form linear ridges while the weak John Valley and Stanley shales

formed the intervening valleys in the Ouachita Mountains areas.

While current gas exploration activities were all inside Oklahoma, the Jackfork sandstone extended along the Ouachita Mountains for more than 150 miles (Montgomery, 1996)[1]. There is no doubt that, in the future, gas reserves will also be discovered on the Arkansas side. For this reason and due to the accessibility to the Jackfork outcrops, Jackfork samples for this experimental investigation were picked from the R.D. Plant Quarry in Kirby, Arkansas, as shown in Figure 5.2.



Figure 5.2: Sampling site of the Jackfork sandstone.

5.3 Petroleum Activities in the Jackfork Formation

The first discovery well in the Jackfork sandstone was drilled in 1992 in southern Latimer County, Oklahoma. Gas was first hit in the lower Jackfork sandstone at the depth of 11,850 ft. Then gas bearing zones occurred twice at the depth of

[1]The major operator of that area indicated that more exploration and development activities would be resumed soon when inquired in a phone call in September 2001.

17,960 ft and 18,750 ft. This well was completed in the lowest productive interval at a rate of 5.7 MMcf per day (Montgomery, 1996).

The second discovery well was drilled 3 miles away from the first well. It encountered several productive sandstones in the upper Jackfork sandstones, between 5,900 and 6,200 ft. The well was completed with a production rate of 1.9 MMcf per day.

A third well was drilled 10 miles away from the first discovery well. This well finally confirmed the discovery of gas reserves in the Jackfork sandstone. It encountered two productive intervals in the Jackfork sandstone between depths of 8,980 ft and 9,450 ft. The production rate was 4.6 MMcf per day.

A total of fifteen wells were drilled in this formation, of which 13 were successfully completed. The range of estimated ultimate recovery of selected wells is 1.9 - 7.6 Bcf/well with calculated drainage areas significantly less than 160 acres at 7,500 - 12,000 ft. Figure 5.3 shows the cross-sectional profile of some of the wells.

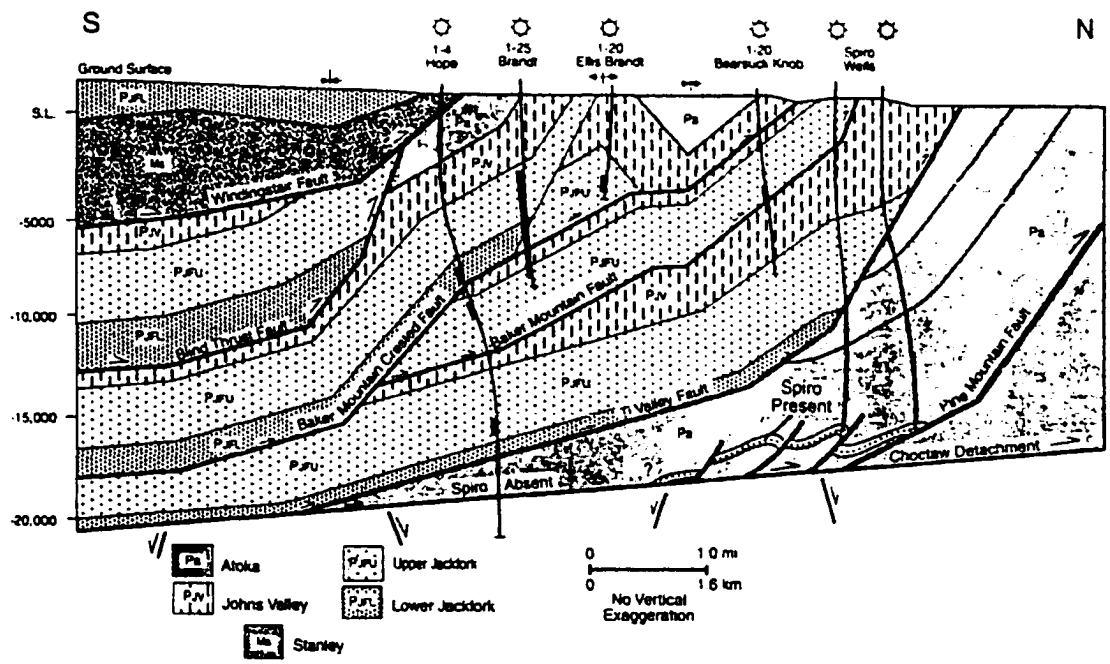


Figure 5.3: Some wells in the Jackfork formation (from Montgomery, 1996).

Sidewall sample analyses showed that porosities might be as high as 11%. But the permeability is extremely low, commonly less than 0.3 mD (Montgomery, 1996). Due to this, hydraulic fracturing stimulation is usually required. The stimulation in Jackfork reservoirs usually results in only a 100-200 ft half fracture length, even though wells were then capable of producing 1-2 Bcf within 2 years. Among all these wells, only one well producing from 18,800 ft, has been completed without successful stimulation. Two frac jobs failed.

From a production point of view, the completed wells in the Jackfork sandstone were not impressive. But the production intervals were scattered within depths ranging from 4,000 to 5,000 ft inside both the upper and the lower part of the Jackfork sandstone; this means that the total volume of the reservoir is huge. The hyperbolically declining production curve lasted for more than two years which means that a significant contribution for the long-term production comes from the matrix. In addition some of the thickest Jackfork sandstone sequences were outside the current explored area. All these indicate that the Jackfork formation has the potential of becoming a major regional gas producer.

5.4 Petrophysical Properties

The petrophysical and geomechanical properties of the sampled Jackfork sandstone were tested in the Petrophysics Laboratory (IC^3) and in the Halliburton Rock Mechanics Laboratory (HRML). The following are the test methods and the results.

5.4.1 Porosity, Bulk Density and Grain Density

The bulk volume, V_b, consists of two parts: the grain volume, V_g, and the pore volume, V_p. Porosity, ϕ, is the percentage of pore volume within the bulk volume. Due to the fact that pores in the reservoir rocks supply both the space for storing the hydrocarbon and the passage for fluids to flow, porosity is one of the most important properties. There are two types of porosities, the absolute porosity

and the effective porosity (Koedertiz et al., 1989). Effective porosity refers to the volumetric percentage of pores that are connected to each other and allow fluid to flow between them. The effective porosity is, therefore, the one that is practically meaningful to reservoir engineering. Hereafter, porosity refers to the effective one, unless specified.

Bulk density, ρ_b, is the weight of the rock within a unit bulk volume. And grain density, ρ_g, is the weight of the solid matrix in unit grain volume.

Obviously, the porosity, the bulk density and the grain density are related to each other. Measurement of these properties could be integrated if proper means, such as the gas compression/expansion method is selected (Tiab and Donaldson, 1996).

In this investigation, six 1-*in* diameter by 1-*in* length cylindrical samples, HKP-1 — HKP-3 and VKP1 — VKP-3, were used to determine the porosity, the bulk density and the grain density. The horizontal samples, HKP-1 — HKP-3, were drilled in the direction parallel to the bedding planes. In contrast, the vertical samples, VKP-1 — VKP-3, were drilled in the direction perpendicular to the bedding planes. All samples were dried in an oven at $150°F$ for 24-hour before testing.

The bulk volume of each sample was calculated using the precisely measured diameter and length.

The grain volume of each sample was measured using an UltraPore^{TM}200A Helium Pycnometer System manufactured by Core Laboratories Instruments. The system was composed of two gas chambers, a high pressure gas source, and a computer-controlled measuring system (Core Lab, 1995). The rock sample was put into one of the gas chambers. The two gas chambers were pressurized to different pressures at the beginning. Then they were connected to each other. Pressures in the two gas chambers were measured before and after they were connected to each other. By assuming that the solid matrix was incompressible under low pressures in the gas chamber, this system automatically calculated the grain volume, according to Boyle's law and the measured pressures. Before measuring the grain volume of

Table 5.1: Bulk density, grain density and porosity

Sample	W, g	V, cm^3	V_g.cm^3	V_p.cm^3	ρ, g/cm^3	ρ_g, g/cm^3	ϕ, %
HKP-1	33.06	13.424	11.343	2.081	2.463	2.915	15.502
HKP-2	33.34	13.334	11.430	1.904	2.500	2.917	14.279
HKP-3	34.08	13.707	11.676	2.031	2.486	2.919	14.817
VKP-1	35.83	14.286	12.239	2.047	2.508	2.927	14.329
VKP-2	33.83	13.540	11.594	1.946	2.499	2.918	14.372
VKP-3	35.87	14.312	12.243	2.069	2.506	2.930	14.456
Average					2.494	2.921	14.626
Std. dev.					0.017	0.006	0.429

the rock samples, the system was calibrated with a steel cylinder of known volume.

The pore volume was then obtained by subtracting the grain volume from the bulk volume.

The sample weight, W, was determined using a scale. Because the samples were dried before being measured, the grain weight was assumed to be the same as the bulk weight of the sample.

Based on the above measured parameters, the porosity, the bulk density and the grain density were obtained for the Jackfork sample, as shown in Table 5.1.

5.4.2 Permeability

Permeability, k, of the reservoir rock characterizes its capability to let the fluid flow inside it. It is one of the most important factors in determining if a reservoir needs stimulation. It also serves as an indicator for potential leak-off of the hydraulic fracturing fluid; hence affects the efficiency of a stimulation treatment.

There are two types of permeability, the absolute permeability and the relative permeability. The absolute permeability refers to the permeability of a single phase fluid. In contrast, the relative permeability refers to the permeability of a specific fluid when two or more phases of fluids flow together through the same media. In this investigation, the absolute permeability was measured using the equipment available at IC^3 in the Tulsa campus. The six samples for density and porosity

Table 5.2: Permeability in different directions

Sample	Direction	Permeability, μD
HKP-1	horizontal	3.70
HKP-2	horizontal	3.72
HKP-3	horizontal	8.89
Average		5.44
Std dev.		2.99
VKP-1	vertical	2.91
VKP-2	vertical	3.63
VKP-3	vertical	3.02
Average		3.19
Std dev.		0.39

measurements were used again in the permeability measurements, shown in Table 5.2.

The measured results indicate that the horizontal permeability along the bedding planes is very anisotropic. More measurements are obviously needed to find out the direction of maximum permeability.

5.4.3 Seismic Velocities

P-wave velocities, V_p, were measured using the experimental setup as shown in Figure 5.4. Two transducers, a pulser and a receiver, were put on each side of the sample. A P-wave was generated using a Panametrics Pulser/Receiver Model 5055PR to control the pulse generation and the waveform acquisition synchronization. The waveforms from the pulser and receiver were sent to a LeCroy9310A Dual 400MHz Oscilloscope. Travel time, t, of the wave in the sample was determined from comparison of the two waveforms recorded on the oscilloscope. The true travel time was obtained after a systematic correction was imposed, which was determined using a standard steel sample of known velocity. The seismic velocity of the rock sample was finally calculated with the sample length divided by the true travelling time.

Using this setup and the method described above, the P-wave velocity of the

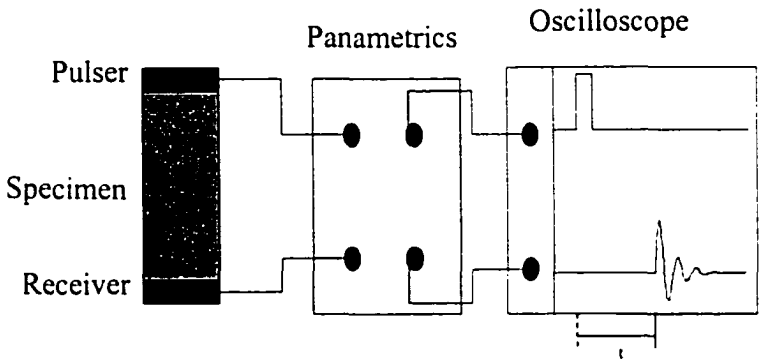


Figure 5.4: Experiemental set-up for seismic velocity measurement.

Table 5.3: Seismic velocity measurement

Sample	**Length, mm**	**True travelling time, μs**	**Velocity, km/s**
HKP-1	26.70	5.57	4.79
HKP-2	26.30	5.55	4.74
HKP-3	27.27	5.75	4.74
Average			4.76
Std dev.			0.03
VKP-1	28.23	6.06	4.66
VKP-2	26.71	5.86	4.56
VKP-3	28.17	6.13	4.60
Average			4.61
Std dev.			0.05

Jackfork sandstone was measured on the samples used in the permeability test. Table 5.3 shows the detailed results.

From these measurements, it is found that the velocity in the horizontal direction is about 3% higher than that in the vertical direction. On the other hand, the three velocities measured in each direction are quite close to each other. This result is consistent with the measurement of the permeability. Strictly speaking, this material should be considered as transversely isotropic. But from a practical point of view, a 3% anisotropy can be neglected. So the Jackfork sandstone can be approximately considered as a isotropic media.

5.5 Geomechanical Properties

5.5.1 Uniaxial Tensile Strength by Point Load Test

5.5.1.1 Point Load Test

Tensile strength describes the capacity of the rock to resist tensile stresses. In the case of hydraulic fracturing, the formation is fractured by increasing the pressure inside a sealed-off section of the borehole.

There are direct and indirect methods for the measurement of tensile strength (ISRM, 1985; Lama and Vutukuri, 1974). The indirect methods have been dominant in determining tensile strength of rocks in the past due to their ease in sample preparation and testing procedure. The point load test is one of these indirect methods; the principle is as follows.

The standardized equipment includes a pair of 60° conical point loading platens installed either on a hydraulic hand-pump, for field use, or on a loading frame for laboratory use, as shown in Figure 5.5 (ISRM, 1985; Farmer, 1983).

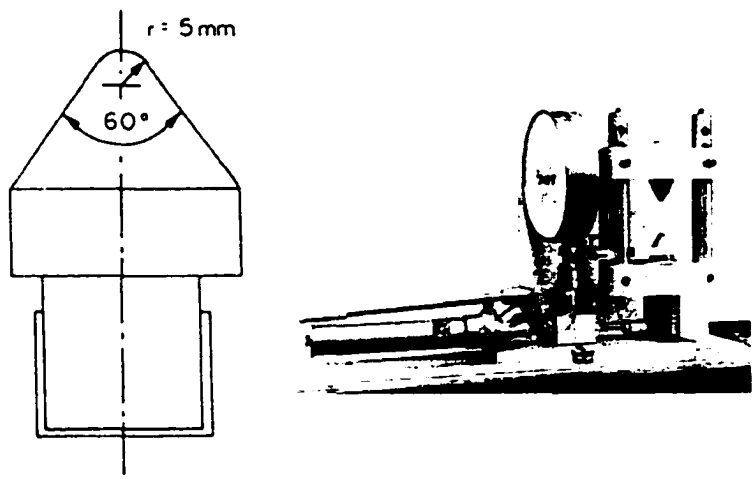
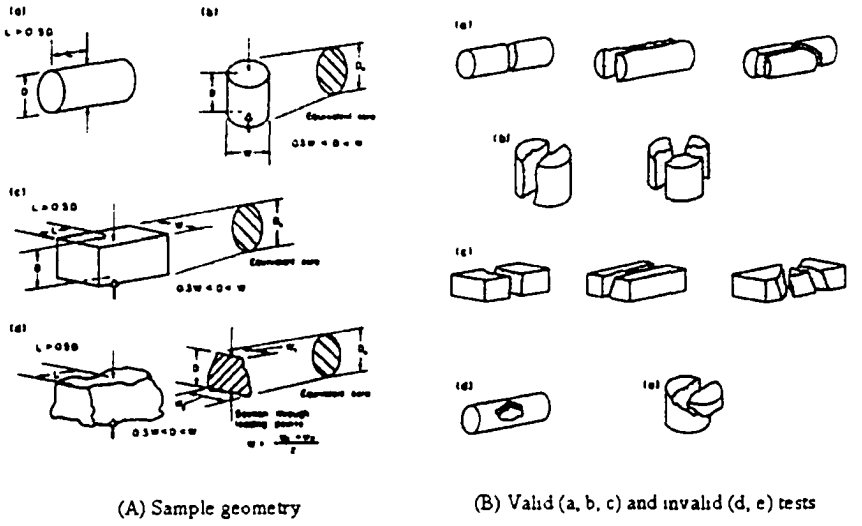


Figure 5.5: The point load test device (from ISRM, 1985 and Farmer, 1983).

The sample can be of regular or irregular shape, as shown in Figure 5.6, and is

compressed to failure. The load at failure, P, is recorded for the strength calculation following these three steps:



(A) Sample geometry (B) Valid (a, b, c) and invalid (d, e) tests

Figure 5.6: Typical geometry of tested samples (from ISRM, 1985).

Step 1: calculate initial index, I_s :

$$I_s = \frac{P}{D_e^2} \tag{5.1}$$

where D_e– equivalent diameter in mm. According to the sample geometry and the loading direction, D_e is calculated as:

$$D_e = \begin{cases} D & \text{for diametral test} \\ 2\sqrt{\frac{WD}{\pi}} & \text{for axial, block and lump test} \end{cases} \tag{5.2}$$

where D, W are the sample size in mm, as shown in Figure 5.6.

Step 2: calculate standard index, $I_{s(50)}$, for the size effect:

$$I_{s(50)} = (D_e/50)^{0.45} I_s \tag{5.3}$$

Step 3: calculate uniaxial tensile strength, T_0 :

Table 5.4: Uniaxial tensile strength

Sample	D, in	W, in	P, lbf	T_0, psi
PL-1	2.00	2.04	13.076	2.819
PL-2	2.00	2.05	12.124	2.574
PL-3	2.00	2.07	13.184	2.713
PL-4	2.00	2.10	14.468	2.844
PL-5	2.00	2.02	13.452	2.992
PL-6	2.00	2.04	14.844	3.102
Average				2.841
Std dev.				189

$$T_0 = \frac{S_a P}{(L - \frac{1.7P}{22 I_{S(50)}})^2} \tag{5.4}$$

where S_a is the shape factor determined by:

$$S_a = \begin{cases} 0.79 & \text{for diametral test} \\ 0.79\frac{D}{L} & \text{for other tests} \end{cases} \tag{5.5}$$

where L is the sample size as defined in Figure 5.6.

Because the initial index is corrected with respect to a sample with a standard size of 50 mm, all other geometrical parameters, such as D, W, L and D_e, should be converted into mm.

5.5.1.2 Test Results

In this investigation, the special platens were installed on the MTS319 frame. Six Jackfork sandstone samples were prepared into 2-in diameter by 2-in length cylinders. The point load was applied at the center of the sample along the longitudinal direction. The loading process was servo-controlled with an constant nominal axial strain rate of $5 \times 10^{-5}/s$. Both the axial load and the axial displacement were recorded by an automatic recording system. Figure 5.7 shows the curves of load vs. axial displacement. Table 5.4 shows the related geometry and the final results.

In test PL-1, the deformations were larger than in any other tests. This particular specimen was broken into three pieces while others resulted in two pieces only.

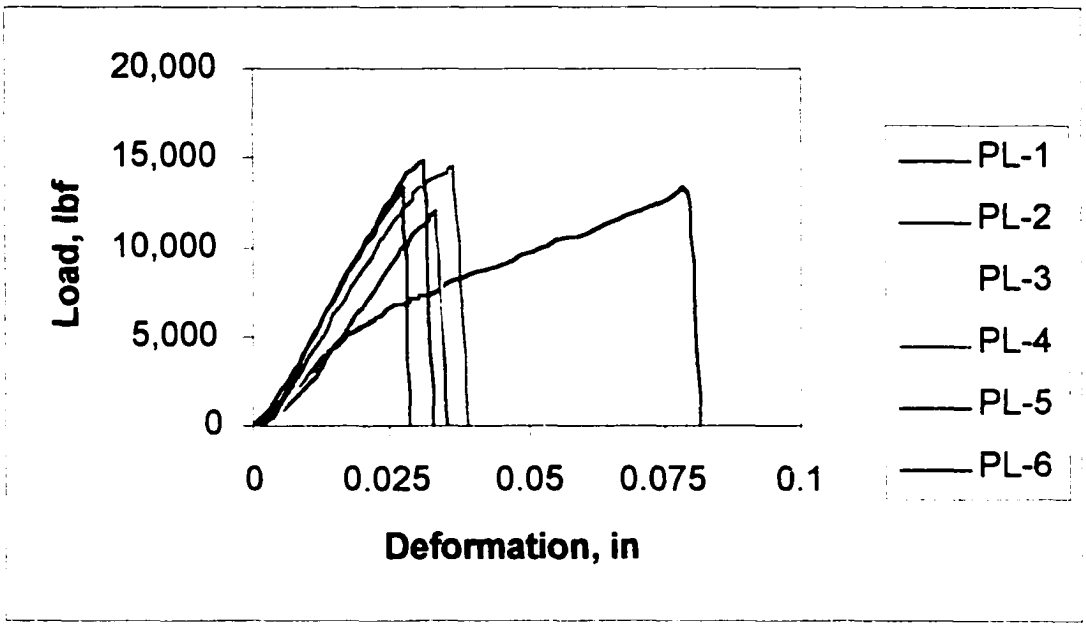


Figure 5.7: Load vs. deformation curves in point load test of Jackfork sandstone.

This triple break caused a deeper indentation on the sample before failure.

5.5.2 Uniaxial Compressive Strength, Young's Modulus and Poisson's Ratio

Uniaxial compressive strength, C_0, describes the material capability in resisting uniaxial compression.

Young's Modulus, E, characterizes the relationship between the stress and strain of a material. The higher the Young's Modulus, the lower the strain induced under the same stress condition. For linear elastic materials, it is defined as the stress divided by the induced strain. For other materials, different types of Young's moduli such as initial modulus, secant modulus and tangential modulus can be introduced (e.g., Roegiers, 1990), each corresponding to different stages of deformation. In this study, a tangential modulus is measured by using the linear portion of the stress-strain curves.

When the sample is compressed axially, it will expand laterally. Poisson's ratio correlates the lateral deformations to the axial deformations. It is defined as the negative ratio of lateral expansion strain divided by the axial compression strain induced under the same stress.

Because of the intrinsic relations among the uniaxial compressive strength, Young's modulus and Poisson's ratio, these three parameters are usually determined from the same experiment.

Following the procedures recommended by the International Society for Rock Mechanics (ISRM), five cylindrical samples of 1-in diameter by 2-in in length were prepared. Two of them, H1 and H2, were horizontal samples drilled parallel to the bedding planes, and the other three, V1,V2 and V3, were vertical samples drilled perpendicular to the bedding planes. Tests were conducted on an MTS319 loading system, using a constant axial strain rate of $5.0 \times 10^{-5}/s$. The axial load was measured by an internal transducer. The axial deformation was measured via the displacement of the stroke in the intensifier. The lateral deformation was measured with an MTS circumferential extensometer. All measurements were digitized and recorded automatically by a computer at the sampling rate of about 1-Hz. The whole system was calibrated using an aluminum standard.

Figures 5.8 and 5.9 show the stress vs. axial- and lateral-strain curves in uniaxial compressive tests for samples cored in the horizontal and vertical directions respectively. In the legends of these two figures, the abbreviations are as follows: H - horizontal samples, V - vertical samples, a - axial strains, and l - lateral strains.

From these experimental results, the uniaxial compressive strength, Young's modulus and Poisson's ratio were calculated, as shown in Table 5.5.

In sample H2, the lateral strain increased rapidly after the first peak. This is because of the non-linear dilatancy after initial failure.

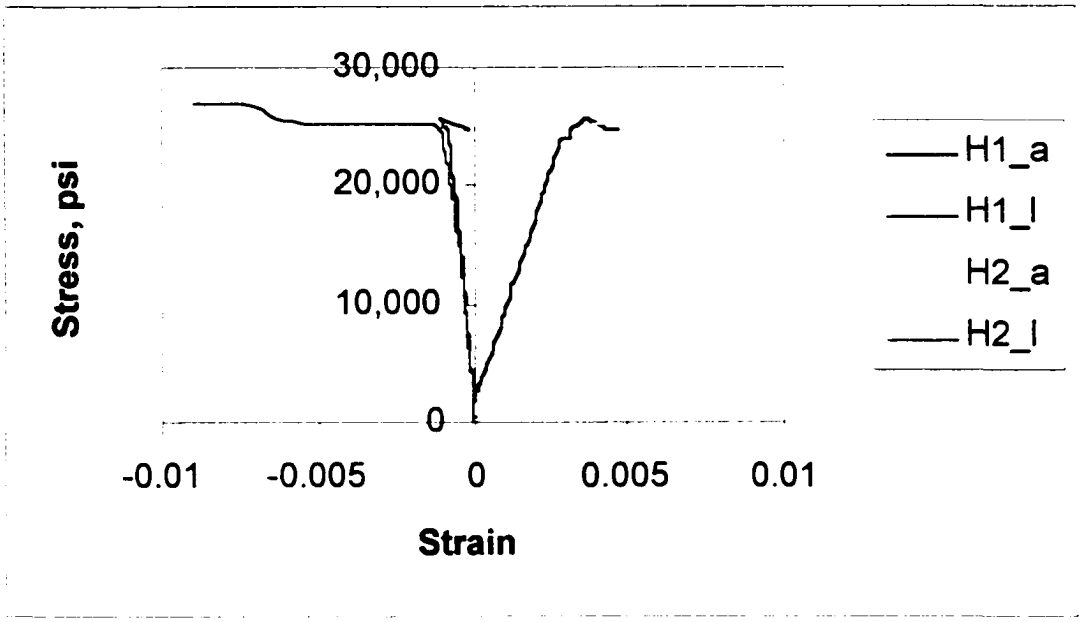


Figure 5.8: Stress-strain curves in uniaxial compressive tests for horizontal samples.

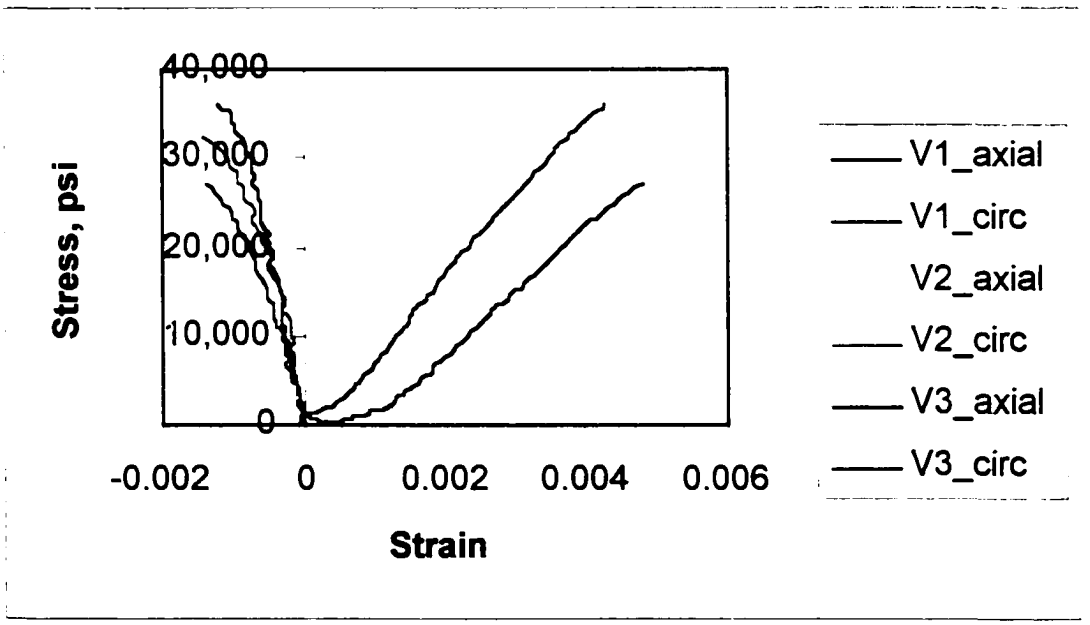


Figure 5.9: Stress-strain curves in uniaxial compressive tests for vertical samples.

Table 5.5: Uniaxial compressive strength and elasticity properties

Sample	Diameter, in	Length, in	C_0, psi	E, 10^6 psi	ν
H1	2	2.14	25,847	7.72	0.21
H2	2	2.03	27,090	6.76	0.28
Average			26,469	7.24	0.25
Std dev.			879	0.68	0.05
V1	2	2.10	27,196	7.44	0.31
V2	2	2.06	32,421	8.19	0.25
V3	2	2.13	36,120	10.18	0.21
Average			31,912	8.60	0.26
Std dev.			4,484	1.41	0.05

5.5.3 Triaxial Compressive Tests, Cohesion and Angle of Internal Friction

In addition to tensile failure, shear failure is another important mechanism for rocks. In 1773 Coulomb developed a criterion to describe the material behavior in shear. According to this criterion, shear failure starts if the shear stress, τ, on the potential shear plane reaches a critical value determined by the following value:

$$\tau = S_0 + \mu\sigma \tag{5.6}$$

where:

σ – normal stress acting on the shear plane;

S_0 – cohesion;

$\mu = \tan\phi$ – coefficient of internal friction; and,

ϕ – angle of internal friction.

While this criterion is simple and has been widely used, the problem is how to determine these parameters, i.e., cohesion and angle of internal friction.

In 1900, Mohr proposed that when shear failure takes place, the stresses on the shear plane satisfy the following function:

$$\tau = f(\sigma) \tag{5.7}$$

Using Cauchy's principal stresses, σ_1 and σ_2, he was able to express the normal and shear stresses on the failure plane as:

$$\left.\begin{aligned} \sigma &= \tfrac{1}{2}(\sigma_1 - \sigma_2) + \tfrac{1}{2}(\sigma_1 - \sigma_2)\cos 2\theta \\ \tau &= -\tfrac{1}{2}(\sigma_1 - \sigma_2)\sin 2\theta \end{aligned}\right\} \tag{5.8}$$

where θ is the angle between σ_1 and the normal to the plane of failure.

Eq.(5.8) can be converted into:

$$\left(\sigma - \frac{\sigma_1 + \sigma_2}{2}\right)^2 + \tau^2 = \left(\frac{\sigma_1 - \sigma_2}{2}\right)^2 \tag{5.9}$$

Obviously, Eq.(5.9) is a circle in the (σ, τ)-plane with the center at $(\frac{\sigma_1+\sigma_2}{2}, 0)$ and the radius as $\frac{\sigma_1-\sigma_2}{2}$. This is the well-known Mohr's circle.

Assuming that the rock obeys the Coulomb failure criterion which is a straight line in the (σ, τ)-plane, then the various Mohr's circles corresponding to failure under different confining pressures will be tangent to this straight line. On the other hand, the Mohr's circles under different confining pressures define the Mohr envelope (Jaeger and Cook, 1979), which is a straight line at low and intermediate pressure and a concave curve at very high pressures. Using the straight line portion of this Mohr envelope, the Coulomb failure criterion can be determined.

In this dissertation, six 1-*in* diameter by 2-*in* length cylindrical samples were tested under three different confining pressures. Three of these samples, H-1K, H-2K and H-3K, were horizontal; the other three, V-1K, V-2K and V-3K, were vertical samples. The confining pressures used were 1,000 *psi*, 2,000 *psi* and 3,000 *psi*. An MTS315 servo-controlled loading system was used and calibrated with an aluminum standard for each confining pressure. A constant axial strain rate of $5 \times 10^{-5}/s$ was used to control the axial loading after the confining pressure reached the required value. The axial load was measured by an internal load transducer. Axial deformations were measured using two parallel LVDTs, and the lateral deformation by a circumferential extensometer. All data were sampled by an automatic system at a rate of $1Hz$. Figures 5.10 and 5.11 show the stress-strain curves of these

Table 5.6: Triaxial compressive strengths

Sample	D, in	L, in	σ_3, psi	$(\sigma_1 - \sigma_3)_{max}$,psi	S_0,psi	ϕ,°	μ
H-1K	2	2.14	1,000	36,294		57	1.54
H-2K	2	2.13	2,000	48,984	3,970		
H-3K	2	2.08	3,000	49,604			
V-1K	2	2.14	1,000	44,255	5,890	55	1.43
V-2K	2	2.10	2,000	52,976			
V-3K	2	2.03	3,000	56,609			

triaxial compressive tests. By using these results together with the uniaxial tensile and uniaxial compressive strengths, a series of Mohr's circles were drawn and the Mohr's envelope was determined, as shown in Figures 5.12.

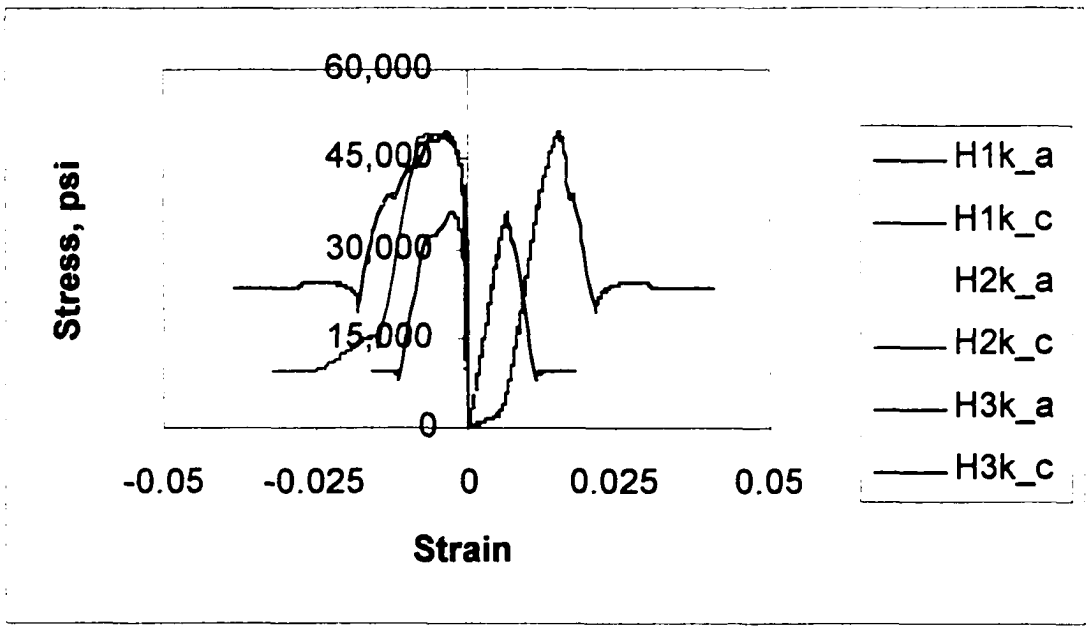


Figure 5.10: Stress-strain curves in triaxial compresive tests of horizontal samples.

Table 5.6 shows the sample parameters, measured results and calculated cohesion and angle of internal friction.

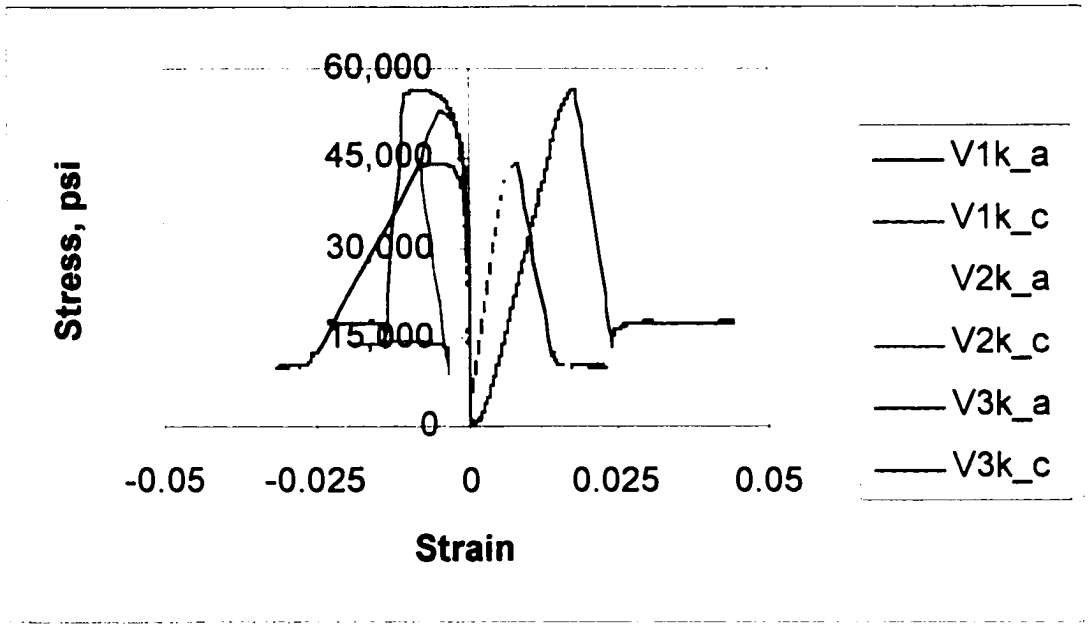
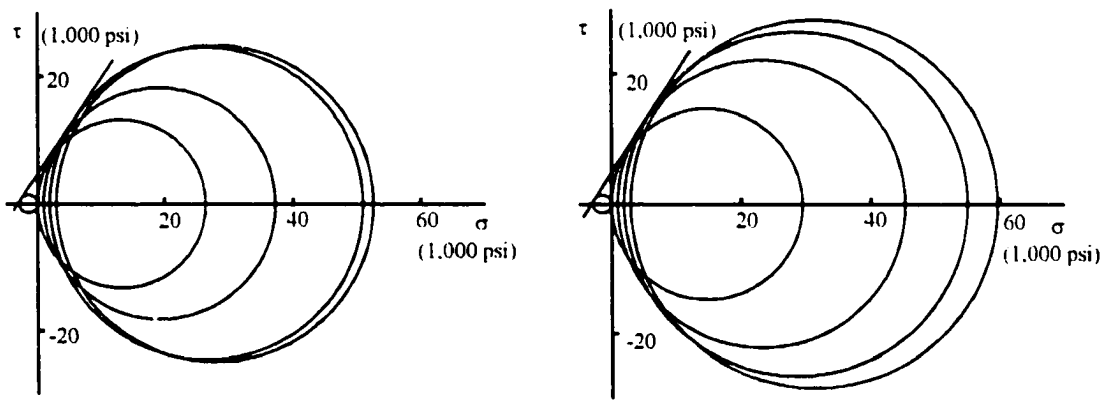


Figure 5.11: Stress-strain curves in triaxial compresive tests of vertical samples.



(a). Mohr circles of horizontal samples.

(b). Mohr circles of vertical samples.

Figure 5.12: Calculating cohesion and angle of internal friction using Mohr circles.

5.5.4 Fracture Toughness Test

5.5.4.1 CDISK Test

From the fracture mechanics' point of view, there are three different pure types of fractures: Mode-I, II and III, as mentioned in Chapter 4. Fracture toughness, K_{JC} ($J = I$, II and III), is the parameter that describes how easy a material containing a crack, can be fractured under certain stress conditions.

In the petroleum industry, Mode-I fracture has been considered as the prevailing mechanism for hydraulic fracturing treatments (Ben-Naceur, 1990; Valko and Economides, 1995). The Mode-I fracture toughness, K_{IC}, is an important parameter for hydraulic fracturing design.

On the other hand, with the diversified change of borehole orientation and stress conditions, non-planar hydraulic fractures have been observed. Roegiers and Detournay (1988) proposed a mixed fracture model (Mode-I plus Mode-II) for these situations. In this case, the fracture toughness of both Mode-I and Mode-II are very important for the design and simulation of these complex hydraulic fractures.

The determination of Mode-II fracture toughness has been investigated by some researchers (e.g., Zhao, 1994), and will not be further discussed in this dissertation, due to its non-dominant status. The attention here will be focused on the development of an easy-to-use method for the determination of Mode-I fracture toughness and using it to measure the fracture toughness of Jackfork sandstone.

There are different recommended methods to determine K_{IC} of rocks (e.g., Ouchterlony, 1983; Atkinson and Meredith, 1987; ISRM, 1988), but most of them are hard to be directly applied to the petroleum industry due to the fact that cylindrical cores retrieved from oil drilling are often not large enough to meet the geometric requirements of those methods.

In order to overcome this difficulty, Zhao and Roegiers (1990) proposed a CDISK method which uses chevron-notched disk specimens to measure K_{IC}. Geometry of the chevron-notched disk is shown in Figure 5.13. This method has two merits in

comparison with other methods. First it can use samples as small as about 2.2-inch in diameter. Secondly, it provides the possibility of measuring the K_{IC} in any desired direction inside the disk plane.

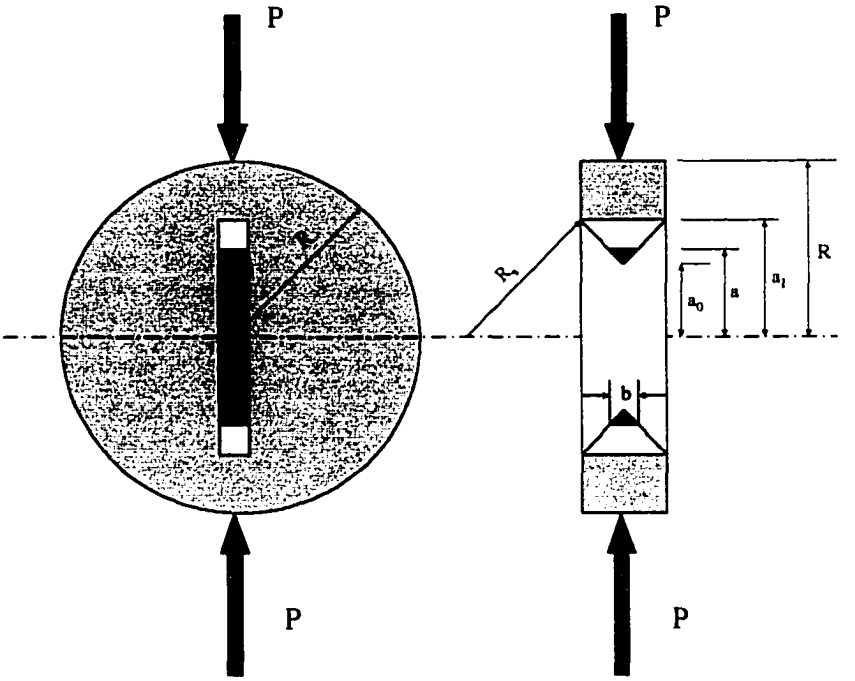


Figure 5.13: Geometry of the CDISK.

In the original reference by Zhao and Roegiers(1990), the expression of K_{IC} was given in an implicit way in terms of surface kerf length, a_1. But it is hard to control a_1 to be precisely the same on both sides of the sample due to the wavy motion of the saw near the surface during sample preparation. Instead, the initial crack length, a_0, has one unique value in each sample and is easy to measure. In addition, a_0 is physically more closely related to K_{IC} than a_1 is. So an expression of K_{IC} in terms of a_0 is needed. This expression is developed below followed by some fracture toughness tests carried out on the Jackfork sandstone.

5.5.4.2 Theoretical background

The theory behind this method is linear fracture mechanics (Knott, 1973). By applying a diametrical load on the disk along the crack, like in a Brazilian test (Yatomi et al., 1989), tensile stress concentrations occur at the crack tip. The crack propagation process can be depicted as follows. With the increment of load P, the Mode-I stress intensity factor, K_I, at the crack tip will increase. At the beginning with the increasing of P, the crack begins to propagate from its initial length, a_0. But without continuous increment of P, propagation of the crack stops. During this stage, the energy consumed to form new crack surfaces is more than the increment of potential energy stored in the crack system due to the incremental deformation induced by the loading.

By continuously increasing P, the crack will keep propagating. Once P reaches such a point, P_m, that the increment of potential energy stored into the crack system equals the energy consumed to form the new crack surface, the crack will propagate stably from that specific crack length, a. From this point on, no more load increment is required to keep the crack propagating. The corresponding stress intensity factor at this point thus defines the fracture toughness, K_{IC}.

In order to measure K_{IC}, P is increased at a proper loading rate. Because at the stage of stable crack propagation, the energy stored into the crack system can be calculated from the load and the displacement of the loading point. On the other hand, the energy consumed in creating new crack surfaces can also be calculated if the crack length, a, crack front width, b, and the fracture energy release rate, G_I, are known. Equilibrium of these two kinds of energy gives the critical fracture energy release rate, G_{IC}. Because the critical fracture energy release rate, G_{IC}, is related to the fracture toughness, K_{IC}, this offers a way to determine K_{IC}.

Although the critical crack length, a, at this critical point is still not known, it has been shown that it is such a value which is between the initial crack length, a_0, and the surface kerf length, a_1. In additon, this critical crack length minimizes the Y-function (stress intensity coefficient, a dimensionless geometric function that

relates the stress intensity factor and the applied load) (Munz, 1980). So the critical crack length, a, can be numerically calculated via minimizing the Y-function by changing a from a_0 to a_1. Following the above theory, an a_0-based formula for the Mode-I fracture toughness, $K_{IC_a_0}$, is derived as:

$$K_{IC_a_0} = \frac{\sqrt{2}P}{W\sqrt{B}} Y^*_{a_0\,\min} \tag{5.10}$$

where:

- P – peak load;
- W – diameter of the disk;
- B – disk thickness; and,
- $Y^*_{a_0\,\min}$ – the minimum dimensionless stress intensity coefficient.

Details of the derivation and the definition of $Y^*_{a_0\,\min}$ are shown in Appendix B.

5.5.4.3 K_{IC} Test Results

Using the above theory and technique, the fracture toughness of the Jackfork sandstone was determined using three disk samples. Diamond wafering blades (3-*in* diameter × 0.006-*in* thickness) manufactured by BMAD (2001) were used in cutting the initial crack.

After preparation, the samples were kept in an oven at $150°F$ for 24-hour. The test was conducted on a MTS319 loading frame using a nominal constant strain rate of $5 \times 10^{-4}/s$. Compressive load was applied along the initial fracture until the sample was fractured. The loads and displacements between the two loading points were recorded. Figure 5.14 shows the load-displacement curves in fracture toughness tests KIC-1, KIC-2,and KIC-3. Table 5.7 shows the geometric parameters, the peak load and the final value of the fracture toughness. From Figure 5.14, it is seen that multiple fracture propagations occurred in test KIC1 and KIC3. Therefore, fracture toughness measured in KIC2 is proposed to represent the material.

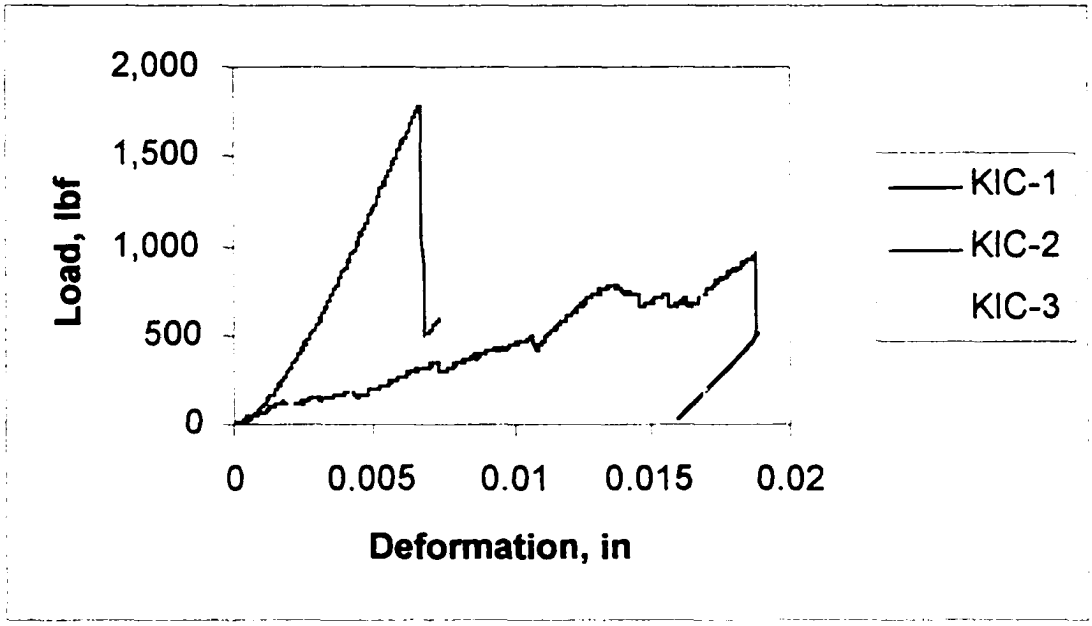


Figure 5.14: Load-displacement curves of fracture toughness tests.

Table 5.7: Parameters and results of fracture toughness test

Sample	W, in	B, in	a_0, in	a_1, in	Y_{min}	P, lbf	K_{IC},psi$\sqrt{in}$
KIC-1	3.125	0.753	0.852	1.125	1.621	952	1,161
KIC-2	3.125	0.710	0.921	1.050	1.435	1,782	2,038
KIC-3	3.125	0.752	0.854	1.100	1.551	1,399	1,637
Used data							2,038

6 Packer Influence on the Initiation of Hydraulic Fractures

6.1 Introduction

Chapter 2 showed that the local stress field controls the initiation of hydraulic fractures. Because the global stress field determines the eventual fracture orientation, the near-wellbore fractures would be reoriented if their orientations were not in the favorable direction. This reorientation would introduce complex tortuosity to the fluid path and increase the pressure loss in the near-wellbore region. In extreme situations, this reorientation could even lead to the failure of the hydraulic fracturing stimulation. For example, due to the influence of this kind of effects, longitudinal fractures were believed to be induced in one of the three pilot horizontal wells in Lost Hills Diatomite, where transverse hydraulic fractures were expected (Emanuele et al., 1998). Therefore, a proper selection of these parameters is important. This chapter will focus on the packer influence on the hydraulic fracturing initiation.

Packers have been widely used in both field hydraulic fracturing operations (Brown et al., 2000) and laboratory experiments (Guo et al., 1993a, b; Morita et al., 1996). The primary function of the packers is to seal the pressurized section from the rest of the borehole. Due to the limited space in laboratory samples, packers used in laboratory tests are usually much smaller than those used in the field. In addition, laboratory tests are usually designed for specific purposes (Holder et al., 1993; Willson et al., 1999), making the utilization of packers difficult to be standardized.

There have been a limited amount of investigations on the influence of packers. von Schoenfeldt and Fairhurst (1968) were the first to mention that the stress field in the borehole would be influenced by the packer, though no quantitative results were given in their paper. Using a 2-dimensional finite element method simulator, Roegiers et al. (1973) investigated the distribution of longitudinal and circumferential stresses in the borehole near a packer. Both influence of the packer rigidity and the steel mandrel length were studied. Ong (1994) investigated the function of different packers on laboratory tests of inclined boreholes and developed an epoxy to backup the packers in the borehole.

In two pilot laboratory hydraulic fracturing experiments, longitudinal and transverse fractures were observed respectively, which were obtained under the same conditions except for the packer lengths. The purpose of those experiments was to select proper packer lengths for other experiments to be introduced in the following two chapters. The one with a longer packer showed normal fracturing behavior, in which the fracture initiated on the borehole wall in the sealed section and propagated in the direction of higher stresses (Scott et al., 2000). On the other hand, the one with a shorter packer showed transverse fracturing behavior, in which the fracture initiated at the end of the packer and propagated in the direction perpendicular to the borehole axis (Zeng and Roegiers, 2001).

The next section introduces the experiments, followed by the observed results, and numerical simulation of the change of local stress in the borehole with the increase of borehole pressures.

6.2 Experimental Setup

In order to determine the proper packer lengths, two pilot experiments, Tenn1 and Tenn2, were conducted on Tennessee sandstone (Tenn SS) under asymmetrical stresses, as shown in Figure 6.1.

The two tests were carried out on two cubic Tennessee sandstone blocks with

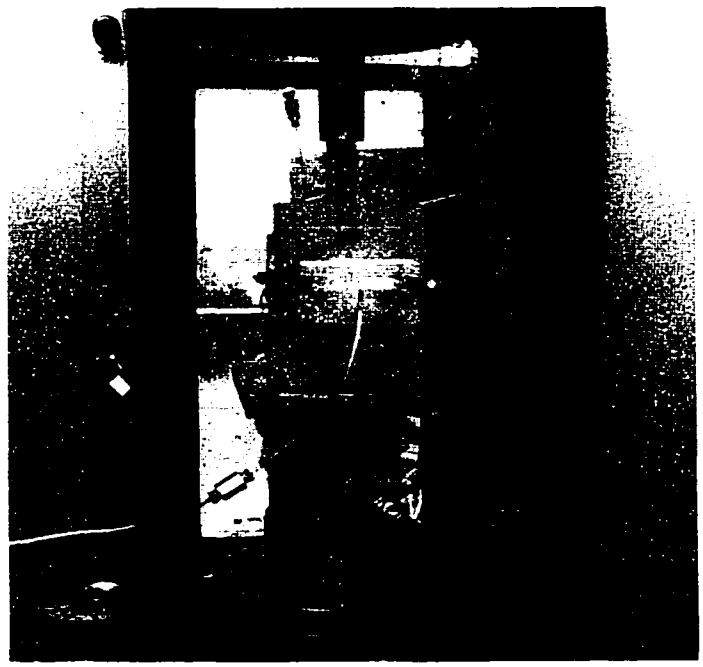


Figure 6.1: Experimental setup for the asymmetrical loading.

each side 160 *mm* long. A 12.6 *mm* diameter borehole was drilled at the center on one surface and through the whole block. A 12.6 *mm* long central portion of the borehole was sealed off with rubber packers from both directions. Lengths of the packers were 12.6 *mm* in sample Tenn1 and 6.3 *mm* in sample Tenn2. A tubing of 3.18 *mm* OD with wall thickness of 0.89 *mm* was used to connect the sealed borehole to the pump. An outlet was designed so air in the sealed part could be expelled before being pressurized. Figure 6.2 schematically shows the borehole structure, the load, and the stresses.

6.2.1 Description of the Materials

The Tennessee sandstone has the characteristics of a typical tight gas sandstone. with a very low porosity (6%) and permeability (nano-Darcy level) (Scott and Nielsen, 1991). The packer is made of $M35$ Green Neoprene produced by Plasticoid Company. The hydraulic fracturing fluid is 0.1 $Pa \cdot s$ silicone oil. Related properties

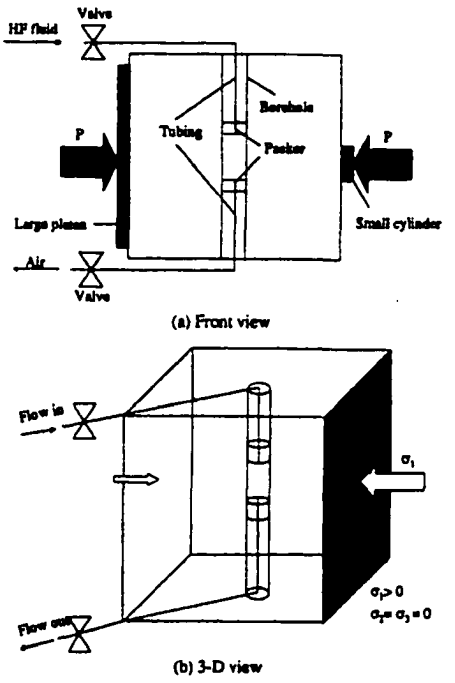


Figure 6.2: Borehole structures (Zeng and Roegiers, 2001).

of the Tennessee sandstone and the rubber of the packers are shown in Table 6.1.

At first, an axial load, $P = 4,450\ N$, was applied at the center in the direction perpendicular to the borehole axis. Two loading platens of different sizes were used to induce asymmetrical stress field in the sample. The large platen was a $140 \times 140 \times 30\ mm$ plate, the small one a $40\ mm$ diameter $\times$ $80\ mm$ length cylinder, as shown in Figures 6.1 and 6.2 (a). Both were of the same Tennessee sandstone as the tested samples. Because of the difference in the loading areas, the external stresses on the two sides are:

$$\begin{cases} \sigma_{1_high} = 3.54\ MPa \\ \sigma_{1_low} = 0.23\ MPa \end{cases}$$

After applying the external stresses, the hydraulic fracturing fluid was pumped into the sealed-off section at a relatively constant pump rate of about $0.07\ ml/\ \text{min}$. The tubing and the sealed portion of the borehole were open so the hydraulic fracturing fluid could drive the air out, as mentioned before. Once all the air in the

Table 6.1: Properties of the materials

Property	Tenn SS	Packer
Density, kg/m^3	2,510	1,380
Porosity	6%	
Young's modulus, MPa	2,000	1.21
Poisson's ratio	0.2	0.4
Uniaxial compressive strength, MPa	195	
Uniaxial tensile strength, MPa	17	62
Contact frictional coefficient	0.5	

sealed section and the tubings was expelled, the outlet valve in the tubing would be closed and the pressure inside the sealed portion of the borehole began to increase until the breakdown of the rock specimen. Figure 6.3 shows the pressurization history of experiment Tenn1.

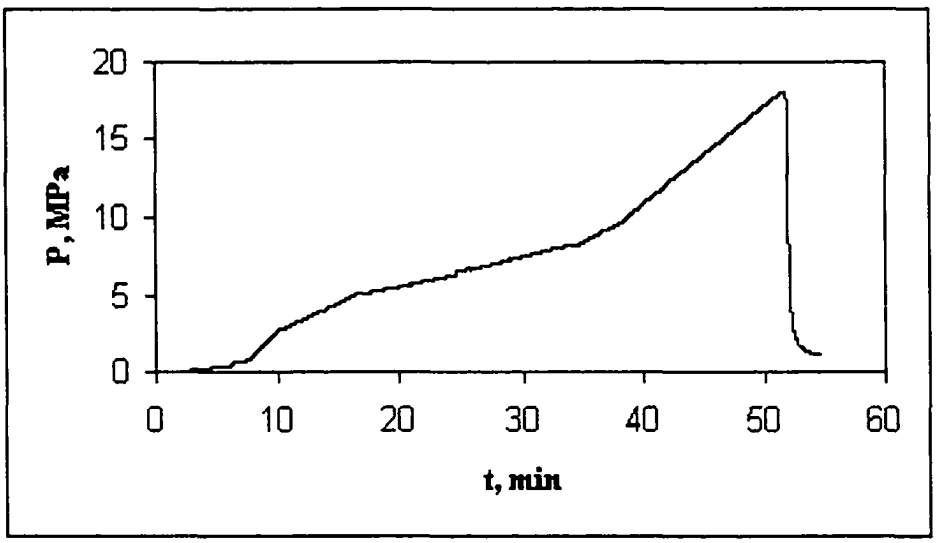


Figure 6.3: Injection time vs. borehole pressure in experiment Tenn1.

6.3 Experimental Observations

6.3.1 Test Tenn1

Induced fractures in the two tested samples were different. In Tenn1, a longitudinal fracture along the borehole was formed on the high stress side of the specimen, as shown in Figure 6.4. In Figure 6.4 (a), the fracture is seen to extend from the borehole upward to the block surface. The profile of the fracture in cross-section AB, which is perpendicular to the borehole, is shown in Figure 6.4 (b). The fracture, indicated by the arrow, was parallel to the dashed line and extended to the concentrated loading surface. A small upward spot of leakoff along the fracture near the borehole is also observed, probably due to the fact that permeability is highly dependent on stress. The rock cylinder on the sliced portion indicated the actual location of loading on that surface (refer to Figure 6.1). It can be seen that the induced fracture goes to the edge of the bottom of the loading cylinder.

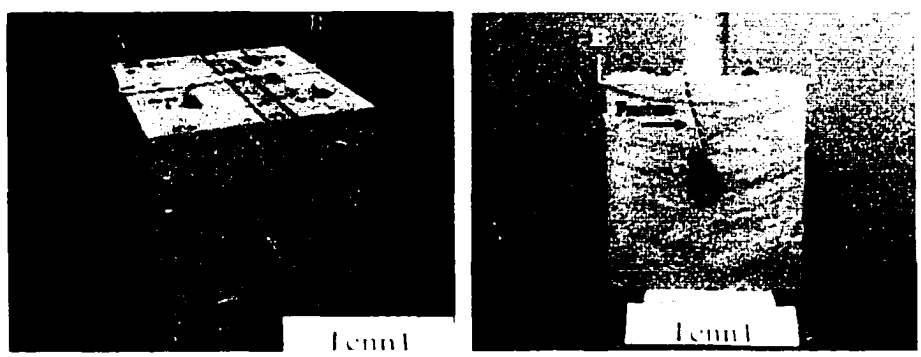


Figure 6.4: The longitudinal fracture in experiment Tenn1.

6.3.2 Test Tenn2

In experiment Tenn2, a transverse fracture perpendicular to the borehole axis was induced by the fracturing fluid, indicated by the leakage on the right surface of the

block, as shown in Figure 6.5 (a). A profile along AB and through the borehole, shown in Figure 6.5 (b), confirmed the transverse fracture. In addition, hydraulic fracturing fluid leakage was observed along the wall of the sealed borehole, forming a circular pattern.

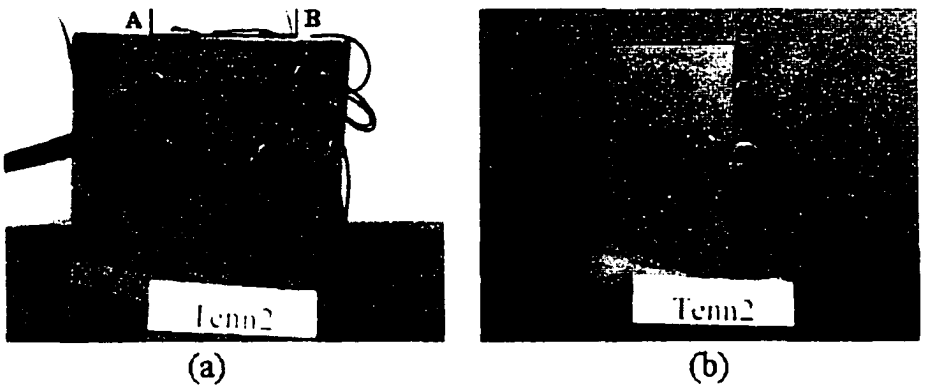


Figure 6.5: The transverse fracture in experiment Tenn2.

Because the two tests were conducted under the same conditions except for the lengths of the packers, the packer length might be the reason for the difference of the fracturing. Leakage in Tenn2 might indicate that the packers in this specific sample failed before the borehole pressure reached the fracture initiating value. This will be further proven through numerical modeling reported in the following section.

6.4 Numerical Modeling

In order to better understand the influence of the packer length on the initiation of the hydraulic fractures in the two experiments mentioned above, numerical modeling was conducted using ABAQUS, a commercially available numerical simulator developed by Hibbit, Karlsson & Sorensen, Inc (HKS, 1998). The one used in this simulation was Version 5.8. Both linear and non-linear modules were used in this simulation.

6.4.1 Assumptions and Simplifications

Mechanically, the sample Tenn1 was simplified as a block of Tennessee sandstone with a rubber packer in contact with the rock surface in the borehole. Contact elements were defined between the rubber packer and the borehole wall. Because no leakage along the borehole was observed during and after the test, no relative motion was allowed between the rubber packer and the borehole rock. This led to defining nodes on the edge as multiple point constraints (HKS, 1998).

In Tenn2, fracturing fluid leakage along the borehole was observed during the later stage of the pressurization. This meant that the packer failed to seal-off the borehole; thus the fluid pressure acted directly onto the epoxy. Based on this observation, Tenn2 was simplified as a borehole sealed by epoxy.

Measurements of seismic velocity showed that both samples had a homogeneous $P-$wave velocity of 4.0 km/s in different directions. So this rock was assumed to be linear, elastic, isotropic and homogeneous. The rubber packer was also simplified as a linear, elastic, isotropic and homogeneous material. Epoxy in the borehole behind the packer had been fully consolidated before the experiments. In the simulation, this material was simplified to have the same properties as the rock. Table 6.1 shows the properties of these materials.

6.4.2 Discretization and Boundary Conditions

Because both the load and the geometry of the studied system were symmetric about the borehole (Figure 6.1), only a quarter of the whole system needs to be studied, as shown in Figure 6.6.

The coordinate system, $OX_1X_2X_3$, was set to be originated from the center of the whole system; that is, the center of the sealed borehole in the studied domain, as shown in Figure 6.6. OX_1 was set to be vertical and upward in the radial direction, parallel to the external load and pointing to the high stress direction. OX_3 was set in the direction of the borehole axis. OX_2 was set in the radial direction of the

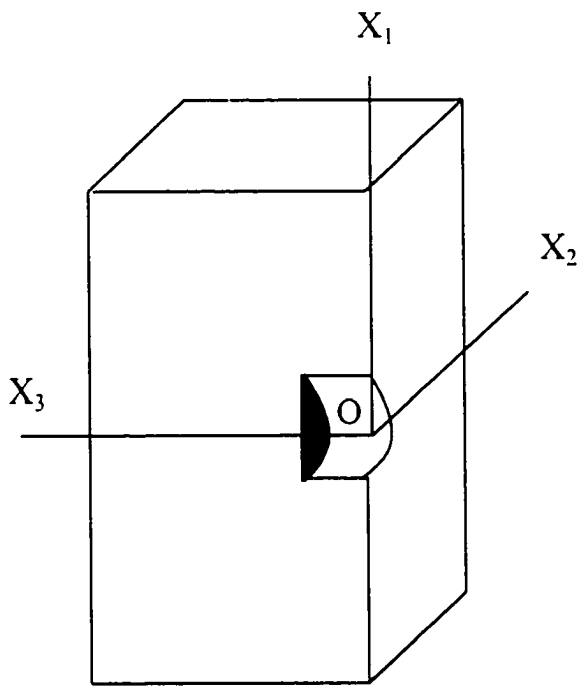


Figure 6.6: Coordinate system (Zeng and Roegiers, 2001).

borehole which formed a right handed system with OX_1 and OX_3. Thus OX_2 was horizontal in the radial direction of the borehole.

Due to the special geometry, the domain was discretized into two portions: the near-wellbore portion and the remote area. The near wellbore portion was considered as asymmetrical about the borehole axis. The remote area was considered as symmetrical about the three coordinate planes. In this area, regular rectangular elements were used. In the near-wellbore portion, gradually changing elements were used so that the two portions could be connected smoothly.

Dense discretization was applied to the portions near the borehole in the radial direction and near the sealed-end along the borehole axis, as shown in Figure 6.7. Two types of elements, $C3D8$ and $C3D6$, were used. The former was a type of continuum, 3-dimensional, 8-node element; and the latter was similar to the former except that the number of node was 6 (HKS, 1998). The $C3D6$ elements were used

in the first layer of elements around the OX_3 axis[1] in the epoxy-filled section of the borehole. The rest was discretized into $C3D8$ elements. In total, 3,678 elements with 4,438 nodes were generated.

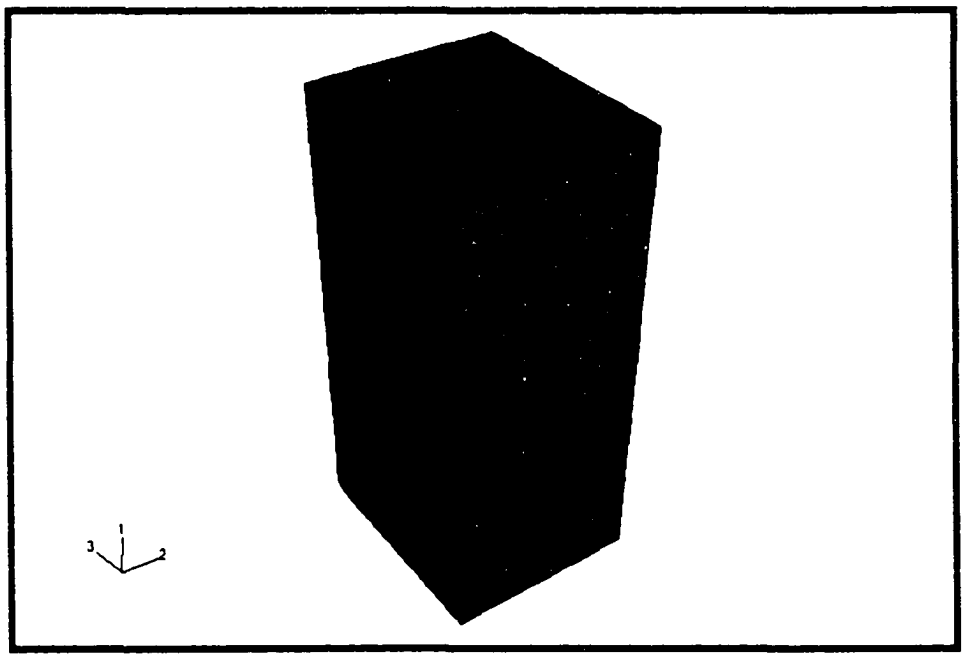


Figure 6.7: The mesh in the studied domain (Zeng and Roegiers, 2001).

Displacement boundary conditions were defined as follows. Nodes on the symmetric planes were constrained in the symmetric directions. This meant null displacements in the X_2-direction for all nodes on its symmetric plane. Similarly, there are no displacements in X_3-direction for all nodes on its symmetric plane. In order to prevent rigid-body motion, the four corner nodes at the bottom surface were set to be fixed in all three directions.

6.4.3 External Load and Borehole Pressures

The total external load, P, was 4,450 N . Because only a quarter of the system was studied, the load on the studied domain was 1,112.5 N. This load was evenly

[1] In Figure 6.7 and other ABAQUS generated figures, OX_1, OX_2 and OX_3 were represented by direction-1, -2 and -3, respectively.

Table 6.2: Cases and borehole pressures

Case	Borehole Pressure, MPa	Case	Borehole Pressure, MPa
Tenn1-A	3.45	Tenn2-A	3.45
Tenn1-B	14.79	Tenn2-B	14.79

distributed on to the area covered by quarter of the top cylinder (platen) and applied to related elements on that top surface.

Two borehole pressures were selected for the numerical simulation. The first pressure was 3.45 MPa which was used to setup a basic case for both tests. The second was 14.79 MPa, corresponding to the beginning of fracture initiation indicated by sparse microseismic activity in test Tenn2. In total, 4 cases were investigated, as shown in Table 6.2.

6.4.4 Simulation and Analysis of the Results

In modeling Tenn1, there was surface contact between the rubber packer and the borehole wall which obviously involved non-linear behavior. A total dimensionless time of 1.0 was used for the non-linear simulation and an initial time step of 0.1, or 10%, was assigned. The maximum number of increments was set as 25 in every time step. The calculation started with an initial magnitude of load estimated from the previous time step or last iteration.

In modeling Tenn2, the linear analysis simulator module was used and no iterations were necessary.

Because tensile failure is generally considered as the mechanism for hydraulic fracturing, and the fracture initiates / starts at the borehole surface when the poroelastic effect is ignored, attention in analyzing the results was concentrated onto the tensile principal stress. As ABAQUS follows the sign convention of elasticity, in which tensile stress is defined as positive (HKS, 1998), this convention has been followed in this chapter. So the analyses here have been focused on the maximum principal stress, σ_1.

6.4.4.1 Case Tenn1-A

Figure 6.8 shows the contour of the overall distribution of maximum principal stress of Case Tenn1-A. The near-wellbore portion is shown in Figure 6.9.

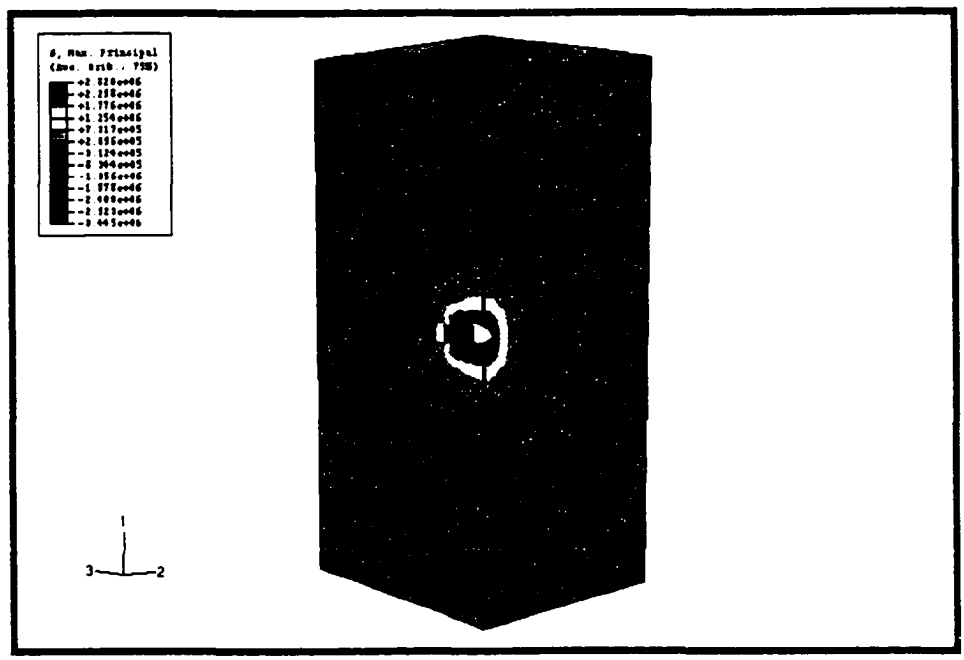


Figure 6.8: Overall σ_1 distribution in Tenn1-A (Zeng and Roegiers, 2001).

From Figures 6.8, the distribution of the maximum principal stress, σ_1, can be easily divided into two regions: the remote region and the near-wellbore region.

In the remote region, σ_1 is always negative (compressive), except for a narrow band around the external loading area on the top. The value of σ_1 in the major part is almost homogeneous and relatively low: varying from $-0.8\ MPa$ to $-0.3\ MPa$. The positive (extensional) σ_1 band near the external loading area is induced by the deformation due to the external loading. The value of σ_1 in this band varies from $+0.2\ MPa$ to $+0.7\ MPa$.

At the near-wellbore region, the distribution of σ_1 is characterized by two features: the concentration of negative (compressive) stress near the packer at the sealed-end in the $+X_3$- direction, and a concentration of tensile stresses in the ra-

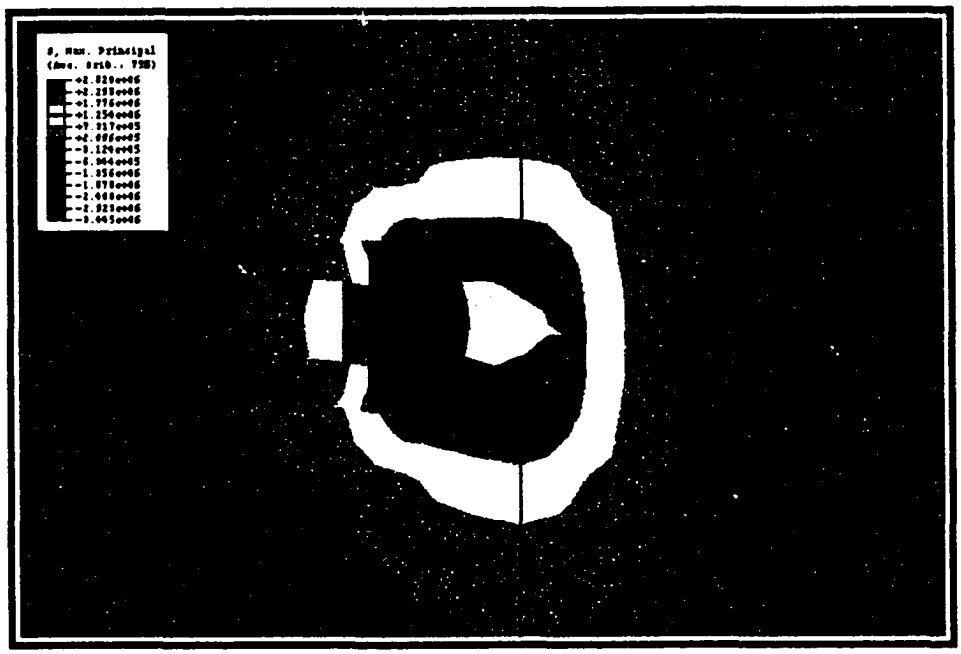


Figure 6.9: Near-wellbore σ_1 distribution in Tenn1-A (Zeng and Roegiers, 2001).

dial direction along the wellbore in the rock. The maximum σ_1 in the packer varies from $-3.4\ MPa$ to $-2.9\ MPa$. The maximum σ_1 in the wellbore rock varies from $+2.3\ MPa$ to $+2.8\ MPa$ in two narrow strips in the $+X_1$ and $-X_1$ directions, as shown in 6.9.

6.4.4.2 Case Tenn2-A

Figure 6.10 shows the overall distribution of σ_1 for the Tenn2-A Case. Figure 6.11 is the near-wellbore distribution of σ_1.

The distribution of σ_1 in Case Tenn2-A can also be divided into two regions: the remote region and the near-wellbore region.

In the remote region, σ_1 also varies from negative (compressive) to positive (extensive). However, the distribution of the volume of negative and positive σ_1 is different from that in the previous case, as described below. Except for the external loading area where compressive stresses are highly concentrated, the compressive σ_1

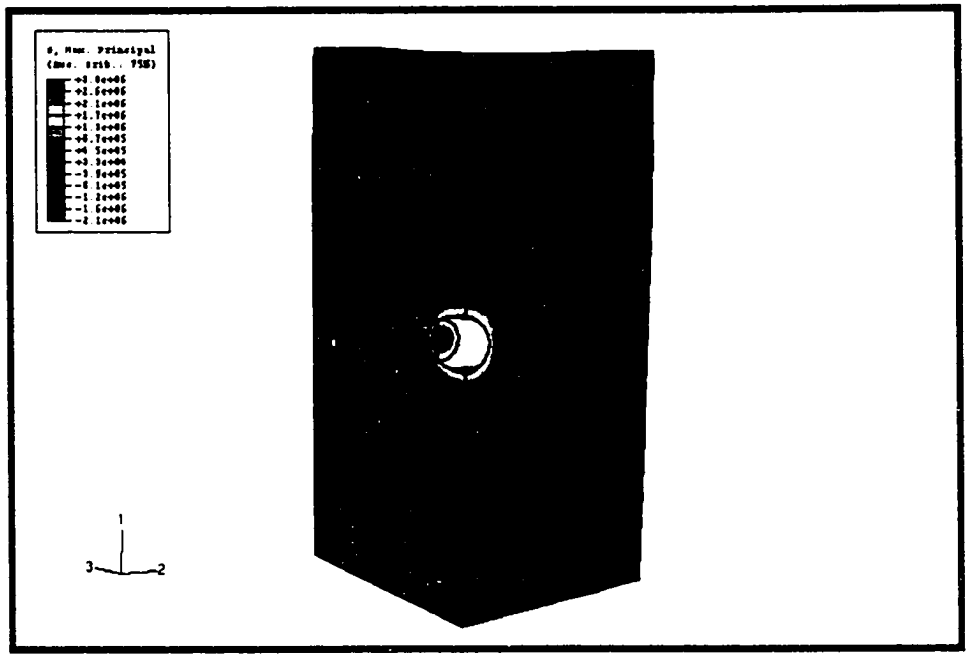


Figure 6.10: Overall σ_1 distribution in Tenn2-A (Zeng and Roegiers, 2001).

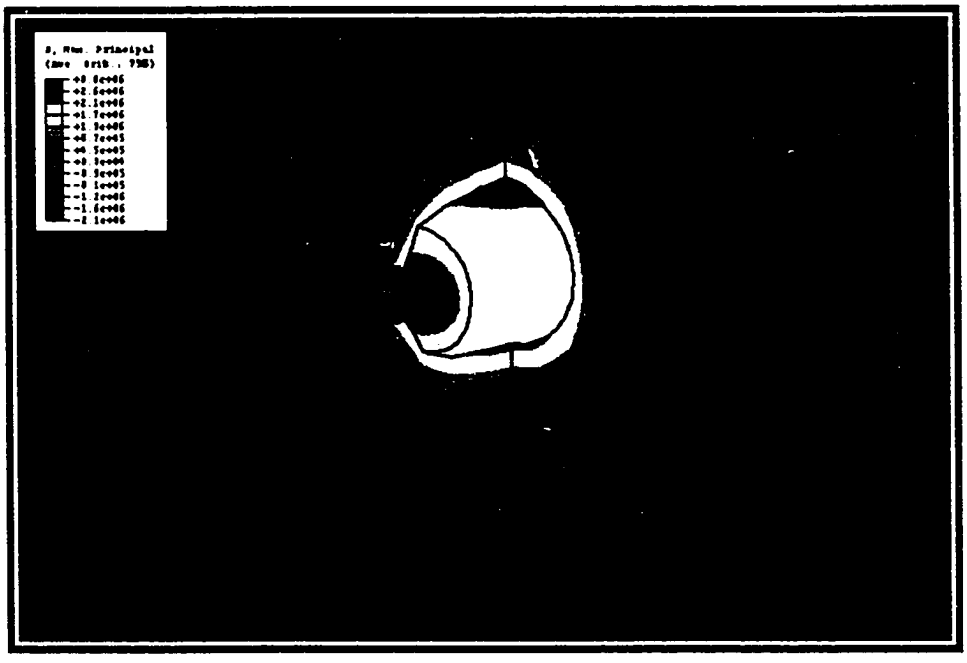


Figure 6.11: Near-wellbore σ_1 distribution in Tenn2-A (Zeng and Roegiers, 2001).

distributes from the bottom up to about $\frac{1}{3}$ of the sample length in the X_1-direction, and on the upper left and upper right corners in Figure 6.10. The value of $\sigma_1$in this part changes from $-0.39\ MPa$ to about $0\ MPa$. The rest of the remote region has positive (extensive) σ_1 with values varying from about $0\ MPa$ to $+0.45\ MPa$.

In the near-wellbore region, the maximum negative (compressive) σ_1 occurs on the central $\frac{1}{3}$ part of the sealed end with a value ranged from $-1.2\ MPa$ to $-0.8\ MPa$. Next to this area is a circular band of positive (extensive) σ_1-distribution with a value of $+2.6\ MPa$ to $+3.0\ MPa$. Actually, this is the maximum positive (extensive) σ_1 concentration in the near-wellbore region. The second highest positive (extensive) $\sigma_1$concentration occurs on the wellbore wall in the $+X_1$- and $-X_1$-directions, as shown in Figure 6.11. In comparing to Figure 6.9 of Case Tenn1-A, the most obvious difference is the shape and location of of the maximum σ_1: striped band along the wellbore in the $+X_1$- and $-X_1$-directions for Case Tenn1-A and circular band at the sealed-end in the $+X_3$-direction for Case Tenn2-A. This difference will be enhanced with the increase of borehole pressure, as will be revealed in the next two cases.

6.4.4.3 Case Tenn1-B

Figures 6.12 and 6.13 show the overall and the near-wellbore maximum principal stress distribution of Case Tenn1-B. In comparing to the stress distribution of Case Tenn1-A shown in Figures 6.8 and 6.9, one can easily see that the major changes occur in the near-wellbore region. With the increase of the borehole pressure, the σ_1 concentration area expands in the wellbore. The magnitude of the maximum σ_1 is now about $+11.3MPa$, mainly extending along the borehole direction. This gives an explanation to the initiation of longitudinal fracture along the wellbore in experiment Tenn-1.

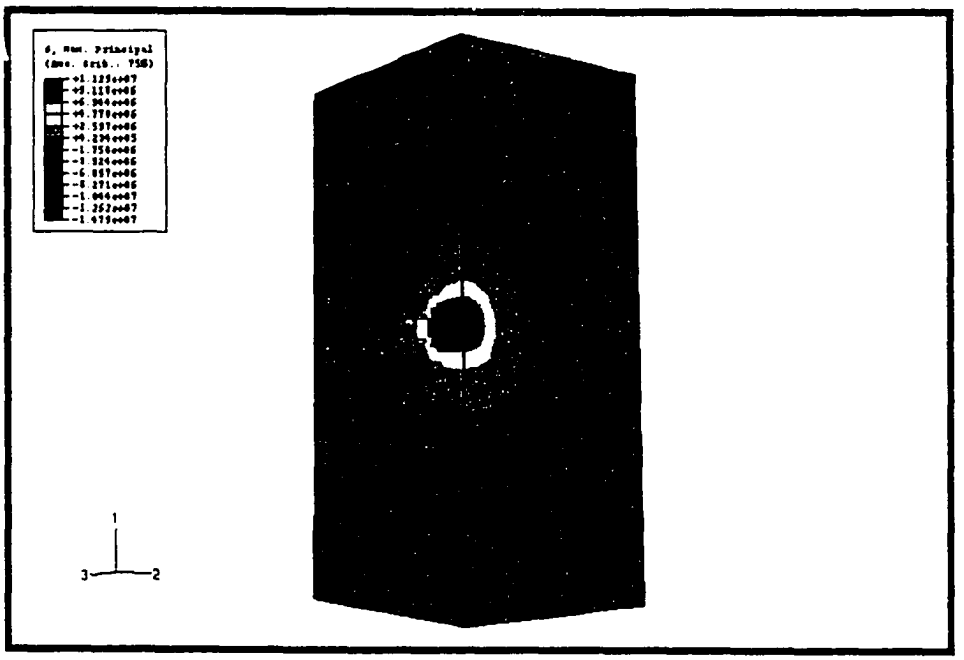


Figure 6.12: Overall σ_1 distribution in Tenn1-B (Zeng and Roegiers, 2001).

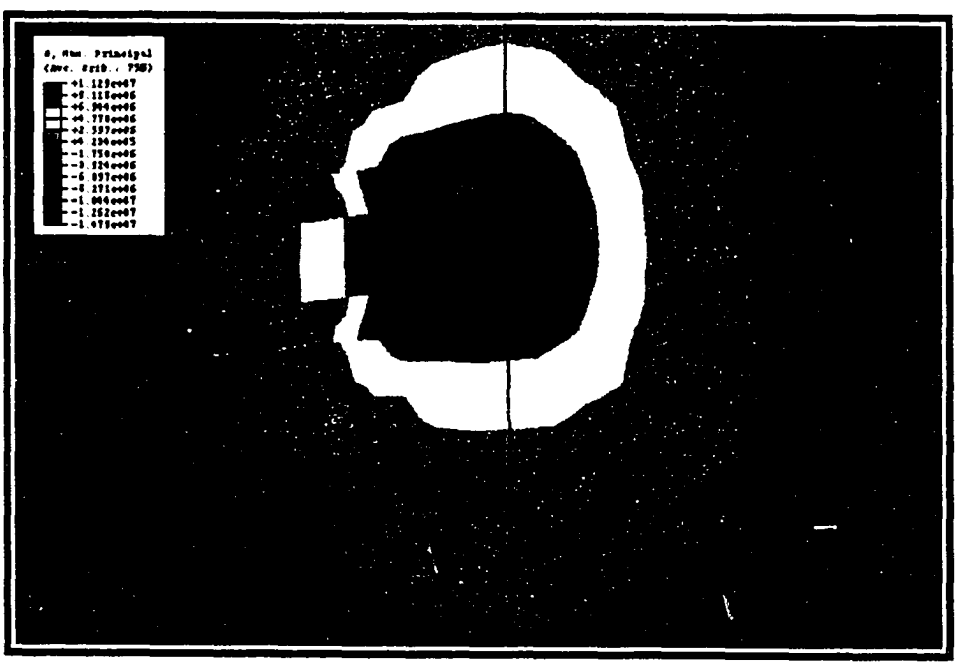


Figure 6.13: Near-wellbore σ_1 distribution in Tenn1-B (Zeng and Roegiers, 2001).

6.4.4.4 Case Tenn2-B

The loading conditions in Case Tenn2-B are similar to that in Case Tenn2-A except for a higher borehole pressure. Distribution of the maximum principal stress σ_1 of Case Tenn2-B is shown in Figures 6.14 and 6.15. By comparing these figures with Figures 6.10 and 6.11, it is clear that, with the increase of borehole pressure, the distribution of $\sigma_1$changes sharply. In the remote region, σ_1 becomes negative (compressive) everywhere. In contrast, σ_1 in the near-wellbore region is all positive (extensive). More importantly, the maximum σ_1 area at the sealed end keeps expanding and replaces the previously compressive area. On the other hand, the maximum σ_1 areas along the borehole wall in Figures 6.10 and 6.11 have shrunk and almost disappeared in Figures 6.14 and 6.15. As to the value of σ_1 in this case, the maximum σ_1 is about $+12.0MPa$ occurring in a circular area of stress concentration at the sealed end of the borehole. This offers a good explanation to the initiation of the transverse fracture in experiment Tenn2.

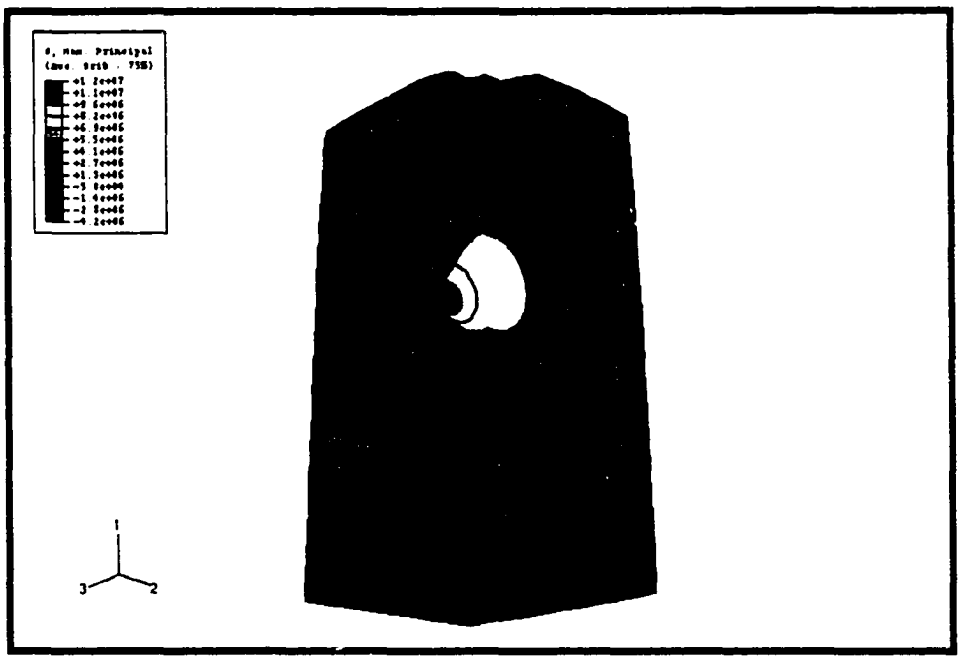


Figure 6.14: Overall σ_1 distribution in Tenn2-B (Zeng and Roegiers, 2001).

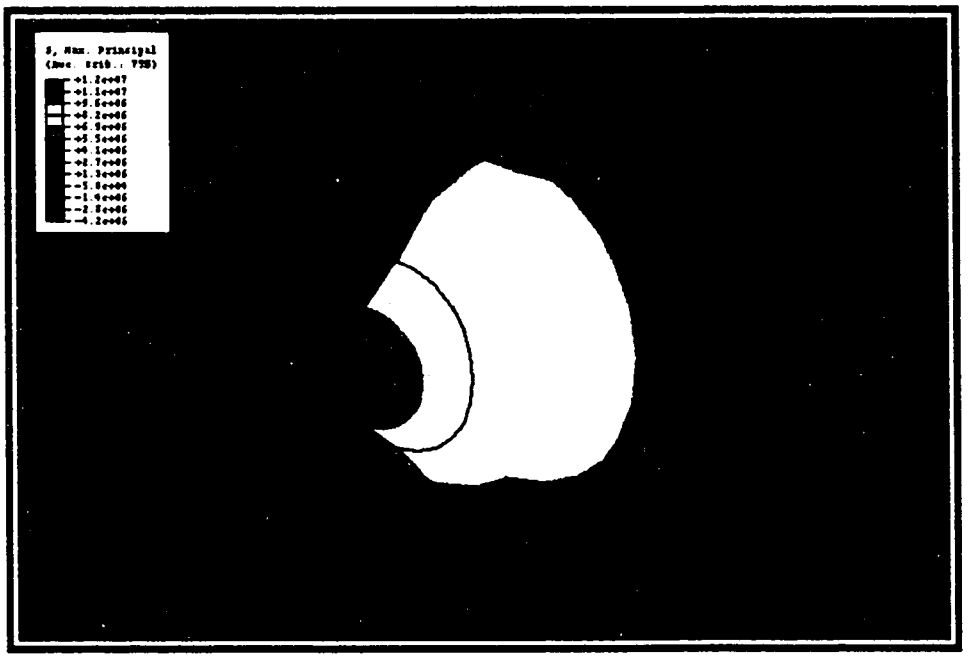


Figure 6.15: Near-wellbore σ_1 distribution in Tenn2-B (Zeng and Roegiers, 2001).

6.5 Discussion

From these two pilot experiments, the following points can be summarized:

1. The initiation of fractures at the wellbore is controlled by the local stress field; and,

2. A properly functioning rubber packer would cause compressive stress concentration in the packer at the sealed-end and extensive stress concentration on the borehole wall. This would result in a longitudinal fracture initiation along the wellbore under the loading conditions in the pilot experiments.

A malfunctioning packer would concentrate the stress field in a different way: with the increase of wellbore pressure, the compressive stress on the "packer" would be transferred to the remote region, and the extensive stress would be transferred from the borehole wall to the "packer". This would result in the initiation of a transverse fracture in the loading conditions described in the two pilot tests.

The initiation and propagation of the fracture in the asymmetrical stress field

has been further confirmed by microseismic imaging which will be introduced in the next chapter.

3. In order to induce the fracture properly, the packer should have a minimum length. Based on the results of these two pilot experiments and the availability of the packers, a packer length of 12.6 mm would be proper. This will be proved valid in subsequent experiments as will be introduced in another chapter.

4. The borehole pressure in Case Tenn2-B corresponds to the fracture initiation. But the induced maximum extensive stresses at the sealed end and on the wellbore wall is about 12 MPa. This value is about $\frac{2}{3}$ of the uniaxial tensile strength, 17 MPa, of the Tennessee sandstone shown in Table 6.1. This result is coincident with the Jaeger and Cook's (1979) observation that the rock stiffness begins to decrease at about $\frac{2}{3}$ of the peak strength in uniaxial compression tests (Jaeger and Cook, 1979).

7 Applications: Imaging Asymmetrical Hydraulic Fractures

7.1 Introduction

In Chapter 6, an asymmetrical hydraulic fracture was induced in test Tenn1 due to asymmetrically loaded stress. This simulation result has significant meaning to the reservoir stimulation. In oil and gas reservoirs, natural fractures of different scales are widely distributed. These fractures induce stress concentrations. When hydraulic fracturing treatments are conducted in these locations, the artificially generated fractures would asymmetrically initiate and propagate towards the concentrations of high compressive stresses: they would be "attracted" by the natural fractures.

In fact, asymmetrical hydraulic fractures have been widely observed in both laboratory tests and in the field. Using some field results from the U.S. DOE's Nevada test site, Warpinski (1985) observed marked asymmetry in the induced hydraulic fractures. Mineback examination showed that tortuous fractures, multiple fracture strands, roughness and even sharp turns (corners) were common along hydraulic fracture paths. Due to these factors, the fracture pressure profile decreased along the fracture length much faster than models predicted; which means the fracture length is often over-estimated.

Jeffrey et al. (1995) also discovered asymmetrical fractures during mineback operations. He noticed that the elastic model could not be used to match the predicted treatment pressure, fracture dimensions, and propped dimensions.

Using net fracture pressure analyses, tiltmeter fracture mapping, hydraulic impedance testing, post-fracture production logging and video logging, Wright et al. (1997) demonstrated that the hydraulic fractures in horizontal wells drilled in Californian diatomite were very complex and far from the predicted symmetrical geometry.

The field results illustrate that the natural situation is much more complex than the simple rule-of-thumb. Factors which may affect the development of asymmetry in the natural setting include stress heterogeneity (in both magnitude and orientation), rock property variations (lithologic heterogeneity) and rock layering (lithologic anisotropy). During an examination of mineback operations in tuff, Warpinski et al. (1982) pointed out that variations in in-situ stresses presented the dominant influence on hydraulic fracture containment, a well-known and accepted statement.

Asymmetrical hydraulic fractures have also been reported in laboratory experiments. Abass et al. (1992) observed three categories of non-planar fractures: namely, multiple parallel fractures, T-shaped fractures, and reoriented fractures, in horizontal wells. Part of these observations have been numerically simulated by Vandamme and Jeffrey (1986) and by Olson (1995).

However, in all these field and laboratory observations, only the final results of the asymmetrically developed hydraulic fractures were obtained. No knowledge about the dynamic process of the initiation and propagation of the hydraulic fractures was available. Obviously, such a knowledge would be highly valuable to better understanding the complex process of the hydraulic fracturing, and thus improving the treatment efficiency.

In Chapter 3, a computer program, LOCATION, was developed for simplex-based microseismic location. This program provides a means for revealing the dynamic process of hydraulic fracturing growth by locating the microseismic events. In this chapter, the initiation and propagation of asymmetrical hydraulic fractures in three different materials: namely, an artificial rock (cement-type), Tennessee

sandstone and Jackfork sandstone, will be analyzed with the images depicted by the locations of detectable microseismic events.

7.2 Case 1: Asymmetrical Hydraulic Fractures in An Artificial Rock

7.2.1 Sample Preparation

7.2.1.1 Fabrication of the Artificial Rock

This artificial rock is a cement-type block having the following characteristics (Ong, 1994): API Class H cement, silicon flour, water, defoamer, and dispersant were mixed thoroughly for 30 minutes according to the weight ratio of 100 : 39 : 43.2 : 0.1 : 0.1. This would give a 17.2 ppg slurry and a yield of 1.27 ft^3/sk. The steel mold has an 18-in cubic volume. So three sacks of cement were used for each block. Silicone flour and other components were added accordingly.

The slurry was then poured into the pre-set steel mold. Grease was sprayed onto the surface of the mold before the slurry was poured in. An electrical vibrator was used to shake the slurry in the mold for 30 minutes so as to make the slurry fill all the space of the mold homogeneously driving out most air bubbles. After initial setting for one to two days in room temperature inside the steel mold in a 100% humidity environment under a steel cover, the cement block was unmolded and immersed into a water tank to mature for 28 days. This was done to avoid as many thermally induced microcracks as possible.

Table 7.1 shows the typical mechanical and petrophysical properties of the cement block prepared this way (Ong, 1994).

7.2.1.2 Wellbore Preparation

The matured cement block was then surface ground to a final size of 16.5 *in* $\times$16.5 *in* $\times$ 17 *in*. The coordinate system OXYZ, originated from the center on

Table 7.1: Petrophysical properties of the artificial rock

Properties	Value	Standard deviation
Porosity, %	22.0	1.5
Nitrogen Permeability, mD	0.064	0.037
Young's modulus, 10^6 psi	2.53	0.36
Poisson's ratio	0.14	0.03
Uniaxial tensile strength, psi	473	59
Uniaxial compressive strength, psi	9564	692
Cohesion, psi	1600	
Angle of internal friction, degree	49.7	
Mode-I fracture toughness, psi$\sqrt{\text{in}}$	633.8	76.6

the 16.5 *in* ×16.5 *in* surface, with OX and OY parallel to the two sides of the surface, and OZ in the 17 *in*-direction. A 1 *in* diameter borehole was then drilled along the OZ-axis through the center of the surface of 16.5 *in* ×16.5 *in*. After that, the sample was air dried for one week. Then two rubber packers were installed into the borehole using a special tool so as to apply suitable torque onto the nut of the packers. By expanding the packers against the wellbore wall at two pre-determined positions, a 2 *in*-section of 2 *in* length was sealed off at the central portion of the borehole.

Attached through with each packer was a 3 *ft* long high pressure tubing. These tubings have an OD of $\frac{1}{8}$ *in* and wall thickness of 0.035 *in*. One tubing would later serve as the inlet conduit to flow the hydraulic fracturing fluid into the borehole. The other would be closed after the system was filled with hydraulic fracturing fluid and the air in the borehole was driven out before pressurization.

The remaining portion of the borehole, beyond the sealed-off section, was filled with epoxy made up of Dow Chemical DER 333 resin (S.G. = 1.16), DEH 26 (TEPA) hardener (S.G.= 0.993), and silica flour. The ratios of resin, silica flour and hardener was 100 : 135 : 12 by weight respectively. The silica flour was mixed with the resin at first. Then the hardener was added and mixed thoroughly[1].

[1]Special measures must be applied in preparing the epoxy and disposing the remainings of the resin and the hardener due to their harmful influences on human skin and on the environments.

Table 7.2: Velocities in the block

Direction	P-wave velocity, ft/s
X	12.155
Y	12.290
Z	12.201

Due to the high viscosity, the epoxy must slowly and continuously flow into the borehole so as to let the air bubbles escape; because voids in the epoxy and along the wellbore wall would indeed influence the stress distribution and the transmission of the microseismic waves. Finally, the tubing was held at the center of the borehole. The epoxy was left setting for 24 hours. Then the block was turned over and the process was repeated. The epoxy-filled borehole was left hardening for one week at room temperature.

P-wave seismic velocities of the sample were then measured using a pair of in-house made P-wave sensors. P-wave velocities were obtained respectively in each direction, as shown in Table 7.2. This seismic velocity information indicated that the cement block was close to be homogeneous and could, therefore, be used later for the microseismic location experiment.

The final step in sample preparation was to install the microseismic sensors. The sensors were installed onto the surfaces of the block at pre-determined locations where the signals would be strong from potential microseismic sources. Determination of the sensor position was based on the simulation of the first motion using the WAVEFORM program developed in Chapter 4. Due to the possibilities of operational damage and environmental noises, extra sensors were normally required in the preparation. In this test, 12 microseismic sensors[2] with a nominal frequency of 600 kHz and a diameter of about 0.5 *in* total were prepared onto five different surfaces of the block, 8 of them were finally used[3]. Because the sensors were adhered onto the sample surfaces using conductive glue, a one week long hardening

[2]These microseismic sensors were custom-made in the Halliburton Rock Mechanics Laboratory at The University of Oklahoma by Dr. Thurman E. Scott, Jr.

[3]The Spartan-8000 acoustic emission system has 8-channels. The extra sensors were used for redundancy purposes.

Table 7.3: Sensor coordinates on the cement block

Sensor	X, in	Y, in	Z, in	Sensor	X, in	Y, in	Z, in
1	5	3	17	5	4	-8.25	12
2	4	8.25	6	6	8.25	-3	12
3	2	8.25	12	7	8.25	3	6
4	2	-8.25	6	8	-8.25	4.5	15

was required for the best coupling and detecting effect. The sensors coordinates are shown in Table 7.3.

7.2.2 Procedures of the HF Experiment

The block was placed in an MTS 315 load frame with the borehole in the horizontal direction, as shown in Figure 7.1. The tubing was then connected to a pump in one direction and to a valve in the other direction.



Figure 7.1: Cement sample in the MTS load frame.

A uniaxial load of $1,000\ lbf$ was applied in the vertical direction, perpendicular to the borehole. Two aluminum platens of different sizes, a $4\ in$ diameter circular platen and a $16\ in \times 12\ in$ rectangular platen, were placed on the top and at

the bottom of the block. This resulted in a stress of 80 *psi* on the top and 5 psi at the bottom. This load was maintained constant for the duration of the experiment. Figure 7.2 schematically shows the load, loading platens, the stresses and the borehole structure.

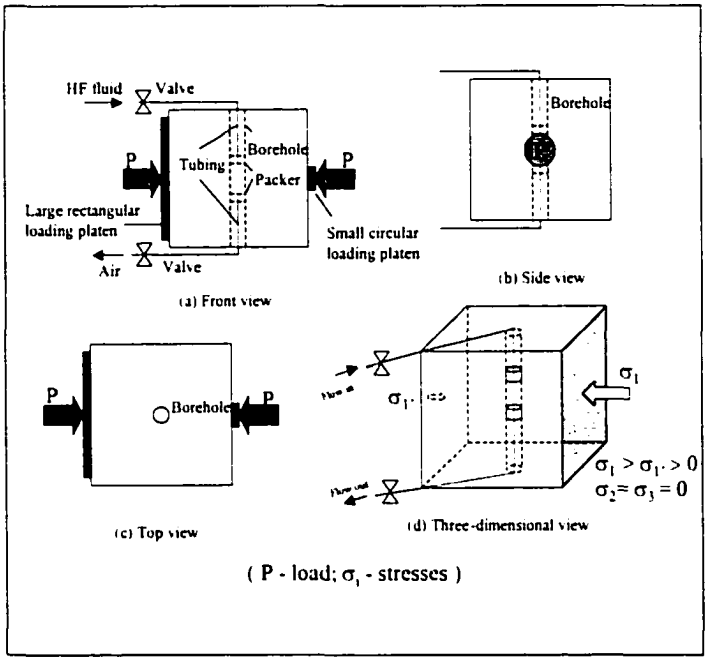


Figure 7.2: Structure of the cement block (Scott, Zeng and Roegiers, 2000).

Silicone oil with a viscosity of 1 *cp* was used as the hydraulic fracturing fluid and was pumped from a servo-controlled intensifier into the borehole. After the air in the sealed-off section was driven out of the borehole through the tubing, the outlet valve was closed; and pumping was continued at a pumping rate of about 0.1 cc/min until the block was fractured. The pumping rate was adjusted during the pressurization so that the induced microseismic activities would not be missed by the microseismic data acquisition system.

7.2.3 Microseismic Data Acquisition and Processing

The pumping process was monitored by an eight channel Physical Acoustic Corporation (PAC) Spartan-8000 system, as mentioned in Chapter 3. The 8 microseismic sensors were connected to the eight channels of PAC system. After the application of the uniaxial load and the filling of the sealed-off section, the PAC system was restarted and re-set to the lowest possible thresholds that would not accidentally trigger the system by inherent environmental noises. In this test, the thresholds of all 8 channels were set to 28 dB. This PAC system has an audio speaker and led indicators for the activity of induced microseismic events. By listening to the speaker and watching the blinking of the led lights, the pumping rate would be modified (reduced) by 0.02 cc/min when the microseismic events were occurring at an excessive rate. Figure 7.3 shows the microseismic monitoring and recording systems during experiment.

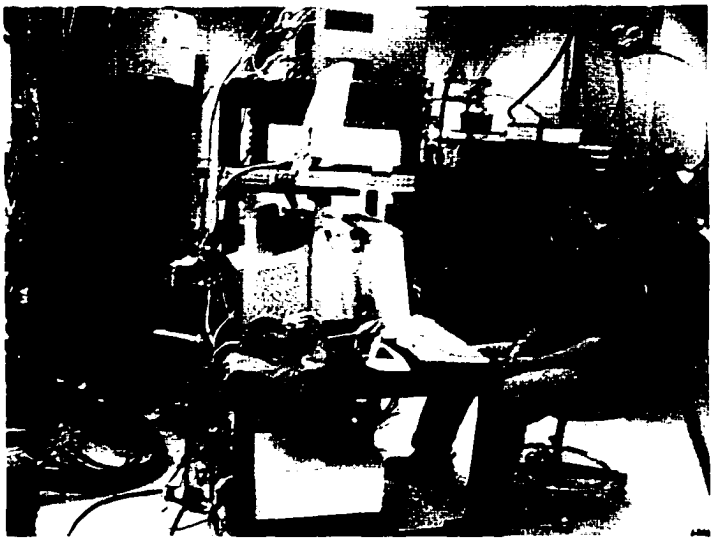


Figure 7.3: Monitoring the microseismic activities during the pressurization.

The recorded microseismic data were processed using the simplex-based LOCATION program developed in Chapter 3. The location coordinates of each locatable microseismic event were determined with an accuracy of ± 5 mm which was the

maximum dimension of the final simplex in the iteration, as described in Chapter 3. These locations traced the evolution of the hydraulic fracture with time. Altogether, 105 events were used in imaging the growth of the hydraulic fracture.

7.2.4 Images of the Asymmetrical Hydraulic Fractures

The location results obtained from the previous subsection indicated that the growth of the asymmetrical hydraulic fracture was confined to a plane including the borehole. However, one wing was strongly developed in the initial stages and propagated towards one side of the block where higher stresses were applied, as shown in Figure 7.4[1]. In this figure, the borehole, with two packers inside it, was vertical along the Z-axis. The load was applied along the Y-axis, with the higher stress in the +Y-side.

In order to reveal more details of the hydraulic fracturing process, plan view images of the located microseismic events were plotted. Figure 7.5 shows the first 47 microseismic events. From Figure 7.5 (a) and (c), it seems that the major fracture did not initiate from the borehole wall, but about half inch out of the wall. (One possibility for this is that the microseismic events corresponding to the well-wall fracture initiation were too weak to be detected. Another possible reason for this is that these events are not locatable under the specific criteria used in this location operation.) They also show that the fracture did not propagate symmetrically in the YZ-plane (also refer to Figure 7.4). In fact, this wing of the fracture had a cusp-shaped geometry, pointing toward the higher stressed location. In Figure 7.5 (b) and (c), a small near borehole reorientation was observed. The less dense of microseismic events near the borehole might represent a poor connection between the far field fracture and the borehole. This would significantly discount the performance of the treatment if it occurred in the field.

[1]The microseismic images in this figure and Figures 7.5, 7.6, 7.8, 7.17, 7.18 and 7.19 were made utilizing 2-D, 3-D, and 4-D acoustic emission imaging programs written by Dr. Thurman E. Scott, Jr. The X, Y, Z and time coordinate data were calculated using the LOCATION software developed by the author.

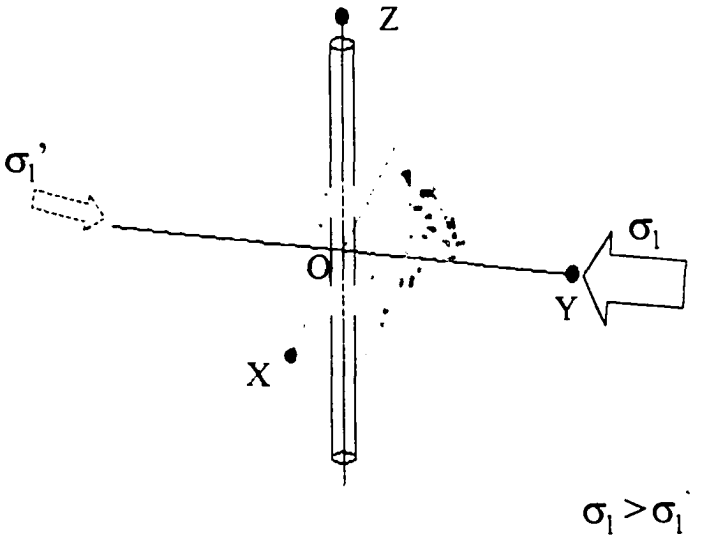


Figure 7.4: A 3D image of the asymmetrical hydraulic fracture in the cement block.

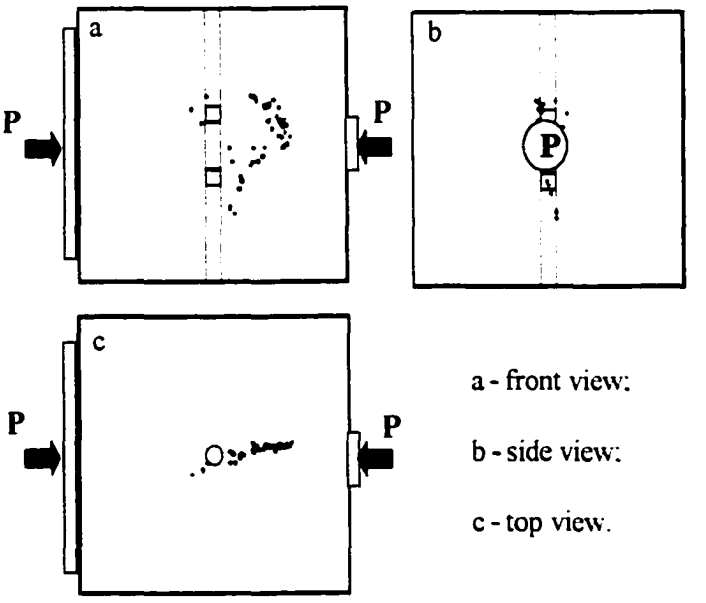


Figure 7.5: Image of the first 47 locatable events (Scott, Zeng and Roegiers, 2000).

In the later stages, growth on this dominant wing was apparently arrested and a much smaller fracture propagated in the opposite direction, as shown in Figure 7.6. This smaller wing was oriented slightly out of the central plane of the block, as seen in Figure 7.6 (c).

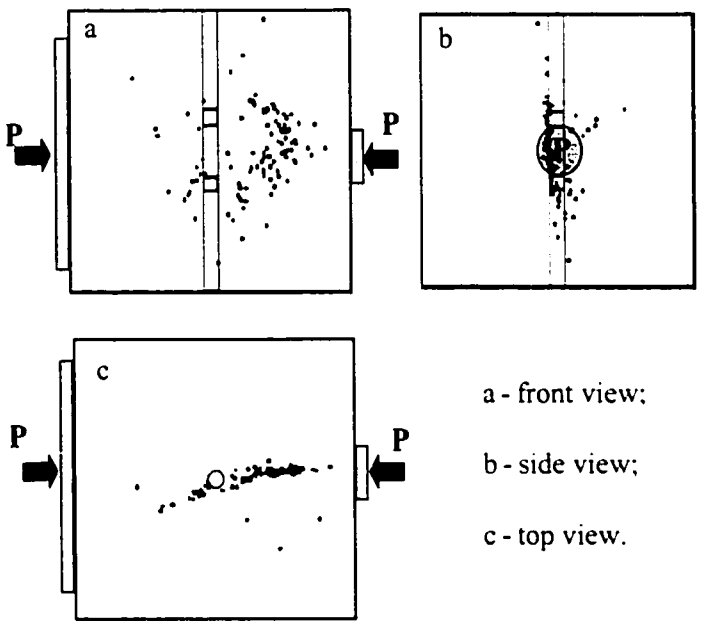


Figure 7.6: Final stage images (Scott, Zeng and Roegiers, 2000).

From the above analysis, it can be seen that the application of microseismic imaging technology can reveal some of the details over the initiation and propagation of hydraulic fractures which might be significant to the field treatment in evaluating the treatment efficiency or explaining the reason for poor stimulation treatment performance.

While the cement block test has the advantage of easy to control the material properties and the desired sample size, it is only an artificial rock; so some of its asymmetrical hydraulic fracturing behavior might not represent what would happen in real rocks such as tight gas sandstones. In the next two sections, two case studies will be carried out on real rocks: Tennessee sandstone (in Case 2) and

Jackfork sandstone (in Case 3).

7.3 Case 2: Asymmetrical Hydraulic Fractures in Tennessee Sandstone

7.3.1 Brief Introduction to the HF Experiment

This section analyzes the characteristics of initiation and propagation of an asymmetrical fracture in Tenn1 introduced in Chapter 6. Based on the experimental observation, this fracture is schematically shown in Figure 7.7. The mechanical behavior of test Tenn1 has been numerically simulated in Chapter 6. The dynamic process of the initiation and propagation of this fracture will be investigated by analyzing the images portrayed with the locations of microseismic events. First the microseismic data acquisition and processing will be introduced.

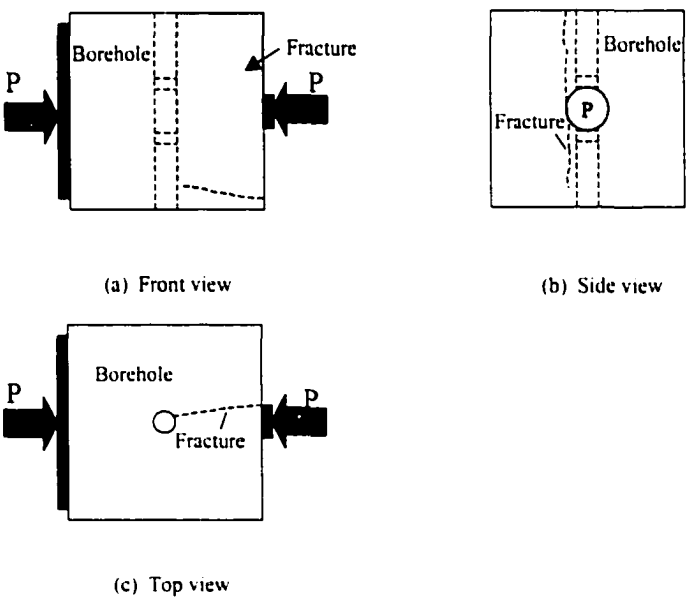


Figure 7.7: Induced fracture in Tenn1 (Scott, Zeng and Roegiers, 2000).

Table 7.4: Sensor coordinates on Tenn1

Sensor	X. mm	Y. mm	Z. mm	Sensor	X. mm	Y. mm	Z. mm
1	80	40	40	11	-45	-80	29
2	80	60	-65	12	45	-80	-42
3	80	-34	-35	13	-12	-80	-58
4	80	–50	50	14	-8	-80	-14
5	-80	58	-58	15	-46	-80	38
6	-38	80	40	16	48	55	80
7	-38	80	0	17	54	-48	80
8	-36	80	-42	18	-53	33	80
9	40	80	-39	19	-43	50	-80
10	43	80	38	20	57	-48	-80

7.3.2 Microseismic Observation and Data Reduction

The microseismic data in this test were recorded by the 20-channel PAC MISTRAS system introduced in Chapter 3. Twenty-four microseismic sensors similar to those used in the previous case, except these were 1.0 cm in diameter, were installed, as partly shown in Figure 6.4 (a) in Chapter 6. Twenty of them were used to connect to the PAC MISTRAS system, four extra ones were for redundancy. In the coordinate system shown in Chapter 6, the sensor coordinates are shown in Table 7.4.

The PAC MISTRAS system was operated in a similar way as the PAC Spartan-8000 system used in the previous test. The LOCATION program was used to process the microseismic data. Coordinates of the sources of microseismic events were determined, similar to Case 1.

7.3.3 The Asymmetrical Hydraulic Fracture Images

Using these source locations, development of the hydraulic fracture was imaged. Figure 7.8 shows the plan view of the fracture images. From these images, it can be seen that the fracture initiated from the borehole. In contrast to the images in the cement block in Case 1, more microseismic events were located in the near borehole region in this test. This is extremely clear and shown in the top view (Figure 7.8

(c)). By comparing this result to the picture of the cross-section shown in Figure 6.4 (b), the densely concentrated microseismic events were found to be corresponding to fluid leakoff around the borehole. Recalling that tensile stress concentration at the borehole wall was the reason for the initiation of the asymmetrical longitudinal fractures, as pointed out in Chapter 6, the coincidence of these three factors, i.e., stress distribution, fluid leakoff, and microseismic events, means that they all reflect some aspect of the same hydraulic fracturing initiation process. The physical meaning is that the tensile stress concentration induced microcracks which in turn triggered microseismic tensile events and enhanced the hydraulic fracturing fluid leakoff near the borehole.

In Figures 7.8 (a) and (b), the fracture shows obvious upward propagation. This vertically selective propagation of the fracture along the borehole can also be traced in Figures 7.5 and 7.6.

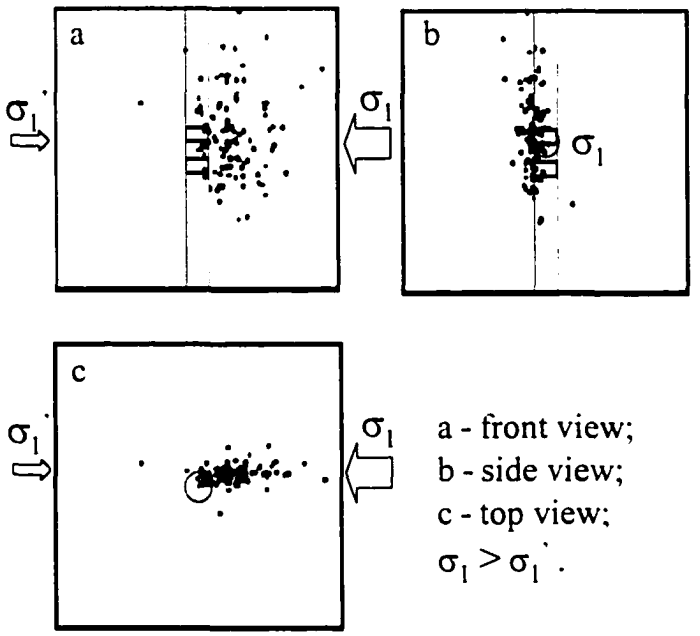


Figure 7.8: Images from microseismic events (Scott, Zeng and Roegiers, 2000).

7.4 Case 3: Asymmetrical Hydraulic Fractures in Jackfork Sandstone

7.4.1 Preparation of the HF Experiment

This hydraulic fracturing experiment was conducted on Jackfork sandstone which was already characterized in Chapter 5. The sample for this test was a rectangular block 182 $mm \times 112\ mm \times 158\ mm$. Preparation of this sample was similar to that of the previous two cases. The half inch diameter borehole was drilled along the Z-axis, as shown in Figure 7.9. Followed the results of numerical simulation from Chapter 6, two half-in long rubber packers were used. A 1-in portion of the central part was sealed-off by the packers.

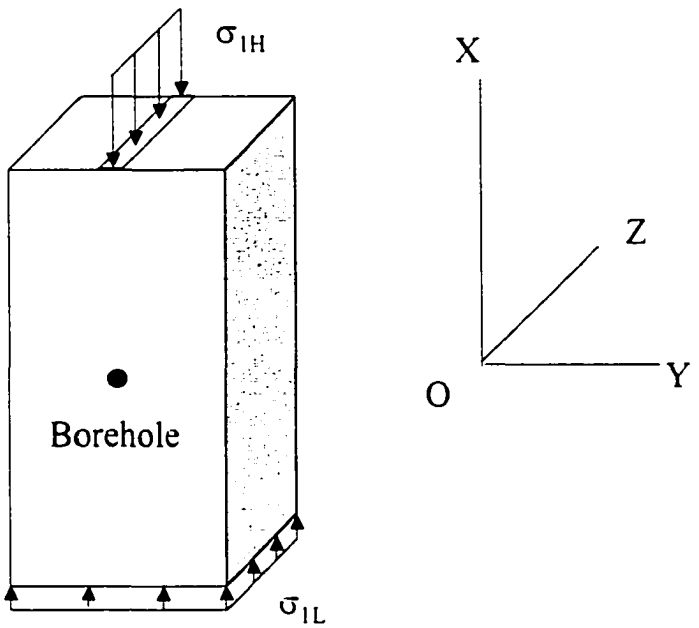


Figure 7.9: Asymmetrical stresses in the Jackfork sandstone block.

This test was conducted using an ENERPAC load frame. A pre-determined uniaxial load was applied to the sample using a hand pump. As shown in Figure 7.10, this hand pump had a needle piston (the blue part) associated with the normal

$3\frac{7}{8}$ *in* piston (the yellow part). The needle piston helped control the uniaxial force to the level of 20 lbf.

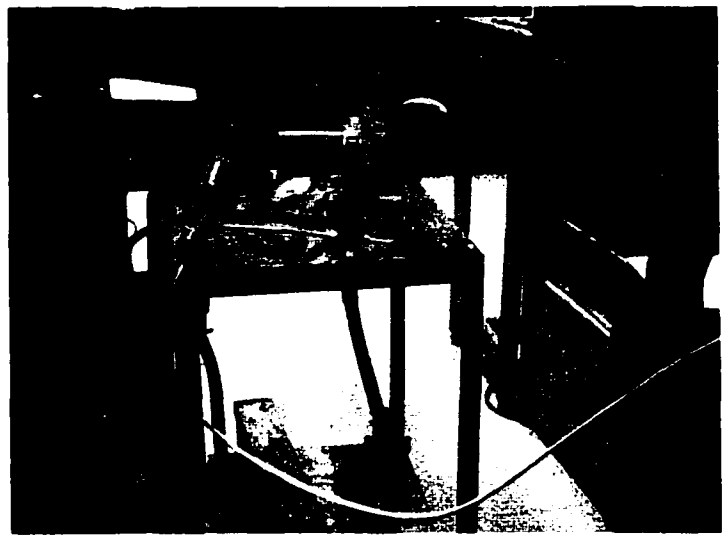


Figure 7.10: The hand pump and the associated needle piston.

In order to induce a large hydraulic fracture, a uniaxial load of 6.665 lbf was applied in the X-direction along which the sample has the largest dimension. Asymmetrical stresses, σ_{1H} and σ_{1L}, were generated by using a narrow steel bar on the top, as shown in Figure 7.9. In this case, the stresses are as follows.

$$\begin{cases} \sigma_{1H} = 1,523 & psi \\ \sigma_{1L} = 250 & psi \end{cases}$$

The hydraulic fracturing pressure was applied using an ISCO Mode 100 SYRINGE pump and was controlled using an ISCO pump controller, as shown in Figure 7.11. The computer recorded and displayed the pumping time, the borehole pressure and the hydraulic fracturing fluid volume in the tank. By measuring the fluid volume at an accuracy of 5×10^{-4} *cc*, this system was capable of controlling the injection rate accurately.



Figure 7.11: The hydraulic fracturing pumping system.

7.4.2 Test Procedures and Observed Results

The test was conducted using the following steps:

Step 1. Synchronize the time on all recording systems by writing down the time of each system at the same instant. Because all data were recorded in time series. this would make the data comparable in future data processing.

Step 2. Trigger 10 pencil break events at one specific location from each of the four free surfaces on the specimen using the WaveformView function of the Vallen system. This step was necessary to make sure that all the microseismic sensors and Vallen channels were properly installed. connected and in working conditions. These microseismic events were recorded as a separate file.

Step 3. Apply the uniaxial load onto the sample. After application of this load. the sample was left undisturbed for stress adjustment for 10 minutes or until the loading induced microseismic activity disappeared.

Step 4. Trigger another 10 pencil break events at each of the same locations as in Step 2 and store the data in another file. Then the sample was kept for another ten minutes. This step was to check if the systems were still in proper conditions

after applying the uniaxial stresses.

Step 5. Fill the tubings and the sealed section at 1.0 $cc/min.$ injection rate with hydraulic fracturing fluid until all or most of the air was driven out. Close the valve at the end of the outlet tubing.

Step 6. Turn on all related monitoring and recording systems for pressure and microseismic data. Start pumping the hydraulic fracturing fluid into the borehole at the pre-selected rate of 0.05 $cc/min.$ Figure 7.12 shows part of the monitor and recording systems during this experiment. The pressurization continued until the sample was broken, indicated by the burst of microseismic activities and the sudden decrease of the borehole pressure. Figure 7.13 shows the pressure vs. time curve for this test.



Figure 7.12: Microseismic monitoring and recording systems.

Step 7. Unload the sample. Stop the pump at first; then release the uniaxial load. Finally, the hydraulic fracturing fluid in the tubings was bled off through the outlet valve.

Step 8. Dissect the sample by cutting it into two pieces to check the induced

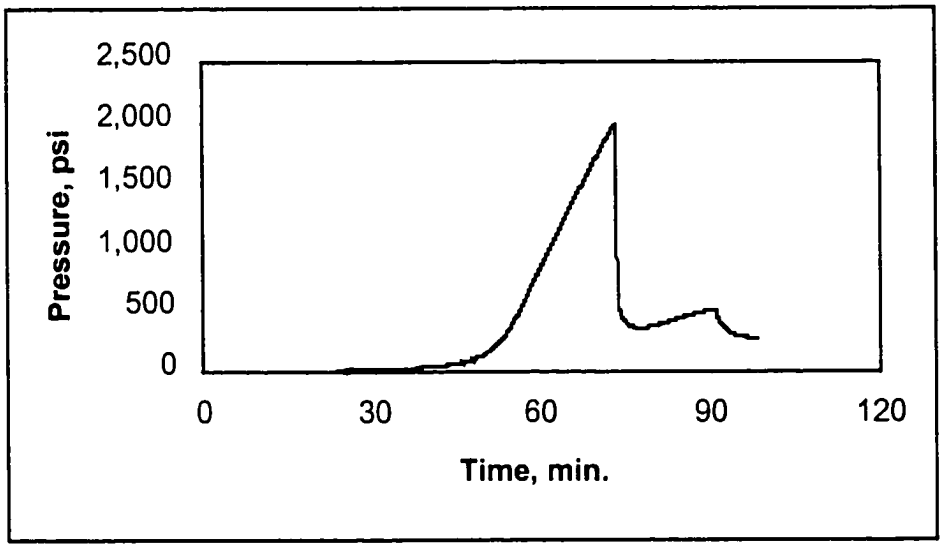


Figure 7.13: Borehole pressure vs. pumping time.

hydraulic fracture geometry, as shown in Figure 7.14[5].

7.4.3 Microseismic Data Acquisition

Twenty YD-8 commercial acceleration sensors, manufactured by Beijing Vibration Measurement Instrument Company (BVMIC), were installed on the surfaces of the sample, as shown in Figure 7.15 (also shown in this figure is the ENERPAC load frame). These sensors were designed to work with a central compression structure, as shown in Figure 7.16 (BVMIC, 1992). In this structure, the PZT crystal and the mass piece were isolated from the cover, so the sensor using this structure has a very high resistance to environmental noises. For the sensors used in this test, the sensitivity, i.e., induced electricity under unit acceleration, was $0.15-0.4\ pC/(m/s^2)$ in terms of electrical charge, and $0.4-1.0\ mV/(m/s^2)$ in terms of electrical voltage, which corresponds to a theoretical sensitivity of $1.5\times10^{-3}-3.8\times10^{-3} m/s^2$ in the Vallen Acoustic Emission system, as detailed in the Appendix D. The maximum

[5]The dissected sample in Figure 7.14 was upside down in comparing to the direction in Figure 7.9.

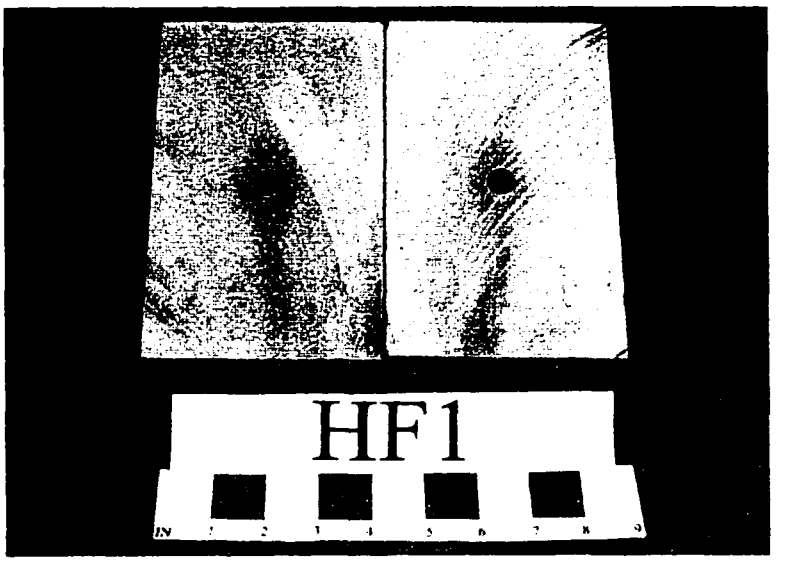


Figure 7.14: The asymmetrical hydraulic fractures in the Jackfork sandstone.

measurable acceleration is $5.000\ m/s^2$. The sensor has a cylindrical body and a hexagon head (9 *mm* in diameter by 9 *mm* in height.) Each sensor weighs about 2.5 *grams*. The working temperature is -40 to $100°C$. The hexagon head has a threaded hole for the installation of the sensor. Using the manufacturer supplied bolt, the sensor can be easily installed and uninstalled onto any surface. In this test, the hexagon head was directly glued onto the sample.

Fifteen of these sensors were finally used to connect to the 15−channel Vallen Acoustic Emission system. Coordinates of these 15 sensors are shown in Table 7.5.

Full waveforms were sampled. The sampling rate was set to 0.1 $\mu s/point$ for all channels. The sample length for each waveform was set to 2048 *points*, which means that the sampling period of time for each channel was 204.8 μs. In order not to miss the low amplitude first motions, a 512-*point* of pre-trigger samples was used, meaning that the recorded data included information generated 51.2 μs earlier. Pool trigger mode, which means once one channel is triggered all other channels will be triggered, was used. Other related parameters were chosen according to manufacturer's default values (Vallen, 1998).

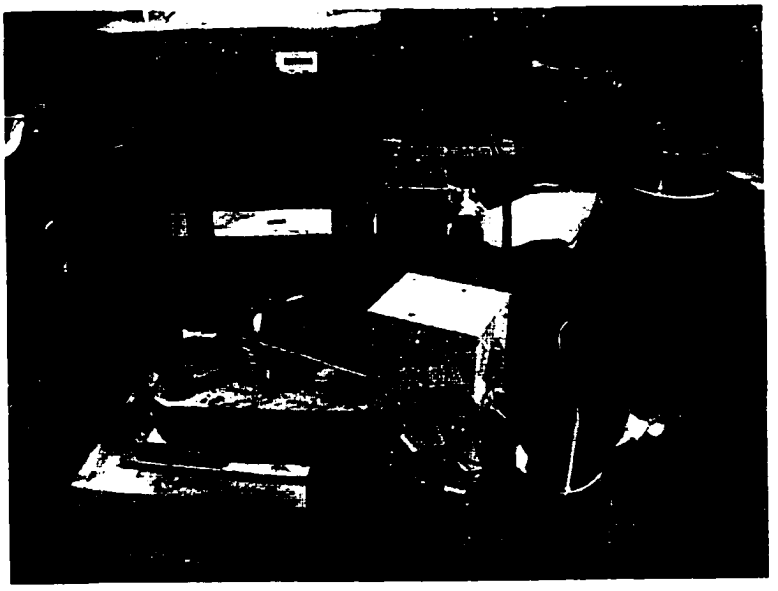
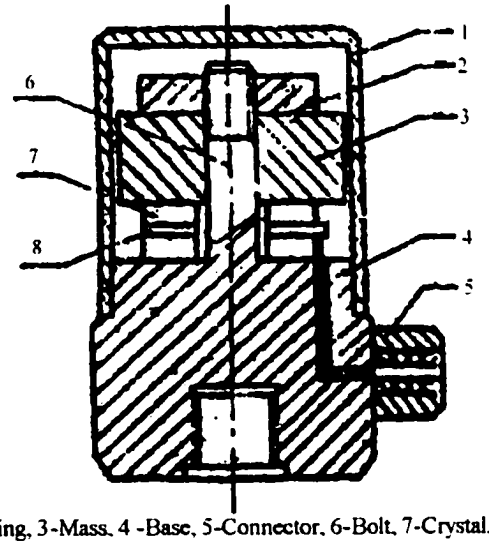


Figure 7.15: The sample and the sensors.



1-Cap, 2-Spring, 3-Mass, 4 -Base, 5-Connector, 6-Bolt, 7-Crystal, 8-Conductor

Figure 7.16: The structure of the YD-8 sensor (from BVMIC, 1992).

Table 7.5: Sensor coordinates on the Jackfork sandstone block

Sensor	X, mm	Y, mm	Z, mm	Sensor	X, mm	Y, mm	Z, mm
1	60	56	0	9	60	0	78
2	0	56	-60	10	-60	0	78
3	-60	56	0	11	60	0	-78
4	0	56	60	12	-60	0	-78
5	60	56	0	13	0	-40	78
6	0	-56	60	14	0	40	78
7	-60	-56	0	15	0	40	-78
8	0	-56	-60				

7.4.4 The Asymmetrical Hydraulic Fracture Images

After the experiment, parameters shown in Table 7.6, were chosen to process the microseismic data using the ArrTime and the LOCATION programs developed in Chapter 3.

Located coordinates, (X_0, Y_0, Z_0), of the microseismic events and the related properties, such as the event identification (MSID), the reference wave set (WaveSet), the event magnitude (Mag.), the diameter of the final simplex (D_{res}), and the time residual (t_{res}) are shown in Tables E.1, E.2 and E.3 in the Appendix E.

From these results, it can be seen that the first microseismic event was located at (-26.8, 19.1, -31.2), far away from the borehole wall. The second microseismic event was located at (2, -10.9, 29.7), much closer to the borehole wall than the first event. The subsequential four events were all located near the borehole. After that, the microseismic events began to scatter away from the borehole, though once in a while there was some event near the borehole wall, possibly due to fracture adjustment.

From the fracture point of view, this process of migration of the microseismic events might indicate that the first two microseismic events were due to the adjustment of local stresses in the far field location. These adjustment triggered the fracture initiation near the wellbore. After the nucleation at the beginning, the fracture started to propagate from the wellbore towards outside. These features

Table 7.6: Prarameters for data process

Parameter	Value
Experiment	HF1
Total channel	15
Max Noise	6
Min Amplitude	66
Min chls for one MS event	6
StartMSID	1
EndMSID	10.000
MaxSpxDia. (D_{res})	10 mm
Max Time Residual (t_{res})	10 μs
MaxIter	200
MaxX	91 mm
MinX	-91 mm
MaxY	56 mm
MinY	-56 mm
MaxZ	79 mm
MinZ	-79 mm

will be further confirmed below by the microseismic images at different stages.

Figure 7.17 shows the images of the first 10 microseismic events. From this figure, it can be seen that there were some microseismic activities in the remote region, but the main events were near the wellbore. These events formed a short fracture in the two opposite directions of the borehole (top view of Figure 7.17). This multiple fracture initiation was consistent with the numerical simulation results introduced in Chapter 6.

In addition, this figure also shows that the initial fracture was about 10°-15° from the principal stress direction.

Figure 7.18 shows the images of the first 20 microseismic events. The microseismic events were more scattered compared to the first 10 events, but the fracture propagated mainly toward the higher-stressed side, the fracture in the opposite direction seemed arrested. This was confirmed by the asymmetrical fractures shown in Figure 7.14.

In Figure 7.19, all the microseismic events are shown. In comparing to the

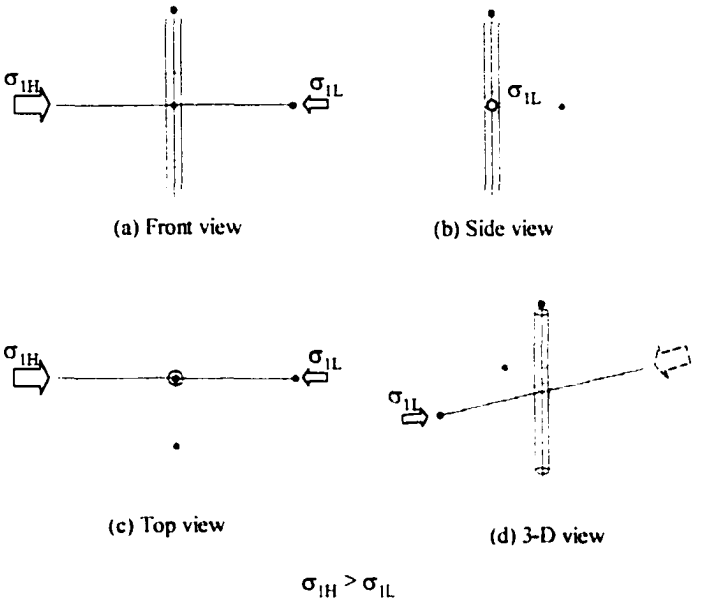


Figure 7.17: Images of the first 10 locatable microseismic events.

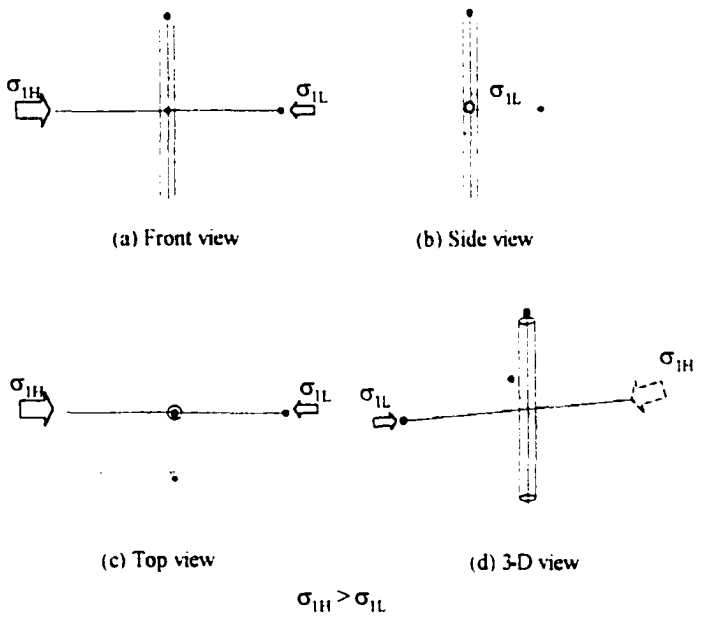


Figure 7.18: Image of the fractures by the first 20 locatable microseismic events.

images of the first 10 and 20 microseismic events, there are two major differences: the fracture has propagated to a larger extent, and the fracture along the stress direction become dominant.

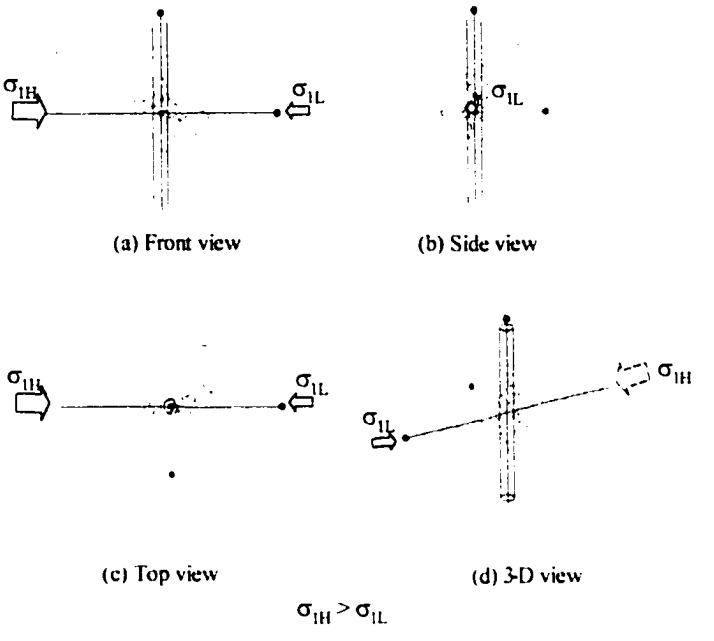


Figure 7.19: Images by all the locatable microseismic events in HF1.

From this case, it is appropriate to say that the starting microseismic events can be far away from the borehole. But the first fracture initiation did start near the borehole. The initial fractures can be multiple, but one will become dominant controlled by the stress field. The direction of the initial fracture can be different from the most favorite stress orientation, but the final fracture will be in the stress-controlled orientation.

7.5 Discussion

From these three cases, it can be seen that the microseismic images can help reveal some information about the dynamic processes of the initiation and propagation of the hydraulic fractures.

In the stress-induced asymmetrical hydraulic fractures introduced above, much more complex aspects of the fracturing process have been demonstrated from these images. In a concise way, the asymmetrical fractures can be characterized as out-borehole initiation, cusp-shaped propagation in the cement block, leakoff dominant initiation, stress-controlled selective propagation in the Tennessee sandstone, and multiple initiation, reoriented propagation in the Jackfork sandstone block.

Obviously, this method can also be applied to other HF experiments.

8 Conclusions and Recommendations

8.1 Conclusions

This dissertation is composed of three parts: problem identification, development of solutions, and verification of solutions through applications. The following conclusions were achieved:

1. A simplex-based algorithm has been derived for locating the coordinates of microseismic events and for eventual imaging the initiation and propagation of hydraulic fractures.

Using this algorithm, a windows-based microseismic event location computer program, LOCATION, has been developed and verified. This simplex-based location algorithm is better than traditional ones in that it is more robust. The algorithm searches the optimized solution in the full space. Using artificial data and third party experimental data, this program has been extensively tested, and verified.

2. A computer program has been developed for automatically searching the first arrival times from the full waveform data.

Based on the fact that the random noise does not vary a lot among neighboring points, a variance-based algorithm has been developed to identify the first arrival time. A computer program, ArrTime, has been created to search the first arrival times using a five-point scanning window. This program was able to find the first arrival time in the full waveform within three points.

3. A forward simulator for first motion of induced waveforms has been developed which can be used to predict the waveform at any observing point from an arbitrary

source.

Using the theory of seismology and the point source assumption, a waveform simulator, WAVEFORM, has been coded. This simulator was created for two purposes: to improve the identification of the first motion in multi-component sensors, and to optimize the distribution of sensors in field and laboratory work. The first purpose was reached by repeatedly comparing the observed first motions and the predicted ones from the estimated sources until the differences were acceptable. The second purpose was achieved by calculating the first motions induced at different observing points induced from expected potential sources. The sensors then should be placed at locations where first motion amplitudes were relatively large.

4. The Jackfork sandstone which has been recently discovered to be a tight gas sandstone has been systematically characterized.

This formation is present in the Ouachita Mountains areas of Oklahoma and Arkansas. Hydraulic fracturing stimulation has been routinely required for economic production and, so far, the treatments have ended with a modest success. No pertinent petrophysical and mechanical properties are available yet; hence the systematic, experimental investigation reported in this dissertation filled this gap. This Jackfork sandstone was also selected as one of the candidate rocks for the application of the developed computer programs.

5. An explicitly expressed formula for the calculation of Mode-I fracture toughness from the CDISK method has been derived.

A new coefficient has been added to the old formula. This upgraded method now allows the measurements of fracture toughness from small core samples in any orientation.

6. The packer influence on hydraulic fracture initiation has been investigated using a three-dimensional, non-linear numerical simulator.

The influence of local stress field on the initiation and propagation of hydraulic fractures has been well demonstrated through a case study. Using a commercially available numerical simulator, ABAQUS, the generation of longitudinal vs. trans-

verse fractures under similar conditions has been analyzed. The study showed that the difference in packer lengths was the reason for the different induced orientations.

7. The initiation and propagation of some asymmetric hydraulic fractures have been successfully imaged.

Based on the investigation results mentioned above, three hydraulic fracturing experiments were conducted to investigate the initiation and propagation of stress-induced asymmetrical fractures in an artificial rock, a typical tight sandstone and a real tight gas sandstone. Using the microseismic image programs, time-step propagation images have been generated. Through analyzing these images, the dynamic process of the initiation and propagation of the fractures have been revealed. These laboratory results showed that the real hydraulic fracturing process is much more complicated than that predicted by the simple, static propagation model.

8.2 Recommendations

In order to further improve the hydraulic fracturing diagnostic technology, the following recommendations are made:

1. Modify the computer program for field applications.

The LOCATION software could be readily applied to the field with some minor modifications. Due to the use of multiple component sensors in the field, the WAVEFORM simulator would be of great value. This same technique could also be applied to monitor such activities as water-flooding, hot steam injections, and waste slurry reinjection.

2. Expand the capabilities to include reservoir production monitoring.

This technique could also be applied to extract information about changes in pore pressures by identifying production-induced microseismic events and the related fracturing kinetics such as the effective stress status. From the production point of view, this would help optimize the overall field development plan so as to avoid such things as uneven compaction, fault re-activation, and casing damage.

3. Carry out additional experiments on large rock samples.

From the three experimental case studies, it can be seen that large samples gave better images of the induced hydraulic fractures. In addition, real rocks give more realistic information about the hydraulic fracturing behavior than artificial rocks do.

4. Integrate all programs.

The current computer programs have been developed to work independently of each other, each addressing a different task. It would be more efficient to integrate these programs by combining all the isolated components.

5. Combine passive and active microseismic monitoring.

So far, all the investigations have been based on passive microseismic information, that is, the microseismic data generated by the initiation and propagation of hydraulic fractures. It would be also possible to use active microseismic data, in which the microseismic waves are triggered from known artificial sources, to image the hydraulic fractures (de Pater et al., 2001).

6. Apply three-dimensional stresses and pore pressure.

So far, all the experiments have been conducted under 1-D stress conditions. In reality, all hydraulic fracturing treatments are carried out under three-dimensional stress fields with the participation of pore pressure. Ideally, there would be no problem for conducting hydraulic fracturing experiments under such conditions. But there are difficulties to conduct the microseismic monitoring in this situation, because there is no free surface for placing the microseismic sensors. Currently, some researchers have tried to stick the sensors on edges which have been intensionally cut at 45°. But simulation results from the WAVEFORM simulator would point out that these locations are the least favorable places due to the small signal amplitudes. A better method would be to install the sensors inside the sample, similar to an underground earthquake observer. This could be achieved by drilling shallow observation holes. According to the Saint Venant's principle (Timoshenko and Goodier, 1970), there should only be minor influences on the observed results

as long as the sensors are small enough in comparing to the observed domain.

7. Consider poroelasticity.

The pore pressure effects on the transmission of the waveforms have not been considered in this dissertation. This poro-dynamic effect deserves further investigations. Poro-mechanics terms could be added to the general equations in developing the general solutions. This would lead to the necessity of using numerical means to obtain the solutions (Cheng and Detournay, 1993).

8. Moment tensor inversion.

As mentioned above, the microseismic method could be used to monitor the reservoir production, as long as the kinetics of the induced microseismic events could be identified. This requires the application of the moment tensor inversion. It is the reverse process of the waveform simulation. By the inversion of the observed microseismic waveforms, the moment tensor of the microseismic event could be calculated. This moment tensor, similar to the stress tensor, could be further decomposed and thus define the kinetic features of the microseismic events. According to these kinetic features, the associated stress field would thus be inferred. Based on the change of this dynamic stress field, the change of the pore pressure in the reservoir could be extracted.

9. Fractal dimension.

The non-planar nature of hydraulic fractures are extensively documented. The distribution of the microseismic events has also confirmed this. But so far, all the descriptions were qualitative. How to quantify this non-planar property could have significant meaning for the characterization of hydraulic fracturing, and further relate to the petrophysical properties of the hydraulic fracturing performance. Using the concept of fractal dimension (Xie, 1993), the problem could probably be tackled.

Nomenclature

a	= radius of the disk-shaped microfracture
	= half length of the crack in the CDISK sample
a_0	= half length of the initial crack in the CDISK sample
a_1	= the surface kerf length
$a_{1,2,3}$	= accelerations in direction-1, -2, and -3
a_{min_true}	= sensor sensitivity, minimum measurable acceleration
A_f	= fracture area
b	= crack front width in CDISK sample
B	= disk thickness in CDISK sample
$[c]$	= transformation matrix of coordiante systems
c_{ijkl}	= material elastic constants
C	= material compliance
C'	= dimensionless compliance
C_0	= uniaxial compressive strength
C_L	= leakoff coefficient
da	= crack extension increment
du	= displacement increment,
dT_J	= travel time from source (X_0,Y_0,Z_0) to sensor (X_J,Y_J,Z_J)
D	= sample size
D_e	= equivalent diameter
D_J	= distance from source (X_0,Y_0,Z_0) to sensor (X_J,Y_J,Z_J)
D_{res}	= residual of the location

E = Young's modulus

E' = Young's modulus for plane strain conditions

f = body force

$\mathbf{f}_1$, $\mathbf{f}_2$ = body forces

$\mathbf{f}(\mathbf{x}, t)$ = general pulse function

F^+, F^- = the two adjacent internal surfaces of a microfracture

g_i = a unidirectional unit impulse

G_I = fracture energy release rate

G_{IC} = critical fracture energy release rate

G_{kn} = Green's function

$G_{x,p,q}$ = spatial derivative of Green's function

G^{free} = Green's function on a free surface

G^{rigid} = Green's function on a rigid surface

h_f = fracture height;

H = depth

$H(t)$ = Heaviside unit step function

i = $\sqrt{-1}$, sign for imaginary number or variable

I_s = initial index of point load test

$I_{s(50)}$ = standardized index of point load test

k = permeability

K_I = stress intensity factor of Mode-I fracture

K_{IC} = Mode-I fracture toughnessghness

$K_{IC_\alpha_0}$ = α_0-based Mode-I fracture toughness

K_{JC} = fracture toughness ($J = I, II, III$)

(l_J, m_J, n_J) = direction cosines from $(X_0.Y_0.Z_0)$ to $(X_J.Y_J.Z_J)$

L = fracture half-length

= sample size

m_{pq} = moment density

n, $\mathbf{n}$ = normal to a surface

n_j = normal to a microfracture ($j = 1, 2, 3$)

N = number of sensors

p, P = pore pressure

p = dummy variable for the calculation of Green's function

p_2 = dummy variable for the calculation of Green's function

p_b = breakdown pressure

$p_{b,lower}$ = lower bound of breakdown pressure

$p_{b,upper}$ = upper bound of the breakdown pressure

p_{net}, $p_{net,w}$ = net pressure

$p_{net}(x,t)$ = net pressure function

p_w = wellbore pressure

q = dummy variable for the calculation of Green's function

q_f = the fracture volume generation rate

q_i = total fluid injection rate

q_L = the leakoff rate

r = radial distance from the borehole

= radial coordinate system variable

r_w = radius of the wellbore

R = radius of the circular fracture

= radius of the CDISK sample

R_s = saw radius for preparing the CDISK sample

$s(\tau)$ = source time function of the fracturing

S = surface of the observed domain

= leakoff-related dummy variable

S_0 = cohesion

S_a = shape factor for point load test

S_p = spurt loss

$S(\mathbf{x_S})$ = internal surface of the microfracture

$S.G.$ = specific gravity

t = time

t_2 = dummy variable for the calculation of Green's function

t_D = dimensionless time

t_{exp} = exposure time of the fracture to the fluid

t_{res} = the time residual for simplex location operation

$[T]$ = differences of tractions on $F^+$and F^-

$\mathbf{T}$ = tractions on the surface

T = absolute value of tensile strength

T_0 = uniaxial tensile strength

= microseismic event occurring time

$T_{ij}(\mathbf{x}.t)$ = traction function on the surface

T_J = microseismic wave arrival time at the sensors-J ($J = 1, 2, ..., N$)

T_J^M = measured arrival time at the sensor-J

T_J^T = theoretical arrival time at sensor-J

T_{res_J} = time residual at sensor-J

T_{res_N} = total time residual in all N sensors

$[u]$ = differences of dislocation on $F^+$and F^-

u, $\mathbf{u}$ = displacement

$\mathbf{u}_1$, $\mathbf{u}_2$ = the two displacement fields induced by $\mathbf{f}_1$and $\mathbf{f}_2$, separately

u_1, u_2, u_3 = components of displacement

$[u_c(\xi)s(\tau)]$ = dislocation distribution on the microfracture

u_c = average dislocation on the microfracture

$u_c(\xi)$ = the dislocation function of the microfracturing source

u_i = displacement boundary conditions

u_L = leakoff velocity

$\mathbf{u}(\mathbf{x}, t)$ = displacement detected by microseismic sensors

$[v_j]$ = dislocation vector ($j = 1, 2, 3$)

V = volume

$V_{1, 2, 3}$ = wave velocity components

V_b	= bulk volume
V_g	= grain volume
V_J	= wave velocity from (X_0, Y_0, Z_0) *to sensor* (X_J, Y_J, Z_J)
V_{min}	= minimum measurable change of voltage
V_{min_true}	= true minimum measurable change of voltage before pre-amplifier
V_p	= pore volume
	= $P-$wave velocity
V_s	= $S-$wave velocity
(V_X, V_Y, V_Z)	= velocity components
$\overline{w}$	= average fracture width.
w_{max}	= maximum fracture width
w_w	= fracture width at the wellbore
$w(x,t)$	= fracture width function
W	= sample weight
	= disk diameter in CDISK test
	= sample size in point load test
x	= fracture length:
(X_0, Y_0, Z_0)	= source coordinates of the microseismic event
$(X_{0I}, Y_{0I}, Z_{0I},$	= initial vertex coordinate in a general simplex
$V_{XI}, V_{YI}, V_{ZI}, T_{0I})$	$(I = 1.2,....8)$
(X_J, Y_J, Z_J)	= microseismic sensor coordinates $(J = 1.2,.....N)$
Y	= stress intensity coefficient
$Y^*_{\alpha_0}$	= α_0-based stress intensity coefficient
(Z_1, Z_2, Z_3)	= transformed coordinate axes
α	= angle from σ_H to borehole projection on (σ_H, σ_h) plane
	= $P-$ wave velocity in deriving Green's function
	= Biot's coefficient of poroelasticity
	= ratio of crack length to the disk radius in CDISK test
α_0	= ratio of initial crack length to the disk radius in CDISK test

β = inclined angle between σ_V and borehole axis

= $S-$wave velocity in deriving Green's function

γ = angle between σ_2 and borehole axis

= dummy variable in deriving Green's function

δ = delta function

ΔU = increased potential energy

ΔW = new crack area

η = an arbitrary point within the observed domain

= dummy variable for poroelasticity

$\eta_{\alpha,\beta}$ = dummy variables for the calculation of Green's function

θ = angle between σ_1 and the normal to the failure plane

= angle around the borehole starting from local $x-$axis

λ = Lamé's elastic constants

μ = Lamé's elastic constants

= fluid viscosity

= coefficient of internal friction

ν = Poisson's ratio.

ξ = an arbitrary point on the microfracture surface

ρ = density

ρ_b = bulk density

ρ_g = grain density

$\rho(h)$ = density at the depth h

σ = normal stress acting on the shear plane

= dummy variable in calculation of Green's function

$\sigma_{1,2,3}$ = principal stresses

σ_{1H}, σ_{1L} = high and low asymmetrical stresses

σ_h = minumum horizontal stress

$\sigma_h^{'}$ = effective minimum horizontal stress

σ_H = maxumum horizontal stress

σ_{rr} = normal stress in the radial direction

σ_v = overburden stress

σ_V = vertical component of far field stresses

$\sigma_x, \sigma_y, \sigma_z$ = normal stresses in local coordinate system

σ_{zz} = local normal stress component in the z-direction

$\sigma_{\theta\theta}$ = local normal stress component in the hoop direction

τ = time

= shear stress

τ_{xy} = shear stress component in the xy-plane

τ_{xz} = shear stress component in the xz-plane

τ_{yz} = shear stress component in the yz-plane

$\tau_{\theta z}$ = local shear stress component

ϕ = porosity

= angle of internal friction

$\Re$ = ratio of the saw radius to sample radius in CDISK test

$\Re e$ = real part of the imaginary variable

$\frac{\partial}{\partial \xi_l} G_{kn}$ = spatial derivatives of the Green's function

∇ $= \frac{\partial}{\partial x_1}\mathbf{x}_1 + \frac{\partial}{\partial x_2}\mathbf{x}_2 + \frac{\partial}{\partial x_3}\mathbf{x}_3$, the del operator

References

[1] Abass, H.H., Hedyati, S. and Meadows, D.L., 1992: "Nonplanar fracture propagation from a horizontal wellbore: experimental study." *paper SPE 24823.*

[2] Abou-Sayed, A.S., Clifton, R.J., Dougherty, R.L. and Morales, R.H., 1984: "Evaluation of the influence of in-situ reservoir conditions on the geometry of hydraulic fractures using a 3D simulator: Part-2 Case studies." *paper SPE 12878.*

[3] Ahmed, U., Strawn, J., Wilson, M. and Schatz, J., 1983: "Effects of stress distribution on hydraulic fracture geometry: a laboratory simulation study in one meter cubic blocs." *paper SPE 11637.*

[4] Aki, K. and Richards, P.G., 1980: *Quantitative Seismology (Vol. 1).* W.H. Freeman and Company, San Francisco, U.S.A.

[5] Albright, J.N. and Pearson, C.F., 1982: "Acoustic emissions as a tool for hydraulic fracturing location: experience at the Fenton Hill Hot Dry Rock Site." *paper SPE 9509.*

[6] Arbenz, J.K., 1989: "Plate 8: Generalized Geological-Structural Map of the Ouachita Mountains and the Arkoma Basin, Oklahoma and Arkansas." *The Geology of North America Volume F-2: The Appalachian-Ouachita Orogen in the United States (*eds. Hatcher, Thomas and Viele*)*, The Geological Society of America, Inc. Boulder, Colorado, USA.

[7] ASNT (American Society for Nondestructive Testing), 1987: *Nondestructive Testing Handbook, Volume 5: Acoustic Emission Testing.* American Society for Nondestructive Testing, Inc., USA.

[8] ASTM (American Society for Nondestructive Testing), 1971: *Materials Research and Standards.* Vol.11 No.3.

[9] ASTM (American Society for Nondestructive Testing), 1994: *Determining the Reproducibility of Acoustic Emission Sensor Response.* ASTM E976.

[10] Atkinson, B.K. and Meredith, P.G., 1987: "Experimental fracture mechanics data for rocks and minerals." *Fracture Mechanics of Rocks (*ed. Atkinson*)*. Academic Press, London, UK. 477-525.

[11] Backus, G., 1970: "A geometrical picture of anisotropic elastic tensors." *Review of Geophysics and Space Physics*, Vol. 8, No.3, 633-671.

[12] Barenblatt, G.I., 1962: "Mathematical theory of equilibrium cracks." *Advances in Applied Mech.*, 7, 56-131.

[13] Batchelor, A.S., Baria, R. and Hearn, K., 1983: "Monitoring the effects of hydraulic stimulation by microseismic event location: a case study." *paper SPE 12109.*

[14] Bell, M. and Kraaijevanger, H., 2000: "Integrated downhole monitoring of hydraulically fractured production well," *paper SPE 65156.*

[15] Bennett, C.O., Rosato, N.D., Reynolds, A.C., Raghavan, R, 1983: "Influence of fracture heterogeneity and wing length on the response of vertically fractured wells." *SPE Journal* (April), 219-230.

[16] Ben-Naceur, K, 1990: "Modeling of Hydraulic Fractures." *Reservoir Stimulation (2nd edition)* (eds. Economides and Nolte), Prentice Hall, New Jersey, USA.

[17] Boone, T.J., Nechtschein, S., Smith, R., Youck, D. and Talebi, S., 1999: "Microseismic monitoring for fracturing in the Colorado Shales above a thermal oil recovery operation," *Proc. 37th U.S. Rock Mech. Symp.(*eds. Amadei, Kranz, Scott and Smeallie*)*, A.A. Balkema, Rotterdam, The Netherlands. 1069-1076.

[18] Boyer, C.M. II, Stubbs, P.B. and Schwerer, F.C., 1986: "Measurement of coalbed properties for hydraulic fracture design and methane production." *paper SPE 15258.*

[19] Bradley, W.B., 1979: "Failure of inclined boreholes." *Trans. ASME*, Vol. 101, 232-239.

[20] Brady, B.H., Ingraffea, A.R. and Morales, R.H., 1993: "Three-dimensional analysis and visualization of the wellbore and the fracturing process in inclined borehole," *paper SPE 25889.*

[21] Bredehoeft, J.D., Wolff, R.G.,Keys, W.S. and Shuter, E., 1976: "Hydraulic fracturing to determine the regional in-situ stress field, Piceance Basin, Colorado," *Bull. Geol. Survey Assoc.*, Vol. .87, 250-258.

[22] Brown, J.E. and Economides, M.J., 1992: "An analysis of hydraulically fractured horizontal wells," *paper SPE 24322.*

[23] Brown, J.E., Thrasher, R.W. and Behrmann, L.A., 2000: "Fracturing operation." *Reservoir Stimulation* (eds. Economides and Nolte), John Wiley & Sons Ltd., New York, USA.

[24] BMAD (Buehler Microstructural Analysis Division), 2001: *Buehler Wafering Blades.* Buehler Microstructural Analysis Division, Illinois, USA.

[25] Bullen, K.E. and Bolt, B.A., 1985: *An Introduction to the Theory of Seismology*, Cambridge University Press, Cambridge, U.K.

[26] Burridge, R. and Knopoff, L., 1964: "Body force equivalents for seismic dislocations," *Bull. Seismol. Soc. Am.*, 54, 1875-1888.

[27] BVMIC (Beijing Vibration Measurement Instrument Company), 1992: *Manual of the YD Series Acceleration Sensors*, Beijing Vibration Measurement Instrument Company, Beijing, China.

[28] Byerlee, J. and Locker, D., 1977: "Acoustic emission during fluid injection into rock," *Proc. of First Conf. on Acoustic Mission / Microseismic Activity in Geologic Structures and Materials*, Trans Tech Publications, Clauthal, Germany, 87-98.

[29] Caceci, M.S. and Cacheris, 1984: "Fitting curves to data," *Byte*, 9, 340-362.

[30] Carter, R.D., 1957: "Derivation of the General Equation for Estimating the Extent of the Fractured Area, Appendix I of Optimum Fluid Characteristics for Fracture Extension (Howard and Fast)," *Drilling and Production Practice*, American Petroleum Institute, New York, USA, 261-269.

[31] Carter, B. J., Ingraffea, A.R. and Heber, G., 2000: "Simulating 3D HF in a parallel computing environment," *Proc. Three Dimensional and Advanced Hydraulic Fracture Modeling (*eds. Jeffrey and McLennan*)*, Seattle, Washington, USA, July 29, 2000.

[32] Cassell, B., Bol, G.M. and Stewart, L., 1990: "Acoustic emission monitoring during hydraulic fracturing," *paper SPE 20970.*

[33] Cheng, A. and Detournay, E., 1993: "Fundamentals of Poroelasticity," *Comprehensive Rock Engineering* Vol. 2 *(*ed. Hudson*)*, Pergamon Press Ltd., Oxford, England, UK.

[34] Chudnovsky, A., Fan, J., Shulkin, Y., Dudley, J.W. Nichols, W.B. and Wong, G.K., 2001: "Hydraulic fracture containment in layered media, experiment and computer simulation," *Proc. 38th U.S. Rock Mech. Symp.* (eds. Ellsworth, Tinucci and Heasley), A.A. Balkema Publishers, Lisse, The Netherlands, 273-279.

[35] Cipolla, C.L. and Wright, C.A., 2000: "State-of-the-art in hydraulic fracture diagnostics," *paper SPE 64434.*

[36] Clark, J.B., 1949: "A hydraulic process for increasing the productivity of wells," *Petrol. Trans. AIME.*, **186,** 1-8.

[37] Core Lab, 1995: *Operation Manual for UltraPore 200A*, Engineering Division, Core Laboratories Instruments, Carrollton, Texas, USA.

[38] Cox, S.J.D. and Meredith, P.G., 1993: "Microcrack formation and material softing in rock measured by monitoring acoustic emissions," *Int. J. Rock Mech. Min. Sci. & Geomech. Abstr.* Vol. 30, No. 1, 11-24.

[39] Daneshy, A.A., 1973: "A study of inclined hydraulic fractures," *SPE Journal.* 61-68.

[40] de Pater, C.J., Groenenboom, J., van, Dam, D.B. and Ranjn, R., 2001: "Active seismic monitoring of hydraulic fractures in laboratory experiments," *Int. J. Rock Mech. & Min. Sci.* Vol. 38, 777-785.

[41] Detournay, E., McLennan, J.D. and Roegiers, J.-C., 1986: "Poroelastic concepts explain some of the hydraulic fracturing mechanisms," *paper SPE 15262.*

[42] Dobkins, T.A., 1981: "Improved methods to determine hydraulic fracture height," *J. Petrol. Tech.* (April), 719-726.

[43] Drouillard, T.F., 1996: "A History of Acoustic Emission," *J. Acoustic Emission*, Vol.14, No. 1, 1-34.

[44] Economides, M.J. and Nolte, K.G. (eds.), 1990: *Reservoir Stimulation (2nd ed.)*, Schlumberger Educational Services, Houston, Texas, USA.

[45] Economides, M.J. and Nolte, K.G. (eds.), 2000: *Reservoir Stimulation (3rd ed.)*, John Wiley & Sons Ltd., Chichester, England, UK.

[46] Emanuele, M.A., Minner, W.A., Weijers, L., Blevens, D.M. and Taylor, B.T.T, 1998: "A case history: Completion and stimulation of horizontal wells with multiple transverse hydraulic fractures in the Lost Hills Diatomite," *paper SPE 39941.*

[47] Evans, R., Gaucher, E., Randall, N., Vuillermoz, C. and Rodriguez, S., 2000: "Borehole seismic: Supplying answers to fractured reservoir questions," *paper SPE 58994.*

[48] Falls, S.D., Young, R.P., Carlson, S.R. and Chow, T., 1992: "Ultrasonic tomography and acoustic emission in hydraulically fractured Lac du Bonnet Grey granite," *J. Geophy. Res.*, Vol. 97, No. B5, 6867-6884.

[49] Farmer, I., 1983: *Engineering Behavior of Rocks*, Chapman and Hall, London, UK.

[50] Fix, J.E., Frantz, J.H. Jr. and Lancaster, D.E., 1991: "Application of microseismic technology in a Devonian shale well in the Appalachian basin," *paper SPE 23425.*

[51] Fraser, C.D. and Pettitt, B.E., 1962: "Results of a field test to determine the type of orientation of a hydraulically induced formation fracture," *J. Petrol. Tech.* (May), 463-466.

[52] Gaucher, E., Cornet, F.H. and Bernard, P., 1998: "Induced seismicity analysis for structure identification and stress field determination," *paper SPE 47324.*

[53] Geertsma, J. and de Klerk, F., 1969: "A rapid method of predicting width and extent of hydraulic induced fractures," *J. Petrol. Tech.* Vol. 21, 1571-1581.

[54] Geertsma, J. and Haafkens, R., 1979: "A comparison of theories for predicting width and extent of vertical and hydraulically induced fractures," *Trans. ASME*, 101, 8-19.

[55] Gibowicz, S.J. and Kijko, A., 1994: *An Introduction to Mining Seismology*, Academic Press, San Diego, California, U.S.A.

[56] Gibowicz, S.J. and Lasoki, S. (eds.), 1997: *Rockburst and Seismicity in Mines, Proc. 4th Int. Symp. Rockbursts and Seismicity in Mines*, A.A. Balkema, Rotterdam, The Netherlands.

[57] Gidley, J.L., Holditch, S.A., Nierode, D.E. and Veatch, R.W. Jr., 1989: *Recent Advances in Hydraulic Fracturing* (SPE Monograph Series), Society of Petroleum Engineers, Richardson, Texas, USA, .

[58] GRI (Gas Research Institute), 1997: *Workshop: Hydraulic Fracture Mechanics—Searching for the Next Breakthrough in Stimulation*, Shell E&P Technology Center, Houston, Texas, USA, September 17-18, 1997.

[59] Gulbis, J. and Hodge, R.M., 2000: "Fracturing Fluid Chemistry and Proppants," *Reservoir Stimulation (3rd ed.)* (eds. Economides and Nolte), John Wiley & Sons Ltd., Chichester, England, UK.

[60] Gulrajani, S.N. and Nolte, K.G., 2000: "Appendix: Background for hydraulic fracturing pressure analysis techniques," *Reservoir Stimulation (3rd ed.)* (eds. Economides and Nolte), John Wiley & Sons Ltd., Chichester, England, UK.

[61] Guo, F., Morgenstern, N.R. and Scott, J.D., 1993a: "An experimental investigation into hydraulic fracture propagation - Part 1. Experimental Facilities," *Int. J. Rock Mech. Min. Sci. & Geomech. Abstr.*, Vol. 30, No. 3, 177-188.

[62] Guo, F., Morgenstern, N.R. and Scott, J.D., 1993b: "An experimental investigation into hydraulic fracture propagation - Part 2. single well tests," *Int. J. Rock Mech. Min. Sci. & Geomech. Abstr.*, Vol. 30, No. 3, 189-202.

[63] Haimson, B. and Fairhurst, C., 1969: "Hydraulic fracturing in porous-permeable materials," *J. Petrol. Tech.*, 811-817.

[64] Haimson, B.C., Roegiers, J.C. and Zoback, M.D.(eds), 1988: *Proc. Second Int. Workshops on Hydraulic Fracturing Stress Measurements (Vol. I and II)*, Minneapolis, Minnesota, USA, June 15-18, 1988.

[65] Haimson, B.C., 1993: "The hydraulic fracturing method of stress measurement: Theory and practice," *Comprehensive Rock Engineering* Vol. 3 (ed. Hudson). Pergamon Press Ltd, Oxford, England. 395-412.

[66] Hallam, S.D. and Last, N.C., 1990: "Geometry of hydraulic fractures from modestly deviated wellbores," *paper SPE 20656.*

[67] Hardy, H.R. Jr., 1977: "Emergency of acoustic emission / microseismic activity as a tool in geomechanics," *Proc. First Conf. on Acoustic Emission / Microseismic Activity in Geologic Structures and Materials*, Trans Tech Publications, Clausthal, Germany. 13-31.

[68] Hardy, H.R. Jr. and Leighton, F.W.(eds.) , 1977: *Acoustic Emission: Proc. First Conf. on Acoustic Emission / Microseismic Activity in Geologic Structures and Materials*, Trans Tech Publications, Clausthal, Germany.

[69] Hardy, H.R. Jr. and Leighton, F.W.(eds.) , 1980: *Acoustic Emission II: Proc. Second Conf. on Acoustic Emission / Microseismic Activity in Geologic Structures and Materials*, Trans Tech Publications, Clausthal, Germany.

[70] Hardy, H.R. Jr. and Leighton, F.W.(eds.) , 1984 *Acoustic Emission III: Proc. Third Conf. on Acoustic Emission / Microseismic Activity in Geologic Structures and Materials*, Trans Tech Publications, Clausthal-Zellerfeld, Germany.

[71] Hardy, H.R. Jr., 1989: *Acoustic Emission IV: Proc. Fourth Conf. on Acoustic Emission / Microseismic Activity in Geologic Structures and Materials*, Trans Tech Publications, Clausthal-Zellerfeld, Germany.

[72] Hardy, H.R. Jr., 1995: *Acoustic Emission V: Proc. Fifth Conf. on Acoustic Emission / Microseismic Activity in Geologic Structures and Materials*, Trans Tech Publications, Clausthal-Zellerfeld, Germany.

[73] Hardy, H.R. Jr., 1998: *Acoustic Emission VI: Proc. Sixth Conf. on Acoustic Emission / Microseismic Activity in Geologic Structures and Materials*, Trans Tech Publications, Clausthal-Zellerfeld, Germany.

[74] Hashida, T. 1993: "Fracture toughness test of core-based specimens by acoustic emission," *Int. J. Rock Mech. Min. Sci. & Geomech. Abstr.*, Vol. 30, No. 1, 61-69.

[75] HKS (Hibbitt, Karlsson and Sorensen), 1998: *ABAQUS/Standard User's Manual (Version 5.8)*, Hibbitt, Karlsson and Sorensen Inc., Pawtucket, Rhode Island, USA.

[76] Holder, J., Kenrick, A.J., Thallak, S. and Gray, K.E., 1993: "Measurements of effective fracture toughness values for hydraulic fracture: dependence on pressure and fluid rheology," *paper SPE 25491.*

[77] Holditch, S., 1989: "Chapter 2 Pretreatment Formation Evaluation," *Recent Advances in Hydraulic Fracturing* (eds. Gidley, Holditch, Nierode and Veatch), Society of Petroleum Engineers, Richardson, Texas, USA.

[78] Hopkins, C.W., Rosen, R.L. and Hill, D.G., 1998: "Characterization of an induced hydraulic fracture completion in an naturally fractured Antrim shale reservoir," *paper SPE 51068.*

[79] Howard, G.C. and Fast, C.R., 1970: *Hydraulic Fracturing*, SPE Monograph Series, Society of Petroleum Engineers, Richardson, Texas, USA.

[80] Hsu, N.N., Simmons, J.A. and Hardy, S.C., 1977: "An approach to acoustic emission signal analysis—theory and experiment," *Material Evaluation*, October 1977, pp.100-106.

[81] Hubbert, M.K. and Willis, D.G., 1957: "Mechanics of hydraulic fracturing," *Trans. AIME.*, Vol. 210, 153-168.

[82] Ishida, T., Chen, Q., and Mizuta, Y., 1997: "Effects of fluid viscosity in hydraulic fracturing deduced from acoustic emission monitoring," *Rockburst and Seismicity in Mines: Proc. 4th Int. Symp. Rockbursts and Seismicity in Mines* (eds. Gibowicz and Lasocki), A.A. Balkema, Rotterdam, The Netherlands, 415-419.

[83] Ishida, T., Mizuta, Y. Matsunaga, I., Sasaki, S. and Chen, Q., 2000: "Effects of grain size in granitic rock on crack extension in hydraulic fracturing.", *Proc. 4th North Am. Rock Mech. Symp.*, A.A. Balkema, Rotterdam, The Netherlands. 1105-1111.

[84] ISRM (International Society for Rock Mechanics), 1985: "Suggested Methods for Determining Point Load Strength," *Int. J. Rock Mech. Min. and Geomech. Abstr.* Vol. 22 No.2. pp.51-60.d

[85] ISRM, 1988: "Suggested methods for determining the fracture toughness of rock by International Society for Rock Mechanics Commission on Testing

Methods," *Int. J. Rock Mech. Min. Sci. and Geomech. Abstr.* Vol. 25, No. 2, 71-96.

[86] Itakura, K.-I., Sato, K., 1998: "AE activity and its fractal properties with hydrofracturing of rock specimens." *Proc. 6th Acoustic Emission / Microseismic Activity in Geologic Structures and Materials*, Trans Tech Publications, Clausthal-Zellerfeld, Germany, 29-42.

[87] Jaeger, J.C. and Cook, N.G.W., 1979: *Fundamentals of Rock Mechanics*, Chapman and Hall Ltd., London, UK.

[88] Jeffrey, R.G., 1995: "Asymmetrically propped hydraulic fractures," *paper SPE 28079.*

[89] Jeffrey, R.G., Settari, A. and Smith, N.P., 1995: "A comparison of hydraulic fracture field experiments, including mineback geometry data, with numerical fracture model simulations," *paper SPE 30508.*

[90] Johnson, L. R., 1974: "Green's function for Lamb's problem," *Geophys. J. R. Astr. Soc.*, 37, 99-131.

[91] Jost, M.L., and Herrmann, R.B., 1989: "A student's guide to and review of moment tensors," *Seismol. Res. Letters*, Vol. 60, No.2, 37-57.

[92] Jung, S.J., Prisbrey, K. and Wu, G., 1994: "Prediction of rock hardness and drillability using acoustic emission signatures during indentation," *Int. J. Rock Mech. Min. Sci. and Geomech. Abstr.*, Vol. 31, No. 5, 561-567.

[93] Jupe, A., Jones, R., Dyer, B. and Wilson, S., 1998: "Monitoring and management of fractured reservoirs using induced microearthquake activity," *paper SPE 47315.*

[94] Keck, R.G. and Whiters, R.J., 1994: "A field demonstration of hydraulic fracturing for solid waste injection with real-time passive seismic monitoring," *paper SPE 28495.*

[95] Khristianovich, S.A. and Zheltov, Y.P., 1955: "Formation of vertical fractures by means of highly viscous liquid," *Proc. fourth World Pet. Congress*, Rome, Italy. 2, 579-586.

[96] Knott, F.K., 1973: *Fundamentals of Fracture Mechanics*, John Wiley & Sons, Ltd., Chichester, England, UK. 106-109.

[97] Koedertiz, L.F., Harvey, A.H., and Honarpour, M., 1989: *Introduction to Reservoir Engineering*, Gulf Publishing Company, Houston, Texas, USA. 25-29.

[98] Kreyszig, E., 1993: *Advanced Engineering Mathematics*, John Wiley & Sons, Inc., New York, U.S.A.

[99] Lama, R.D. and Vutukuri, V.S., 1974: *Handbook on Mechanical Properties of Rocks, Volume I*, Trans Tech Publications, Clausthal, Germany, 87-138.

[100] Lay, T. and Wallace, T.C., 1995: *Modern Global Seismology*, Academic Press, San Diego, California, U.S.A.

[101] Lockner, D., and Byerlee, J.D., 1977: "Hydrofracture in Weber Sandstone at high confining pressure and differential stress," *J. Geophys. Res.*, Vol. 82, No. 14, 2018-2026.

[102] Lockner, D., 1993: "The role of acoustic emission in the study of rock fracture," *Int. J. Rock Mech. Min. Sci. & Geomech. Abstr.*, Vol. 30, No. 7, 883-899.

[103] Lord, A.E., Jr., 1975: "Acoustic Emission," *Physical Acoustics: Principles and Methods, Vol. XI*, (eds. Mason and Thurston), Academic Press, New York, Chap. 6, pp. 289-353.

[104] Mack, M. and Warpinski, N., 2000:"Mechanics of Hydraulic Fracturing," *Reservoir Stimulation (3rd ed.)* (eds. Economides and Nolte), John Wiley & Sons Ltd., Chichester, England, UK.

[105] Majer, E.L. and Doe, T.W., 1986: "Studying hydrofracures by high frequency seismic monitoring," *Int. J. Rock Mech. Min. Sci. & Geomech. Abstr.*, Vol. 23, No. 3, 185-199.

[106] Masuda, K., Nishizawa, O., Kusunose, K. and Sato, T., 1993: "Laboratory study of effects of in-situ stress state and strength on fluid induced seismicity," *Int. J. Rock Mech. Min. Sci. & Geomech. Abstr.*, Vol. 30, No. 1, 1-10.

[107] Matsunaga, I., Kobayashi, H., Sasaki, S. and Ishida, T., 1993: "Studying hydraulic fracturing mechanism by laboratory experiments with acoustic emission monitoring," *Int. J. Rock Mech. Min. Sci. & Geomech. Abstr.*, Vol. 30, No. 7, 909-912.

[108] Maxwell, S.C., Young, R.P., Bossu, R., Jupe, A. and Dangerfield, J., 1998: "Microseismic logging of the Ekofisk Reservoir," *paper SPE 47276*.

[109] McClain, W.C., 1971: *Seismic Mapping of Hydraulic Fractures*, ORNL-TM-3502, Oak Ridge National Laboratory, Oak Ridge, Tennessee, USA, 1-32.

[110] McLennan, J.D., Roegiers, J.-C. and Economides, M.J., 1990: "Chapter 19 Extended Reach and Horizontal Wells," *Reservoir Stimulation (2nd ed.)* (eds. Economides and Nolte), Schlumberger Educational Services, Houston, Texas, USA.

[111] Mogi, K., 1962: "Magnitude-frequency relation for elastic shocks accompanying fracture of various materials and some related problems in earthquakes(2)." *Bull. Earthq. Res. Inst.*, 40, 831-853.

[112] Montgomery, S.L., 1996: "Jackfork Group, Southern Oklahoma: New Gas Play in the Ouachita Overthrust," *AAPG Bulletin*, Vol. 80, No. 11.

[113] Morita, N., Black, A.D. and Fuh, G.F., 1996a: "Borehole breakdown pressure with drilling fluids-I. Empirical results." *Int. J. Rock Mech. Min. Sci. & Geomech. Abstr.*, Vol. 33, No. 1, 39-51.

[114] Morita, N., Fuh, G.-F. and Black, A.D., 1996b: "Borehole breakdown pressure with drilling fluids-II. Semi-analytical solution to predict borehole breakdown pressure." *Int. J. Rock Mech. Min. Sci. & Geomech. Abstr.*, Vol. 33, No. 1, 53-69.

[115] Morris, R.C., Proctor, K.E.,and Koch, M.R., 1979: "Petrology and diagenesis of deep-water sandstones, Ouachita Mountains, Arkansas and Oklahoma.", *Aspect of Diagenesis* (eds. Scholle and Schluger), Soc. Econ. Paleontologists Mineralogists, Spec. Pub. No. 26, 263-278.

[116] Moschovidis, Z.A., Gardner,D.C., Sundand, G.V. and Veatch, R.W., 1994: "Disposal of oily cuttings by downhole periodic fracturing injections in Valhall, North Sea: Case study and modeling concepts." *SPE25757*.

[117] Moschovidis, Z.A., Steiger, R., Weng, X., and Abou-Sayed, A., 1998: "The Mounds drill cuttings experiment: determining placement of drill cuttings by hydraulic fracturing injection." *paper SPE 48987*.

[118] Munz, D., Bubsey, R.T., and Srawley, J.E., 1980: "Compliance and stress intensity coefficients for short bar specimens with chevron notches." *Int. J. Fracture*, Vol. 16, No. 4, 359-374.

[119] Murphy, H., Niitsuma, H. and Asanuma, H., 1999: "Results and next steps of the More-Than-Clouds and successor projects: International Joint Research on the New Mapping and HDR/HWR reservoir development technologies." *Geoth. Resources Council Trans.*, 23, 289-293.

[120] Nelder J. A. and Mead, R., 1965: "A simplex method for function minimization," *Computer Journal*, 7.

[121] Nolte, K.G., 2000: "Evolution of hydraulic fracturing design and evaluation." *Reservoir Stimulation (3rd ed.)* (eds. Economides and Nolte), John Wiley & Sons, Ltd., Chichester, England, UK.

[122] Nordgren, R.P., 1972: "Propagation of a vertical hydraulic fracture," *SPE Journal*, Vol. 12, No. 8, 306-314.

[123] Nur, A., 1971: "Effects of stress on velocity anisotropy in rock with cracks." *J. Geophys. Res.*, Vol. 76, 2022-2034.

[124] Obert, L., 1977: "The Microseismic method: discovery and early history." *Proc. First Conf. on Acoustic Emission / Microseismic Activity in Geologic Structures and Materials*, Trans Tech Publication, Clauthal, Germany, 11-12.

[125] Ohtsu, M. and Ono, K., 1984: "A generalized theory of acoustic emission and Green's functions in a half space." *J. Acoustic Emission*, Vol. 3, No.1, 27-40.

[126] Ohtsu, M. and Ono, K., 1986: "A generalized theory and source representations of acoustic emission." *J. Acoustic Emission*, Vol. 5, No.4, 124-133.

[127] Ohtsu, M., Yuyama, S. and Imanaka, T., 1987: "Theoretical treatment of acoustic emission sources in microfracturing due to disbonding." *J. Acoust. Soc. Am.*, Vol. 82, No. 2, 506-512.

[128] Ohtsu, M., 1988: "Source inversion of acoustic emission waveforms." *Structural Eng./Earthquake Eng.*, Vol. 5, No. 2, 275s-283.

[129] Ohtsu, M., Yuyama, S., and Iwase, H., 1989: "Microseismic observation in the pull-out process of shallow hook anchors." *Proc. JSCE*, No. 408/V-11: 177-186.

[130] Olson, J.E., 1995: "Fracturing from highly deviated and horizontal wells: numerical analysis of nonplanar fracture propagation," *paper SPE 29573.*

[131] Ong, S. H., 1994: *Borehole Stability*, PhD Dissertation, The University of Oklahoma, Norman, Oklahoma, USA.

[132] Ouchterlony, F., 1983: "Fracture toughness testing of rock." *Rock Fracture Mechanics* (ed. Rossmanith), Springer, Verlag/Wien, New York, USA. 69-150.

[133] PAC (Physical Acoustics Corporation), 1995: *MISTRAS 2001 User's Manual*, Physical Acoustics Corporation, Princeton, New Jersey, USA.

[134] Palmer, I.D. and Craig, H.R., 1984: "Modeling of axisymmetric vertical growth in elongated hydraulic fractures and application to first MWX stimulations," *paper SPE 12879.*

[135] Palmer, I.D., King, N.S. and Sparks, D.P., 1991: "The character of coal fracture treatments in Oak Grove Field, Black Warrior Basin." *paper SPE 22914.*

[136] Pauli, D., 1994: "Friable submarine channel sandstones in the Jackfork Group, Lynn Mountain syncline, Pushmataha and Le Flore counties, Oklahoma." *Geology and resources of the eastern Ouachita Mountains frontal*

belt and southeastern Arkoma basin, Oklahoma (eds. Suneson and Hemish), Oklahoma Geology Guidebook 29, 179-202.

[137] Perkins, T.K. and Kern, L.R., 1961: "Widths of hydraulic fractures," J. Petrol. Tech., Vol. 13, No. 9, 937-949.

[138] Pestman, B.J. and Van Munster, J.G., 1996: "An acoustic emission study of damage development and stress-memory effects in sandstone," *Int. J. Rock Mech. Min. Sci. & Geomech. Abstr.*, Vol. 33, No.6, 585-593.

[139] Peterson, R.E., Wolhart, S.L., Frohne, K.H., Branagan, P.T., Warpinski, N.R. and Wright, T.B., 1996: "Fracture diagnostics research at the GRI/DOE Multi-Site Project: Overview of the concept and results," *paper SPE 36449.*

[140] Phillips, W.S., Rutledge, J.T., Fairbanks, T.D., Gardner, T.L., Miller, M.E. and Maher, B.S., 1998: "Reservoir fracture mapping using microearthquakes: Two oilfield case studies," *SPE Reservoir Evaluation and Engineering.*

[141] Poe, B.D. Jr., Elbel, J.L., Spath, J.B., and Wiggins, M.L.L, 1995: "Prediction of future well performance, including reservoir depletion effects," *paper SPE 29465.*

[142] Poe, B.D. Jr. and Economides, M.J., 2000: "Chapter 12 Post-Treatment Evaluation and Fractured Well Performance," *Reservoir Stimulation (3rd ed.)* (eds. Economides and Nolte), John Wiley & Sons, Ltd. Chichester, England, USA.

[143] Power, D.V., Schuster, C.L., Hay, R. and Twombly, J., 1975: "Detection of hydraulic fracture orientation and dimensions in cased wells," *paper SPE 5626.*

[144] Power, D.V., 1977: "Acoustic emission following hydraulic fracturing in a gas well," *Proc. First Conf. on Acoustic Emission / Microseismic Activity in Geologic Structures and Materials*, Trans Tech Publication, Clauthal, Germany, 291-308.

[145] Prugger, A. and Gendzwill, D.J., 1988: "Microearthquake location: a nonlinear approach that makes use of a simplex stepping procedure," *Bull. Seismol. Soc. America*, Vol. 78, No.2.

[146] Robinson, B.M., Holditch, S.A., Whitehead, W.S., and Peterson, R.E., 1991: "Hydraulic fracturing in East Texas through the Gas Research Institute's third Staged Field Experiment," *paper SPE 22878.*

[147] Robinson, E.S., Potter, R.M., McInteer, B.B., Rowley, J.C., Armstrong, D.E., Mills, R.L. and Smith, M.C. (eds.), 1971: *A Preliminary Study of Nuclear Subterrene*, Los Alamos Scientific Laboratory Report LA-4547, USA.

[148] Roegiers, J.C., Kudo.O. and Fairhurst, C., 1973: "Influence of the type of packer on the stress distribution around a borehole." *J. Japanese Assoc. Petrol. Tech.*, Vol. 38, No.4, 209-222.

[149] Roegiers, J.-C. and Detournay, E., 1988: "Consideration on fracture initiation in inclined borehole." *Proc. 29th US Symp. Rock Mech.*, 461-469.

[150] Roegiers, J.-C., 1990: "Chapter 2 Elements of Rock Mechanics", *Reservoir Stimulation (2nd ed.)* (eds. Economides and Nolte), Schlumberger Educational Services, Houston, Texas, USA.

[151] Rothman, R.L., 1977: "Acoustic emissions in rock stresses to failure," *Proc. First Conf. on Acoustic Emission / Microseismic Activity in Geologic Structures and Materials*, Trans Tech Publication, Clauthal, Germany, 109-133.

[152] Sarda, J.-P., Perreau, P.J. and Deflandre, J.-P., 1988: "Acoustic emission interpretation for estimating hydraulic fracture extent: Laboratory and field studies," *paper SPE 18192*.

[153] Savic, M., Cockram, M.J. and Ziolkowski, A.M., 1993: "Active ultrasonic monitoring of laboratory-scale hydraulic fracturing experiments: numerical modeling vs. experiment," *paper SPE 26793*.

[154] Schmitt, D.R. and Zoback, M.D., 1993: "Infiltration effects in the tensile rupture of thin walled cylinders of glass and granite: Implications for the hydraulic fracturing breakdown equation," *Int. J. Rock Mech. Min. Sci. & Geomech. Abstr.*,Vol. 30, No. 3, 289-303.

[155] Scholz, C.H., 1968: "The frequency-magnitude relation of microfracturing in rock and its relation to earthquakes," *Bull. Seismol. Soc. America.*, Vol. 58, 399-415.

[156] Schlumberger, 2001: "Advances in Fracturing Technology," *A Supplement to HART's E&P*, September, 2001, 1-15.

[157] Schuster, C.L., 1978: "Detection within the wellbore of seismic signals created by hydraulic fracturing," *paper SPE 7448*.

[158] Scott, I. G., 1991: *Basic Acoustic Emission*, Gordon and Breach Science Publishers, New York, USA.

[159] Scott, T.E. and Nielsen, K.C., 1991: "The effects of porosity on the brittle-ductile transition in sandstones," *J. of Geophys. Res.*, Vol. 96, No.1, 405-414.

[160] Scott, T.E., Zeng, Z.-W. and Roegiers, J.-C., 2000: "Acoustic emission imaging of induced asymmetrical hydraulic fractures," *Pacific Rocks: Proc. 4th North American Rock Mech. Symp.* (eds. Girard, Liebman, Breeds and Doe), AA. Balkeman, Rotterdam, The Netherlands, 1129-1134.

[161] Shah, S.N., Asadi, M. and Lord, D.L., 1998: "Proppant transport characterization of hydraulic fracturing fluids using a high pressure simulator integrated with a fiber optic/LED vision system." *paper SPE 49040.*

[162] Shuck, L.Z., 1974: "The determination of direction and length of hydraulically induced fractures in petroleum reservoirs: a field experiment." *paper SPE 5160.*

[163] Shuck, L.Z. and Keech, T.W., 1975: "Monitoring acoustic emission from propagating fractures in petroleum reservoir rocks." *Proc. First Conf. on Acoustic Emission / Microseismic Activity in Geologic Structures and Materials*, Trans Tech Publication, Clauthal, Germany. 309-338.

[164] Sleef, G.E., Warpinski, N.R. and Engler, B.P., 1993: "The use of broadband microseisms for hydraulic fracture mapping." *paper SPE 26485.*

[165] Smith, M.B., Rosenberg, R.J. and Bowen, J.F., 1982: "Fracture width: Design vs. measurement." *paper SPE 10965.*

[166] Smith, M.B. and Shlyapobersky, J.W., 2000: "Basics of Hydraulic Fracturing," *Reservoir Stimulation (3rd ed.)* (eds. Economides and Nolte). John Wiley & Sons, Ltd., Chichester, England, UK.

[167] Smith, M.C., 1982: "Progress of the U.S. hot dry rock program." *Papers presented at the International Conference on Geothermal Energy* (eds. Stephens and Stapleton), Vol. 2, BHRA Fluid Engineering, Bedford, England, UK. 303-319.

[168] Sneddon, I.N., 1946: "The distribution of tress in the neighborhood of a crack in an elastic solid." *Proc. Royal Soc. London*, 187, Ser. A, 229-260.

[169] Sneddon, I.N. and Elliot, A.A., 1946: "The opening of a Griffith crack under internal pressure," *Quarterly of Appl. Math.*, 4, 262-267.

[170] Snell, J.S. and Close, A.D., 1999: "Yates Field steam pilot applies latest seismic and logging monitoring techniques." *paper SPE 56791.*

[171] Snell, J.S., Wadleigh, E.E. and Tilden, J., 2000: "Fracture characterization of a key factor in Yates steam pilot design and implementation." *paper SPE 59060.*

[172] Solberg, P., Lockner, D. and Byerlee, J. D., 1980: "Hydraulic fracturing in granite under geothermal conditions." *Int. J. Rock Mech. Min. Sci. & Geomech. Abstr.*, Vol. 17, No. 1, 25-33.

[173] Song, I. and Haimson, B.C., 2001: "Effect of pressurization rate and initial pore pressure on the magnitude of hydrofracturing breakdown pressure

in tablerock sandstone," *Proc. 38th U.S. Rock Mech. Symp.*, A.A. Balkema Publishers, Lisse, The Netherlands, 235-242.

[174] Sorrells, G.G. and Mulcahy, C.C., 1986: "Advances in the microseismic method of hydraulic fracture azimuth estimation," *paper SPE 15216.*

[175] Taff, J.A., 1902: "Description of the Atoka Quadrangle (Indian Territory)," *USGS Geol. Atlas, Atoka Folio*, (No. 98).

[176] Teufel, L.W., Hart, C.M., Sattler, A.R. and Clark, J.A., 1984: "Determination of hydraulic fracture azimuth by geophysical, geological, and oriented-core methods at the Multi-well Experimental Sit, Rifle, Colorado," *paper SPE 13226.*

[177] Thiercelin, M.C. and Roegiers, J.-C., 2000: "Formation Characterization: Rock Mechanics," *Reservoir Stimulation (3rd ed.)* (eds. Economides and Nolte), John Wiley & Sons, Ltd., Chichester, England,UK.

[178] Thorne, B.J. and Morris, H.E., 1988a: "Advances in borehole seismic fracture diagnostics," *paper SPE 16405.*

[179] Thorne, B.J. and Morris, H.E., 1988b: "An assessment of borehole seismic fracture diagnostics," *paper SPE 18193.*

[180] Tiab, D. and Kumar, A., 1980: "Application of the pD′ function of interference analysis," *paper SPE 6053.*

[181] Tiab, D. and Donaldson, E.C., 1996: *Petrophysics*, Gulf Publishing Company, Houston, Texas, USA.

[182] Tillman, R.W., 1994: "Sedimentology and sequence stratigraphy of Jackfork Group, U.S. Highway 259, Le Flore County, Oklahoma," *Geology and resources of the eastern Ouachita Mountains frontal belt and southeastern Arkoma basin, Oklahoma: Oklahoma Geology Guidebook 29* (eds. Suneson and Hemish), 203-223.

[183] Timoshenko, S.P. and Goodier, J.N., 1970: *Theory of Elasticity*, McGraw-Hill Book Company, Singapore.

[184] USG (United States Gypsum Company), 1995: *The Hydro-Stone Family of Products*, United States Gypsum Company, Chicago, USA

[185] Valko, P. and Economides, M. J., 1995: "Hydraulic Fracture Mechanics," Johns Wiley & Sons, Chichester, UK.

[186] Vallen, 1998: *AMSY4 User's Manual*, Vallen Systeme GmbH, Munich, Germany.

[187] Vandamme, L. and Jeffrey, R.G., 1986: "Pressure distribution in three-dimensional hydraulic fractures," *paper SPE 15265.*

[188] Veatch, R.W. Jr., Moschovidis, Z.A. and Fast, C.R., 1990: "Chapter 1 An Overview of Hydraulic Fracturing," *Recent Advances in Hydraulic Fracturing (eds.* Gidley, Holditch, Nierode and Veatch), SPE Monograph Series, Society of Petroleum Engineers, Richardson, Texas, USA.

[189] Vinegar, H.J., Wills, P.B., DeMartini, D.C., Shlyuapobersky, J., Deeg, W.F.J., Adair, R.G., Woerpel, J.G., Fix, J.E. and Sorrells, G.G.,1992: "Active and passive seismic imaging of a hydraulic fracture in diatomite," *J. Petrol. Tech.*

[190] von Schoenfeldt, H. & Fairhurst, C., 1968: "The influence of the elastic constants and other parameters on the stress distribution at the wall of a circular hole in transversely isotropic medium", *Special Research Paper*, University of Minnesota, USA.

[191] Warpinski, N. R., Schmidt, R.A. and Northrup, D.A., 1982: "In-situ stresses: the predominant influence on hydraulic fracture containment," *J. Petrol. Tech.*, Vol. 34, 653-664.

[192] Warpinski, N.R., 1985: "Measurement of width and pressure in a propagating hydraulic fracture," *SPE Journal.*

[193] Warpinski, N.R., Moschovidis, Z.A., Parker, C.D. and Abou-Sayed, I.S., 1994: "Comparison study of hydraulic fracturing models—Test case: GRI Staged Field. Experiment No. 3," *SPE Production and Facilities* (February), 7-16.

[194] Warpinski, N.R., Engler, B.P., Young, C.J., Peterson, R., Branagan, P.T. and Fix, J.E., 1995: "Microseismic mapping of hydraulic fractures using multi-level wireline receivers," *paper SPE 30507.*

[195] Warpinski, N.R.,Wright, T.B., Uhl, J.E., Engler, B.P., Drozda, P.M., Peterson, R.E. and Branagan, P.T., 1996: "Microseismic monitoring of the B-Sand hydraulic fracture experiment at the GRI/DOE Multi-Site Project," *paper SPE 36450.*

[196] Warpinski, N.R., Branagan, P.T., Peterson, R.E., Fix, J.E., Uhl, J.E. and Engler, B.P., 1997: "Microseismic and deformation imaging of hydraulic fracture growth and geometry in the C-Sand interval, GRI/DOE M-Site Project," *paper SPE 38573.*

[197] Warpinski, N.R., Branagan, P.T., Peterson, R.E., Wolhart, S.L. and Uhl, J.E., 1998: "Mapping hydraulic fracture growth and geometry using microseismic events detected by a wireline retrievable accelerometer array," *paper SPE 40014.*

[198] Warpinski, N.R., Branagan, P.T., Mahrer, K.D., Wolhart, S.L. and Moschovidis, Z.A., 1999: "Microseismic monitoring of the Mounds drill cuttings injection tests," *Proc. 37th U.S. Rock Mech. Symp.*, A.A. Balkema, Rotterdam, The Netherlands. 1025-1032.

[199] Wedman, M.L., Lynch, K.W. and Spearman, J.W., 1999: "Hydraulic fracturing for sand control in unconsolidated heavy-oil reservoir," *paper SPE54628.*

[200] Weijers, L., de Pater, C.J., Owens, K.A., and Kogsboll, H.H., 1992: "Geometry of hydraulic fractures induced from horizontal wellbores," *paper SPE 25049.*

[201] Weijers, L. and de Pater, C.J., 1994: "Interaction and link-up of hydraulic starter fractures close to a perforated wellbore," *paper SPE 28077.*

[202] Weijers, L., Wright, C.A., Sugiyama, H., Sato, K. and Zhigang, L., 2000: "Simultaneous propagation of multiple hydraulic fractures-evidence, impact and modeling implications," *paper SPE 64772.*

[203] Weng, X., 1993: "Fracture initiation and propagation from deviated wellbores," *paper SPE 26597.*

[204] Willson, S.M., Steiger, R.P., Moschovidis, Z.A., Abou-Sayed, A.S., de Bree, Ph., and Sirevag, G., 1999: "Laboratory investigation of drill cuttings disposal by downhole injection," *Proc. 37th U.S. Rock Mech. Symp.*, A.A. Balkema Rotterdam, The Netherlands. 1009-1016.

[205] Winkler, K.W., 1995: "Hydrofrac mapping using acoustic emission," *Acoustic Emission V: Proc. Fifth Conf. on Acoustic Emission / Microseismic Activity in Geologic Structures and Materials*, Trans Tech Publications, Clausthal-Zellerfeld, Germany. 121-131.

[206] Winters, J.A., 1984: *Comparative Sandstone and Mudrock Diagenesis in the Jackfork Group, Northern Flank of the Broken Bow-Benton Anticline, Southeastern Oklahoma*, Master Degree Thesis, The University of Oklahoma, Norman, Oklahoma, USA.

[207] Wolhart, S.L., Berumen, S., Cippola, C.L., Barton, C.A. and Branagan, P.T., 2000: "Use of hydraulic fracture diagnostics to optimize fracturing jobs in the Arcabuz-Culebra field," *paper SPE 60314.*

[208] Wright, C.A., Minner, W.A.,Weijers, L, Davis, E.J., Golich, G.M. and Kikuchi, H., 1997: "Wellbore-to-fracture communication problems pose challenges in Californian diatomite horizontal wells," *paper SPE 38632.*

[209] Wright, C.A., Davis, E.J., Minner, W.A., Ward, J.F., Weijers, L., Schell, E.J. and Hunter, S.P., 1998a: "Surface tiltmeter fracture mapping reaches new depths-10,000 feet, and beyond?" *paper SPE 39919.*

[210] Wright, C.A., Davis, E.J., Weijers, L., Golich, G.M., Ward, J.F. and Minner, W.A., 1998b: "Downhole tiltmeter fracture mapping: A new tool for directly measuring hydraulic fracture dimensions," *paper SPE 49193.*

[211] Xie, H., 1993: "Fractals in Rock Mechanics," A.A. Balkema, Rotterdam, The Netherlands.

[212] Yamaguchi, K., Takahashi, H. and Niitsuma, H.(eds.), 1990: *Progress in Acoustic Emission V. Proc. 10th Int. Acoustic Emission Symp.*, Japanese Soc. for Non-Destructive Inspection, Tokyo, Japan.

[213] Yarema, S.Y. and Krestin, G.S., 1966: "Determination of the modulus of cohesion of brittle materials by compressive tests on disc specimens containing cracks," *Soviet Material Science*, 2, 7-10.

[214] Yatomi, C., Fujii, K. and Nakagawa, K., 1989: "Combined stress hypothesis for mixed-mode fracture toughness criterion," *Eng. Fracture Mech.*, Vol. 32, No.6, 881-888.

[215] Young, R., 1998: *Introduction to Seismic Exploration Lecture Notes*, The University of Oklahoma, Norman, Oklahoma, USA.

[216] Yuyama, S., Imanaka, T. and Ohtsu, M., 1988: "Quantitative evaluation of microfracturing due to disbonding by waveform analysis of acoustic emission," *J. Acoust. Soc. Am.*, Vol. 83, No.3, 976-983.

[217] Zemanek, J., Caldwell, R.L., Glenn, E.E., Holcomb, S.V., Norton, L.J. and Straus, A.J.D., 1969: "The borehole televiewer—A new logging concept for fracture location and other types of borehole inspection," *J. Petrol. Tech.* (June), 762-774.

[218] Zeng, Z.-W. and Roegiers, J.-C., 2001: "Modeling of packer influence on hydraulic fracture initiation in laboratory tests," *Rock Mechanics in the National Interest: Proc. 38th US Rock Mech. Symp.* (eds. Ellsworth, Tinucci and Heasley), A.A. Balkeman Publishers, Lisse, The Netherlands, Vol. 1, 221-225.

[219] Zeng, Z.-W. 2002: *User's Manual of Microseismicity LOCATION and WAVEFORM*, The University of Oklahoma, Norman, Oklahoma, USA.

[220] Zhao, X.L. and Roegiers, J.-C., 1990: "The measurement of fracture toughness of rocks," *Proceedings, III Congreso Suramericano de Mecanica de Rocas*, 641-652.

[221] Zhao, X.L., 1994: "Determination of In-Situ Mixed-Mode Fracture Parameters," *Rock Mechanics Consortium Report RMC-94-12*, The University of Oklahoma, Norman, Oklahoma, USA.

[222] Zietlow, W.K. and Labuz, J.F., 1998: "Measurement of the intrinsic process zone in rock using acoustic emission," *Int. J. Rock Mech. Min. Sci.*, Vol. 35, No. 3, 291-299.

[223] Zoback, M.D., Rummel, F., Jung, R. and Raleigh, C.B., 1977: "Laboratory hydraulic fracturing experiments in intact and pre-fractured rock," *Int. J. Rock Mech. Min. Sci. & Geomech. Abstr.* Vol. 14, No. 2, 49-58.

Appendix A: Derivation of Equation 4.25

Burridge and Knopoff (1964) developed the general reciprocal relation for Green's functions:

$$g_{ij}(\mathbf{x}, t; \mathbf{x}', t') = g_{ji}(\mathbf{x}', -t'; \mathbf{x}, -t) \tag{A.1}$$

Applying this result to the general solution of Green's function for a source at S $(0, 0, L_3, 0)$ and a receiver D (x_1, x_2, x_3, t), the following expression is obtained:

$$g_{ij}(x_1, x_2, x_3, t; 0, 0, L_3, 0) = g_{ji}(0, 0, L_3, 0; x_1, x_2, x_3, -t) \tag{A.2}$$

Applying the result of Eq. (4.23), i.e., translation of the source and the receiver, to the right-hand side of Eq.(A.2), results in:

$$\begin{aligned} g_{ji}(0, 0, L_3, 0; x_1, x_2, x_3, -t) &= g_{ji}(0 - x_1, 0 - x_2, L_3, 0 - (-t); \\ &\quad x_1 - x_1, x_2 - x_2, x_3, -t - (-t)) \\ &= g_{ji}(-x_1, -x_2, L_3, t; 0, 0, x_3, 0) \end{aligned} \tag{A.3}$$

Combining Eqs.(A.2) and (A.3) gives:

$$g_{ij}(x_1, x_2, x_3, t; 0, 0, L_3, 0) = g_{ji}(-x_1, -x_2, L_3, t; 0, 0, x_3, 0) \tag{A.4}$$

This is the requested result of Eq.(4.25).

Appendix B: Mode-I Fracture Toughness Formula for CDISK Test

Referring to Figure 5.13, assume that at the critical crack length, a, the displacement at the loading point is u. Now under constant load, P, the crack stably propagates a small increment, da, corresponding to a displacement increment, du, of the loading point. The potential energy increase in the system is balanced by the energy consumed in creating new surfaces. The increased potential energy, ΔU, in the system and the energy consumed in creating the new crack area, ΔW, can be calculated as follows:

1. Increased potential energy, ΔU

Due to the increment of deformation in the system, some potential energy is stored in the system. This energy corresponds to the driving force for propagation of the crack. It can be calculated as:

$$\Delta U = \frac{1}{2} P du \tag{B.1}$$

where P - load, and du-increment of displacement.

Assuming the system is under linear elastic conditions, so:

$$u = PC \tag{B.2}$$

where C is the compliance.

Then,

$$du = PdC + CdP \tag{B.3}$$

But at the critical point, the load, P, is constant; so:

$$dP = 0 \tag{B.4}$$

and,

$$du = PdC \tag{B.5}$$

This results in:

$$\Delta U = \frac{1}{2}P^2 dC \tag{B.6}$$

2. Energy consumed in crack creation, ΔW

In order to create new crack area, energy needs to be consumed. The consumption of energy can be calculated as:

$$\Delta W = G_I \; b \; da \tag{B.7}$$

where,

$\begin{cases} G_I - \text{fracture energy release rate;} \\ b - \text{crack front width corresponding to crack length } a\text{; and,} \\ da - \text{crack extension.} \end{cases}$

At the critical point, the fracture energy release rate, G_I, becomes the critical fracture energy release rate, G_{IC}. In linear fracture mechanics, G_{IC} and fracture toughness, K_{IC}, are connected by (Knott, 1973):

$$G_{IC} = \frac{K_{IC}^2}{E'} \tag{B.8}$$

where $E' = \begin{cases} E & \text{for plane stress cases} \\ \frac{E}{1-\nu^2} & \text{for plane strain cases} \end{cases}$.

So, finally,

$$\Delta W = \frac{K_{IC}^2}{E'} \; b \; da \tag{B.9}$$

3. Energy Equilibrium

As mentioned before, because of the stable propagation assumption, the potential energy stored in the system due to the deformation, du, is balanced with the energy consumed by the creation of the new crack area due to the crack propagation, da. Therefore,

$$\Delta U = \Delta W \tag{B.10}$$

so,

$$\frac{1}{2}P^2 dC = \frac{K_{IC}^2}{E'}\, b\, da \tag{B.11}$$

Simplification of this equation gives:

$$\begin{aligned} K_{IC} &= P\sqrt{\frac{E'}{2b}\frac{dC}{da}} \\ &= P\sqrt{\frac{E'}{2b}\frac{dC}{d(\frac{a}{R})}\frac{1}{R}\frac{B}{B}} \end{aligned} \tag{B.12}$$

Let $\alpha = \frac{a}{R}$, $W = 2R$, $C' = E'BC$, then:

$$K_{IC} = P\sqrt{\frac{1}{WBb}\frac{dC'}{d\alpha}} \tag{B.13}$$

where,

- W – diameter of the disk;
- C' – dimensionless compliance; and,
- B – disk thickness.

Assuming that $\frac{dC'}{d\alpha}$ in the chevron-notched disk follows the same relationship as that in straight-through specimens (Munz, 1980): then,

$$\frac{dC'}{d\alpha} = 2Y^2 \tag{B.14}$$

where Y is the dimensionless stress intensity coefficient.

Applying Eq.(B.14) to Eq.(B.13), it becomes:

$$K_{IC} = PY\sqrt{\frac{2}{WBb}} \tag{B.15}$$

According to Yarema(1966), for a disk specimen,

$$Y = \sqrt{\alpha}(1 + \frac{3}{2}\alpha^2 + \frac{3}{4}\alpha^6 + \frac{3}{64}\alpha^8) \tag{B.16}$$

Combining Eqs.(B.15) and (B.16) gives:

$$K_{IC} = P\sqrt{\frac{2\alpha}{WBb}}(1 + \frac{3}{2}\alpha^2 + \frac{3}{4}\alpha^6 + \frac{3}{64}\alpha^8) \tag{B.17}$$

From here on, the crack front width, b, can be expressed in terms of either initial crack length, a_0, or crack surface kerf length a_1.

4. Initial Crack Length-based K_{IC} Formula

Referring to Figure 5.13, for an arbitrary crack length, a, the crack front width, b, can be expressed, in terms of crack initial length, a_0, as follows:

$$\begin{aligned}
b &= 2\,(\sqrt{R_s^2 - a_0^2} - \sqrt{R_s^2 - a^2}) \\
&= 2R\left[\sqrt{\left(\frac{R_s}{R}\right)^2 - \left(\frac{a_0}{R}\right)^2} - \sqrt{\left(\frac{R_s}{R}\right)^2 - \left(\frac{a}{R}\right)^2}\right] \\
&= W\left[\sqrt{\left(\frac{R_s}{R}\right)^2 - \left(\frac{a_0}{R}\right)^2} - \sqrt{\left(\frac{R_s}{R}\right)^2 - \left(\frac{a}{R}\right)^2}\right] \\
&= W\,(\sqrt{\Re^2 - \alpha_0^2} - \sqrt{\Re^2 - \alpha^2}) \\
&= W\left[(\Re^2 - \alpha_0^2)^{\frac{1}{2}} - (\Re^2 - \alpha^2)^{\frac{1}{2}}\right]
\end{aligned} \tag{B.18}$$

where,

R – diskradius:

$W = 2R$, disk diameter:

R_s – saw radius:

a_0 – half length of the initial crack:

a – half length of the crack at an arbitrary point during propagation:

$\Re = \frac{R_s}{R}$;

$\alpha_0 = \frac{a_0}{R}$; and,

$\alpha = \frac{a}{R}$.

Applying Eq.(B.18) to Eq.(B.17) leads to:

$$\begin{aligned} K_{IC} &= P\sqrt{\frac{2\alpha}{WBb}}(1+\frac{3}{2}\alpha^2+\frac{3}{4}\alpha^6+\frac{3}{64}\alpha^8) \\ &= P\sqrt{\frac{2\alpha}{WBW\left[(\Re^2-\alpha_0^2)^{\frac{1}{2}}-(\Re^2-\alpha^2)^{\frac{1}{2}}\right]}}(1+\frac{3}{2}\alpha^2+\frac{3}{4}\alpha^6+\frac{3}{64}\alpha^8) \\ &= \frac{\sqrt{2}P}{W\sqrt{B}}\frac{\sqrt{\alpha}(1+\frac{3}{2}\alpha^2+\frac{3}{4}\alpha^6+\frac{3}{64}\alpha^8)}{\sqrt{(\Re^2-\alpha_0^2)^{\frac{1}{2}}-(\Re^2-\alpha^2)^{\frac{1}{2}}}} \end{aligned} \tag{B.19}$$

Let

$$Y^*_{\alpha_0} = \frac{\sqrt{\alpha}(1+\frac{3}{2}\alpha^2+\frac{3}{4}\alpha^6+\frac{3}{64}\alpha^8)}{\sqrt{(\Re^2-\alpha_0^2)^{\frac{1}{2}}-(\Re^2-\alpha^2)^{\frac{1}{2}}}} \tag{B.20}$$

where $Y^*_{\alpha_0}$ is the α_0-based dimensionless stress intensity coefficient expression.

Denoting this α_0-based fracture toughness as $K_{IC_\alpha_0}$, then

$$K_{IC_\alpha_0} = \frac{\sqrt{2}P}{W\sqrt{B}}Y^*_{\alpha_0} \tag{B.21}$$

Munz (1980) showed that $Y^*_{\alpha_0}$ has its minimum at the critical point. Denoting this minimum $Y^*_{\alpha_0}$ as $Y^*_{\alpha_0\,\min}$, it can be found numerically by changing α from α_0 to α_1. That is:

$$Y^*_{\alpha_0} = Y^*_{\alpha_0\,\min}$$

$$= \min \left\{ \frac{\sqrt{\alpha}(1 + \frac{3}{2}\alpha^2 + \frac{3}{4}\alpha^6 + \frac{3}{64}\alpha^8)}{\sqrt{(\Re^2 - \alpha_0^2)^{\frac{1}{2}} - (\Re^2 - \alpha^2)^{\frac{1}{2}}}}, \quad \alpha_0 < \alpha < \alpha_1 \right\} \tag{B.22}$$

With this notation, the α_0-based K_{IC} can finally expressed as:

$$K_{IC_\alpha_0} = \frac{\sqrt{2}P}{W\sqrt{B}} Y^*_{\alpha_0 \min} \tag{B.23}$$

where $Y^*_{\alpha_0 \min}$ is the minimum dimensionless stress intensity coefficient as defined above.

Appendix C: Hydraulic Fracturing Tests under Biaxial Stresses

Efforts have been made to conduct hydraulic fracturing experiments under more realistic test conditions. Experiments, similar to the granite tests by Ishida et al.(2000), were conducted on hydrostone specimens. While experience obtained from these experiments contributed to the completion of this dissertation, lessons learned from these pilot experiments might be valuable to future research. This appendix presents the observations and results of two of these pilot hydraulic fracturing experiments conducted under biaxial loading conditions using a polyaxial loading frame.

1. Preparation of the Specimens

Two 10 inch cubic hydrostone blocks were prepared. These specimens were prepared using gypsum cement mixed with water at the ratio of 100 *lbs* gypsum cement to 32 *lbs* water (USG, 1995). This slurry was then poured into a 10 inch cubic mold and levelled on the top surface. The slurry was left to set for 30 minutes, then the mold was removed. The hydrostone block was kept at room temperature to cure for 28 days.

After curing, a borehole was drilled in a way similar to that described in Chapter 7. The diameter of the wellbore was half-inch, and the sealed-off section was 1-inch long (Refer to Figure C.1).

2. Loading Frame

The biaxial hydraulic fracturing experiments were conducted in a polyaxial loading frame. This polyaxial loading frame was originally developed by Scientific Ap-

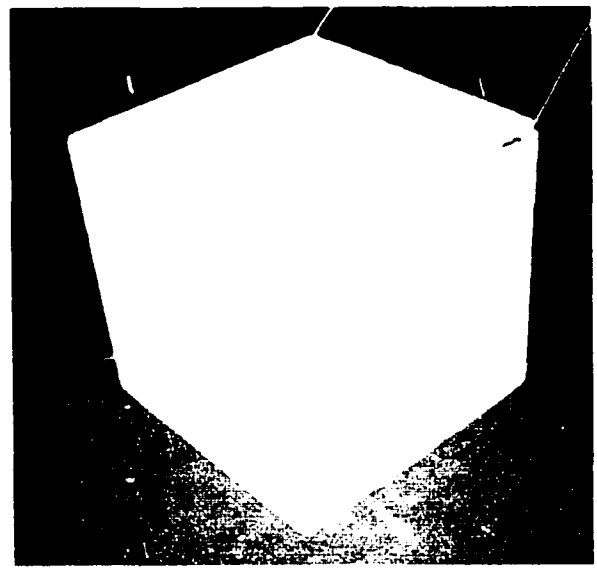


Figure C.1: A 10 inch cubic hydrostone block with borehole and tubing.

plication International Corporation (SAIC) (Ong, 1994). The loading cell had the following dimensions: 18.75 inch (length) × 18.75 inch (width) × 18 inch (depth), as schematically shown in Figure C.2.

In the standard test, the specimen was designed to be set inside the cell and loaded with flat-jacks in three orthogonal directions, as shown in Figure C.3. The biaxial loads were supplied using rams, as shown in Figure C.4. Four 10-in long, 1-in thick square steel plates were used to transfer the load from the rams to the specimens. The lateral stresses were applied onto the specimens in two directions: parallel and perpendicular to the wellbore axis. Microseismic sensors were installed on the two free surfaces in the third direction that had no applied stresses.

The hydraulic fracturing pressure was supplied using an MTS Test Star II loading frame. Constant pumping rates were obtained by using a constant stroke speed through an intensifier, as shown in Figure C.5. Calibrations for the control of constant pumping rates were conducted before each experiment. Based on this calibration, the stroke speed was calculated to be 0.00014 $inch/s$ which the pumping rate was 0.0605 cc/s. It was also found that the stroke speed and the pumping

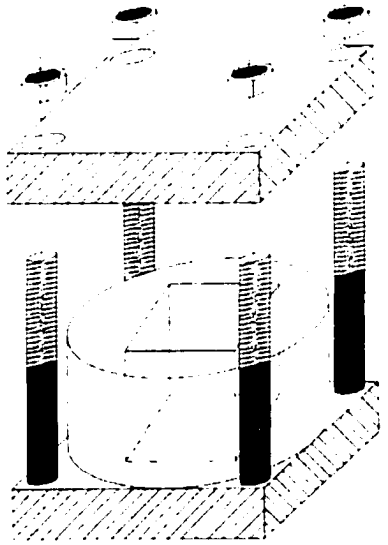


Figure C.2: The polyaxial loading frame (from Ong, 1994).

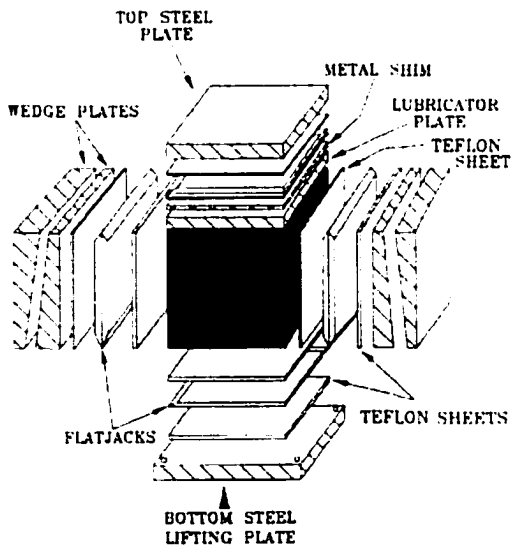


Figure C.3: Polyaxial loading using the flatjacks (from Ong, 1994).



Figure C.4: Rams used to supply the lateral stresses.

rate followed a linear relationship. Using this calibration and the control program of MTS Test Star II, the hydraulic fracturing pressurization was controlled, and related data were recorded.

3. Experimental Procedure

The following steps were followed:

Step 1. Placing of the specimen.

First the specimen was put into the polyaxial cell. Then the tubing was connected to the pumping system. The microseismic sensors were connected to the recording system. Finally, the rams were set into the polyaxial cell and connected to the hand pumps. Due to space limitations, special attention had to be paid to protect the microseismic sensors during this step.

Step 2. Application of biaxial stresses.

First, the tubing and the sealed-off section were filled with the hydraulic fracturing fluids until all air-bubbles were vented from the outlet. Then lateral stresses were applied alternatively with an increment of 50 *psi* until the stresses reached their pre-set values.

During the process of applying the lateral stresses, microseismic events might be

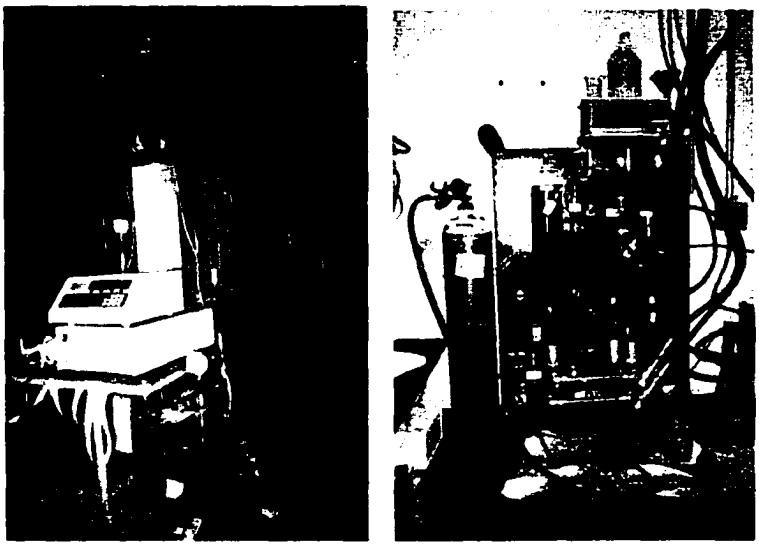


Figure C.5: The MTS Test Star II loading frame (left) and the intensifier (right).

generated. After the lateral stresses were applied, the whole experimental system was left for about 30 minutes until the microseismic activity became low and the background noise level were recorded.

Step 3. Breaking the specimen.

All recording systems were restarted. The MTS Test Star II and the intensifier started to apply the hydraulic fracturing pressure at pre-set pumping rates until the block was hydraulically fractured. Different rates might be used at different stages of the experiments. The pumping rates could be changed by holding the stroke using the MTS Test Star II.

Step 4. Removing the block from the polyaxial cell.

When the block was fractured, the MTS Test Star II and the intensifier pumping system were stopped first. After a while the hydraulic pressure in the tubing no longer declined; then the recording systems were stopped. The lateral stresses were decreased by gradually releasing the pressures in the hand pumps. The loading and pumping systems were disassembled one by one. Finally the fractured block was moved out of the polyaxial cell for further analyses.

4. Experimental Observations

Two hydrostone specimens were hydraulically fractured during these pilot experiments. The laboratory results were as follows:

(1) Experiment 98052

This specimen was prepared on April 21, 1998 and tested on May 21, 1998. Assigning the wellbore as Z-direction, the final dimensions of the block were 10 $in \times 10\ in \times 9.75\ in$ in the X-, Y- and Z -direction, respectively.

P-wave seismic velocities were measured in different directions using different raypaths. The velocities in different directions were the same, which were:

$$V_x = V_y = V_z = 3.25\ km/s$$

These results indicated that the hydrostone block was homogeneous.

The laterally applied stresses were:

$$\begin{cases} \sigma_x = 300\ psi \\ \sigma_y = 0\ psi \\ \sigma_z = 400\ psi \end{cases}$$

All the microseismic sensors were installed onto the two free surfaces in the $\pm Y$ - direction.

The hydraulic fracturing fluid, WG-17, was a very viscous blue gel supplied by an industrial service company. The viscosity was approximately 1000 cp.

After the experiment started, the hydraulic fracturing fluid was pumped into the sealed-off section at a constant rate of $0.025\ cc/s$ from time $t = 0$ to $t = 3660$ seconds. Figure C.6 shows the pressurization history of the experiment.

From this curve, three stages can be outlined: slow, transient and rapid. The slow stage was roughly from $t = 0$ to $t = 2670$ seconds. During this period of time, the pressure increased from 0 to 261 psi, the rate was about 0.1 psi/s.

The transient stage could be roughly defined from $t = 2671$ seconds to $t = 3000$ seconds. During this period, the pressure increased 340 psi, with a rate of about 1 psi/s.

From $t = 3001$ seconds to $t = 3450$ seconds, the pressure increased rapidly, at a rate of about 5 psi/s.

The block was fractured at a peak pressure of 2858 psi at time $t = 3451$ seconds. Then the pressure rapidly dropped to 1724 psi at $t = 3527$ seconds, an average rate of -14.7 psi/s.

From $t = 3528$ seconds to $t = 3578$ seconds the pressure was building up slowly, at a rate of -0.3 psi/s, reaching 1739 psi.

After that, the pressure declined gradually at a rate of -0.7 psi/s. The shut-in of the pumps at $t = 3660$ seconds had little influence on the depressurization: the rate changed to -0.9 psi/s.

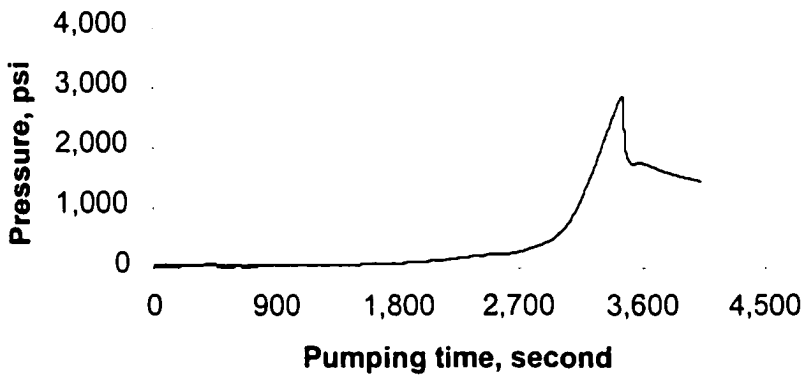


Figure C.6: Pressure vs time curve in hydraulic fracturing Experiment 980521.

After the experiment, the specimen was sectioned to check the fracture geometry. A planar fracture was developed along the wellbore in the plane that was parallel to the zero stress surfaces, as shown in Figure C.7.

From the blue dye left by the hydraulic fracturing fluid, it was noticed that hydraulic fracturing fluid moved from the sealed-off section to the fracture tip along radiating paths, which might indicate that the hydraulic fracturing was a very rapid process.

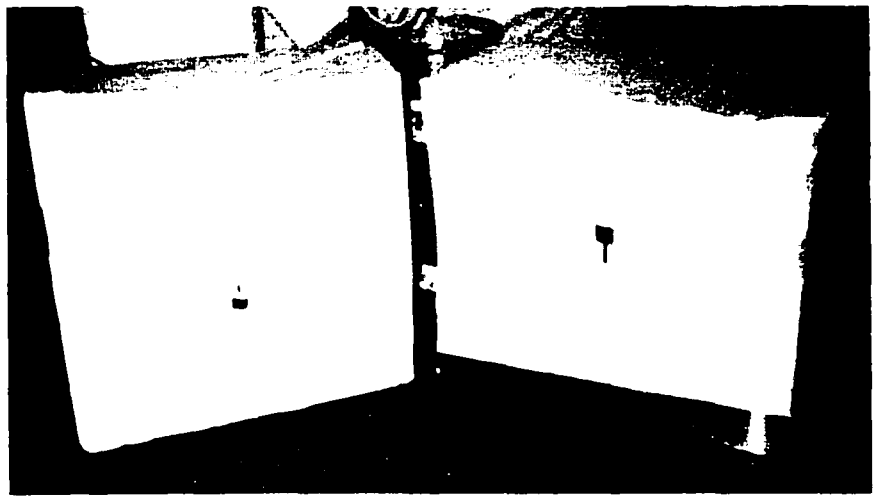


Figure C.7: The hydraulic fracture in Experiment 980521.

As mentioned above, no load was applied in the Y-direction. Therefore, eight in-house made microseismic sensors were installed onto the two surfaces in the Y-direction. These sensors were connected to the 8-channel PAC Spartan-8000 system.

During the pressurization, microseismic events were detected. But using the LOCATION program developed in Chapter 3, no meaningful image about the fracture could be obtained.

This failure to image the fracture resulted in efforts to perform a similar experiment, but under lower stress levels; due to the consideration that high lateral stresses might have induced microfractures and complicated the imaging.

(2) Experiment 980701

This experiment was conducted under similar conditions as Experiment 980521, except that the stresses were lower, i.e.:

$$\begin{cases} \sigma_x = 100\ psi \\ \sigma_y = 0\ psi \\ \sigma_z = 200\ psi \end{cases}$$

The pressurization curve is shown in Figure C.8. This pressure response curve

was not as smooth as the one in Experiment 980521. The breakdown pressure was 2628 *psi* reached at $t = 3306$ seconds.

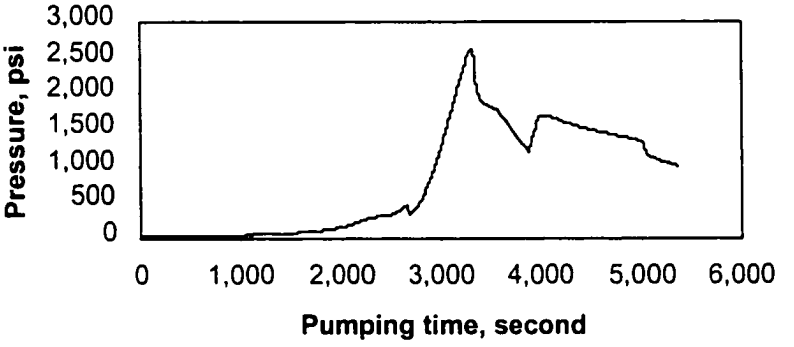


Figure C.8: Pressure-time curve in Experiment 980701.

The sectioned specimen showed that a hydraulic fracture was developed, not parallel but at a small angle, crossing the wellbore, as shown in Figure C.9. The fracture was less planar compared to Experiment 980521. However, the breakdown pressures in these two experiments followed Eq. 2.8; that is, the difference between the breakdown pressures were roughly the same as that between the lateral stresses in the experiments.

The small teeth in the pressure curve might indicate that the fracturing process in this specimen was not completed in one step. Instead, two small fractures might have occurred, one before and one after the major fracturing. The complicated geometry of the fracture supported this explanation.

Microseismic events were detected in a similar way as described in Experiment 980521. But again, no meaningful image was obtained from the recorded arrival times. Further analyses showed that the velocity difference between the hydrostone and the steel loading plates was responsible for complicating the microseismic imaging, as explained below.

5. An Explanation to the Failure of Microseismicity Analyses

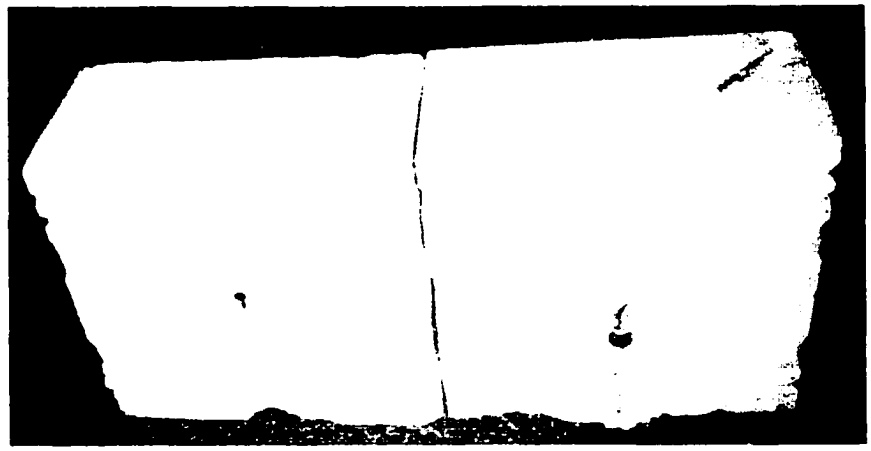


Figure C.9: Non-planar hydraulic fracture in Experiment 98701.

Although no meaningful microseismic event were located using the recorded arrival times in these two experiments, it was found that when the lockout time[1] was reduced, the location results would be improved.

One possible reason for this was that the seismic velocities between the hydrostone ($V = 3.25\ km/s$) and the steel plates ($V = 5.96\ km/s$) were so large that the seismic waves were not travelling directly from the sources to the sensors; instead, a complex route via the high velocity plates might have used.

This explanation was supported by the fact that in other experiments, when loading plates of similar velocities were used, the location results were much better, as shown in Chapter 7.

Therefore, from these two pilot experiments, an important lesson learned was that in order to obtain a good microseismic image, the velocities between the loading plates and the tested materials should be as small as possible.

[1]Lockout time is also called Re-arm Time Out. It is defined as the time for the detecting system to be ready to accept data of a new microseismic event after storing the data of a precedent microseismic event (PAC, 1995).

Appendix D: Sensitivity of the Microseismic Sensor

The Vallen Acoustic Emission system is a 16-bit system. The hardware measures voltage from $-5.000\ mV$ to $+5.000\ mV$. The system has a preamplifier of 40 dB, i.e., 100 times, for each channel. The YD-8 acceleration sensor has a sensitivity of $\pm(0.4 \sim 1.0)\ mV/(m/s^2)$. Based on this information, the theoretical sensitivity can be estimated as follows:

1. The hardware resolution, R:

$$\begin{aligned} R &= \frac{1}{\frac{2^{16}}{2} - 1} \\ &= \frac{1}{32,767} \end{aligned} \tag{D.1}$$

2. Minimum measurable change of voltage, V_{min} :

$$\begin{aligned} V_{min} &= \pm 5.000\ mV \times R \\ &= \pm 5.000\ mV \times \frac{1}{32,767} \\ &= \pm 0.15\ mV \end{aligned} \tag{D.2}$$

3. True minimum measurable change of voltage before the 40 dB pre-amplifier, V_{min_true} :

$$\begin{aligned} V_{min_true} &= \frac{V_{min}}{100} \\ &= \pm 0.0015\ mV \end{aligned} \tag{D.3}$$

4. Minimum measurable acceleration at the sensor, i.e., sensitivity, a_{min_true} :

$$\begin{aligned} a_{min_true} &= \frac{V_{min_true}}{\pm(0.4 \sim 1.0)\ mV/(m/s^2)} \\ &= \frac{\pm 0.0015\ mV}{\pm(0.4 \sim 1.0)\ mV/(m/s^2)} \\ &= (0.0015 \sim 0.0038)\ m/s^2 \\ &= (1.5 \sim 3.8) \times 10^{-12}\ mm/\mu s^2 \end{aligned} \tag{D.4}$$

So the theoretical sensitivity of this system is $(1.5 \sim 3.8) \times 10^{-12}\ mm/\mu s^2$. Comparing this sensitivity to the simulation results in Chapter 4, it is obvious that the hydraulic fracturing induced microseismics are strong enough to be detected by this system.

Appendix E: Location Results of Experiment HF1

Table E.1: Location results of the Jackfork sandstone test

No.	MSID	WvSet	Mag.	X_0.mm	Y_0.mm	Z_0.mm	D_{res}.mm	t_{res}.μs
1	29	435	291	-26.8	19.1	-31.2	9.05	2.05
2	55	825	298	2	-10.9	29.7	9.05	5.05
3	92	1380	408	18.6	-4.9	-1	8.05	1.05
4	94	1410	261	-11.4	4.2	-5.1	8.05	2.05
5	105	1575	132	-7.5	7.4	3.9	9.05	1.05
6	119	1785	242	5.7	2.7	2.8	7.05	2.05
7	147	2205	286	-12.7	11.1	23.2	9.05	3.05
8	363	5197	483	40.9	-20.1	-56.9	8.05	5.05
9	517	6737	121	-47.1	21.4	-8.6	9.05	9.05
10	576	7419	215	17.4	5.2	29.6	9.05	4.05
11	591	7635	222	60.3	-49.7	-21.8	8.05	3.05
12	592	7650	181	33.2	-6.7	-27.5	8.05	3.05
13	593	7665	586	-4	37.8	57	7.05	8.05
14	600	7770	417	-32.1	-4.2	-22	7.05	0.05
15	621	8085	196	29.2	-18.2	-17.2	9.05	1.05
16	650	8520	321	17.8	4.2	13.4	9.05	1.05
17	665	8745	193	15.8	-10.6	6.9	8.05	2.05
18	666	8760	111	33.8	-14	5.1	7.05	2.05
19	676	8910	114	78.7	-33.3	-9.7	9.05	2.05
20	677	8925	226	-9.1	-1.7	15	9.05	3.05
21	682	9000	459	38.1	-28.4	0.4	7.05	4.05
22	685	9015	308	-19.3	-3.8	23.2	9.05	2.05
23	715	9495	366	1.8	10.7	11.1	9.05	3.05
24	726	9660	211	-70.8	12.8	4	9.05	5.05
25	728	9690	204	8.3	-0.9	12.4	7.05	4.05
26	738	9840	105	-4.6	3.7	5.9	8.05	1.05
27	743	9915	161	-5.9	-0.7	-9.5	9.05	1.05
28	754	10080	402	8.1	-27.7	-3.5	8.05	4.05
29	757	10125	132	-46.3	16.7	3.2	8.05	2.05
30	760	10170	109	3.2	-2.8	2.4	7.05	1.05
31	764	10230	118	-35	14.7	33.1	9.05	2.05
32	781	10485	154	0	-23	2.6	9.05	1.05
33	785	10545	162	-49.7	-20.7	35.2	8.05	5.05
34	791	10635	174	25.9	-7.8	31.7	7.05	2.05
35	795	10695	130	-70.8	39.7	-16.5	9.05	2.05
36	803	10815	344	-40.6	-0.3	13.8	9.05	0.05
37	805	10845	132	25	-4.2	2.7	7.05	3.05
38	814	10980	376	-20.3	27.5	19.4	8.05	5.05
39	819	11055	181	11.5	-5.3	13.7	9.05	1.05

Table E.2: Location results of the Jackfork sandstone test (Cont. 1)

No.	MSID	WvSet	Mag.	X_0.mm	Y_0.mm	Z_0.mm	D_{res}.mm	t_{res}.μs
40	824	11130	165	-14.6	-8.7	1.5	9.05	1.05
41	838	11340	115	-82.3	13.3	27.5	9.05	3.05
42	857	11625	179	-10.9	32.5	20.3	8.05	5.05
43	868	11790	120	15.2	-8.8	-5.5	9.05	2.05
44	872	11850	115	-60.2	12.3	62.3	8.05	2.05
45	877	11925	166	-31.1	10.7	12.2	9.05	2.05
46	879	11955	198	-16.4	3.6	-1.3	8.05	1.05
47	887	12075	470	10	-8.2	4	8.05	3.05
48	896	12210	575	-15.7	6.7	10.3	8.05	3.05
49	907	12375	135	-10	3	8.4	9.05	2.05
50	912	12450	171	11.5	-7.5	-3.3	8.05	3.05
51	934	12780	98	-20.3	-9.3	19.3	7.05	5.05
52	935	12795	212	-28.6	2.3	8.8	8.05	1.05
53	970	13320	344	-53.2	-4.1	-5	9.05	1.05
54	977	13425	198	58.1	-4.9	-3.3	7.05	4.05
55	988	13590	101	4.6	0.3	16.5	9.05	2.05
56	990	13620	157	-51.2	6.4	4.4	7.05	2.05
57	996	13710	181	17.5	-16.8	-6	9.05	2.05
58	997	13725	103	-16.5	7.1	-7.5	8.05	0.05
59	1006	13860	131	42.9	-3.9	-10.6	9.05	4.05
60	1037	14325	134	1.8	5.7	13.7	9.05	3.05
61	1040	14370	169	-13.6	3.9	11.6	7.05	1.05
62	1063	14715	421	-22.6	33.9	10.5	9.05	4.05
63	1066	14760	305	5.2	-2.5	9.3	7.05	4.05
64	1074	14880	106	36.2	-12.1	2.4	8.05	2.05
65	1083	15015	138	22	-5.3	-2.9	8.05	1.05
66	1092	15150	282	3.6	-3.9	23.4	8.05	3.05
67	1093	15165	285	-22.2	-0.7	2.8	9.05	1.05
68	1223	17115	178	-5.5	1.3	15.5	8.05	3.05
69	1266	17760	275	-20.1	-2.7	30.5	9.05	4.05
70	1274	17880	148	29.1	-20.3	29	9.05	3.05
71	1275	17895	200	3.1	5.6	-33.1	7.05	2.05
72	1280	17970	210	-69.2	18.7	26.6	9.05	4.05
73	1281	17985	157	36.2	-13.2	18.8	8.05	4.05
74	1293	18165	93	43.7	-15.1	23.9	6.05	2.05
75	1301	18285	196	-6.9	8.2	39.2	9.05	3.05
76	1363	19215	287	40.8	-29.2	-2.3	9.05	5.05
77	1393	19665	290	31.3	21.4	-19.2	8.05	5.05
78	1398	19740	388	32.6	-53	1.6	9.05	5.05

Table E.3: Location results of the Jackfork sandstone test (Cont. 2)

No.	MSID	WvSet	Mag.	X_0,mm	Y_0,mm	Z_0,mm	D_{res},mm	t_{res},μs
79	1419	20055	191	-57.1	34.7	27	9.05	1.05
80	1476	20910	128	-73.7	-1.7	-14.5	7.05	4.05
81	1503	21315	115	86.7	-16	-6.6	9.05	2.05
82	1536	21810	143	82.1	-19.1	-2.3	8.05	4.05
83	1571	22335	426	12.1	-40.7	7.9	8.05	3.05
84	1579	22455	295	29.4	-55	-6.5	8.05	2.05
85	1591	22635	298	29.3	-5.4	10.4	6.05	2.05
86	1605	22845	277	41.6	-8.9	-5.3	7.05	4.05
87	1619	23055	347	-15.1	-0.4	38.2	9.05	3.05
88	1632	23250	315	-75.5	13.7	45.3	8.05	1.05
89	1637	23325	296	-62.2	-5.5	5.5	9.05	0.05
90	1657	23625	162	-36.7	-7.5	4.9	9.05	2.05
91	1681	23985	433	37.8	-48.2	22.7	8.05	2.05
92	1683	24015	174	-19.7	-9.1	-21.1	7.05	4.05
93	1697	24225	198	-0.2	7.4	-21.8	9.05	3.05
94	1702	24300	303	-89.2	31	53.2	7.05	1.05
95	1768	25290	184	57.3	-45.8	15.2	7.05	5.05
96	1784	25530	341	21.3	-8.5	23.7	8.05	5.05
97	1820	26070	129	-8.2	1.3	5.3	9.05	2.05
98	1831	26235	279	-53	37.4	17.7	8.05	2.05
99	1851	26535	158	-18.2	-2.8	-15	9.05	3.05
100	1852	26550	190	7.6	3.5	-0.3	9.05	2.05
101	1875	26895	244	-47.9	3.4	-6.5	7.05	2.05
102	1878	26940	110	17.7	-3.2	-12.1	9.05	1.05
103	1910	27420	193	-52.3	6.3	-11	9.05	2.05
104	1911	27435	128	-1	2.4	11.7	7.05	1.05
105	1913	27465	140	20.4	-14.4	15.8	9.05	2.05
106	1924	27630	91	11.8	-0.7	-20.2	8.05	2.05
107	1928	27690	106	13.1	-10.5	-0.9	8.05	0.05
108	1933	27765	140	0.3	-7	26.8	30.05	8.05